UNIVERSITY OF VERONA
DEPARTMENT OF MEDICINE
Health and Life Sciences PhD School

PhD IN BIOMOLECULAR MEDICINE
Biochemistry curriculum
XXXVI cycle

GCAP1 in Autosomal Dominant Cone-Rod Dystrophy: A Multifaceted Biochemical Investigation and Therapeutic Perspectives

S.S.D. BIO/10

Course Coordinator:
Prof.ssa Lucia De Franceschi

Supervisior:
Prof. Daniele Dell'Orco

PhD Candidate:
Amedeo Biasi

Creative Commons Licensing Disclaimer

"GCAP1 in Autosomal Dominant Cone-Rod Dystrophy: A Multifaceted Biochemical Investigation and Therapeutic Perspectives"

Amedeo Biasi

August 14, 2024

Abstract

University of Verona

Ph.D. Course in Biomolecular Medicine, XXXVI Cycle

Doctor of Philosophy

GCAP1 in Autosomal Dominant Cone-Rod Dystrophy: A Multifaceted Biochemical Investigation and Therapeutic Perspectives

Amedeo Biasi

Vision, the sense that enables light perception and image formation, begins with the intricate process of phototransduction in the retina. This biochemical cascade converts photons into electrical signals, triggering sight. Central to this process are photoreceptor cells, rods and cones, which employ a complex array of proteins to transduce light into neural signals. Among these proteins, guanylate cyclase-activating proteins (GCAPs) and retinal degeneration protein 3 (RD3) play a crucial role in modulating the vision process. By sensing subtle changes in intracellular Ca^{2+} levels, GCAP dimers regulate the activity of guanylate cyclases (GCs), enzymes responsible for synthesizing cyclic guanosine monophosphate (cGMP). Within human photoreceptors, GCAP1 appears to be the main actively participating in this process, serving as a regulator of GC1 isozyme. RD3 further modulates this pathway by vehiculating GC1 from the inner to the outer segment of photoreceptors and strongly inhibiting its activity, thus representing a critical regulatory factor in the phototransduction cascade. This concerted regulation is essential for maintaining the homeostasis of cGMP and Ca^{2+} levels, crucial second messengers in photoreceptors, ensuring the proper function of the visual process. Studying GCAP1 and its interactions within the phototransduction pathway is vital for understanding the fundamental mechanisms underlying vision and the pathogenesis of inherited retinal dystrophies (IRDs) caused by mutations in this protein. Disruptions in

the GCAP-mediated feedback mechanism can lead to abnormal photoreceptor responses and, ultimately, progressive vision loss. Therefore, investigating the biochemical and biophysical characteristics of GCAP1 variants and their impact on photoreceptor functionality provides critical insights into the biochemical signatures of IRDs. This thesis investigates the molecular basis and therapeutic avenues for autosomal dominant cone dystrophy (adCOD) and cone-rod dystrophy (adCORD), focusing on mutations in the *GUCA1A* gene coding for GCAP1. Through biochemical and computational investigations it elucidates the impacts of the N104H-GCAP1 and E111V-GCAP1 variants on photoreceptor functionality. The N104H mutant, characterized by a novel missense mutation in *GUCA1A*, reveals a unique biochemical profile with diminished calcium sensitivity and doubled affinity for retinal guanylate cyclase 1 (GC1), diverging from previously studied mutations and suggesting a mechanism for photoreceptor cell degeneration through aberrant cGMP and calcium accumulation. On the other hand, the E111V variant maintains the monomer-dimer equilibrium essential for phototransduction, despite its constitutive activation of GC1, indicating the mutation's specific impact on enzyme stimulation rather than the dimerization processes. Molecular docking and dynamics simulation highlight the subtle alterations induced by the E111V substitution, offering insights into its enhanced mobility and altered interaction with GC1. Moreover, the strong inhibitory activity of RD3 was successfully exploited to modulate the abnormal cGMP production induced by the E111V variant, demonstrating RD3's potential in restoring photoreceptor cell homeostasis. In addition, the therapeutic potential of delivering recombinant GCAP1, both directly and via liposomes, is explored as a strategy to modulate the phototransduction cascade in IRDs. This approach proves that targeted protein delivery can effectively alter photoreceptor responses in mice models, marking a promising avenue for treating retinal diseases. Through a comprehensive analysis, this thesis provides novel insights into the complex regulatory mechanisms of phototransduction and underscores the potential of innovative therapeutic strategies for IRDs.

List of Figures

List of Equations

List of Abbreviations

5,5'Br2-BAPTA	5,5'-dibromo-1,2-bis(O-amino-phenoxy)- ethane-N,N,N,'N'-tetraacetic acid
AEC	anion exchange chromatography
APS	ammonium persulfate
BM	Buch's membrane
CD	circular dichroism
cGMP	3',5'-cyclic guanosine monophosphate
CMV	cytomegalovirus
COD	cone distrophy
CORD	cone-rod dystrophy
Da	Dalton
DLS	dinamyc light scattering
DTT	dithiothreitol
E.coli	Escherichia coli
EDTA	ethylenediaminetetraacetic acid
EGTA	ethyleneglycoltetraacetic acid
ELM	external limiting membrane
EV	extracellular vescicle
FF	force field
FFT	fast Fourier transform
FPLC	fast protein liquid chromatography
GC	guanylate cyclase

GCAP	guanylate cyclase-activating protein
GCL	ganglion cell layer
GDP	guanosine 5-diphosphate
GPCR	G protein-coupled receptor
GTP	guanosine 5-triphosphate
HPLC	high performance liquid chromatography
IMAC	immobilized metal ion affinity chromatography
INL	inner nuclear layer
IPL	inner plexiform layer
IPTG	isopropyl β-D-1-thiogalactopyranoside
IRD	inherited retinal dystrophy
IS	inner segment
LP	liposome
MCR	mean count rate
MD	molecular dynamics
MRE	mean residue ellipticity
MSD	mean square displacement
NCS	neuronal calcium sensor
NFL	nerve fiber layer
NMT	N-terminal myristoil transferase
OD	optical density
ONL	outer nuclear layer
OPL	outer plexiform layer
OS	outer segment
PCA	principal component analysis
PDE6	phosphodiesterase 6
PEI	polyethylenimine
R.U.	resonance unit

RD3	retinal degeneration protein 3
ROS	rod outer segment
RPE	retinal pigmented epithelium
SDS	sodium dodecyl sulfate
SDS-PAGE	SDS polyacrylamide gel electrophoresis
SEC	size cxclusion chromatography
TEMED	N,N,N',N'-tetramethyl-ethane-1,2-diamine
UV	ultraviolet

Index

Introduction

1 Functional Architecture of the Human Retina

The human retina is a neural tissue located at the back of the eye and serves as the critical sensory component responsible for capturing and processing visual information, including reading this thesis. Its architecture is elegantly organized, with five major neuronal cell classes including photoreceptor cells, bipolar cells, amacrine cells, and retinal ganglion cells, playing essential roles in encoding and transmitting visual data. Photoreceptors, categorized into rods and cones and located in the outer nuclear layer (ONL), trigger the initial stages of visual processing, with rods demonstrating extraordinary sensitivity to light, particularly suited for dim-light vision, and cones specializing in bright-light, high-acuity color vision [12]. Photoreceptors synapse onto bipolar cells, with synaptic transmission modulated by horizontal cells, resulting in the establishment of ON and OFF pathways, critical for processing changes in light intensity [13]. Within the inner plexiform layer (IPL), bipolar cells engage in intricate interactions with retinal ganglion cells and amacrine cells, facilitating the integration and conveyance of visual signals to higher visual centers in the brain (**Figure 1**).

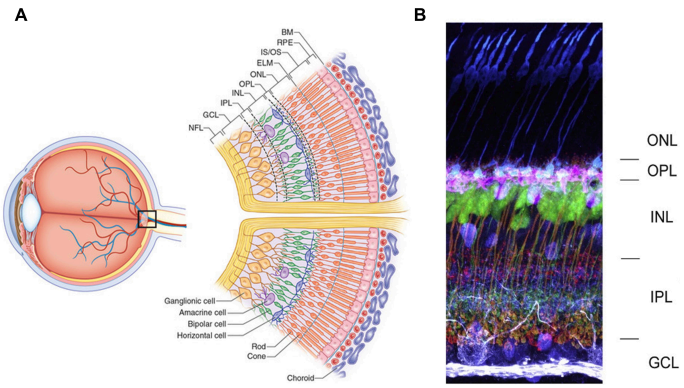

Figure 1 – (**A**) Schematic representation of the human eye: nerve fiber layer (NFL), ganglion cell layer (GCL), inner plexiform layer (IPL), inner nuclear layer (INL), outer plexiform layer (OPL), outer nuclear layer (ONL), external limiting membrane (ELM), inner and outer segments of photoreceptors (IS/OS), retinal pigment epithelium (RPE), Bruch's membrane (BM). (**B**) Immunostaining performed on mouse retina highlighting the major retinal components. Adapted from [1]

1.1 The Phototransduction Cascade

Phototransduction is an intricate biochemical process that converts light stimuli into electrical signals within the photoreceptor cells of the retina. This complex mechanism, shared by both vertebrate and invertebrate species [14], takes place in rod and cones outer segments and is modulated by the levels of the second messengers cyclic guanosine monophosphate (cGMP) and Ca^{2+} [15]. In the absence of light, cGMP maintains cation channels open in the plasma membrane of the photoreceptor outer segment, allowing the influx of Na^{+} and Ca^{2+}, thus maintaining a depolarized state and continuous glutamate release. Phototransduction commences with light-induced isomerization of 11-cis-retinal to the all-trans form within cone and rod opsins. All-trans-retinal promotes conformational variations in the structure of the opsin leading to the formation of an active intermediate. This cascade, initiated by photons rather than chemical ligands, exemplifies a general mechanism in G protein-coupled receptors (GPCRs) signaling, showcasing their typical ligand activation pattern [16]. During phototransduction, the ligand, specifically 11-cis retinal in this case, transitions from an inverse agonist in its dark state to an agonist upon light absorption. The activation of cone and rod opsins catalyzes the exchange of GDP for GTP on the α-subunit of a heterotrimeric G-protein, transducin, thereby conveying the signal to downstream effector proteins (**Figure 2**). Multiple activated transducin molecules ensue signal amplification within the photoreceptor by activating phosphodiesterase 6 (PDE6) which in turn hydrolyzes cGMP, closing cation-permeable ion channels. As a result, the cell membrane undergoes hyperpolarization leading to a drastic drop of intracellular Ca^{2+} concentration from $\sim$ 500 nM to less than 100 nM [17, 18].

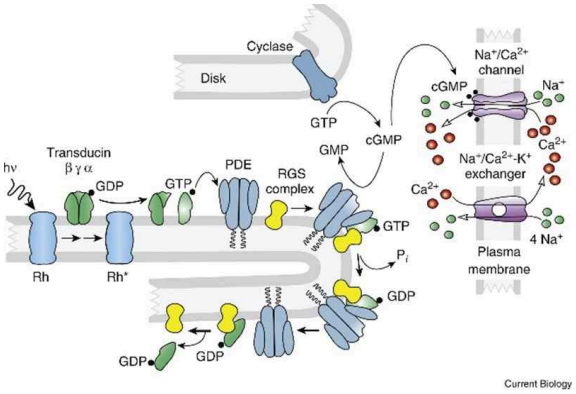

Figure 2 – Schematic representation of the phototransduction cascade occurring in cones and rods outer segments. Adapted from [2]

Alterations in the levels of second messengers cGMP and Ca^{2+}, evoked by light exposure within the photoreceptor outer segment, trigger critical feedback mechanisms which are vital for the appropriate shut-off of the phototransduction cascade and for adjusting to varying light and dark conditions [19, 20]. Subtle variations in intracellular Ca^{2+} concentration strongly influence such regulatory processes and are sensed by guanylate cyclase-activating proteins (GCAPs). GCAPs emerge as key modulators in photoreceptors [21] by finely tuning the balance between guanylate cyclase (GC) and PDE6 activities, effectively adjusting cGMP levels in accordance with Ca^{2+} content. Retinal membrane GC is present as two isozymes, GC1 and GC2 [22, 23] and their concerted action represents the exclusive source of cGMP during phototransduction. Nonetheless, GC1 and GC2 display differential contributions to cGMP synthesis in photoreceptors, along with distinct distribution patterns between rod and cone cells [24, 25, 26]. GC1 is considered to be the main isozyme of the cyclase and predominates in both cell types, with a major role in cGMP production in rods ($\geq$70%), while GC2 acts as a supplementary component and is almost undetectable in cone cells. In their functional state, GC1 and GC2 are present as homodimers and they share a similar domain structure (**Figure 4**) consisting of an extracellular domain (ECD) primarily exposed in the intradiskal space in photoreceptor outer segments, while the cytoplasmic portion includes kinase-homology (KHD) and catalytic domains (CAT) connected by a dimerization domain (DD). In addition, by complementing the action of GCAPs, the regulation of cGMP homeostasis in phototransduction is further enhanced by retinal degeneration protein 3

(RD3) [3]. Among its functions, elucidated later in this thesis (see 1.3), RD3 acts as a critical inhibitor of GC1 in a Ca^{2+}-independent manner, adding another layer of control over cGMP synthesis. By suppressing GC1 activity in the photoreceptor's inner segment, RD3 effectively modulates cGMP levels, preventing excessive activation that could lead to photoreceptor degeneration.

1.2 Guanylate Cyclase-Activating Proteins (GCAPs): focus on GCAP1

Guanylate Cyclase-Activating Proteins (GCAP1-5) are a subfamily of the neuronal Ca^{2+}-sensor (NCS) proteins within the EF-hand superfamily of Ca^{2+}-binding proteins [27, 28, 29, 30]. These proteins modulate the activity of membrane-bound GCs in a Ca^{2+}-dependent manner, playing an essential role in shaping the photoresponse of both rod and cone cells under varying light conditions [31]. In this thesis, we will focus on the most ubiquitous form among different species, GCAP1 [32], an alpha-helical 23 kDa protein comprising a non-metal binding EF-hand (EF1), 3 active EF-hand motifs (EF2-4) able to accommodate either 3 Ca^{2+} or at least one Mg^{2+} ion in EF2-3-4 and EF2-3 respectively [33, 34, 35] and a covalently attached myristoyl group to the N-terminal glycine (**Figure 3**).

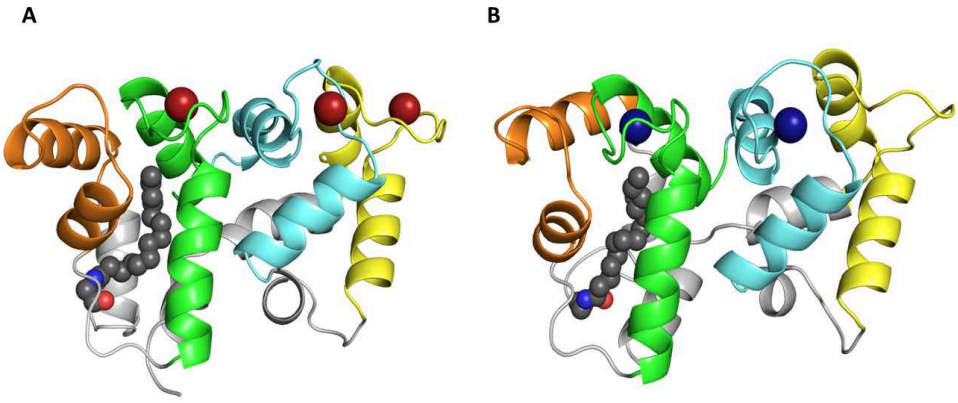

Figure 3 – Cartoon representation of the three-dimensional homology model of human WT-GCAP1 in its inhibiting (**A**) and activating (**B**) state; EF1 is colored in orange, EF2 in green, EF3 in cyan and EF4 in yellow. N and C-terminal are represented in light grey while the myristoyl group is represented as grey spheres and colored according to secondary structure. Ca^{2+} and Mg^{2+} ions are represented as red and blue spheres.

While losing the typical bipiramidal-pentagonal coordination of divalent cations during evolution due to substitutions in conserved residues (Cys29 and Pro30) [36, 37], EF1 comprises residues fundamental for the interaction with the target enzyme, GC1 [36, 38, 39]. While for some NCS proteins, N-terminal myristoylation is fun-

damental to provide an anchorage to cellular membranes in a process called Ca^{2+}-myristoyl switch [40, 41] and promotes Ca^{2+}-induced membrane targeting [40, 42], GCAP1 represents an exception since the attached fatty acyl group lays buried in the hydrophobic core of the protein [36] as demonstrated by both the Ca^{2+}-bound crystal structure [43] and the Mg^{2+}-bound NMR structure [35]. GCAP1 regulates GC1 activity by forming a functional dimer [36, 35], with a monomer-dimer equilibrium that fluctuates and is influenced by Ca^{2+} or Mg^{2+} binding [44] [**Paper 2**]. The dimerization process is driven by intermolecular hydrophobic interactions between the side chains of residues H19, Y22, F73, and V77, and substitution at these amino acids have been shown to dramatically impair GCAP1 assembly, highlighting their critical role in dimer formation [32]. In light-exposed rods, binding of Mg^{2+} to GCAP1 is required to secure a stable form of the protein to activate GC1, thereby promoting the synthesis of cGMP and the ongoing phototransduction cascade [22, 45]. On the other hand, in the dark-adapted state, replenishment of cGMP levels restores Ca^{2+} influx in the cell, thus promoting the association of the Ca^{2+}-bound form of GCAP1 which dims GC1 activity to a sub-basal level (**Figure 4**) [46].

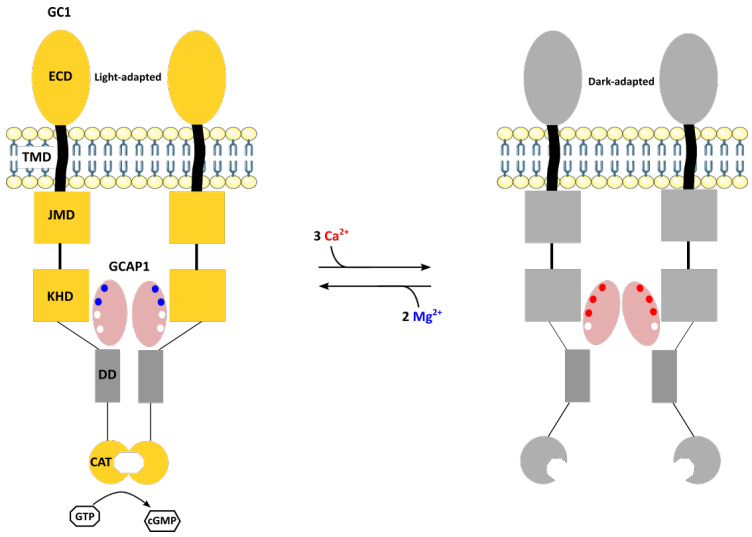

Figure 4 – Main structure of GC1 and its regulation by GCAP1 in light- (left) and dark-adapted (right) conditions: extracellular domain (ECD), trans-membrane domain (TMD), juxtamembrane domain (JMD), kinase homology domain (KHD), dimerization domain (DD) and catalytic cyclase domain (CAT). Ca^{2+} ions are depicted as red dots while Mg^{2+} ions as blue dots.

1.3 Retinal Degeneration Protein 3 (RD3)

Distinct from the well-established role of GCAPs in modulating GC activity in response to light-induced Ca^{2+} concentration changes, RD3 emerges as a high-affinity modulator of GC1, strongly inhibiting the cyclase activity at submicromolar concentrations [3, 47]. Such inhibition is fundamental both in the absence and presence of GCAPs, underscoring RD3s pivotal role in maintaining GC activity within optimal physiological ranges. In the absence of GCAP1, RD3 ensures controlled basal activity of the cyclase, while in light-induced conditions, RD3 competes with Mg^{2+}-bound GCAP1 for GC1, thus preventing excessive cGMP production. RD3 is also involved in the trafficking of GC1 from the endoplasmic reticulum to the outer segment, and this association not only drives the translocation process but also acts as a regulatory mechanism to prevent premature or inappropriate activation of GC1 by GCAP1 in the inner segment [48, 49, 50] (**Figure 5**).

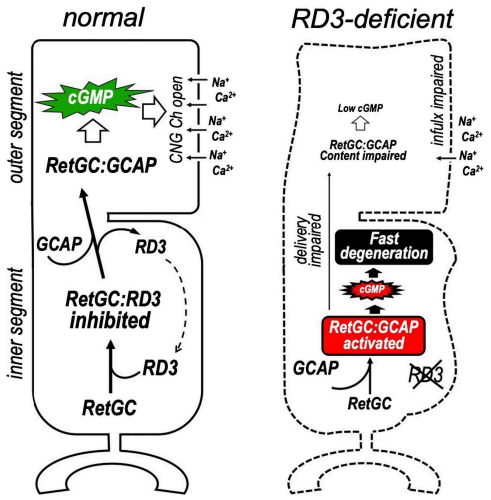

Figure 5 – Diagram illustrating the functional impact of RD3 on photoreceptor cells. Normal photoreceptors utilize RD3 for GC transport to the outer segment and to prevent premature activation by GCAPs. RD3 deficiency leads to reduced cyclase levels in the outer segment, impaired phototransduction due to suboptimal cGMP synthesis, and photoreceptor degeneration caused by abnormal GC activation. Taken from [3]

Furthermore, RD3's functional significance has been elucidated in the context of retinal degenerations, as mutations impairing RD3 expression or its interaction with GC1 lead to a substantial reduction of GC1 levels in the photoreceptor outer seg-

ment, consequently leading to retinal degeneration [51, 52]. Additionally, RD3 does not completely shut down GC1 activity, most likely due to the yet unclarified interaction with endogenous GCAP1 [53], further highlighting the remarkable regulatory role that RD3 plays in the phototransduction cascade. Ultimately, RD3 is able to attenuate the abnormal cGMP production induced by the pathogenic E111V-GCAP1 variant [**Paper 2**], known to constitutively activate GC1 and lead to progressive retinal degeneration, thus representing an interesting therapeutic tool to modulate the anomalous activity of GC1. RD3 structure comprises a 143 amino acid stretched α-helical bundle with a long unstructured loop connecting helices α1 and α2. The structure's stability is ensured by a core of hydrophobic residues, including Leu29, Leu33, Phe100, Val114, Phe118, and Leu122, which form the internal structure of the helix bundle [54]. RD3 plays a central role in inhibiting GC1, as proven by site-directed mutagenesis, which pinpointed essential surface-exposed residues for this purpose, notably in the loop between helices α1 and α2 (*i.e.* cluster 1) and on the surface of helix α3 (*i.e.* cluster 2) [4]. These two clusters are defined by specific residues, some of which are critically involved in the association with GC1: Tyr60, Trp62, and Leu63 from cluster 1 in the loop connecting α1 and α2, and Arg99, Arg101, and Gln102 from cluster 2 on α3 (**Figure 6**).

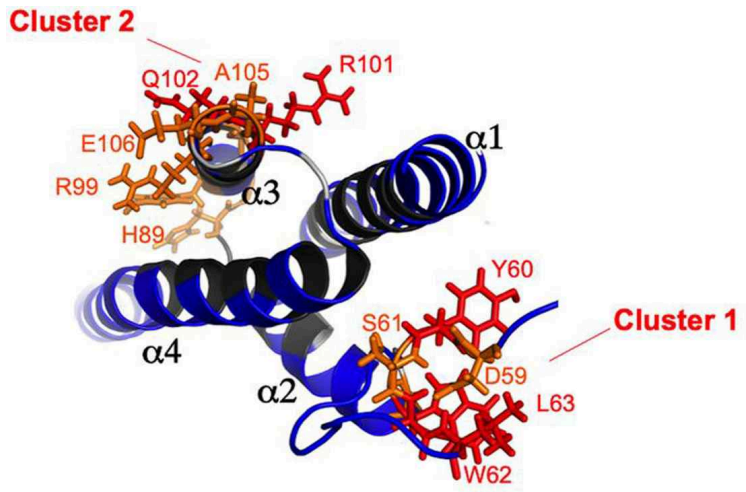

Figure 6 – Cartoon representation of the three-dimensional NMR structure of RD3 (PDB entry: 6DRF) reporting the two key clusters critical for high-affinity inhibitory binding to GC1. Critical binding residues are highlighted in red, moderately involved residues in orange, and non-critical residues in blue. Adapted from [4]

1.4 Inherited Retinal Dystrophies (IRDs)

IRDs encompass a broad spectrum of genetic disorders affecting photoreceptor structure, metabolic processes, transcription factors, and phototransduction proteins, resulting in progressive visual impairment and eventual blindness [55]. These rare diseases manifest in diverse clinical forms, ranging from isolated retinal disorders affecting the macula (e.g. Stargardt disease, Best disease [56, 57]) to multisystemic diseases involving the entire retina. The latter include disorders such as retinitis pigmentosa (RP) that typically affects the rod system, leading to night blindness and peripheral vision loss [58] (**Figure 7**, central panel), while the cone system is affected in cone dystrophies, manifesting as loss of central vision and color vision defects [55, 59][**Paper 2**]. In particular, autosomal-dominant cone dystrophy (adCOD) and cone-rod dystrophy (adCORD) represent severe forms of IRDs. adCOD primarily impacts cone photoreceptors, responsible for the photopic response, leading to early symptoms like reduced visual acuity, color vision defects, and photophobia [60] (**Figure 7**, right panel). Similarly, adCORD initially affects cone photoreceptors and later involves rod photoreceptors, responsible for peripheral and scotopic vision. This progression in adCORD leads to a broad range of symptoms, including night blindness and peripheral vision loss, following the initial central vision impairment [61, 62].

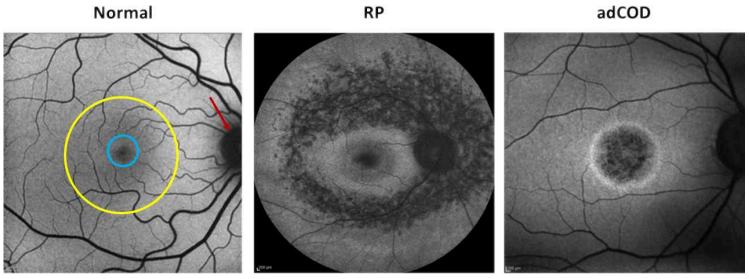

Figure 7 – Fundus autofluorescence images of: (left panel) normal human retina showing the fovea (blue circle), the macula (yellow circle) and the optic nerve (red arrow), (central panel) patient affected by retinitis pigmentosa and charachterized by a peripheral degeneration of rod opsins [5] and (right panel) macular degeneration phenotype induced by the N104H-GCAP1 mutant (**Paper 2**).

At the molecular level, many IRDs, including adCOD and adCORD, are often linked to disruptions in the homeostasis of key second messengers in photoreceptor cells, particularly Ca^{2+} and cGMP. As previously highlighted, an essential regulator in this context is GCAP1 which plays a pivotal role in the recovery phase of phototransduction by regulating GC1. Mutations in *GUCA1A* have been found to promote various forms of IRDs, including adCOD, adCORD, and macular dystrophy (MACD) [63, 64, 65, 66, 67, 68, 69, 70, 71, 72, 73, 74]. Such mutations affect residues located in different hot-spots of GCAP1 (e.g. dimerization interface, GC1-contacting patch, Ca^{2+}-binding loops) and lead to an improper regulation of GC1 activity, resulting in the abnormal accumulation within retinal cells of Ca^{2+} and cGMP. The overgathering of second messengers potentially trigger mechanisms such as apoptosis, ultimately leading to photoreceptor cell degeneration [75]. These considerations highlight the complexity and critical role of GCAP1 in maintaining photoreceptor health and underscore the ongoing need for research in this area to develop effective therapies for IRDs.

2 Liposomes as Therapeutic Protein-Delivery Nano Carriers

adCOD and adCORD are currently incurable due to their complex genetic nature and often dominant transmission, making gene therapy in this context a complex challenge. Indeed, while representing the most intriguing therapeutic approach for IRDs treatment [76], genome editing approaches are still denoted by some limitations like: *(i)* an increased propensity for oncogenesis induced by the incorporation of viral genome into the host DNA, *(ii)* the limited housing-compartment of viral vectors does not allow for the delivery of large genes and *(iii)* the anti-viral immune responses solicited by viral vescicles [77]. This necessitates alternative treatment strategies, such as protein delivery systems, to mitigate the effects of mutations and restore physiological functionality. Liposomes, spherical vesicles composed of phospholipids, are excellent candidates for this task due to their biocompatibility, biodegradability, and ability to encapsulate a variety of substances including proteins [78]. Initially conceptualized in the mid-1960s [79], liposomes have since evolved into versatile drug delivery vehicles [80]. They range in size from nanometers to micrometers and can be unilamellar (ULV) or multilamellar (MLV), enclosing an aqueous compartment ideal for housing therapeutic agents (**Figure 8**). Their phospholipid bilayers protect encapsulated substances from degradation, extend drug half-lives, offer controlled release mechanisms and is able to accomodate hydrophobic molecules [81]. Phospholipidic composition on their surface can be finely tuned in order to allow tissue specific release of their content while maximizing therapeutic efficacy and minimizing side effects [82, 81]. Their ability to deliver high molecule concentrations, along with the potential for targeted delivery, is particularly relevant in the context of adCOD and adCORD since it has been shown *in vitro* that wild-type GCAP1 could partially compensate the aberrant GC1 activation induced by mutant GCAP [83], especially if supplied in combination with RD3 [**Paper 2**]. During this thesis work, two types of ROS-like liposomes have been produced: condensed DNA- and protein-loaded liposomes. The former, conceptu-

alized over a gene-supply approach, saw the utilization of polyethylenimine (PEI) as condensing agent [84, 85] to compact GFP-expressing cytomegalovirus (CMV) DNA and follow its photodistribution among retinal layers. While preliminary data about the stability over time and size of DNA-loaded liposomes is reported (**Figures 12** and **18**), future studies will be conducted to investigate their functionality and reliability as an effective gene-supply approach. On the other hand, protein-loaded lipid vescicles, involved the conjugation of CF640R (Biotium, Fremont, CA, USA), a far-red fluorescent dye, to GCAP1 offering a valuable tool for monitoring the distribution and localization of delivered protein within the retinal tissue. The efficacy of liposomes as vehicles for transporting small molecules and proteins was determined through the analysis of size and uniformity in distributions by means of dynamic light scattering (DLS) and nanoparticle tracking analysis (NTA) techniques. Interestingly, liposomes have already proven to be a viable option to effectively deliver recombinant GCAP1 *in cyto* and *in vivo* and induce a pathogenic phenotype upon E111V-GCAP1 administration [**Paper 3**], paving for promising protein-delivery therapeutic approaches as an alternative to the most challenging gene therapies.

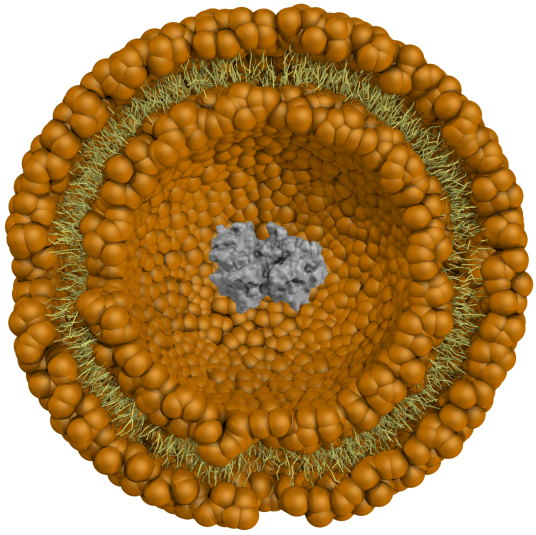

Figure 8 – Representative coronal section of liposomes strucure. Phospholipids hydrophilic heads are depicted as golden spheres, hydrophobic tails as yellow sticks and enclosed GCAP1 as grey surface. Image obtained using PyMOL software (v. 2.2.3, Schrödinger, [6]).

Materials & Methods

3 Expression and Purification of Recombinant GCAP1 and RD3

The accurate *in vitro* characterization of proteins heavily relies on the precise implementation of expression and purification techniques to achieve high-purity protein samples. This not only ensures the reliability of the data obtained but also facilitates a deeper understanding of the intricate relationships between structure and function in proteins [86]. In this thesis recombinant DNA transformation was employed to express human GCAP1 (UniProt entry: P43080) and RD3 (UniProt entry: Q7Z3Z2) in *E.coli* cells, the most commonly used prokaryotic host for recombinant protein production thanks to its ease of genetic manipulation, rapid growth, and cost-effectiveness [87, 88]. The pET-11a vector was employed for cloning both wild-type human GCAP1-E6S, GCAP1-E6S-His-tag cDNAs and mutant E111V-GCAP1. The rationale behind introducing the E6S modification was to create a consensus sequence amenable to myristoylation at the N-terminal post-translation by *S. cerevisiae* N-myristoyltransferase (yNMT), as detailed previously [89]. Subsequently, GCAP1 variants were expressed heterologously in BL21 *E. Coli* DE3 cells after co-transformation with pBB131-yNMT. Bacterial cells were grown for 4 hours at 37°C after the addition of myristic acid and IPTG to boost recombinant protein expression at 0.4 and 0.6 OD, respectively [90]. To isolate proteins from inclusion bodies, denaturation was achieved using 6 M guanidine-HCl, followed by renaturation through dialysis against a buffer consisting of 20 mM Tris-HCl pH 7.5, 150 mM NaCl, and 7.2 mM β-mercaptoethanol. The refolded WT- and E111V-GCAP1 variants were then purified through a series of chromatographic steps. Fast protein liquid chromatography (FPLC) is a crucial chromatographic technique that allows the sorting of different compounds, e.g proteins, in a heterologous solution by exploiting their biophysical properties like hydrophobicity, size or charge [91]. In particular,

purification of human GCAP1 variants involved preparative size exclusion chromatography (SEC, HiPrep 26/60 Sephacryl S-200 HR, GE Healthcare) followed by anion exchange chromatography (AEC, HiPrep Q HP 16/10, GE Healthcare) which represents a well-established pipeline for NCS purification [92].

His-tagged WT-GCAP1 was purified using a one-step affinity purification method, specifically the immobilized metal affinity chromatography (IMAC), employing 5 mL His-trap columns (Cytiva) and a linear imidazole gradient ranging from 0 to 500 mM. The concentration of the purified proteins was determined through the Bradford assay [93], utilizing a GCAP1-specific reference curve based on the amino acid hydrolysis assay (Alphalyze). Protein purity was assessed through a 15% SDS-PAGE gel, a powerful electrophoretic technique that allows separation of compounds on the basis of their molecular mass [94]. Subsequently, GCAP1 variants were exchanged with 50 mM NH_4HCO_3 buffer, lyophilized, and flash-frozen in liquid nitrogen. The samples were stored at -80°C until usage. RD3 expression and purification followed a different paradigm due to its high tendecy to aggregate in solution. The RD3 cDNA-containing plasmid, kindly provided by Professor Koch K.W. from the University of Oldenburg, was expressed in BL21 *E. coli* DE3 cells and purified through a series of centrifugation steps [47]. Briefly, harvested cells underwent mechanical lysis with 3 ultrasonication cycles (30s ON, 30s OFF). Following centrifugation at 10,000 x g for 10 min, the insoluble material was washed three times with a buffer consisting of 10 mM Tris-HCl pH 7.5, 2 mM EDTA, 14 mM β-mercaptoethanol, 100 μM PMSF, and 1X protein inhibitor cocktail (PIC). The resulting sample was centrifuged at 15,000 x g for 15 min, and the insoluble fraction was subjected to overnight denaturation using the aforementioned buffer supplemented with 8 M Urea. The following day, RD3 was renatured against 2 x 300 volumes of 10 mM Tris-HCl pH 7.5, 0.1 mM EDTA, and 14 mM β-mercaptoethanol, followed by centrifugation at 10,000 x g for 10 min. The supernatant, containing RD3, was collected to evaluate protein purity again via SDS-PAGE and stored at -80°C with 50% v/v glycerol to preserve its integrity.

4 Spectroscopic Charachterization

4.1 Circular Dichroism

Circular Dichroism (CD) spectroscopy, an invaluable tool in biomolecular research, provides essential insights into the secondary structure and conformational changes of proteins [95, 8, 96]. This technique leverages the differential absorption of left and right circularly polarized light by chiral centers in biomolecules, resulting in elliptically polarized light (**Figure 9**). The resulting CD spectrum offers a unique perspective on the microenvironment of these chiral centers, crucial for understanding protein structures.

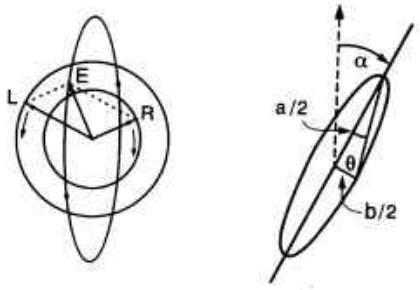

Figure 9 – Illustration of elliptically polarized light (E) generated by the different intensities of right (R) and left (L) circularly polarized components. Angle θ represents the ellipticity while α represents the optical rotation. [7]

The far-UV CD spectra, spanning 190-250nm, primarily highlight peptide bonds, offering critical insights into the protein's secondary structure. This includes the identification and quantification of α-helices, β-sheets, and random coil structures, each exhibiting distinct spectral patterns (**Figure 10A**). The near-UV CD spectrum (250-320 nm), on the other hand, allows the investigation in the microenvironment of aromatic amino acid side chains of phenylalanine, tyrosine, and tryptophan, thereby shedding light on the tertiary structure of proteins (**Figure 10B**). The ability to dissect the tertiary structure is especially beneficial in understanding the conforma-

tional dynamics and stability of recombinant proteins, which are central to their biological function and therapeutic efficacy [97].

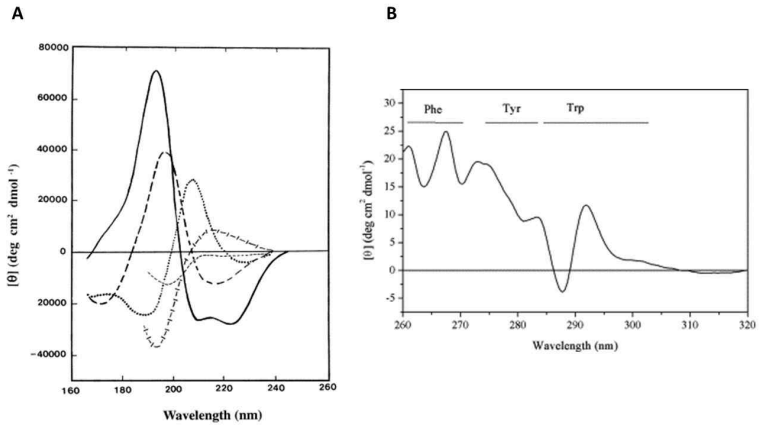

Figure 10 – Representative CD sepctra. (**A**) Far-UV spectra representing main secondary structures of proteins: α-helix (solid black line), anti-parallel β-sheet (long dashed line), type I β-turn (dotted line), poly (Pro) II helix (cross-dashed line), random coil (short dashed line). (**B**) Near-UV CD spectrum highlighting the optical contribution from Phe, Tyr and Trp side chains Adapted from [8]

CD spectroscopy's applicability extends to studying conformational changes in response to various stimuli, such as ligand binding or temperature shifts [98, 99]. This is particularly valuable in evaluating the structural stability and folding dynamics of recombinant proteins under different environmental conditions. For instance, changes in the CD spectra in the presence of different ions can reveal how metal binding affects the structure and function of specific proteins. Moreover, CD spectroscopy is adept at assessing thermal stability, allowing researchers to monitor the denaturation process of proteins under thermal stress. CD spectroscopy proved to be fundamental in the devolpment of this work and provided useful insights in conformational changes of GCAP1 variants upon Ca^{2+} and Mg^{2+}binding [**Paper 1**, **2** and **3**], their thermal stability [**Paper 1**] and the interaction with RD3ppt and RD3 [**Paper 2**]. Anaylises were conducted using a Jasco J-710 spectropolarimeter equipped with a Peltier-type cell holder and each recorded spectrum was an average of 5 accumulations. To mimick a physiological environment, experiments were carried out at 37°C and GCAP1 variants were resuspended in 20 mM Tris-HCl pH 7.5,

150 mM KCl, 1 mM DTT, while the peptide and full RD3 in 20 mM Tris-HCl pH 7.5, 1 mM DTT. Far-UV CD spectra of 10 µM proteins were acquired in a 0.1-cm quartz cuvette after addition of 300 µM EGTA and 300 µM free Ca^{2+}. Near-UV CD spectra of ∼35 µM GCAP1 variant or RD3 were recorded in a 1-cm quartz cuvette after serial additions of 500 µM EGTA and 500 µM free Ca^{2+}. Both far and near-UV were normalized according to mean residue ellipticity (MRE) using the following formula:

$$MRE = \frac{mdeg}{(\text{cm} \times [\text{mol/L}] \times \#\text{ of residues}) \times 10} \tag{1}$$

where $mdeg$ is the dichroic signal, cm is the path length, $[mol/L]$ is the protein concentration in the sample. Furthermore, thermal denaturation profiles of 4 µM N104H-GCAP1 were collected from 20°C to 96°C (scan rate 90°C/h) following the ellipticity signal at 222nm. While CD spectroscopy may not provide the high-resolution structural details obtainable through X-ray crystallography or NMR, its ease of use, rapid data acquisition, and minimal sample requirements make it an invaluable tool in protein research expecially if coupled with dynamic light scattering (DLS), which further enhances its utility in the comprehensive study of proteins and macromolecules.

4.2 Dynamic Light Scattering

Dynamic light scattering (DLS), by evaluating the Brownian motion of particles in solution, facilitates the determination of hydrodynamic diameters, polydispersity, and inter-particle interactions, which are crucial in understanding the colloidal stability of proteins [100, 101]. **Figure 11** summarizes the basic workflow of a DLS measurement. When a coherent and monochromatic light beam, typically a laser, radiates a colloidal solution, particles moving according to Brownian motion scatter the light, behaving as secondary light sources. The interference between the scattered radiation by these entities generates a time dependent variation of scattering intensity that is directly influenced by the diffusion coefficient of the particles. Since smaller molecules diffuse more rapidly than larger ones, they result in quicker fluctuations of the scattered light intensity compared to the slower oscillations exhibited by larger particles. The core principle of DLS revolves around the analysis of these fluctuations, carried out by processing the signal with the autocorrelation technique. The autocorrelation function, which follows an exponential decay for a suspension of monodisperse, spherical particles, is intimately related to the diffusion coefficient of the particles. Consequently, using the Stokes-Einstein equation [102, 101], one can derive the equivalent sphere radius of the particles, representing the hydrodynamic radius R :

$$D = \frac{k_B T}{6\pi\eta R} \tag{2}$$

where D is the diffusion coefficient [m²/s], k is Boltzmann's constant [m²kg/Ks²], T is the absolute temperature [K] and η is the solvent viscosity [Pa.s]. The technique is highly sensitive to the sample's quality, and it's recommended that samples be preferably filtered to remove large aggregates and other contaminants.

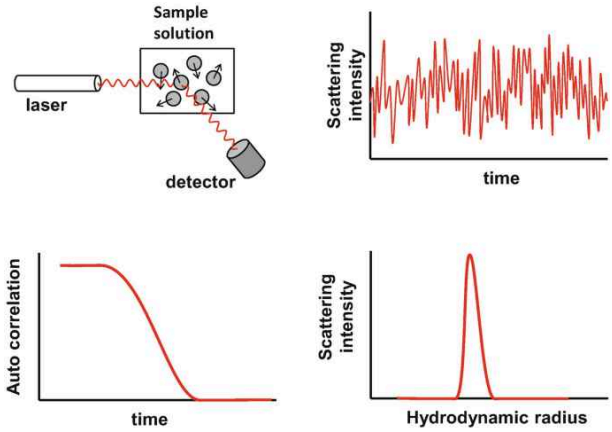

Figure 11 – Schematic representation of DLS experiment depicting light scattering intensity fluctuations over time and the derived hydrodynamic radius distribution of particles in solution. [9]

The use of DLS, particularly in conjunction with other non-disruptive methods, like CD spectroscopy or aSEC chromatography, has become a cornerstone in the field of protein characterization, offering a powerful means to evaluate the physical stability and structural integrity of recombinant proteins under various conditions. The results outlined in this thesis prove how DLS represents a powerful technique able to provide complementary information about the oligomeric state of GCAP1 variants as well as their structural changes upon ion binding . In particular, DLS measurements were useful in gaining insights into the variations in hydrodynamic diameter, oligomeric state, and aggregation propensity of WT, N104H and E111V-GCAP1 in different cation-loading states [**Paper 1** and **3**]. In addition, DLS provided valuable insights into the size and polydispersity of liposomes loaded with PEI-DNA polyplexes in solution highlighting a strongly monodisperse population of liposomes characterized by an average hydrodynamic diameter in line with the extrusion process through a polycarbonate membrane with 200 nm pores (**Figure 12**).

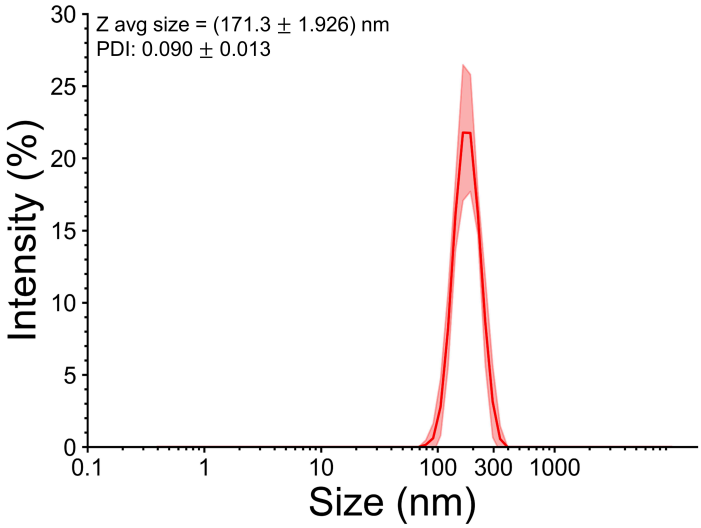

Figure 12 – Hydrodynamic diameter of liposomes loaded with PEI-DNA polyplexes determined by DLS measurements. Inset shows the main output values of the DLS analysis, specifically: average size of the sample (Z avg size) and polydispersion index (PDI) of the sample in solution. Values are reported as ± standard deviation of 10 technical replicates.

4.3 Chelator Assay

The chelator assay emerges as a refined indirect technique for probing the calcium-binding affinities of sensor proteins, particularly useful when direct measurement approaches encounter constraints such as high protein affinity or low protein concentrations [10]. In this assay, a chromophoric chelator sensitive to calcium ion presence, competes with the target protein for calcium binding. The ensuing spectroscopic changes in the chelator, manifested as shifts in fluorescence or absorbance, are meticulously monitored to infer the protein's calcium-binding constants. However, the technique assumes that the protein's binding sites have a higher affinity for calcium than the chelator used, a condition met by carefully selecting suitable chromophoric chelators with affinities spanning from the low nanomolar to the high micromolar range [10, 103]. Computational tools such as CaLigator [104] simplify the complex data interpretation process inherent to this method, allowing researchers to extract macroscopic constants from an array of microscopic interactions. Chelator assay using the 5,5'Br2-BAPTA chromophoric chelator (Ca^{2+} affinity = 2.3 μM) has been partcularly valuable in estimating Ca^{2+} affinity for GCAP1 variants in the past [105, 92] (**Figure 13B**). The same approach has been engaged in **Paper 1** in order to test whether or not the N104H substitution could also impact Ca^{2+} affinity as previously observed for the E111V, and many others, mutants.

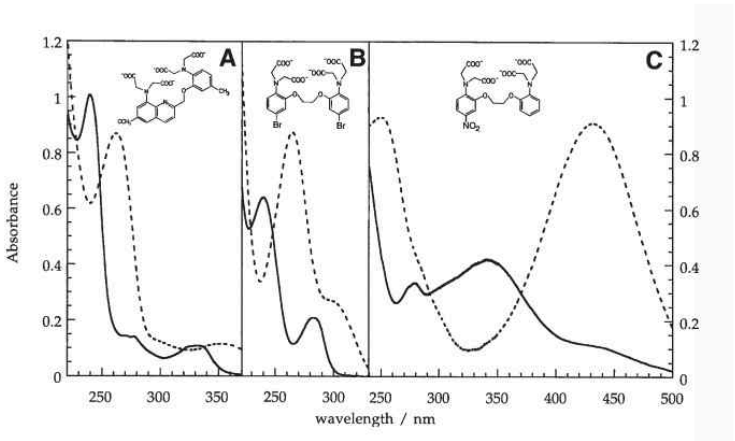

Figure 13 – Molecular structures and absorbance spectra of (**A**) quin-2; (**B**) 5,5'Br2-BAPTA; and (**C**) 5N-BAPTA. (dashed line) calcium free and (black line) calcium bound forms. [10]

4.4 Surface Plasmon Resonance

Surface Plasmon Resonance (SPR) represents a sophisticated optical sensing technology useful for the real-time, label-free investigation of biomolecular interactions across a spectrum ranging from ions to viruses. This technique relies on the detection of changes in the refractive index, measured as resonance units (R.U.), near thin metallic layers, notably gold, silver, or aluminum films, facilitated by the resonant collective oscillations of valence electrons stimulated by incident light [106] (**Figure 14**). Notably, SPR biosensors have become instrumental in the analysis of kinetic parameters, specificity, and affinity in macromolecule binding processes, including protein-protein, protein-DNA, and receptor-drug interactions [107]. Despite its extensive application in biochemical and biophysical research, SPR has been relatively underutilized for monitoring conformational changes in proteins, often replced by techniques offering atomistic resolution such as X-ray crystallography and NMR. However, the unique advantage of SPR technology lies in its minimal protein requirement for immobilization, down to a few nanograms, and its label-free approach that minimizes system perturbation, coupled with the capacity for real-time process kinetics monitoring [108].

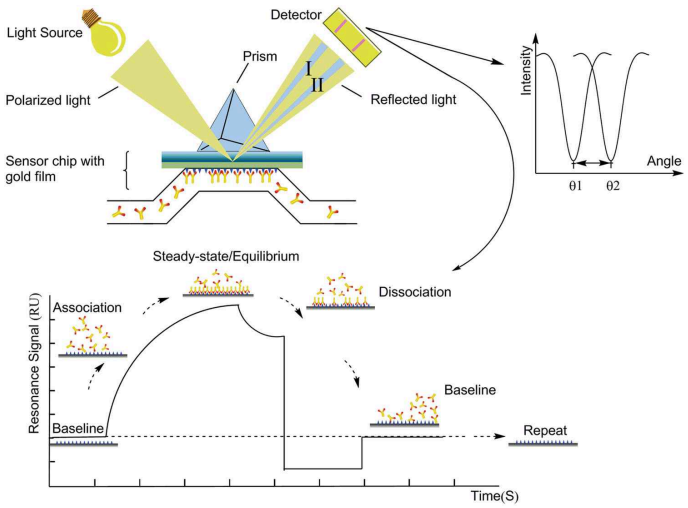

Figure 14 – Diagrammatic representation of Surface Plasmon Resonance (SPR) measurement. Taken from [11].

In this thesis, SPR was engaged to elucidate the kinetics governing GCAP1 dimerization process in patients carrying the E111V substitution. His-tagged WT-GCAP1 in its Ca^{2+}-bound monomeric form ($\sim$ 4 μM) has been immobilized onto a His-cap chip (Sartorius) for a total of $\sim$200 R.U by exploiting the functional groups of nitrilotriacetic resin that chelate Nickel ions for the selective capture of 6X His-tagged proteins. SPR experiments were carried out using a SensiQ Pioneer (ICx Technologies) and although preliminary data were collected (**Figure 15**), technical challenges were encountered. Specifically, the C-terminal positioning of the His tail proved suboptimal, leading to unstable and transient immobilization of GCAP1, which compromised the reliability and reproducibility of the subsequent data. As a result of these unforeseen technical difficulties, the use of SPR for studying the GCAP1 dimerization process was ultimately discontinued in favor of alternative methods that ensured more consistent results.

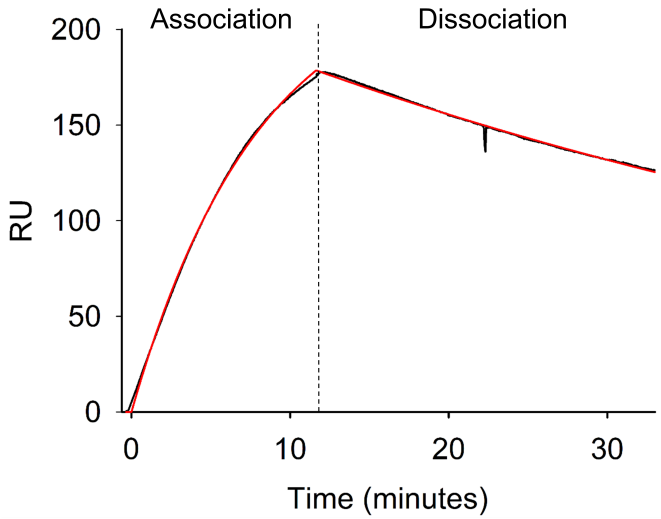

Figure 15 – Surface Plasmon Resonance kinetic analysis of WT/WT-GCAP1 interaction. 10 μM WT-GCAP1 was injected on immobilized His-tagged WT-GCAP1 in the presence of 1 mM Mg^{2+} and 0.5 mM Ca^{2+}. Experimental curve is displayed (black curve) along with theoretical curve (red curve) after fitting experimental data to a simple 1:1 binding model.

4.5 Analytical Gel Filtration

Following the challenges encountered with SPR in our initial attempts to dissect the GCAP1 oligomerization process, our research strategy deviated towards analytical size exclusion chromatography (aSEC) which proved to be valuable in this context [44, 109]. Employing aSEC, a spectrum of protein concentrations, from 0.8 µM to 80 µM, was evaluated through a Superose 12 10/300 column (GE Healthcare) in the presence of saturating Mg^{2+} or Ca^{2+} conditions (**Figure 16**). This approach was instrumental in revealing that both the wild-type and the E111V mutant of GCAP1 exhibited similar elution profiles and dissociation constants across the examined conditions, thereby affirming the dimerization process's resilience to the E111V mutation. The consistency observed in the elution profiles achieved under a physiological buffer and monitored at 280 nm offered a clear window into the structural stability of GCAP1's oligomeric states despite the mutation's potential for pathological over-activation of GC1. Dissociation constants (K_d) were calculated by fitting the elution volume (V_e) to the concentration curves using equation [2] adapted from [44]:

$$V_e = A \cdot \log\left(\frac{\left(P_{\mathrm{TOT}} - \frac{-K_d+\sqrt{K_d^2+4\cdot K_d\cdot P_{\mathrm{TOT}}}}{2}\right)}{P_{\mathrm{TOT}}} \cdot 22.9 + 22.9\right) + B \qquad (3)$$

where V_e represents the elution volume at the peak, A represents the slope of the curve, $[P_{TOT}]$ is the concentration of the protein at the time of injection, B is the y-intercept and 22.9 is the monomer theoretical M_w of hGCAP1.

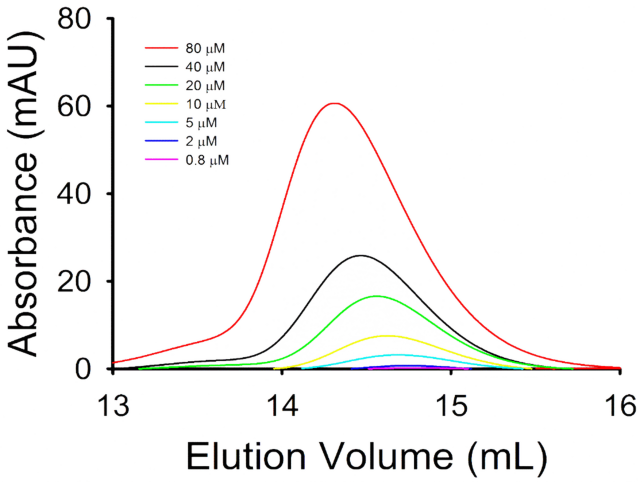

Figure 16 – Representative aSEC experiment of WT-GCAP1 in the presence of 1 mM Mg^{2+} and 0.5 mM Ca^{2+}. Legend reports injected GCAP1 concentrations. Adapted from [**Paper 2**].

5 GC1 Enzymatic Activity Assays

Guanylate cyclase assays are crucial for the precise evaluation of GC activity, offering a direct measure of its regulatory mechanisms under various physiological and pathological conditions [92, 110]. Throughout the development of this thesis, GC1 assays have proven indispensable in characterizing a newly discovered *GUCA1A* pathogenic variant (*i.e.* N104H-GCAP1, **Paper 1**) and underlying how RD3 and its derivative RD3ppt play a major role in the phototransduction cascade by almost re-establishing cGMP homeostasis [**Paper 2**]. Using human recombinant GFP-GC1 expressed in HEK293 cells, these assays provided a robust framework for examining GC1 activity by isolating membranes prepared under physiological ionic conditions. The assay was carried out investigating different enzymatic properties. Maximal and minimal activation levels of GC1 were tested using K_2H_2EGTA and K_2CaEGTA buffers to simulate GC1-activating (< 19 nM free-Ca^{2+}) and inhibiting ($\sim$ 30 µM free-Ca^{2+}) conditions in the presence of GCAP1 (**Figure 17A**) and, when contemplated, RD3 [**Paper 1**, **2** and **3**]. In addition, measuring the cGMP synthesis levels after addition of increasing concentrations of GCAP1 with or without RD3 allowed for the EC_{50} determination, namely the GCAP1 concentration at which GC1 exhibits half of its maximal activity (**Figure 17B**). EC_{50} quantitavely estimates the affinity for the cyclase and is performed in the presence of solely K_2H_2EGTA buffer. Hence, the obtained data was fitted using a one site saturation ligand binding curve:

$$y = \frac{B_{\text{max}} \cdot x}{K_d + x} \tag{4}$$

where B_{max} is the max number of cGMP detected (pmol), K_d is the EC_{50} value (μM) and x is the [GCAP1] used in the assay (5 μM). Furthermore, by using specific combinations of K_2H_2EGTA and K_2CaEGTA buffers the [Ca^{2+}] at which GC1 is half inhibited, IC_{50}, was determined and provided valuable insights into the capacity of each GCAP1 variant in coordinating Ca^{2+} ions and shutting down GC1 activity (**Figure 17C**).

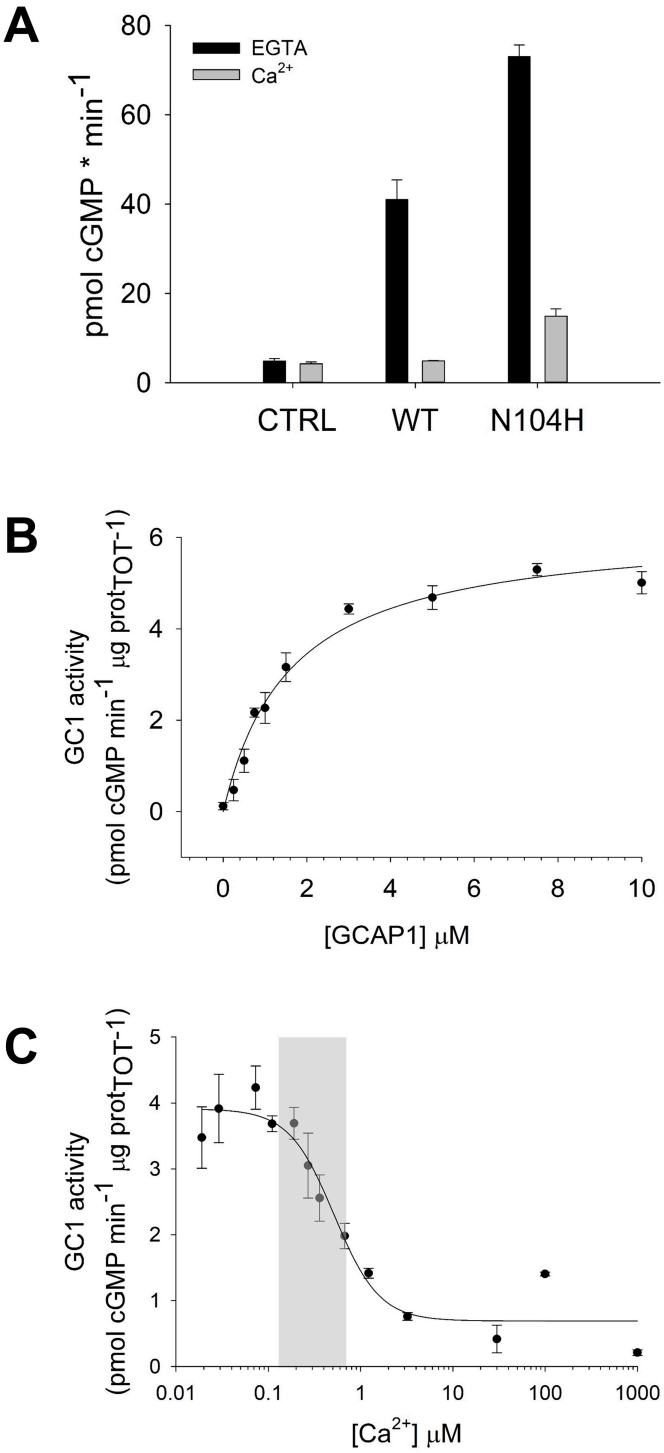

Figure 17 – Exemplary GC1 enzymatic assays. Investigation of (**A**) maximal and minimal GC1 activity, (**B**) GCAP1 concentration at which GC1 is active by half (EC_{50}) and (**C**) Ca^{2+} concentration needed to inactivate GC1 by half (IC_{50}). Adapted from [**Paper 1**]

6 Preparation of ROS-like liposomes

The preparation of liposomes, designed to be biocompatible with retinal tissue for potential topical and intravitreal administration, were crafted to mimic the lipidic composition of photoreceptor ROS membranes [111] (phosphatidylethanolamine, phosphatidylcholine, phosphatidylserine, and cholesterol at a molar ratio of 40:40:15:5). Through the process of lipid film hydration followed by 200 nm pore-sized polycarbonate filter extrusion, liposomes were generated with defined dimensional control, encapsulating either PEI-DNA polyplexes aimed at gene delivery applications or CF640R-GCAP1 conjugates for advanced imaging purposes *in cyto*, *in vivo* and *ex vivo*. To formulate PEI-DNA liposomes, a systematic protocol was refined across several steps:

- Preparation of two aliquots of 500 μL each, one of PEI with a final concentration of 130 ng/μl and the other of DNA with a final concentration of 100 ng/μl. The reported concentrations are relative to an N/P ratio of 10.
- Drop-wise addition of DNA to PEI solution while stirring.
- Incubation of PEI-DNA polyplexes for 30 minutes at room temperature (r.t.).
- Centrifugation of polyplexes at 5000 rpm for 5 minutes at 4°C to remove excess PEI and large aggregates.
- Use of PEI-DNA complexes to resuspend an aliquot of ROS-like lipid mix concentrated at 2 mg/mL while stirring at 45°C for 15 minutes, with pipetting every 5 minutes.
- Extrusion of the solution 20 times through a polycarbonate membrane with 200 nm cutoff for the formulation of $\sim$200 nm liposomes.
- Dialysis in 1 mL tubes to remove any unencapsulated PEI and/or PEI-DNA complexes.

Dynamic light scattering analyses (see 4.2) and Nanoparticle tracking analyses (NTA) (see 6.1) revealed that the most optimal conditions involve the use of H_2O as the resuspension buffer and a PEI nitrogen to nucleic acid phosphate ratio (N/P ratio) of 10 to ensure optimal DNA condensation. Conversely, the protein-loaded liposomes involved the conjugation of CF640R dye to wild-type GCAP1, utilizing NHS chemistry to target primary amines on the protein. This process, carefully conducted to preserve protein functionality, was followed by the removal of unconjugated dye through repeated washing steps, ensuring a high degree of labeling. The encapsulation of this conjugate into liposomes was achieved by incorporating the protein-dye complex during the lipid film hydration stage, with subsequent washing steps effectively separating non-encapsulated molecules [**Paper 3**].

6.1 Biophysical Charachterization: Nanoparticle Tracking Analysis

Nanoparticle Tracking Analysis (NTA) emerges as a sophisticated light-scattering technique for the precise evaluation of nanoparticle size and concentration, including extracellular vesicles (EVs) [112, 113]. The core of NTA's functionality lies in its software's capacity to identify and track the movement of each particle individually, calculating the mean square displacement (MSD) from these movements. Utilizing the Stokes-Einstein equation (see paragraph 4.2), which integrates the MSD along with the fluid's temperature and viscosity, NTA facilitates the accurate determination of particle size. NTA is renowned for its ability to analyze EVs at a singular particle level, offering both scatter and fluorescence mode analysis (F-NTA), thereby enriching its utility by enabling the distinction of particles based on their inherent or labeled fluorescence. This precision arises from the detection of particles' trajectories, which reflect Brownian motion within a defined volume, thus allowing not only for the sizing of each tracked particle but also for the quantification of particle concentration relative to the sample volume (**Figure 18**). In this thesis, liposomes formulations were analysed at 25 °C by means of a NanoSight NS300 instrument (Malvern, UK) by recording 3 independent videos (*i.e.* technical replicates) to assess liposomes size and concentration in solution [**Paper 3**].

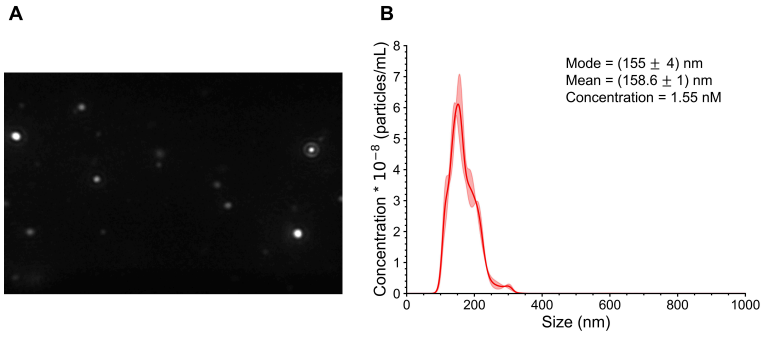

Figure 18 – NTA analysis of PEI-DNA polyplexes-loaded liposomes extruded through a 200 nm pore-sized polycarbonate filter. (**A**) Live recording snapshot of the colloidal solution under a constant flow (20 μL/min) recorded by the instrument. (**B**) Size of liposomes as a function of their concentration.

7 *In Silico* Studies

7.1 Molecular Dynamics Simulations

Molecular Dynamics (MD) simulations represent a powerful tool in the field of computational biology, offering valuable insights into the dynamic behaviors of biomolecules at an atomistic level [114]. The principle of MD simulations lies in their ability to predict the time evolution of a molecular system, such as proteins, DNA, and membranes, by calculating the trajectories of all atoms based on Newton's laws of motion. This computational approach fills a crucial gap left by traditional structural determination methods like X-ray crystallography and NMR spectroscopy, which, despite providing atomistic resolution of static structures, fall short of capturing the dynamic essence of biomolecules in action. X-ray crystallography offers a snapshot of a molecule in a crystalline state, while NMR spectroscopy, despite its versatility, requires high concentrations and sometimes non-physiological conditions, limiting its ability to elucidate molecular dynamics comprehensively. MD simulations, based on classical mechanics, facilitate a detailed exploration of protein folding, biomolecule interactions, and the temporal evolution of complex molecular systems over significant time frames. While quantum mechanics (QM) delivers high-accuracy results, it demands substantial computational resources and evaluates systems of limited size. Classical mechanics, utilized in most MD simulations, approximates quantum-mechanical effects through empirical potentials calculated using molecular mechanics (MM) force fields. These fields simulate the physical forces acting on particles, including bonded interactions modeled after Hooke's law and non-bonded interactions such as electrostatic and van der Waals forces, thus enabling the accurate modeling of molecular motion. Performing MD simulations encompasses a series of critical decisions, from the selection of computing hardware to the choice of force fields and simulation software (**Figure 19**). Graphics processing units (GPUs) have emerged as a favorable option for conducting fast, cost-effective simulations. Different force fields are available, with AM-

BER, CHARMM, and OPLS [115, 116, 117] being among the most prevalent, each offering unique strengths tailored to different molecular systems. For instance, CHARMM36m is particularly optimized for proteins and lipids, while OPLS3 excels in ligand parameterization. The choice of software additionally influences the results of simulations, with options such as GROMACS, NAMD, OpenMM and AMBER [118, 119, 120, 121] offering a range of features and performance capabilities. Preparing the molecular system involves adding missing atoms, solvents, and assigning force field parameters, a step facilitated by various system preparation tools included in common simulation software that strongly influences the reliability of MD simulations. In addition, replicates and statistical analyses, such as principal component analysis (PCA) [122] or root-mean square inner product (RMSIP) [123], are essential for ensuring the consistency and reproducibility of results. The complex nature of MD output data, characterized by the Cartesian positions of potentially millions of atoms recorded across extensive trajectories, necessitates sophisticated analytical tools to extrapolate meaningful information. Techniques such as Root Mean Square Deviation (RMSD) and Root Mean Square Fluctuation (RMSF) are instrumental in this process. RMSD offers a quantitative measure of structural changes over time, calculating the average distance between atom sets across different trajectory time points, thereby highlighting conformational shifts in the protein structure. RMSF further complements this analysis by measuring the average deviation of particles, such as protein residues, from their reference position over time, thus exposing regions of significant structural variability. MD simulations have proven useful for elucidating the altered molecular mechanisms underlying adCOD and adCORD-associated conditions. By integrating spectroscopic data, MD simulations facilitated a detailed ex-

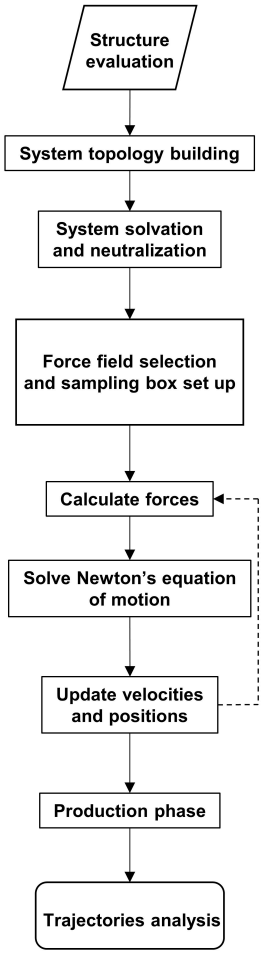

Figure 19 – MD simulations workflow.

ploration of how the N104H [**Paper 1**] and E111V [**Paper 2**] genetic alterations impact the structure and oligomerization process of GCAP1 under activating and inhibiting conditions. RMSF was particularly useful in underpinning major side-chain fluctuations and ion displacement localized in the Ca^{2+}-coordinating EF3 as a consequence of the amino acidic substitution induced by the pathogenic missense mutations.

7.2 Homology Modeling

Homology modeling, also known as comparative modeling, relies on the principle that proteins sharing evolutionary lineage exhibit similar structural features [124]. This technique has become an important tool in structural biology, enabling the prediction of protein structures by exploiting known structures of evolutionarily related proteins (templates) to model those with undetermined structures (targets). The efficacy of homology modeling is inherently linked to the evolutionary proximity between the target and template proteins, with a closer relationship suggesting a higher accuracy of the predicted model. The process, outlined in **Figure 20**, begins with the identification of templates with solved 3D structures that are evolutionarily related to the target protein. The next step involves aligning the target sequence with those of the templates, constructing a preliminary model based on this alignment, and refining it through MD simulations to improve the accuracy of predictions. The final stage entails a thorough evaluation and validation of the generated model to assess its reliability. Despite its successes, homology models are approximations that may harbor inaccuracies, primarily due to the reliance on sequence identity (SI) between the target and template sequences. A SI below 50% often results in structural deviations from the actual experimental structure, highlighting the method's limitations. Indeed, models based on sequences with less than 25% identity are generally considered speculative. For proteins with low sequence identity, multiple sequence alignment and the use of multiple templates can significantly improve model accuracy by incorporating structural information from various homologous structures. This multifaceted approach allows for a comprehensive understanding of protein structure and function, despite the challenges posed by sequence variability and structural flexibility, particularly in regions like exposed

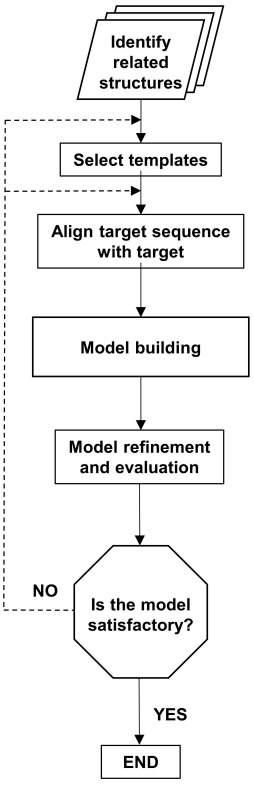

Figure 20 – Schematic representation of homology modeling workflow.

loops that are prone to deviations. Several software, employing slightly different approaches in structure prediction, are commercially available [125] and here the Prime tool offered by the software Bioluminate (Maestro package v. 12.5.139, Schrödinger) [126] was used. Using the *G. Gallus* variant (PDB:2R2I, sequence identity of 84%) [43] as template, homology modeling has been instrumental in obtaining the human form of Ca^{2+}-loaded myristoylated GCAP1 used here [**Paper 1** and **2**] and in the past [92, 39, 105]. In addition, homology modeling extended its utility by facilitating the acquisition of a full-lenght and wild-type model of the RD3 protein using its NMR structure (PDB:6DRF) [54] as template. This accomplishment was pivotal, providing a robust foundation for subsequent docking experiments that explored the interaction dynamics between RD3 and GCAP1.

7.3 Molecular Docking

Molecular docking is a computational technique offering a systematic approach to predict the interaction and binding configurations of molecular complexes, such as protein-protein and ligand-protein associations [127]. Understanding this interaction is crucial for the development of new pharmaceuticals and investigating fundamental biochemical processes. Virtual docking experiments involve two main phases: the search phase, where the best-fit orientation of the two molecules is identified through global and local searches of the conformational space, and the scoring phase, where the top binding poses are evaluated to predict the strength and mode of binding (**Figure 21**). Docking strategies have been refined to address both rigid and flexible aspects of protein interactions. Rigid-body docking investigates the interaction by treating molecules as static entities and assuming no major conformational changes occur between their bound and unbound states. This approach is governed by six degrees of freedom, involving three translations and three rotations within a Cartesian framework [128]. Conversely, flexible docking acknowledges the inherent variability in protein conformations, incorporating a broader array of coordinates to map out these internal movements [129]. Critical to the success of docking studies is the scoring function, which must discern native-like binding modes from less favorable interactions. This has led to the creation of sophisticated scoring schemes, combining empirical, knowledge-based, and molecular mechanics-based potentials to properly estimate binding affinities. Modern approaches also leverage machine learning to enhance prediction accuracy, highlighting the continuous innovation in the field as assessed during the CASP15-CAPRI protein assembly prediction challenge [130]. Protein-protein docking specifically addresses the challenge of predicting the structure of a protein complex based on the structures of the individual molecules, emphasizing the importance of steric and physicochemical complementarities at the interaction interface. In this thesis PIPER [131] and Z-DOCK [132] docking software have been used. The former, by engaging a fast Fourier transform-based (FFT) approach with pairwise potentials and a scoring function that considers shape complementarity, electrostatic, and desolvation contributions

($E = E_{\text{shape}} + w_2 E_{\text{elec}} + w_3 E_{\text{pair}}$), is able to sample billions of docking poses and rank their energies. PIPER's output poses are then clustered using pairwise ligand RMSD as the distance measure. Z-DOCK uses a similar FFT-based docking algorithm and a pair wise complementarity function (PSC) combined with electrostatic and desolvation terms. By sampling 16000 possible conformations and grouping resulting poses into cohorts of structurally analogous conformations exhibiting RMSD values of less than 1 Å from the reference complex, Z-DOCK provided valuable insights in the oligomerization process of GCAP1 in the context of adCORD. In addition, PIPER was engaged to study the interaction occurring *in vitro* between GCAP1 and RD3 and identify possible binding modalities. The most energetically favourable binding poses were used as reference complexes for the same type of docking experiment performed with Z-DOCK, thus enabling a muti-faceted approach to elucidate GCAP1-RD3 interaction [**Paper 2**].

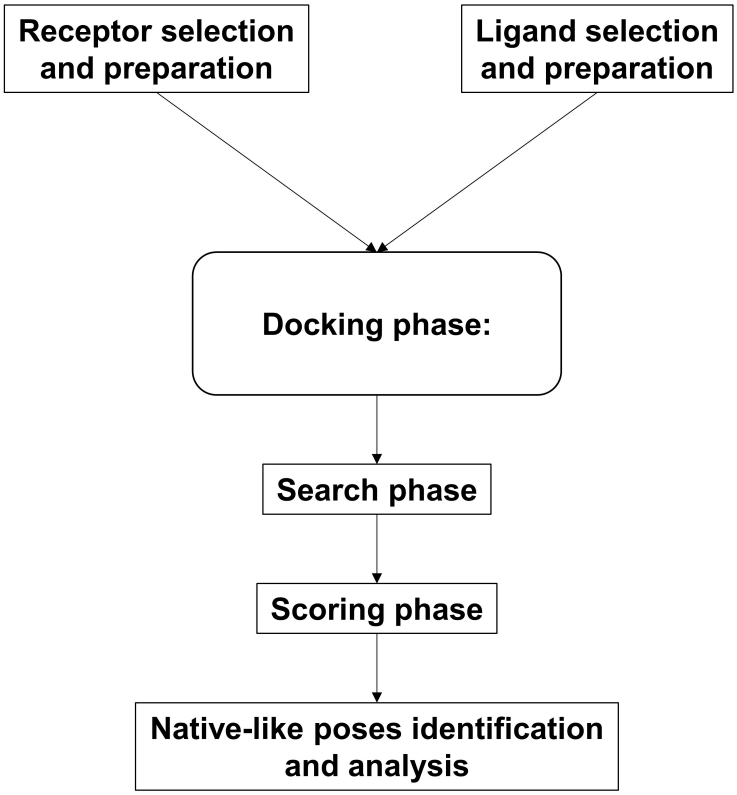

Figure 21 – Molecular docking basic workflow.

Introduction to Published Papers and Results

The results collected during my PhD comprehend three manuscripts attached in the appendix, two of which are already published [**Paper 1** and **3**] and one [**Paper 2**] is under review at the moment of writing. In the following pages a brief summary of results and conclusions of each of them is provided.

8.1 Paper 1: A Novel *GUCA1A* Variant Associated with Cone Dystrophy Alters cGMP Signaling in Photoreceptors by Strongly Interacting with and Hyperactivating Retinal Guanylate Cyclase

Published in *International Journal of Molecular Sciences* (2021)

Biasi A.[1], Marino V.[1], Dal Cortivo G.[1], Maltese PE.[2], Modarelli AM.[3], Bertelli M.[2 4], Colombo L.[3], Dell'Orco D.[1]

[1] Department of Neurosciences, Biomedicine and Movement Sciences, Section of Biological Chemistry, University of Verona, 37134 Verona, Italy.

[2] MAGI'S Lab s.r.l., 38068 Rovereto, Italy.

[3] Department of Ophthalmology, ASST Santi Paolo e Carlo Hospital, University of Milan, 20142 Milano, Italy.

[4] MAGI Euregio, 39100 Bolzano, Italy.

The study underscores the biochemical heterogeneity of *GUCA1A* mutations and aims at elucidating the molecular alterations of autosomal dominant cone dystrophy (adCOD) linked to a novel variant of GCAP1, identified within an Italian family. The study investigates the biochemical alterations of the N104H-GCAP1 variant, originating from a missense mutation in the *GUCA1A* gene, affecting the Ca^{2+}-binding EF3 motif. This variant exhibits diminished calcium sensitivity without causing significant structural perturbations, as evidenced through circular dichroism and proteolytic analyses. Notably, N104H-GCAP1 demonstrates a doubled affinity for retinal GC1 compared to the wild type form, diverging from the effects of previously studied mutations at the same position. Unlike the N104K mutation, which exhibited reduced GC1 activation capability, N104H-GCAP1 demonstrated a constitutive activation of GC1, suggesting a hyperactivity under both low and high calcium conditions. 2 µs molecular dynamics simulations support the idea of a strengthened interaction which introduce enhanced flexibility at the GC1 interface under calcium-bound conditions, potentially leading to an aberrant accumulation of cGMP and calcium in photoreceptor cells, thereby inducing cellular degeneration.

8.2 Paper 2: Supramolecular complexes of GCAP1: implications for inherited retinal dystrophies

Manuscript under review

Biasi A.[1], Marino V.[1], Dal Cortivo G.[1], Dell'Orco D.[1]

[1] Department of Neurosciences, Biomedicine and Movement Sciences, Section of Biological Chemistry, University of Verona, 37134 Verona, Italy.

This study firstly investigates the impact on the dimerization process of the E111V-GCAP1 variant associated with adCORD. Utilizing an integrative approach combining *in silico* and biochemical assays, the research delineates how the E111V mutation, located within the high-affinity Ca^{2+}-binding motif EF3, prompts a constitutive activation of GC1 without disrupting the homo and hetero-dimerization capability of GCAP1. Despite this mutation, both WT and mutant GCAP1 maintain a similar monomer-dimer equilibrium, suggesting that the fundamental dimerization process critical for GCAP1's functional role in phototransduction remains unaffected. Moreover, molecular docking and dynamics simulation studies corroborate these findings, revealing minor alterations in the binding energy upon dimer formation and increased mobility of the EF3 motif for the E111V variant, as suggested by estimates of the free energy of association (ΔG^0) and RMSF calculations. In addition, further exploration into therapeutic approaches to modulate aberrant GC1 activity, led to the analysis of GC1 activity regulated by WT and/or E111V GCAP1 variants in the presence of RD3 and its derived peptide, RD3ppt. The study finds that while RD3ppt exhibits partial inhibitory control over GC1 in the presence of GCAP1 variants, full-length RD3 significantly attenuates abnormal cGMP production induced by the E111V-GCAP1 variant, particularly when in the presence of extra-supplied WT-GCAP1. In conclusion, despite the pathological overstimulation of GC1 by the E111V mutation, the equilibrium between monomeric and dimeric forms of GCAP1 remains intact, underscoring the mutation's specific impact on GC1 stimulation rather than on GCAP1's dimerization capacity. These findings illuminate the complex regulatory mechanisms governing phototransduction and highlight the potential of RD3 as a modulator of GC1 activity, offering

insights into new therapeutic strategies for adCOD and adCORD.

8.3 Paper 3: Recombinant protein delivery enables modulation of the phototransduction cascade in mouse retina

Published in *Cellular and Molecular Life Sciences* (2023)

Asteriti S.[1 2], Marino V.[1], Avesani A. [1], Biasi A. [1], Dal Cortivo G.[1], Cangiano L. [3] Dell'Orco D.[1]

[1] Department of Neurosciences, Biomedicine and Movement Sciences, Section of Biological Chemistry, University of Verona, 37134, Verona, Italy.

[2] Department of Translational Research, University of Pisa, 56123, Pisa, Italy.

[3] Department of Translational Research, University of Pisa, 56123, Pisa, Italy. lorenzo.cangiano@unipi.it.

[4] Department of Neurosciences, Biomedicine and Movement Sciences, Section of Biological Chemistry, University of Verona, 37134, Verona, Italy. daniele.dellorco@univr.it.

This study investigates the therapeutic potential of protein delivery strategies for targeting IRDs by modulating the phototransduction cascade through the administration of exogenous GCAP1. By comparing the effects of both direct and liposome-mediated delivery of recombinant human WT and CORD-associated E111V-GCAP1 variants, the research elucidates the protein's integration into HEK293 and mouse retinal cells and its impact on photoreceptor functionality. Experiments across *in cyto*, *ex vivo*, and *in vivo* models reveal that exogenous free and liposome-encapsulated GCAP1, with specific internalization kinetics, successfully incorporate into different neuronal layers of the mouse retina. Intriguingly, only the presence of the E111V mutation in GCAP1 induced alterations in rod photoresponses comparable to a disease-like electrophysiological phenotype, suggesting a mutation-specific effect. Furthermore, the study reveals the differential uptake between cell types, highlighting how liposome-mediated delivery proved to be a critical facilitator for protein transport across HEK293 cellular barriers. On the other hand both free and liposome-encapsulated GCAP1, even though at different time points, were able to reach mice photoreceptor outer segments. These apparent discrepancies can be attributed to the different cell membrane composition and the complex molecular interactions within the retinal environment. The effectiveness of this approach in modulating photoreceptor cell responses points to promising avenues for treating autosomal dominant genetic diseases affecting the retina.

Conclusions

The results outlined in this thesis highlight the intricate interplay between genetic mutations in the *GUCA1A* gene and their profound impact on photoreceptor function and viability, offering novel insights into the pathophysiology of adCOD and adCORD. Adopting different experimental and computationl approaches, the studies collectively underscore the biochemical heterogeneity of *GUCA1A* mutations, notably the N104H and E111V variants, and their differential effects on GCAP1 functionality, dimerization, and interaction with retinal GC1. Despite the severe physiological consequences induced by these mutations, such as the aberrant stimulation of GC1 leading to photoreceptor cell death, the fundamental biophysical properties largely remain unaffected. The unique biochemical behavior of the N104H mutation, notably its doubled affinity for GC1 compared to the wild-type or the E111V variant, underscores the complex molecular scenario where mutations affecting the same domain, EF3, induce specific biochemical and functional alterations without causing major structural disruptions. Furthermore, despite the E111V mutation's capacity to abnormally stimulate retinal GC1, and induce photoreceptor cell death, it does not alter the intrinsic monomer-dimer equilibrium of GCAP1, indicating that the dimerization process, crucial for GCAP1's role in phototransduction, remains unaffected by the mutation. Importantly, the potential of RD3 to mitigate the E111V mutation's adverse effects on cGMP synthesis, suggests novel regulatory mechanisms in the phototransduction pathway that could be exploited for the treatment of IRDs. Furthermore, the explored therapeutic potential of protein delivery, both direct and liposome-mediated, opens new avenues for treating IRDs. This approach demonstrates that targeted delivery of recombinant proteins can effectively modulate the phototransduction cascade, offering a promising strategy for overcoming the pathological effects of mutant proteins. In conclusion, these findings not only advance our molecular understanding of adCOD and adCORD but also lay a solid foundation for the development of targeted therapeutic interventions. By elucidating the specific biochemical impacts of *GUCA1A* mutations and exploring

innovative delivery methods for endogenous proteins, this research paves the way for targeted therapeutic strategies that can potentially restore photoreceptor function and prevent progressive vision loss in inherited retinal dystrophies.

References

[1] M. Hoon, H. Okawa, L. D. Santina, and R. O. L. Wong, "Functional architecture of the retina: Development and disease," *Progress in Retinal and Eye Research* **42**, pp. 44–84, 12 2014.

[2] G. L. Fain, R. Hardie, and S. B. Laughlin, "Phototransduction and the evolution of photoreceptors," *Current Biology* **20**, pp. R114–R124, 12 2010.

[3] A. M. Dizhoor and I. V. Peshenko, "Regulation of retinal membrane guanylyl cyclase (retgc) by negative calcium feedback and rd3 protein," *Pflügers Archiv - European Journal of Physiology* **473**, pp. 1393–1410, 9 2021.

[4] I. V. Peshenko and A. M. Dizhoor, "Two clusters of surface-exposed amino acid residues enable high-affinity binding of retinal degeneration-3 (rd3) protein to retinal guanylyl cyclase," *Journal of Biological Chemistry* **295**, pp. 10781–10793, 7 2020.

[5] H. Rameez and A. Giridhar, "Fundus autofluorescence of retinitis pigmentosa showing hyperautofluorescent rings or foveal hyperautofluorescence.," *C Care Wellkin Hospital, Mauritius* , 2014.

[6] Schrödinger, LLC, "The PyMOL molecular graphics system, version 1.8." November 2015.

[7] R. W. Woody, *Theory of Circular Dichroism of Proteins*, pp. 25–67. Springer US, 1996.

[8] S. M. Kelly, T. J. Jess, and N. C. Price, "How to study proteins by circular dichroism," *Biochimica et Biophysica Acta (BBA) - Proteins and Proteomics* **1751**, pp. 119–139, 8 2005.

[9] T. Misono, *Dynamic Light Scattering (DLS)*, pp. 65–69. Springer Singapore, 2019.

[10] S. Linse, *Calcium Binding to Proteins Studied via Competition with Chromophoric Chelators*, pp. 015–024. Humana Press, 2002.

[11] C. Song, S. Zhang, and H. Huang, "Choosing a suitable method for the identification of replication origins in microbial genomes," *Frontiers in MICROBIOLOGY* **6**, 9 2015.

[12] D. Dell'Orco, K.-W. Koch, and G. Rispoli, "Where vision begins," *Pflügers Archiv - European Journal of Physiology* **473**, pp. 1333–1337, 12 2021.

[13] J. Snellman, T. Kaur, Y. Shen, and S. Nawy, "Regulation of on bipolar cell activity," *Progress in Retinal and Eye Research* **27**, pp. 450–463, 7 2008.

[14] K.-W. Yau and R. C. Hardie, "Phototransduction motifs and variations," *Cell* **139**, pp. 246–264, 12 2009.

[15] U. B. Kaupp and K. W. Koch, "Role of cgmp and ca^{2+} in vertebrate photoreceptor excitation and adaptation," *Annual Review of Physiology* **54**, pp. 153–176, 10 1992.

[16] E. N. Pugh and T. D. Lamb, *Chapter 5 Phototransduction in vertebrate rods and cones: Molecular mechanisms of amplification, recovery and light adaptation*, pp. 183–255. 2000.

[17] M. L. Woodruff, A. P. Sampath, H. R. Matthews, N. V. Krasnoperova, J. Lem, and G. L. Fain, "Measurement of cytoplasmic calcium concentration in the rods of wild-type and transducin knock-out mice," *The Journal of Physiology* **542**, pp. 843–854, 8 2002.

[18] J. I. Korenbrot, "Speed, sensitivity, and stability of the light response in rod and cone photoreceptors: Facts and models," *Progress in Retinal and Eye Research* **31**, pp. 442–466, 9 2012.

[19] K.-W. Koch and D. Dell'Orco, "A calcium-relay mechanism in vertebrate phototransduction," *ACS Chemical Neuroscience* **4**, pp. 909–917, 6 2013.

[20] K.-W. Koch and D. Dell'Orco, "Protein and signaling networks in vertebrate photoreceptor cells," *Frontiers in Molecular Neuroscience* **8**, 11 2015.

[21] S. Lim, A. M. Dizhoor, and J. B. Ames, "Structural diversity of neuronal calcium sensor proteins and insights for activation of retinal guanylyl cyclase by gcap1," *Frontiers in Molecular Neuroscience* **7**, 12 2014.

[22] A. Dizhoor, "The human photoreceptor membrane guanylyl cyclase, retgc, is present in outer segments and is regulated by calcium and a soluble activator," *Neuron* **12**, pp. 1345–1352, 6 1994.

[23] D. G. Lowe, A. M. Dizhoor, K. Liu, Q. Gu, M. Spencer, R. Laura, L. Lu, and J. B. Hurley, "Cloning and expression of a second photoreceptor-specific membrane retina guanylyl cyclase (retgc), retgc-2.," *Proceedings of the National Academy of Sciences* **92**, pp. 5535–5539, 6 1995.

[24] W. Baehr, S. Karan, T. Maeda, D.-G. Luo, S. Li, J. D. Bronson, C. B. Watt, K.-W. Yau, J. M. Frederick, and K. Palczewski, "The function of guanylate cyclase 1 and guanylate cyclase 2 in rod and cone photoreceptors," *Journal of Biological Chemistry* **282**, pp. 8837–8847, 3 2007.

[25] I. V. Peshenko, E. V. Olshevskaya, A. B. Savchenko, S. Karan, K. Palczewski, W. Baehr, and A. M. Dizhoor, "Enzymatic properties and regulation of the native isozymes of retinal membrane guanylyl cyclase (retgc) from mouse photoreceptors," *Biochemistry* **50**, pp. 5590–5600, 6 2011.

[26] J. Xu, L. Morris, A. Thapa, H. Ma, S. Michalakis, M. Biel, W. Baehr, I. V. Peshenko, A. M. Dizhoor, and X.-Q. Ding, "cgmp accumulation causes photoreceptor degeneration in cng channel deficiency: Evidence of cgmp cytotoxicity independently of enhanced cng channel function," *The Journal of Neuroscience* **33**, pp. 14939–14948, 9 2013.

[27] K. Palczewski, A. S. Polans, W. Baehr, and J. B. Ames, "Ca^{2+}-binding proteins in the retina: Structure, function, and the etiology of human visual diseases," *BioEssays* **22**, pp. 337–350, 3 2000.

[28] K.-W. Koch, T. Duda, and R. K. Sharma, "Ca^{2+}-modulated vision-linked ros-gc guanylate cyclase transduction machinery," *Molecular and Cellular Biochemistry* **334**, pp. 105–115, 1 2010.

[29] K. Palczewski, I. Subbaraya, W. A. Gorczyca, B. S. Helekar, C. C. Ruiz, H. Ohguro, J. Huang, X. Zhao, J. W. Crabb, R. S. Johnson, K. A. Walsh, M. P. Gray-Keller, P. B. Detwiler, and W. Baehr, "Molecular cloning and characterization of retinal photoreceptor guanylyl cyclase-activating protein," *Neuron* **13**, pp. 395–404, 8 1994.

[30] A. Scholten and K.-W. Koch, "Differential calcium signaling by cone specific guanylate cyclase-activating proteins from the zebrafish retina," *PLoS ONE* **6**, p. e23117, 8 2011.

[31] O. Gross, E. Pugh, and M. Burns, "Calcium feedback to cgmp synthesis strongly attenuates single-photon responses driven by long rhodopsin lifetimes," *Neuron* **76**, pp. 370–382, 10 2012.

[32] S. Lim, G. Roseman, I. Peshenko, G. Manchala, D. Cudia, A. M. Dizhoor, G. Millhauser, and J. B. Ames, "Retinal guanylyl cyclase activating protein 1 forms a functional dimer," *PLOS ONE* **13**, p. e0193947, 3 2018.

[33] S. Sulmann, D. Dell'Orco, V. Marino, P. Behnen, and K. Koch, "Conformational changes in calcium-sensor proteins under molecular crowding conditions," *Chemistry – A European Journal* **20**, pp. 6756–6762, 5 2014.

[34] A. M. Dizhoor, E. V. Olshevskaya, and I. V. Peshenko, "Mg^{2+}/ca^{2+} cation binding cycle of guanylyl cyclase activating proteins (gcaps): role in regulation of photoreceptor guanylyl cyclase," *Molecular and Cellular Biochemistry* **334**, pp. 117–124, 1 2010.

[35] S. Lim, I. V. Peshenko, E. V. Olshevskaya, A. M. Dizhoor, and J. B. Ames, "Structure of guanylyl cyclase activator protein 1 (gcap1) mutant v77e in a ca^{2+}-free/mg^{2+}-bound activator state," *Journal of Biological Chemistry* **291**, pp. 4429–4441, 2 2016.

[36] S. Lim, I. Peshenko, A. Dizhoor, and J. B. Ames, "Effects of ca^{2+} , mg^{2+} , and myristoylation on guanylyl cyclase activating protein 1 structure and stability," *Biochemistry* **48**, pp. 850–862, 2 2009.

[37] J. B. Ames and S. Lim, "Molecular structure and target recognition of neuronal calcium sensor proteins," *Biochimica et Biophysica Acta (BBA) - General Subjects* **1820**, pp. 1205–1213, 8 2012.

[38] I. V. Peshenko, E. V. Olshevskaya, S. Lim, J. B. Ames, and A. M. Dizhoor, "Calcium-myristoyl tug is a new mechanism for intramolecular tuning of calcium sensitivity and target enzyme interaction for guanylyl cyclase-activating protein 1," *Journal of Biological Chemistry* **287**, pp. 13972–13984, 4 2012.

[39] V. Marino and D. Dell'Orco, "Allosteric communication pathways routed by ca^{2+}/mg^{2+} exchange in gcap1 selectively switch target regulation modes," *Scientific Reports* **6**, p. 34277, 10 2016.

[40] M. Kobayashi, K. Takamatsu, S. Saitoh, and T. Noguchi, "Myristoylation of hippocalcin is linked to its calcium-dependent membrane association properties.," *Journal of Biological Chemistry* **268**, pp. 18898–18904, 9 1993.

[41] D. Dell'Orco, S. Sulmann, S. Linse, and K.-W. Koch, "Dynamics of conformational ca^{2+} -switches in signaling networks detected by a planar plasmonic device," *Analytical Chemistry* **84**, pp. 2982–2989, 3 2012.

[42] C. Li, W. Pan, K. H. Braunewell, and J. B. Ames, "Structural analysis of mg^{2+} and ca^{2+} binding, myristoylation, and dimerization of the neuronal calcium sensor and visinin-like protein 1 (vilip-1)," *Journal of Biological Chemistry* **286**, pp. 6354–6366, 2 2011.

[43] R. Stephen, G. Bereta, M. Golczak, K. Palczewski, and M. C. Sousa, "Stabilizing function for myristoyl group revealed by the crystal structure of a neuronal calcium sensor, guanylate cyclase-activating protein 1," *Structure* **15**, pp. 1392–1402, 11 2007.

[44] F. Bonì, V. Marino, C. Bidoia, E. Mastrangelo, A. Barbiroli, D. Dell'Orco, and M. Milani, "Modulation of guanylate cyclase activating protein 1 (gcap1) dimeric assembly by ca^{2+} or mg^{2+}: Hints to understand protein activity," *Biomolecules* **10**, p. 1408, 10 2020.

[45] A. M. Dizhoor, E. V. Olshevskaya, W. J. Henzel, S. C. Wong, J. T. Stults, I. Ankoudinova, and J. B. Hurley, "Cloning, sequencing, and expression of a 24-kda ca^{2+}-binding protein activating photoreceptor guanylyl cyclase," *Journal of Biological Chemistry* **270**, pp. 25200–25206, 10 1995.

[46] A. M. Dizhoor, S. G. Boikov, and E. V. Olshevskaya, "Constitutive activation of photoreceptor guanylate cyclase by y99c mutant of gcap-1," *Journal of Biological Chemistry* **273**, pp. 17311–17314, 7 1998.

[47] I. V. Peshenko, E. V. Olshevskaya, S. Azadi, L. L. Molday, R. S. Molday, and A. M. Dizhoor, "Retinal degeneration 3 (rd3) protein inhibits catalytic activity of retinal membrane guanylyl cyclase (retgc) and its stimulation by activating proteins," *Biochemistry* **50**, pp. 9511–9519, 11 2011.

[48] S. Azadi, L. L. Molday, and R. S. Molday, "Rd3, the protein associated with leber congenital amaurosis type 12, is required for guanylate cyclase trafficking in photoreceptor cells," *Proceedings of the National Academy of Sciences* **107**, pp. 21158–21163, 12 2010.

[49] I. V. Peshenko, E. V. Olshevskaya, and A. M. Dizhoor, "Functional study and mapping sites for interaction with the target enzyme in retinal degeneration 3 (rd3) protein," *Journal of Biological Chemistry* **291**, pp. 19713–19723, 9 2016.

[50] L. L. Molday, T. Jefferies, and R. S. Molday, "Insights into the role of rd3 in guanylate cyclase trafficking, photoreceptor degeneration, and leber congenital amaurosis," *Frontiers in Molecular Neuroscience* **7**, 5 2014.

[51] J. B. Ames, "Structural basis of retinal membrane guanylate cyclase regulation by gcap1 and rd3," *Frontiers in Molecular Neuroscience* **15**, 9 2022.

[52] A. M. Dizhoor, E. V. Olshevskaya, and I. V. Peshenko, "Retinal guanylyl cyclase activation by calcium sensor proteins mediates photoreceptor degeneration in an rd3 mouse model of congenital human blindness," *Journal of Biological Chemistry* **294**, pp. 13729–13739, 9 2019.

[53] R. Zulliger, M. I. Naash, R. V. Rajala, R. S. Molday, and S. Azadi, "Impaired association of retinal degeneration-3 with guanylate cyclase-1 and guanylate cyclase-activating protein-1 leads to leber congenital amaurosis-1," *Journal of Biological Chemistry* **290**, pp. 3488–3499, 2 2015.

[54] I. V. Peshenko, Q. Yu, S. Lim, D. Cudia, A. M. Dizhoor, and J. B. Ames, "Retinal degeneration 3 (rd3) protein, a retinal guanylyl cyclase regulator, forms a monomeric and elongated four-helix bundle," *Journal of Biological Chemistry* **294**, pp. 2318–2328, 2 2019.

[55] J.-A. Sahel, K. Marazova, and I. Audo, "Clinical characteristics and current therapies for inherited retinal degenerations," *Cold Spring Harbor Perspectives in Medicine* **5**, pp. a017111–a017111, 2 2015.

[56] P. Tanna, R. W. Strauss, K. Fujinami, and M. Michaelides, "Stargardt disease: clinical features, molecular genetics, animal models and therapeutic options," *British Journal of Ophthalmology* **101**, pp. 25–30, 1 2017.

[57] E. M. Stone, B. E. Nichols, L. M. Streb, A. E. Kimura, and V. C. Sheffield, "Genetic linkage of vitelliform macular degeneration (best's disease) to chromosome 11q13," *Nature Genetics* **1**, pp. 246–250, 7 1992.

[58] A. Milam, L. Zhong-Yi, and F. Fariss, "Hystopathology of the human retina in retinitis pigmentosa," *Progress in Retinal and Eye Research* **17**, pp. 175–205, 1998.

[59] D. Bessant, "Molecular genetics and prospects for therapy of the inherited retinal dystrophies," *Current Opinion in Genetics & Development* **11**, pp. 307–316, 6 2001.

[60] V. Marino, G. D. Cortivo, P. E. Maltese, G. Placidi, E. D. Siena, B. Falsini, M. Bertelli, and D. Dell'Orco, "Impaired ca^{2+} sensitivity of a novel gcap1 variant causes cone dystrophy and leads to abnormal synaptic transmission between photoreceptors and bipolar cells," *International Journal of Molecular Sciences* **22**, p. 4030, 4 2021.

[61] G. Dal Cortivo, V. Marino, F. Bonì, M. Milani, and D. Dell'Orco, "Missense mutations affecting ca^{2+}-coordination in gcap1 lead to cone-rod dystrophies by altering protein structural and functional properties," *Biochimica et Biophysica Acta (BBA) - Molecular Cell Research* **1867**, p. 118794, 10 2020.

[62] C. P. Hamel, "Cone rod dystrophies," *Orphanet Journal of Rare Diseases* **2**, p. 7, 12 2007.

[63] I. Sokal, W. J. Dupps, M. A. Grassi, J. Brown, L. M. Affatigato, N. Roychowdhury, L. Yang, S. Filipek, K. Palczewski, E. M. Stone, and W. Baehr, "A novel gcap1 missense mutation (l151f) in a large family with autosomal dominant cone-rod dystrophy (adcord)," *Investigative Opthalmology & Visual Science* **46**, p. 1124, 4 2005.

[64] D. Dell'Orco, P. Behnen, S. Linse, and K.-W. Koch, "Calcium binding, structural stability and guanylate cyclase activation in gcap1 variants associated with human cone dystrophy," *Cellular and Molecular Life Sciences* **67**, pp. 973–984, 3 2010.

[65] S. Abbas, V. Marino, N. Weisschuh, S. Kieninger, M. Solaki, D. Dell'Orco, and K.-W. Koch, "Neuronal calcium sensor gcap1 encoded by *GUCA1A* exhibits heterogeneous functional properties in two cases of retinitis pigmentosa," *ACS Chemical Neuroscience* **11**, pp. 1458–1470, 5 2020.

[66] G. Manes, S. Mamouni, E. Hérald, A.-C. Richard, A. Sénéchal, K. Aouad, B. Bocquet, I. Meunier, and C. P. Hamel, "Cone dystrophy or macular dystrophy associated with novel autosomal dominant guca1a mutations.," *Molecular vision* **23**, pp. 198–209, 2017.

[67] A. Payne, “A mutation in guanylate cyclase activator 1a (guca1a) in an autosomal dominant cone dystrophy pedigree mapping to a new locus on chromosome 6p21.1,” *Human Molecular Genetics* **7**, pp. 273–277, 2 1998.

[68] V. Marino, A. Scholten, K.-W. Koch, and D. Dell’Orco, “Two retinal dystrophy-associated missense mutations in *GUCA1A* with distinct molecular properties result in a similar aberrant regulation of the retinal guanylate cyclase,” *Human Molecular Genetics* **24**, pp. 6653–6666, 12 2015.

[69] S. E. Wilkie, Y. Li, E. C. Deery, R. J. Newbold, D. Garibaldi, J. B. Bateman, H. Zhang, W. Lin, D. J. Zack, S. S. Bhattacharya, M. J. Warren, D. M. Hunt, and K. Zhang, “Identification and functional consequences of a new mutation (e155g) in the gene for gcap1 that causes autosomal dominant cone dystrophy,” *The American Journal of Human Genetics* **69**, pp. 471–480, 9 2001.

[70] L. Jiang, D. Wheaton, G. Bereta, K. Zhang, K. Palczewski, D. G. Birch, and W. Baehr, “A novel gcap1(n104k) mutation in ef-hand 3 (ef3) linked to autosomal dominant cone dystrophy,” *Vision Research* **48**, pp. 2425–2432, 10 2008.

[71] K. Kamenarova, M. Corton, B. García-Sandoval, P. F.-S. Jose, V. Panchev, A. Ávila Fernández, M. I. López-Molina, C. Chakarova, C. Ayuso, and S. S. Bhattacharya, “Novel *GUCA1A* mutations suggesting possible mechanisms of pathogenesis in cone, cone-rod, and macular dystrophy patients,” *BioMed Research International* **2013**, pp. 1–15, 2013.

[72] V. B. Kitiratschky, P. Behnen, U. Kellner, J. R. Heckenlively, E. Zrenner, H. JÃ¤gle, S. Kohl, B. Wissinger, and K.-W. Koch, “Mutations in the guca1a gene involved in hereditary cone dystrophies impair calcium-mediated regulation of guanylate cyclase,” *Human Mutation* **30**, pp. E782–E796, 8 2009.

[73] I. V. Peshenko, A. V. Cideciyan, A. Sumaroka, E. V. Olshevskaya, A. Scholten, S. Abbas, K.-W. Koch, S. G. Jacobson, and A. M. Dizhoor, “A

g86r mutation in the calcium-sensor protein gcap1 alters regulation of retinal guanylyl cyclase and causes dominant cone-rod degeneration," *Journal of Biological Chemistry* **294**, pp. 3476–3488, 3 2019.

[74] F. Vocke, N. Weisschuh, V. Marino, S. Malfatti, S. G. Jacobson, C. M. Reiff, D. Dell'Orco, and K.-W. Koch, "Dysfunction of cgmp signalling in photoreceptors by a macular dystrophy-related mutation in the calcium sensor gcap1," *Human Molecular Genetics* , p. ddw374, 12 2016.

[75] A. Wenzel, C. Grimm, M. Samardzija, and C. E. Remé, "Molecular mechanisms of light-induced photoreceptor apoptosis and neuroprotection for retinal degeneration," *Progress in Retinal and Eye Research* **24**, pp. 275–306, 3 2005.

[76] S. Suh, E. H. Choi, A. Raguram, D. R. Liu, and K. Palczewski, "Precision genome editing in the eye," *Proceedings of the National Academy of Sciences* **119**, 9 2022.

[77] A. L. Yan, S. W. Du, and K. Palczewski, "Genome editing, a superior therapy for inherited retinal diseases," *Vision Research* **206**, p. 108192, 5 2023.

[78] A. Akbarzadeh, R. Rezaei-Sadabady, S. Davaran, S. W. Joo, N. Zarghami, Y. Hanifehpour, M. Samiei, M. Kouhi, and K. Nejati-Koshki, "Liposome: classification, preparation, and applications," *Nanoscale Research Letters* **8**, p. 102, 12 2013.

[79] A. Bangham and R. Horne, "Negative staining of phospholipids and their structural modification by surface-active agents as observed in the electron microscope," *Journal of Molecular Biology* **8**, pp. 660–IN10, 1 1964.

[80] N. Singh, A. Joshi, and G. Verma, *Engineered nanomaterials for biomedicine*, pp. 307–328. Elsevier, 2016.

[81] P. Liu, G. Chen, and J. Zhang, "A review of liposomes as a drug delivery system: Current status of approved products, regulatory environments, and future perspectives," *Molecules* **27**, p. 1372, 2 2022.

[82] V. L. Colvin, “The potential environmental impact of engineered nanomaterials,” *Nature Biotechnology* **21**, pp. 1166–1170, 10 2003.

[83] D. Dell’Orco and G. D. Cortivo, “Normal gcaps partly compensate for altered cgmp signaling in retinal dystrophies associated with mutations in guca1a,” *Scientific Reports* **9**, p. 20105, 12 2019.

[84] A. Baker, M. Saltik, H. Lehrmann, I. Killisch, V. Mautner, G. Lamm, G. Christofori, and M. Cotten, “Polyethylenimine (pei) is a simple, inexpensive and effective reagent for condensing and linking plasmid dna to adenovirus for gene delivery,” *Gene Therapy* **4**, pp. 773–782, 8 1997.

[85] A. P. Pandey and K. K. Sawant, “Polyethylenimine: A versatile, multifunctional non-viral vector for nucleic acid delivery,” *Materials Science and Engineering: C* **68**, pp. 904–918, 11 2016.

[86] H. P. Sørensen, H. U. Sperling-Petersen, and K. K. Mortensen, “Production of recombinant thermostable proteins expressed in escherichia coli: completion of protein synthesis is the bottleneck,” *Journal of Chromatography B* **786**, pp. 207–214, 12 2003.

[87] D. Stüber, H. Matile, and G. Garotta, *System for High-Level Production in Escherichia coli and Rapid Purification of Recombinant Proteins: Application to Epitope Mapping, Preparation of Antibodies, and Structure—Function Analysis*, pp. 121–152. Elsevier, 1990.

[88] H. Tegel, J. Steen, A. Konrad, H. Nikdin, K. Pettersson, M. Stenvall, S. Tourle, U. Wrethagen, L. Xu, L. Yderland, M. Uhlén, S. Hober, and J. Ottosson, “High-throughput protein production - lessons from scaling up from 10 to 288 recombinant proteins per week,” *Biotechnology Journal* **4**, pp. 51–57, 1 2009.

[89] J.-Y. Hwang and K.-W. Koch, “Calcium- and myristoyl-dependent properties of guanylate cyclase-activating protein-1 and protein-2,” *Biochemistry* **41**, pp. 13021–13028, 12 2002.

[90] D. M. Francis and R. Page, "Strategies to optimize protein expression in e. coli," *Current Protocols in Protein Science* **61**, 8 2010.

[91] B. W. J. Pirok, D. R. Stoll, and P. J. Schoenmakers, "Recent developments in two-dimensional liquid chromatography: Fundamental improvements for practical applications," *Analytical Chemistry* **91**, pp. 240–263, 1 2019.

[92] V. Marino, G. D. Cortivo, E. Oppici, P. E. Maltese, F. D'Esposito, E. Manara, L. Ziccardi, B. Falsini, A. Magli, M. Bertelli, and D. Dell'Orco, "A novel p.(glu111val) missense mutation in guca1a associated with cone-rod dystrophy leads to impaired calcium sensing and perturbed second messenger homeostasis in photoreceptors," *Human Molecular Genetics* , 12 2018.

[93] M. Bradford, "A rapid and sensitive method for the quantitation of microgram quantities of protein utilizing the principle of protein-dye binding," *Analytical Biochemistry* **72**, pp. 248–254, 5 1976.

[94] U. K. LAEMMLI, "Cleavage of structural proteins during the assembly of the head of bacteriophage t4," *Nature* **227**, pp. 680–685, 8 1970.

[95] N. J. Greenfield, "Using circular dichroism spectra to estimate protein secondary structure," *Nature Protocols* **1**, pp. 2876–2890, 12 2006.

[96] S. Y. Venyaminov and J. T. Yang, *Determination of Protein Secondary Structure*, pp. 69–107. Springer US, 1996.

[97] C. Bertucci, M. Pistolozzi, and A. D. Simone, "Structural characterization of recombinant therapeutic proteins by circular dichroism," *Current Pharmaceutical Biotechnology* **12**, pp. 1508–1516, 10 2011.

[98] K. Huynh and C. L. Partch, "Analysis of protein stability and ligand interactions by thermal shift assay," *Current Protocols in Protein Science* **79**, 2 2015.

[99] E. R. Simons, E. G. Schneider, and E. R. Blout, "Thermal effects on the circular dichroism spectra of ribonuclease a and of ribonuclease s-

protein," *Journal of Biological Chemistry* **244**, pp. 4023–4026, 8 1969. doi: 10.1016/S0021-9258(17)36379-2.

[100] S. Beretta, L. Lunelli, G. Chirico, and G. Baldini, "Dynamic light scattering from small particles: expected accuracy in hemoglobin data reduction," *Applied Optics* **35**, p. 3763, 7 1996.

[101] J. Stetefeld, S. A. McKenna, and T. R. Patel, "Dynamic light scattering: a practical guide and applications in biomedical sciences," *Biophysical Reviews* **8**, pp. 409–427, 12 2016.

[102] P. Pusey, "Photon correlation and light beating spectroscopy," *Plenum Press, New York* , 1974.

[103] V. Marino, M. Riva, D. Zamboni, K.-W. Koch, and D. Dell'Orco, "Bringing the ca^{2+} sensitivity of myristoylated recoverin into the physiological range," *Open Biology* **11**, 1 2021.

[104] I. André and S. Linse, "Measurement of ca^{2+}-binding constants of proteins and presentation of the caligator software," *Analytical Biochemistry* **305**, pp. 195–205, 6 2002.

[105] D. Dell'Orco, P. Behnen, S. Linse, and K.-W. Koch, "Calcium binding, structural stability and guanylate cyclase activation in gcap1 variants associated with human cone dystrophy," *Cellular and Molecular Life Sciences* **67**, pp. 973–984, 3 2010.

[106] H. Nguyen, J. Park, S. Kang, and M. Kim, "Surface plasmon resonance: A versatile technique for biosensor applications," *Sensors* **15**, pp. 10481–10510, 5 2015.

[107] Y. Zeng, R. Hu, L. Wang, D. Gu, J. He, S.-Y. Wu, H.-P. Ho, X. Li, J. Qu, B. Z. Gao, and Y. Shao, "Recent advances in surface plasmon resonance imaging: detection speed, sensitivity, and portability," *Nanophotonics* **6**, pp. 1017–1030, 8 2017.

[108] D. Dell'Orco and K.-W. Koch, "Fingerprints of calcium-binding protein conformational dynamics monitored by surface plasmon resonance," *ACS Chemical Biology* **11**, pp. 2390–2397, 9 2016.

[109] A. Avesani, V. Marino, S. Zanzoni, K.-W. Koch, and D. Dell'Orco, "Molecular properties of human guanylate cyclase–activating protein 2 (gcap2) and its retinal dystrophy–associated variant g157r," *Journal of Biological Chemistry* **296**, p. 100619, 1 2021.

[110] P. Zägel, D. Dell'Orco, and K.-W. Koch, "The dimerization domain in outer segment guanylate cyclase is a ca^{2+}-sensitive control switch module," *Biochemistry* **52**, pp. 5065–5074, 7 2013.

[111] C. Lange and K.-W. Koch, "Calcium-dependent binding of recoverin to membranes monitored by surface plasmon resonance spectroscopy in real time," *Biochemistry* **36**, pp. 12019–12026, 10 1997.

[112] C. Gardiner, Y. J. Ferreira, R. A. Dragovic, C. W. Redman, and I. L. Sargent, "Extracellular vesicle sizing and enumeration by nanoparticle tracking analysis," *Journal of Extracellular Vesicles* **2**, 1 2013.

[113] D. Bachurski, M. Schuldner, P. Nguyen, A. Malz, K. S. Reiners, P. C. Grenzi, F. Babatz, A. C. Schauss, H. P. Hansen, M. Hallek, and E. P. von Strandmann, "Extracellular vesicle measurements with nanoparticle tracking analysis – an accuracy and repeatability comparison between nanosight ns300 and zetaview," *Journal of Extracellular Vesicles* **8**, 12 2019.

[114] M. Karplus and J. A. McCammon, "Molecular dynamics simulations of biomolecules," *Nature Structural Biology* **9**, pp. 646–652, 9 2002.

[115] P. Robustelli, S. Piana, and D. E. Shaw, "Developing a molecular dynamics force field for both folded and disordered protein states," *Proceedings of the National Academy of Sciences* **115**, 5 2018.

[116] E. Harder, W. Damm, J. Maple, C. Wu, M. Reboul, J. Y. Xiang, L. Wang, D. Lupyan, M. K. Dahlgren, J. L. Knight, J. W. Kaus, D. S. Cerutti, G. Krilov,

W. L. Jorgensen, R. Abel, and R. A. Friesner, "Opls3: A force field providing broad coverage of drug-like small molecules and proteins," *Journal of Chemical Theory and Computation* **12**, pp. 281–296, 1 2016.

[117] J. Huang, S. Rauscher, G. Nawrocki, T. Ran, M. Feig, B. L. de Groot, H. Grubmüller, and A. D. MacKerell, "Charmm36m: an improved force field for folded and intrinsically disordered proteins," *Nature Methods* **14**, pp. 71–73, 1 2017.

[118] M. J. Abraham, T. Murtola, R. Schulz, S. Páll, J. C. Smith, B. Hess, and E. Lindahl, "Gromacs: High performance molecular simulations through multi-level parallelism from laptops to supercomputers," *SoftwareX* **1**, pp. 19–25, 2015.

[119] J. C. Phillips, R. Braun, W. Wang, J. Gumbart, E. Tajkhorshid, E. Villa, C. Chipot, R. D. Skeel, L. Kalé, and K. Schulten, "Scalable molecular dynamics with namd," *Journal of Computational Chemistry* **26**, pp. 1781–1802, 12 2005.

[120] P. Eastman, J. Swails, J. D. Chodera, R. T. McGibbon, Y. Zhao, K. A. Beauchamp, L.-P. Wang, A. C. Simmonett, M. P. Harrigan, C. D. Stern, R. P. Wiewiora, B. R. Brooks, and V. S. Pande, "Openmm 7: Rapid development of high performance algorithms for molecular dynamics," *PLOS Computational Biology* **13**, p. e1005659, 7 2017.

[121] R. Salomon□Ferrer, D. A. Case, and R. C. Walker, "An overview of the amber biomolecular simulation package," *WIREs Computational Molecular Science* **3**, pp. 198–210, 3 2013.

[122] I. T. Jolliffe and J. Cadima, "Principal component analysis: a review and recent developments," *Philosophical Transactions of the Royal Society A: Mathematical, Physical and Engineering Sciences* **374**, p. 20150202, 4 2016.

[123] A. Amadei, M. A. Ceruso, and A. D. Nola, "On the convergence of the conformational coordinates basis set obtained by the essential dynamics analysis

of proteins' molecular dynamics simulations," *Proteins: Structure, Function, and Genetics* **36**, pp. 419–424, 9 1999.

[124] C. Chothia and A. Lesk, "The relation between the divergence of sequence and structure in proteins.," *The EMBO Journal* **5**, pp. 823–826, 4 1986.

[125] R. Kumar and A. Sharma, *Computational strategies and tools for protein tertiary structure prediction*, Elsevier, 2023.

[126] M. P. Jacobson, R. A. Friesner, Z. Xiang, and B. Honig, "On the role of the crystal environment in determining protein side-chain conformations," *Journal of Molecular Biology* **320**, pp. 597–608, 7 2002.

[127] G. M. Morris and M. Lim-Wilby, *Molecular Docking*, pp. 365–382. Humana Press, Totowa, NJ, 2008.

[128] I. Halperin, B. Ma, H. Wolfson, and R. Nussinov, "Principles of docking: An overview of search algorithms and a guide to scoring functions," *Proteins: Structure, Function, and Bioinformatics* **47**, pp. 409–443, 6 2002.

[129] N. Andrusier, E. Mashiach, R. Nussinov, and H. J. Wolfson, "Principles of flexible protein–protein docking," *Proteins: Structure, Function, and Bioinformatics* **73**, pp. 271–289, 11 2008.

[130] M. F. Lensink, G. Brysbaert, N. Raouraoua, P. A. Bates, M. Giulini, R. V. Honorato, C. van Noort, J. M. C. Teixeira, A. M. J. J. Bonvin, R. Kong, H. Shi, X. Lu, S. Chang, J. Liu, Z. Guo, X. Chen, A. Morehead, R. S. Roy, T. Wu, N. Giri, F. Quadir, C. Chen, J. Cheng, C. A. D. Carpio, E. Ichiishi, L. A. Rodriguez□Lumbreras, J. Fernandez□Recio, A. Harmalkar, L. Chu, S. Canner, R. Smanta, J. J. Gray, H. Li, P. Lin, J. He, H. Tao, S. Huang, J. Roel□Touris, B. Jimenez□Garcia, C. W. Christoffer, A. J. Jain, Y. Kagaya, H. Kannan, T. Nakamura, G. Terashi, J. C. Verburgt, Y. Zhang, Z. Zhang, H. Fujuta, M. Sekijima, D. Kihara, O. Khan, S. Kotelnikov, U. Ghani, D. Padhorny, D. Beglov, S. Vajda, D. Kozakov, S. S. Negi, T. Ricciardelli, D. Barradas□Bautista, Z. Cao, M. Chawla, L. Cavallo, R. Oliva, R. Yin, M. Cheung,

J. D. Guest, J. Lee, B. G. Pierce, B. Shor, T. Cohen, M. Halfon, D. Schneidman□Duhovny, S. Zhu, R. Yin, Y. Sun, Y. Shen, M. Maszota□Zieleniak, K. K. Bojarski, E. A. Lubecka, M. Marcisz, A. Danielsson, L. Dziadek, M. Gaardlos, A. Gieldon, A. Liwo, S. A. Samsonov, R. Slusarz, K. Zieba, A. K. Sieradzan, C. Czaplewski, S. Kobayashi, Y. Miyakawa, Y. Kiyota, M. Takeda□Shitaka, K. Olechnovic, L. Valancauskas, J. Dapkunas, C. Venclovas, B. Wallner, L. Yang, C. Hou, X. He, S. Guo, S. Jiang, X. Ma, R. Duan, L. Qui, X. Xu, X. Zou, S. Velankar, and S. J. Wodak, "Impact of *AlphaFold* on structure prediction of protein complexes: The *CASP15-CAPRI* experiment," *Proteins: Structure, Function, and Bioinformatics* **91**, pp. 1658–1683, 12 2023.

[131] D. Kozakov, R. Brenke, S. R. Comeau, and S. Vajda, "Piper: An fft-based protein docking program with pairwise potentials," *Proteins: Structure, Function, and Bioinformatics* **65**, pp. 392–406, 11 2006.

[132] R. Chen, L. Li, and Z. Weng, "Zdock: An initial-stage protein-docking algorithm," *Proteins: Structure, Function, and Bioinformatics* **52**, pp. 80–87, 7 2003.

International Journal of
Molecular Sciences

MDPI

Article

A Novel *GUCA1A* Variant Associated with Cone Dystrophy Alters cGMP Signaling in Photoreceptors by Strongly Interacting with and Hyperactivating Retinal Guanylate Cyclase

Amedeo Biasi [1], Valerio Marino [1], Giuditta Dal Cortivo [1], Paolo Enrico Maltese [2], Antonio Mattia Modarelli [3], Matteo Bertelli [2,4], Leonardo Colombo [3,*] and Daniele Dell'Orco [1,*]

[1] Department of Neurosciences, Biomedicine and Movement Sciences, Section of Biological Chemistry, University of Verona, 37134 Verona, Italy; amedeo.biasi@univr.it (A.B.); valerio.marino@univr.it (V.M.); giuditta.dalcortivo@univr.it (G.D.C.)
[2] MAGI'S Lab s.r.l., 38068 Rovereto, Italy; paolo.maltese@assomagi.org (P.E.M.); matteo.bertelli@assomagi.org (M.B.)
[3] Department of Ophthalmology, ASST Santi Paolo e Carlo Hospital, University of Milan, 20142 Milano, Italy; antoniomattia.modarelli@gmail.com
[4] MAGI Euregio, 39100 Bolzano, Italy
* Correspondence: leonardo.colombo.82@gmail.com (L.C.); daniele.dellorco@univr.it (D.D.); Tel.: +39-02-81844301 (L.C.); +39-045-802-7637 (D.D.)

Citation: Biasi, A.; Marino, V.; Dal Cortivo, G.; Maltese, P.E.; Modarelli, A.M.; Bertelli, M.; Colombo, L.; Dell'Orco, D. A Novel *GUCA1A* Variant Associated with Cone Dystrophy Alters cGMP Signaling in Photoreceptors by Strongly Interacting with and Hyperactivating Retinal Guanylate Cyclase. *Int. J. Mol. Sci.* **2021**, *22*, 10809. https://doi.org/10.3390/ijms221910809

Academic Editor: Kai Kaarniranta

Received: 7 September 2021
Accepted: 4 October 2021
Published: 6 October 2021

Abstract: Guanylate cyclase-activating protein 1 (GCAP1), encoded by the *GUCA1A* gene, is a neuronal calcium sensor protein involved in shaping the photoresponse kinetics in cones and rods. GCAP1 accelerates or slows the cGMP synthesis operated by retinal guanylate cyclase (GC) based on the light-dependent levels of intracellular Ca^{2+}, thereby ensuring a timely regulation of the phototransduction cascade. We found a novel variant of *GUCA1A* in a patient affected by autosomal dominant cone dystrophy (adCOD), leading to the Asn104His (N104H) amino acid substitution at the protein level. While biochemical analysis of the recombinant protein showed impaired Ca^{2+} sensitivity of the variant, structural properties investigated by circular dichroism and limited proteolysis excluded major structural rearrangements induced by the mutation. Analytical gel filtration profiles and dynamic light scattering were compatible with a dimeric protein both in the presence of Mg^{2+} alone and Mg^{2+} and Ca^{2+}. Enzymatic assays showed that N104H-GCAP1 strongly interacts with the GC, with an affinity that doubles that of the WT. The doubled IC_{50} value of the novel variant (520 nM for N104H vs. 260 nM for the WT) is compatible with a constitutive activity of GC at physiological levels of Ca^{2+}. The structural region at the interface with the GC may acquire enhanced flexibility under high Ca^{2+} conditions, as suggested by 2 µs molecular dynamics simulations. The altered interaction with GC would cause hyper-activity of the enzyme at both low and high Ca^{2+} levels, which would ultimately lead to toxic accumulation of cGMP and Ca^{2+} in the photoreceptor outer segment, thus triggering cell death.

Keywords: GUCA1A; phototransduction; cone dystrophy; guanylyl cyclase; photoreceptors; neuronal calcium sensor; retinal degeneration; calcium binding proteins

1. Introduction

The phototransduction cascade in photoreceptors is the first signaling event initiating vision, permitting the conversion of the energy carried by light and absorbed by the opsins in the photoreceptor outer segment into a chemical signal, namely the transient drop in the release of glutamate from the synaptic term, which is sensed by downstream neurons [1]. The extraordinary capability of phototransduction to kinetically adapt to a broad variety of light conditions relies on the fine regulation of the cascade by two second messengers,

namely Ca^{2+} and cyclic guanosine monophosphate (cGMP). Subtle alterations of their levels in the outer segment during the response to light triggers feedback mechanisms, which permit a timely shutoff of the cascade as well as adaption to specific light or dark conditions [1,2]. Absorption of light by (rhod)opsin activates phosphodiesterase 6, which catalyzes the hydrolysis of cGMP, thereby causing its dissociation from cyclic nucleotide-gated channels (CNG) and their closure. The light-independent extrusion of Ca^{2+} from the Na^+/Ca^{2+}, K^+-exchanger further adds to the drop of Ca^{2+} concentration in the photoreceptor outer segments below 100 nM in the light [3] and contributes to the hyperpolarization of the cell membrane, which propagates to the photoreceptor synaptic terminal.

Subtle changes in Ca^{2+} concentration are promptly detected by the neuronal calcium sensors Guanylate Cyclase-Activating Proteins (GCAPs). Two isoforms (GCAP1 and GCAP2) are expressed in human rods and cones, but only GCAP1 seems to be actively involved in the phototransduction cascade as a modulator of retinal guanylate cyclase (GC) activity, GCAP2 being probably involved in other biochemical processes [4,5]. In the dark, the Ca^{2+}-loaded GCAP1 adopts a conformation that prevents the activation of GC, thereby inhibiting the synthesis of cGMP. The light-induced drop in Ca^{2+} concentration induces the replacement of Ca^{2+} ions for Mg^{2+} in the same binding sites in GCAP1 [6,7]. The conformation adopted by Mg^{2+}-GCAP1 stimulates the accelerated synthesis of cGMP by GC, thus permitting rapid restoration of dark-adapted cell conditions by reopening of the CNG channels [8,9]. Although two isoforms of retinal GC have been found in photoreceptors, namely GC1 (or RetGC-1, GC-E) and GC2 (RetGC-2, GC-F), the latter produces less than 30% of cGMP in murine retina [10]; therefore, the major player in phototransduction is GC1—which we will refer to as GC throughout this paper.

The gene coding for GCAP1, named *GUCA1A*, has been associated with autosomal dominant cone dystrophies (adCOD) [11–25], a class of severe retinal degeneration diseases characterized by central vision loss, impaired color vision, and photophobia [26]. More than twenty point-mutations in *GUCA1A* have been found to be pathogenic and the highly heterogeneous phenotype seems to be strictly related to the specific amino acid substitution; indeed, different side chains at the same position can lead to dramatically different biochemical properties at the protein level [27].

In this work, we identify a novel variant of GCAP1 associated with adCOD, resulting in the substitution of Asn 104 with the positively charged residue His (p.N104H) within the high affinity binding site EF-hand 3 (EF3), a highly conserved region among vertebrates. The same position has been previously associated with adCOD in two independent studies, where a single amino acid replacement (p.N104K) [20] and a double amino acid substitution (p.N104K and p.G105R) have been detected in two different families [28]. Clinical data based on a long follow-up of 16 years for the oldest patient point to a relatively slow progression: the boundaries of the lesion remained confined within the macula, with no sign of rod system involvement. To unveil the perturbed mechanisms in the signaling cascade at a molecular level, we expressed N104H-GCAP1 in a heterologous system and characterized its structural and functional properties through a thorough integration of biochemical and biophysical studies with molecular dynamics simulations. We found that, despite the significant loss of Ca^{2+} sensitivity, the novel GCAP1 variant activates the target GC at higher levels as compared to the wild type (WT), both under conditions of low and high intracellular Ca^{2+}. The interaction of the novel GCAP1 variant with GC is tighter than that of its WT counterpart and induces a constitutive activity of the cyclase at physiological levels of Ca^{2+}. Structural alterations induced by the N104H mutation are minor at all levels of GCAP1 structural organization, but they are enough to alter the allosteric communication with the N-terminal lobe.

2. Results

2.1. Clinical Phenotype and Disease Progression

2.1.1. Patient 1

The proband was an 18-year-old female. She came to our attention at the age of 12 because her father, here referred to as patient 2, was affected by COD. She only complained mild photophobia. At the first visit her visual acuity (VA) was 1.0 in both eyes. At the last follow-up, at the age of 18, VA was 0.9 in both eyes. Refractive error was −3.00 sph −1.75 cyl/95 in her right eye and −2.00 sph −1.50 cyl/60 in her left eye. Ophthalmoscopic examination did not show any sign of macular affection. Fundus autofluorescence (FAF) revealed a mild perifoveal hyper-autofluorescence in both eyes (Figure 1), while optical coherence tomography (OCT) imaging showed irregularities of hyper-reflective outer retinal bands, with the line corresponding to interdigitation zone not clearly detectable (Figure 2). Anatomically, the foveal lesion did not show any detectable sign of progression during the 7-year follow-up.

Full-field ERG examination showed characteristically reduced cone single-flash responses and a normal implicit time in the flicker amplitudes. The patient's rod function was normal: in *GUCA1A*-related adCOD generally rod system remains preserved, although in some cases progression may occur over time (Figure 3).

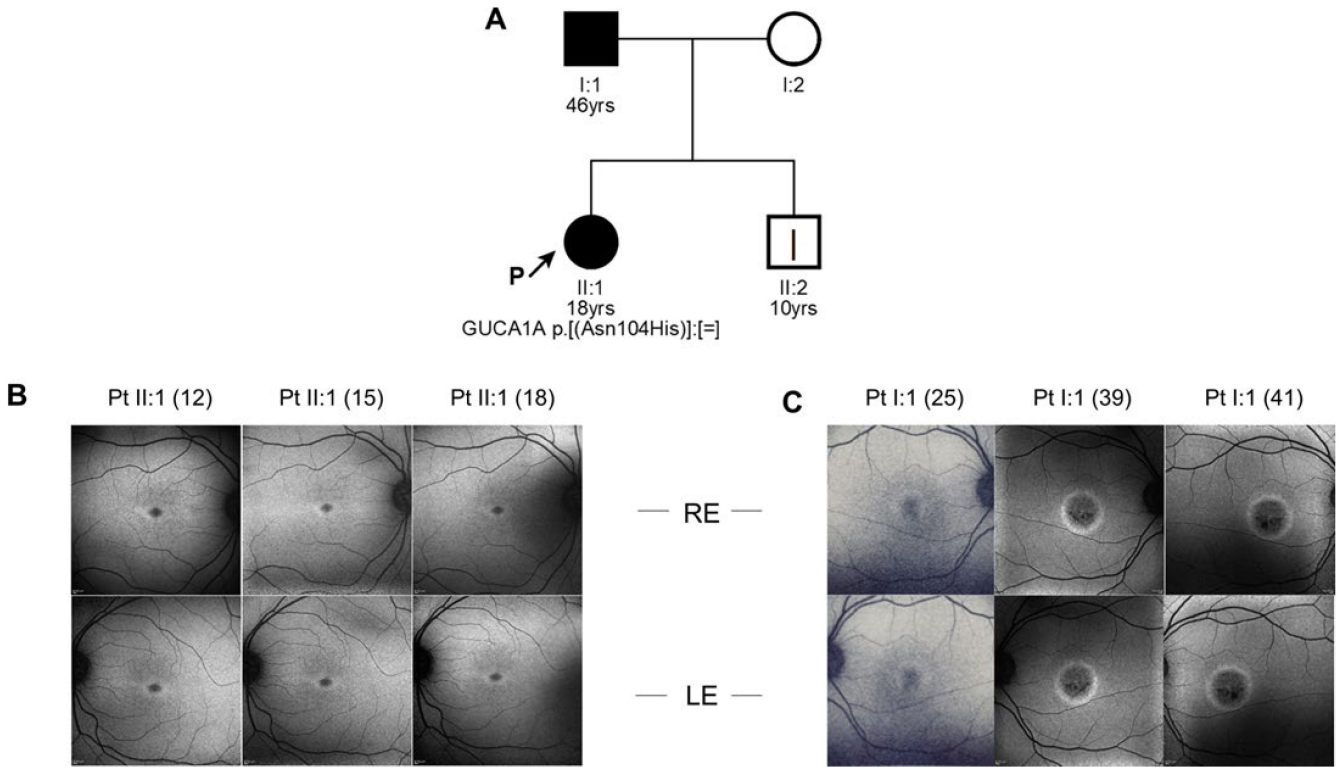

Figure 1. Clinical data and mutation inheritance. (**A**) Pedigree showing the matching genotype–phenotype segregation of the mutant allele of *GUCA1A*, harboring the c.310A > C mutation causing the amino acid substitution N104H. Legend: square, male subject; circle, female subject; black symbol, affected subject; white symbol, healthy subject; yrs, subject age at his/her last clinical evaluation; P, proband; square brackets ([;];[;]), maternal and paternal chromosome; =, no change; |, sub-clinic phenotype. Fundus images of (**B**) patient II:1 (age 12, 15, 18) and (**C**) patient I:1 (age 25, 39, 41)'s right (upper panels) and left eyes (lower panels).

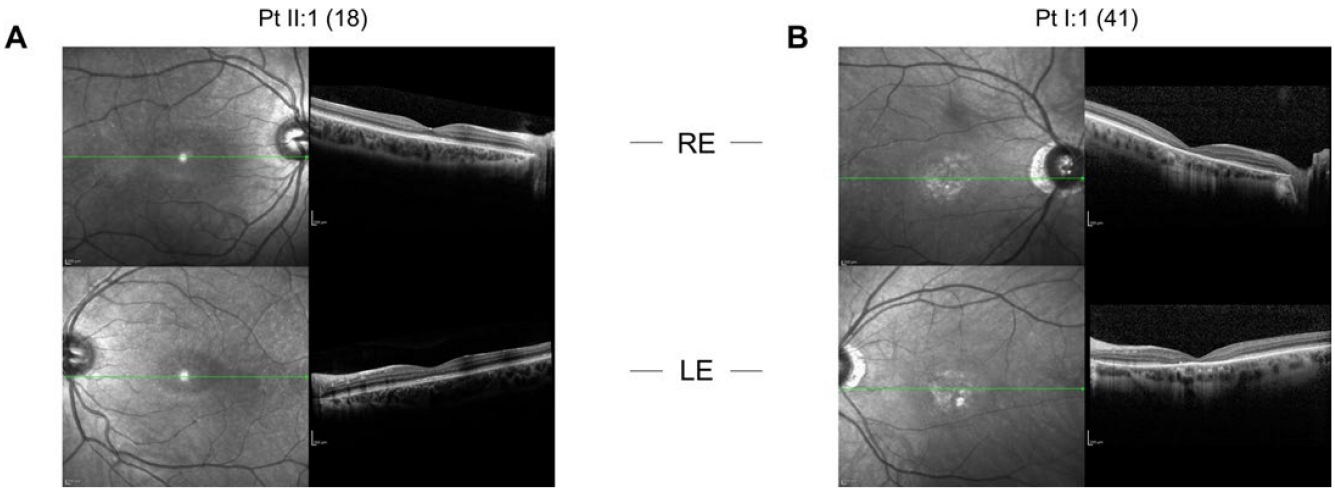

Figure 2. Spectral-domain optical coherence tomography (SD-OCT) scans of the right (upper panels) and left eyes (lower panels) of (**A**) the proband at the age of 18 and (**B**) of patient 2 I:1 at the age of 41. The green line indicates the interdigitation zone.

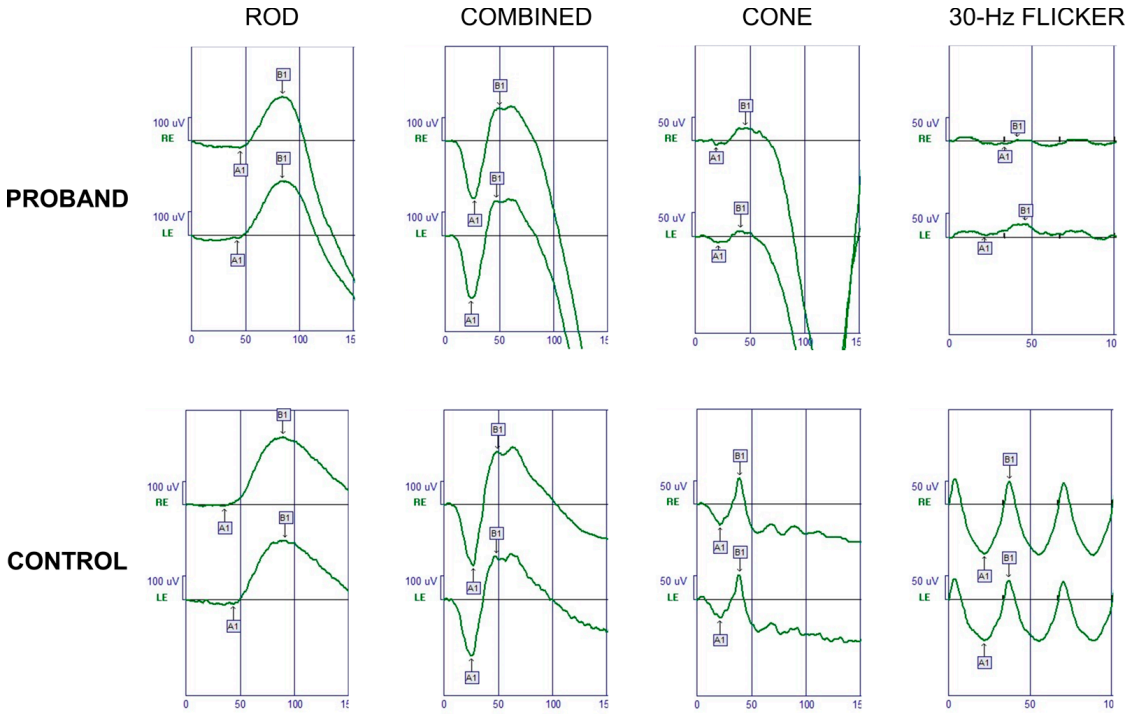

Figure 3. Full-field ERG of the proband's right eye (RE) and left eye (LE). Normal responses are provided for comparison (Control). After a 30-min dark adaptation, dark-adapted responses (Rod and Combined) were within normal limits, while photopic components were reduced (Cone and 30-Hz flicker).

2.1.2. Patient 2

Patient 2, the proband's father, was 46 years old at the time of the observation. He complained photophobia and a decrease in VA from the age of 15. At the age of 25, his VA was 0.2 in both eyes. At his last follow-up, at the age of 41, his VA was 0.05 in both eyes, with also a −0.75 sph refractive error in both eyes. The fundus examination showed normal optic disks and retinal vessels with signs of foveal atrophy. Fundus autofluorescence (FAF) revealed macular hypo-autofluorescence circumscribed by a hyper-autofluorescent ring in each eye (Figure 1), while optical coherence tomography (OCT) imaging showed a marked reduction in central macular thickness and an atrophy of outer retinal layers (Figure 2). Full-field ERG examination showed normal scotopic responses and reduced

responses for the photopic component (data not shown), in line with the diagnosis of COD. In patient 2 the macular lesion enlarged over time: we can thus hypothesize that his age and the longer time passed between the two follow-ups might have played a crucial role in the development of the condition, as compared to the clinical stability of the proband.

2.1.3. Patient 3

Patient 3 is the 10-year-old brother of the proband and son of patient 2. He did not report symptoms related to macular disease. At the time of his first visit in our department (at the age of 10), VA was 0.9 in both eyes. Refractive error was −0.50 sph −1.50 cyl/15 in his right eye and −1.50cyl/180 in his left eye. Ophthalmoscopic examination did not show any sign of macular affection. Both FAF and OCT features resembled the alterations observed in the proband, as shown in Figure S1.

2.2. Identification of a Novel Variant of GUCA1A in Heterozygosis

The NGS genetic testing resulted in a mean coverage of targeted bases of 170.4X, with 97.4% covered at least 25X. We identified the novel heterozygous variant c.310A > C, p.(Asn104His) in the exon 4 of *GUCA1A* gene (NM_000409.4). With the help of the online tool VarSome [29] (accessed on 18 August 2021) the variant was classified as likely pathogenic, in accordance with the American College of Medical Genetics and Genomics guidelines (ACMG) [30], by the following scores:

- PM1: Located in a mutational hot spot and/or critical and well-established functional domain (e.g., active site of an enzyme) without benign variation.
- PM2: Absent from controls (or at extremely low frequency if recessive) in the Exome Sequencing Project, 1000 Genomes Project, or Exome Aggregation Consortium.
- PM5: Novel missense change at an amino acid residue where a different missense change determined to be pathogenic has been seen before. Alternative variant chr6:42146128 C⇒A (Asn104Lys) is classified as Likely Pathogenic, one star, by ClinVar (and confirmed using ACMG).
- PP2: Missense variant in a gene that has a low rate of benign missense variation and in which missense variants are a common mechanism of disease.
- PP3: Multiple lines of computational evidence support a deleterious effect on the gene or gene product (conservation, evolutionary, splicing impact, etc.).

Unfortunately, the proband's father and brother were not available for genetic testing. However, the phenotypes of all three subjects and their autosomal dominant inheritance pattern are in line with the association to the *GUCA1A* gene.

2.3. Retinal Guanylate Cyclase Is Hyperactivated by N104H-GCAP1

The functional effects of the identified amino acid substitution were probed at the protein level by the heterologous expression and purification of the N104H-GCAP1 variant and by testing its ability to activate and inhibit GC in reconstitution experiments. We initially probed the functionality of N104H-GCAP1 by monitoring the regulation of GC at: (i) high Ca^{2+} levels, corresponding to the levels in dark-adapted photoreceptors; (ii) very low Ca^{2+} levels, such as in light-activated photoreceptors. The enzymatic activity, that is the rate of cGMP synthesis, was then compared with that of WT-GCAP1. N104H-GCAP1 showed an increased ability to activate GC in both conditions, as shown by the significantly higher cGMP production at both high ($p < 0.001$) and low ($p < 0.001$) Ca^{2+} concentration (Figure 4A). Despite the hyperactivation of GC observed at both Ca^{2+} levels, the relative activation capability (X-fold = 3.9, Table 1) was approximately half of that of the WT (X-fold = 7.4), which is indicative of a compromised ability of the GC-GCAP complex to switch between activated and inhibited. We then measured the apparent affinity (EC_{50}) of GC for N104H-GCAP1 by evaluating the enzymatic activity as a function of the concentration of GCAP1 (Figure 4B). The affinity of the novel variant for GC (EC_{50} = 1.6 μM) was double that of the WT (EC_{50} = 3.2 μM; Table 1). Finally, we measured the Ca^{2+}-dependence of GC-activity (IC_{50}) for N104H-GCAP1 (Figure 4C and Table 1). The variant showed a

clear inability to fully inhibit the GC target over the physiological range of Ca^{2+} variation (gray-shaded area): indeed, the IC_{50} corresponding to the activation profile (0.52 μM, Table 1) was doubled as compared to the one observed for WT-GCAP1 (0.26 μM). The co-operativity of the regulation process was slightly reduced (h = 1.77 for N104H vs. h = 2.04 for WT-GCAP1, Table 1).

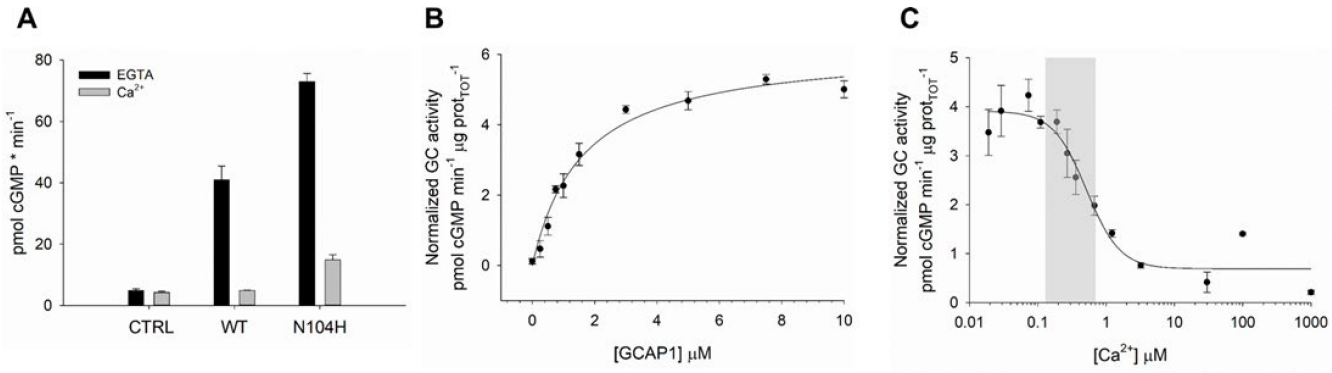

Figure 4. Ca^{2+}-dependent Guanylate Cyclase (GC) regulation by GCAP1 variants. (**A**) Membranes containing GC were reconstituted with 5 μM WT or N104H-GCAP1 and <19 nM Ca^{2+} (black) or ~30 μM free Ca^{2+} (grey); control data were obtained using membranes without addition of GCAP1; reported data refer to average ± standard deviation of 6 technical replicates. (**B**) GC activity as a function of N104H-GCAP1 concentration (0 - 10 μM) in the presence of <19 nM Ca^{2+}. (**C**) GC activity as a function of Ca^{2+} concentration (<19 nM - 1 mM) in the presence of 5 μM N104H-GCAP1. The physiological window of variation in Ca^{2+} concentration in photoreceptors is represented by the grey-shaded area. Measured enzymatic parameters are reported in Table 1.

Table 1. Enzymatic regulation and Ca^{2+}-affinity of GCAP1 variants. [a] [Ca^{2+}] at which GCs activity is half-maximal; [b] Hill coefficient; [c] [N104H] at which GCs activity is half-maximal; [d] calculated as $(GC_{max}\text{-}GC_{min})/GC_{min}$, where GC_{max} and GC_{min} represents the maximal and minimal cGMP production; [e] decimal logarithm of the macroscopic Ca^{2+}-binding constants after data fitting to a three independent binding sites model obtained with CaLigator [31]; [f] apparent affinity values calculated after averaging $logK_i$; [g] WT data are taken from Ref. [27].

Variant	IC_{50} [a] (μM)	h [b]	EC_{50} [c] (μM)	X-fold [d]	$logK_1$ [e]	$logK_2$ [e]	$logK_3$ [e]	K_d^{app} [f] (μM)
WT [g]	0.26 ± 0.01	2.05 ± 0.21	3.2 ± 0.3	7.4	7.07 ± 0.13	5.55 ± 0.19	-	0.49
N104H	0.52 ± 0.1	1.77 ± 0.59	1.6 ± 0.2	3.9	5.92 ± 0.09	4.7 ± 0.48	4.23 ± 0.34	11.2

2.4. Ca^{2+}-Affinity Is Slightly Reduced in N104H-GCAP1

The N104H amino acid substitution affects the highly conserved residue 5 of the Ca^{2+}-binding loop in EF3 (Figure 5). The carbonyl group constitutes a Ca^{2+}-coordinator in Asn104 (Figure 5B, left) and it is lost in the N104H variant, which introduces a positively charged imidazole (Figure 5B, right), expected to perturb the Ca^{2+} coordination.

To experimentally assess the effects of the amino acid substitution we used sodium dodecyl sulphate-polyacrylamide gel electrophoresis (SDS-PAGE) and monitored the differential electrophoretic migration of GCAP1 variants upon ion binding. This method allows the assessment of conformational changes and highlights alterations in Ca^{2+} affinity of neuronal calcium sensors (NCS) [32]. Indeed, in the absence of ions NCS migrate with a mobility expected from their theoretical molecular weight (MW); however, upon Ca^{2+}-binding their electrophoretic mobility exhibits a shift toward a lower apparent MW, which has been found to be proportional to their affinity [33]. Figure 6A reports the assay for WT-GCAP1 and for N104H-GCAP1. In line with previous studies [5], the mobility of WT-GCAP1 shifted from ~23 kDa in the absence of Ca^{2+} to ~17 kDa in the presence of Ca^{2+}, without substantial alterations observed in the Mg^{2+}-bound form compared to the apo-protein. The N104H variant showed a less prominent shift upon Ca^{2+}-binding, suggesting a reduced affinity for Ca^{2+}.

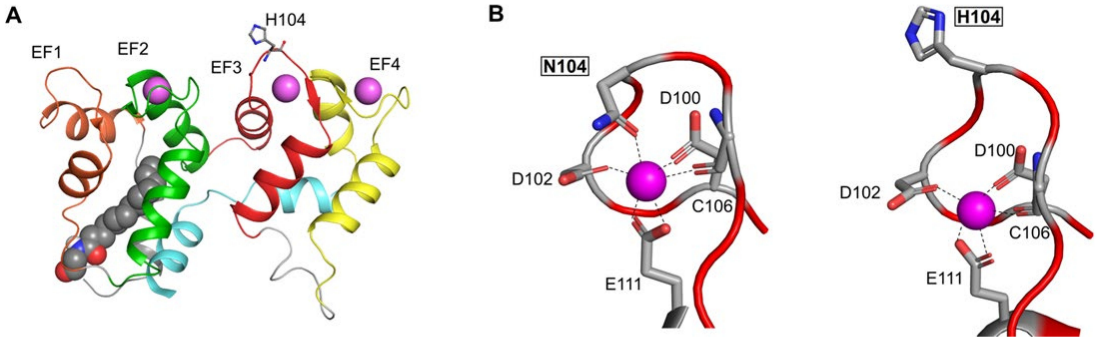

Figure 5. Structural model of N104H-GCAP1. (**A**) The 3D structural model of N104H-GCAP1 in the Ca^{2+}-loaded form is depicted in the cartoon, with the N-terminal helix in grey, EF1 in orange, EF2 in green, EF3 in red, EF4 in yellow, the C-terminal helix in cyan. Ca^{2+} ions and the myristoyl group are represented as pink and grey spheres, respectively, and mutated residue H104 is represented as sticks and colored by element. (**B**) Ca^{2+} ion coordination is shown by key residues of EF3 in WT-GCAP1 (left) and N104H-GCAP1 (right). Structures depicted represent the last frames extracted from the first replica trajectories of both variants.

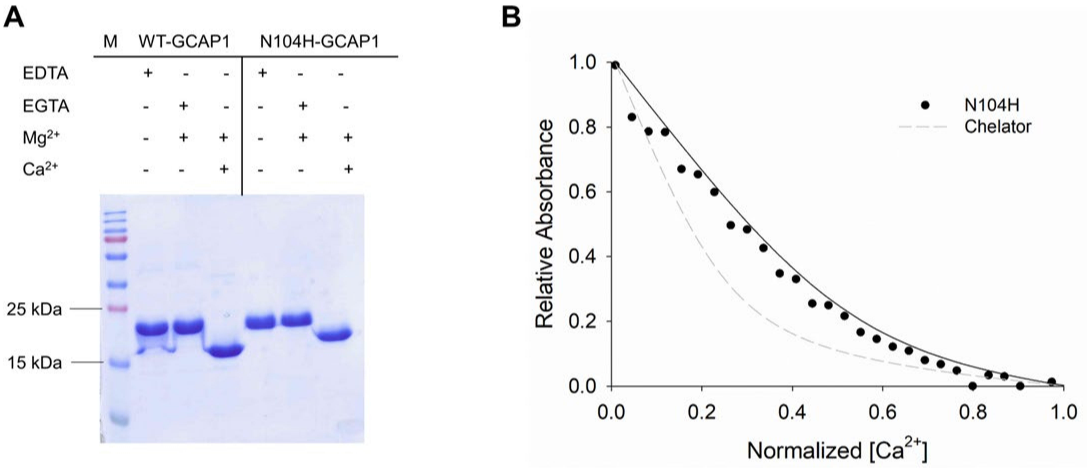

Figure 6. Ca^{2+}-binding assays for N104H-GCAP1. (**A**) The 15% SDS-PAGE gel of 30 µM of WT and N104H-GCAP1 in the presence of 2 mM EDTA, 1 mM EGTA + 1.1 mM Mg^{2+}, 1 mM Mg^{2+} and 1 mM Ca^{2+}. (**B**) Example of a Ca^{2+}-titration curve for N104H-GCAP1. The normalized absorption of 5,5′Br_2-BAPTA in competition with N104H-GCAP1 upon Ca^{2+}-titration in the presence of 1 mM Mg^{2+} is shown as black circles, together with data fitting to a three-Ca^{2+}-binding site model using CaLigator [31] (black line), and the theoretical curve of the chelator in the absence of competition (grey dashed line).

Differences in Ca^{2+}-affinity of the novel variant as compared to the WT were quantitatively evaluated by an assay based on the competition for Ca^{2+} of the chromophoric Ca^{2+}-chelator 5,5′Br_2-BAPTA [10,11,34], whose absorption decreases upon ion binding. The pattern of Ca^{2+}-titration of N104H-GCAP1 (Figure 6B) is typical of a protein that competes with the chelator, but whose affinity for Ca^{2+} is significantly reduced as compared to that shown by the WT (see Refs. [21,33] for typical titrations of WT-GCAP1). The individual macroscopic binding constants were all significantly reduced for N104H-GCAP1 and, accordingly, the apparent affinity for Ca^{2+} was approximately 20-fold lower than that of the WT (Table 1). Such a low affinity (K_d^{app} = 11.2 µM) would make the novel variant unable to correctly regulate the GC in the physiological Ca^{2+}-range (200–600 nM).

2.5. Protein Secondary, Tertiary and Quaternary Structure Are Slightly Affected by the N104H Mutation

Conformational changes in NCS proteins in response to ion binding can be conveniently studied by circular dichroism (CD) spectroscopy, which provides information on protein tertiary structure in the near UV range (250–320 nm) as well as on the secondary

structure, in the far UV (200–250 nm). Moreover, by heating the system under controlled conditions and following the ellipticity at a fixed wavelength, CD can be used to assess protein thermal stability.

The far UV CD spectrum of N104H-GCAP1 (Figure 7A) showed the typical features of an all α-helix protein with two minima at 222 and 208 nm. Only subtle differences in the spectral shape were detected when comparing the variant with the WT. The ratio between the minima at 222 and 208 nm ($\theta_{222}/\theta_{208}$) is a valuable descriptor of the spectral shape. While this ratio slightly increased in both variants when switching from the apo- to the Mg^{2+}-bound form (Table 2), no change could be detected for the N104H variant upon addition of Ca^{2+} ($\theta_{222}/\theta_{208}$ = 0.92). Characteristic of the mutant was also the slightly lower value of relative variation in ellipticity at 222 nm upon ion binding ($\Delta\theta/\theta$), which was 5.5% as compared to the 7.7% of the WT. The analysis of near UV CD spectra (Figure 7B) showed virtually no difference between WT and N104H-GCAP1 in the apo or Mg^{2+}-bound forms (see Ref. [13] for WT spectra). The only slight difference was a completely negative band in the Tyr-Trp region (275–310 nm), shown by the mutant upon addition of Ca^{2+}, which is at odds with the WT spectrum displaying positive dichroism in the 274–290 nm range. Overall, results from CD spectroscopy suggest very minor structural rearrangements of GCAP1 following the N104H substitution in all cation-bound states.

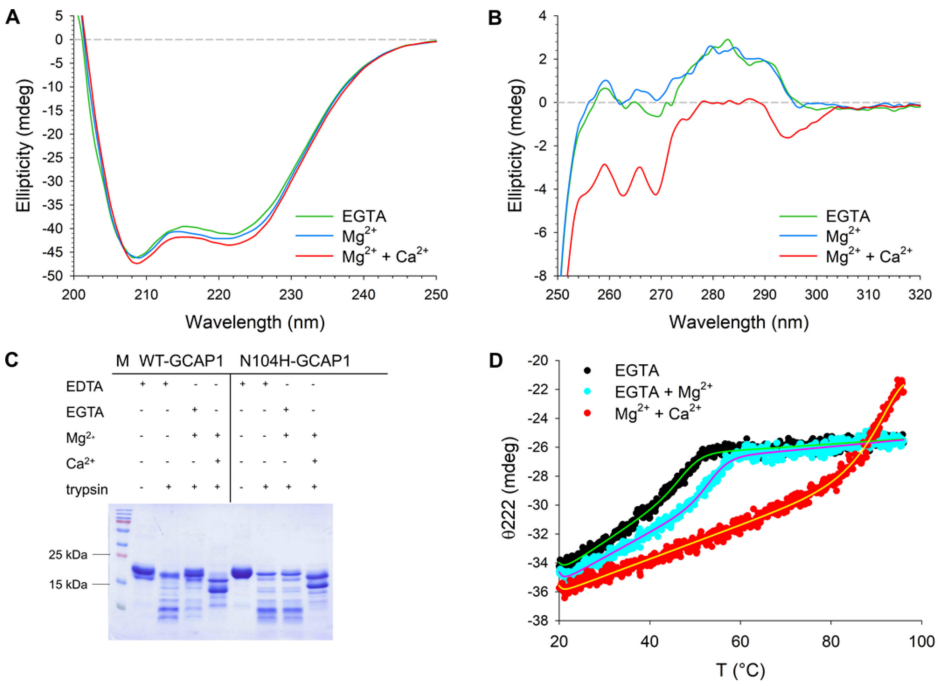

Figure 7. Structural and stability changes occurring in N104H-GCAP1 upon ion binding. (**A**) Far-UV CD spectra of 15 μM N104H-GCAP1 in the presence of 300 μM EGTA (green) and after serial additions of 1 mM Mg^{2+} (blue) and 300 μM free Ca^{2+} (red). (**B**) Near-UV spectra of ~39 μM N104H-GCAP1 in the presence of 500 μM EGTA (green) and after serial additions of 1 mM Mg^{2+} (blue) and 500 μM free Ca^{2+} (red). (**C**) Limited proteolysis of 20 μM WT and N104H-GCAP1 after 10 min incubation with 0.3 μM trypsin in the presence of 2 mM EDTA, 1 mM EGTA + 1.1 mM Mg^{2+} or 1 mM Mg^{2+} and 1 mM Ca^{2+}. Variants in the presence of 2 mM EDTA and in the absence of trypsin represent the reference MW of the undigested protein. (**D**) Thermal denaturation profiles of 10 μM N104H-GCAP1 in the presence of 300 μM EGTA (black), 300 μM EGTA + 1 mM Mg^{2+} (blue) or 1 mM Mg^{2+} + 300 μM Ca^{2+} (red). CD spectroscopy measurements were carried out in 20 mM Tris-HCl pH 7.5, 150 mM KCl, 1 mM DTT buffer. Thermal denaturation profiles were collected by monitoring the ellipticity at 222 nm in a temperature range spanning from 20 °C to 96 °C and were fitted to a function accounting for thermodynamic contributions (see Methods section).

Table 2. Structural and stability descriptors extrapolated from CD spectroscopy, hydrodynamic diameter estimation by DLS, and apparent MW monitored by analytical SEC. [a] calculated as (θ_{222}^{ion}–θ_{222}^{EGTA})/θ_{222}^{EGTA}; [b] melting temperature estimated by fitting ellipticity at 222 nm, as described in the Methods; [c] calculated as ($\theta_{222}^{96\ °C}$–$\theta_{222}^{20\ °C}$)/$\theta_{222}^{20\ °C}$; [d] average hydrodynamic diameter ± s.e.m.; [e] number of measurements used for hydrodynamic diameter calculations; [f] apparent MW estimated by analytical gel filtration; [g] data were taken from Ref. [27]; [h] data were taken from Ref. [13].

Variant	Condition	$\theta_{222}/\theta_{208}$	$\Delta\theta/\theta$ [a] (%)	T_m [b] (°C)	Unfolding [c] (%)	d [d] (nm) [n] [e]	MW [f] (kDa)
WT	EGTA	0.90 [g]	-	54.1 [h]	24.6 [h]	-	-
	Mg^{2+}	0.91 [g]	2.8 [g]	58 [h]	30.8 [h]	6.35 ± 0.07 [g] [27]	45.9 [g]
	Ca^{2+}	0.95 [g]	7.7 [g]	>96 [h]	30.4 [h]	6.85 ± 0.17 [g] [20]	47.8 [g]
N104H	EGTA	0.89	-	48.1	24.9	-	-
	Mg^{2+}	0.92	1.97	53.9	26.1	6.98 ± 0.1 [30]	42.9
	Ca^{2+}	0.92	5.41	>96	38.0	6.97 ± 0.09 [30]	41.7

To investigate whether the N104H mutation could alter the exposure of GCAP1 to proteases, both variants were digested using trypsin in the absence and in the presence of Mg^{2+} and Ca^{2+} (Figure 7C). The time dependence of the proteolytic digestion of WT-GCAP1 in the presence of EDTA (Figure S2A), EGTA and Mg^{2+} (Figure S2B), or Mg^{2+} and Ca^{2+} (Figure S2C) highlighted a clear stabilizing effect of Ca^{2+}. Indeed, 60 min after initiating the proteolytic digestion some traces of undigested protein were still visible. A comparison between WT and N104H-GCAP1 after 10 min of proteolysis showed essentially the same pattern in the apo-variants (Figure 7C), while WT-GCAP1 showed a slightly higher stability in the Mg^{2+}-bound form compared to N104H, as shown by the higher intensity of undigested bands. A similar proteolytic pattern was observed in the presence of Ca^{2+} for the two variants, with proteolytic fragments of bigger MW compared to the Mg^{2+}-bound case.

We corroborated limited proteolysis by thermal stability studies by monitoring the CD signal at 222 nm, corresponding to the minimum in the spectrum displaying the largest variation upon ion addition. The analysis of thermal denaturation profiles is reported in Table 2. In its apo-form, N104H-GCAP1 was 6 °C less stable than WT (T_m = 48.1 °C vs. 54.1 °C, Table 2). In line with proteolysis experiments, Mg^{2+} stabilized the structure of the mutant (T_m = 53.9 °C) less than that of the WT (T_m = 58 °C). Ca^{2+}-binding significantly stabilized both variants, and no clear folded-to-unfolded transition could be detected under the experimental conditions (Figure 7D). The percentage of unfolding was however higher for N104H-GCAP1 (38%) as compared to WT (30%); Table 2).

WT-GCAP1 forms functional dimers under physiological conditions [35,36]. We tested whether this was the case also for N104H-GCAP1 by running analytical gel filtration (Figure 8A) and DLS (Figure 8B) measurements. Analytical gel filtration showed that both in the presence of Mg^{2+} alone and in the co-presence of Mg^{2+} and Ca^{2+} the protein elutes as a dimer, as indicated by the very similar apparent MW (42.9 kDa and 41.7 kDa, respectively; Table 2). This is substantially in line with what has been previously observed for WT-GCAP1 in the same experimental conditions (Table 2) and confirms that the N104H substitution does not modify the oligomeric state of GCAP1. A similar hydrodynamic diameter was measured by DLS for both variants, although the Mg^{2+}-bound form of N104H-GCAP1 showed a small (0.6 nm) but significant ($p < 0.001$) increase in hydrodynamic radius with respect to the WT.

The time evolution of the mean count rate (MCR) provides useful information to monitor the stability and colloidal properties of the protein dispersion. We thus monitored the MCR profile over 22 h (Figure 8B) for N104H-GCAP1. Interestingly, both the Mg^{2+} and Ca^{2+}-bound forms of the GCAP1 variant did not show any aggregation propensity, but rather displayed regular and wide MCR oscillations, with a period of approximately 15 h. The largest oscillations were observed in the presence of Ca^{2+}, which also showed a higher average MCR (~250 kcps) as compared to the Mg^{2+}-bound form (~100 kcps). These wide oscillations, not commonly observed for GCAP1 variants, did not imply a clear change in the oligomeric state of N104H-GCAP1, as proven by the plot of the intensity of the main

light scattering peak over the 22 h time frame (Figure 8D), which shows high stability in both conditions. Interestingly, while the average hydrodynamic diameter was in line with that reported in Table 2 and substantially the same applied for the Mg^{2+}- and Ca^{2+}-bound forms, data were more scattered in the presence of Mg^{2+}, despite the smaller oscillations observed in the relative MCR profile.

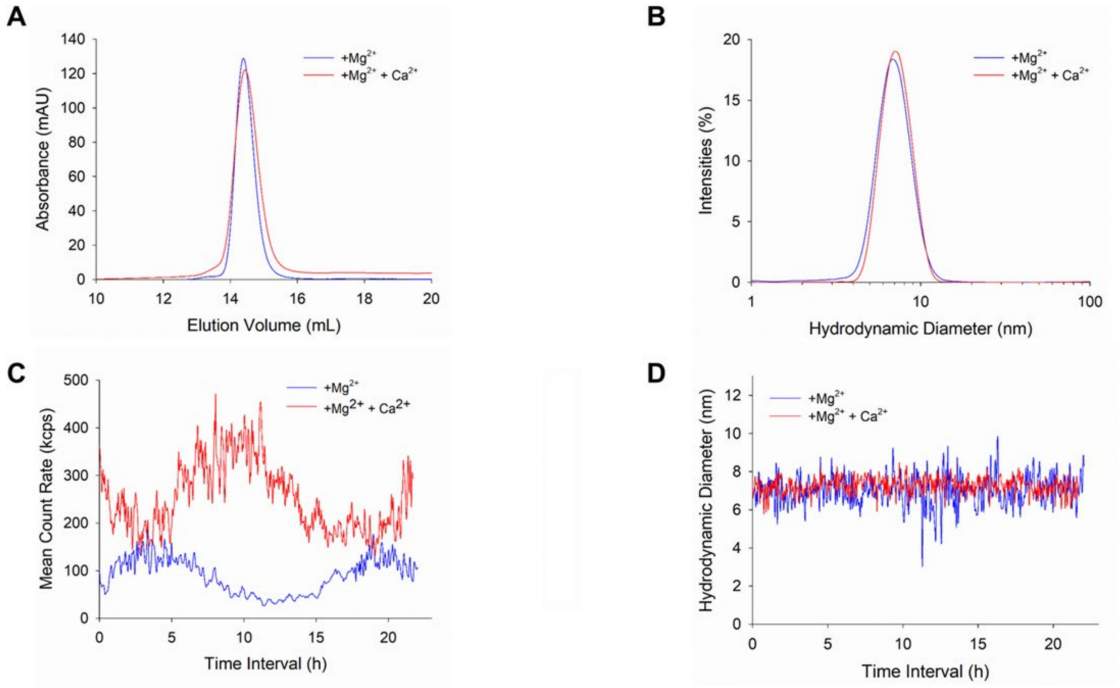

Figure 8. Analysis of N104H-GCAP1 quaternary structure. (**A**) Analytical gel filtration profile of ~45 µM N104H-GCAP1. Chromatographic runs were carried out in either 500 µM EGTA + 1 mM Mg^{2+} (blue) or 1 mM Mg^{2+} + 1 mM Ca^{2+} (red). (**B**) Hydrodynamic diameter of ~45 µM N104H-GCAP1 monitored by DLS in the presence of 500 µM EGTA + 1 mM Mg^{2+} (blue) or 1 mM Mg^{2+} + 1 mM Ca^{2+} (red). Solid lines represent the mean curve of 30 measurements. Time evolution over 22 h of the mean count rate (**C**) and (**D**) peak 1 mean intensity of ~45 µM N104H-GCAP1 in the presence of 500 µM EGTA + 1 mM Mg^{2+} (blue) or 1 mM Mg^{2+} + 1 mM Ca^{2+} (red).

2.6. Exhaustive Molecular Dynamics Simulations Show Altered Structural Flexibility for N104H-GCAP1 in Different GC1-Activating States

CD spectroscopy did not show any major structural rearrangement of the COD-associated GCAP1 variant following the N104H substitution; however, both the altered sensitivity for Ca^{2+} and the dysregulation of GC activity induced by the mutant suggest that subtle alterations may occur at the atomic level. We therefore ran exhaustive (2 µs) comparative molecular dynamics (MD) simulations of WT and N104H-GCAP1 with two Mg^{2+} ions or three Ca^{2+} ions bound, corresponding to the GC-activating and GC-inhibiting state, respectively. In line with the spectroscopic data, MD simulations did not highlight major structural rearrangements for the variant in any tested state (Figure 9); however, the analysis of protein structural flexibility, as described by the Cα Root-Mean Square Fluctuation, (RMSF) highlighted an altered flexibility of the N104H-GCAP1 backbone as compared to the WT in both signaling states. In detail, significantly higher flexibility of the exiting helix of EF3 and of the unoccupied ion-binding loop of EF4 was observed for the mutant in its Mg^{2+}-bound form; in addition, both Mg^{2+} ions bound to EF2 and EF3 showed higher RMSF as compared to the WT. This finding, together with the overall higher RMSF detected throughout the protein sequence (Figure S3) is in line with the lower thermal stability observed for the variant (Table 2 and Figure 7D) in the Mg^{2+}-bound form, and it is indicative of an allosteric effect exerted by the variant. Interestingly, a significant alteration of backbone flexibility was observed also in the Ca^{2+}-bound state (Figure 9). The

C-terminal domain was essentially more rigid in N104H-GCAP1 as compared to the WT; in particular, the mutation stabilized the transient helix (residues 120–135) connecting EF3 and EF4. The only exception is represented by the higher flexibility (i.e., lower stability) of the Ca^{2+} ions bound to EF3 and especially to EF4, thus in the EF-hand adjacent to that where the amino acid substitution occurred. Very interestingly, the 2 μs simulations highlighted a major increase in flexibility of the N-terminal domain, as clearly shown by the higher RMSF of the entering helix of EF1 (Figure S3), where residues interacting with the GC are located [37–39]. This is a purely allosteric effect of the N104H mutation, affecting a distal site in the protein with crucial functional properties.

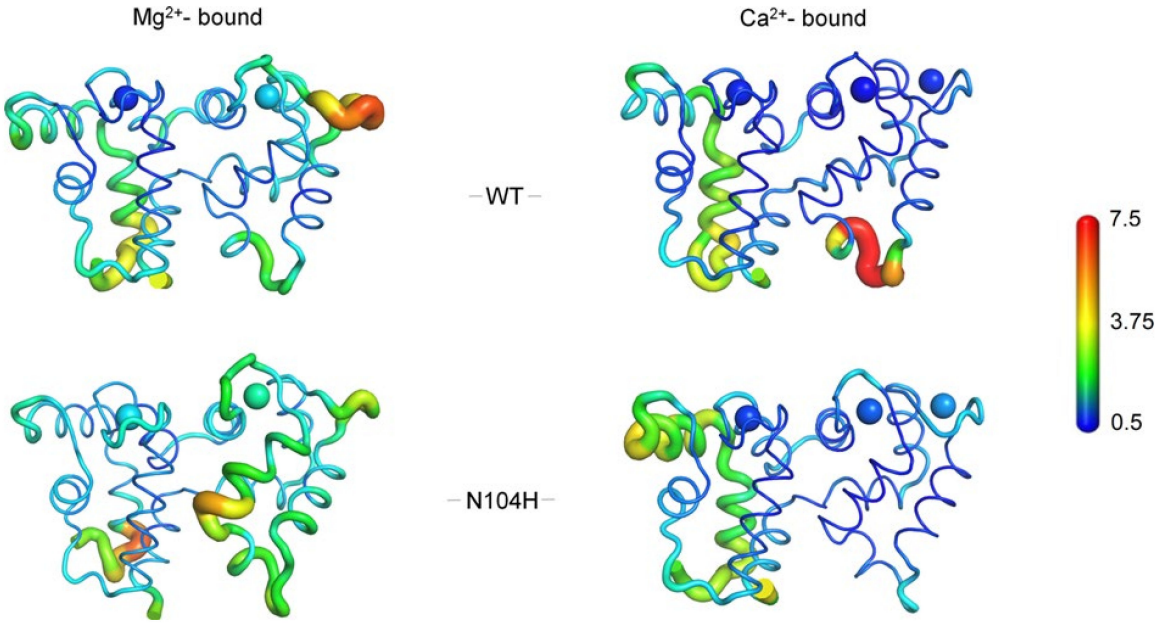

Figure 9. Cα Root-Mean Square Ffluctuation (RMSF) projected on the 3D structure of WT (upper panels) and N104H (lower panels) GCAP1 in their GC-activating Mg^{2+}-bound (left panels) and inhibiting Ca^{2+}-loaded (right panels) forms. Protein structure is displayed as tube cartoons, with radius proportional to the RMSF; Mg^{2+} and Ca^{2+} are depicted as spheres. Structures and ions are colored in a rainbow scheme representing RMSF values ranging from 0.5 to 7.5 Å (see Supplementary Figure S3 for Cα-RMSF profiles).

3. Discussion

A clear association between *GUCA1A* and adCOD was established over 20 years ago [15] and in the last years the number of point mutations found in the same gene has significantly raised [11–25]. Mutations are biochemically heterogeneous; therefore, a detailed molecular analysis is needed to infer general genotype–phenotype relations. We presented a complete clinical and biochemical characterization of the novel N104H-GCAP1 variant associated with adCOD in an Italian family with three affected members. Missense mutations in Asn104 associated with COD were found in two previous studies, which makes the genotype–phenotype comparison especially intriguing. The first mutation (N104K) was found in two members of the same family, for whom double-flash ERGs showed significantly delayed rod recovery from an intense flash, which were attributed to dominant-negative effects that slowed the stimulation of GC [20]. Similarly to our study, Jiang et al. [20] reported a case with a long follow-up (12 years vs. 16 years in our study). Both data showed that rod system remained fairly unaffected during the follow-up while the disease - as evaluated by means of FAF in our case and ffERG in their case—showed signs of progression at the levels of cones.

Results from gel-shift experiments and limited proteolysis in N104K-GCAP1 [20] were very similar to those observed in this study for N104H, which might indicate similar biochemical features. However, despite the alike physicochemical characteristics of the

substituted side chain (a lysine or a histidine, in both cases a positively charged residue at neutral pH), some peculiarities emerged. A first noticeable difference regards regulation of GC activation by the two GCAP1 variants. While WT-GCAP1 exhibited an IC_{50} value (~250 nM) compatible with the physiological Ca^{2+} range, the N104K substitution shifted the IC_{50} to a ~3-fold higher value, in contrast to the ~2-fold shift observed for N104H in this study. Most importantly, the apparent affinity of N104H for GC was double that of the WT-GCAP1 (Figure 4B and Table 1), at odds with N104K, which showed reduced capability to activate GC and thus required more GCAP1 to achieve a similar activation level [20]. It should be noted, however, that reconstitution experiments in Ref. [20] were performed with murine GC1 and human GCAP1, and that species-dependent biochemical characteristics may exist for the GCAP-GC signaling complex [4,5].

Very recently, some of us identified an isolated case of COD where the patient carried a double *GUCA1A* mutation affecting Asn104 and the adjacent Gly105 (N104K-G105R), thus introducing two positively charged side chains (lysine and arginine, respectively) [28]. The clinical phenotype was significantly different as compared to both N104K [20] and N104H-GCAP1, and quite unusual. Indeed, severe alterations of the ERG were observed under both scotopic and photopic conditions, with abnormally attenuated b-wave components and a negative pattern not observed in other COD patients [28]. At the protein level, Ca^{2+}-sensitivity was severely reduced, and the variant constitutively activated both human GC1 and GC2, although the X-fold value was 80-fold lower compared to the WT for GC1, and 18-fold lower for GC2. This is a major difference with N104H-GCAP1, which showed a less perturbed (approximately halved) X-fold compared to WT (Table 1). We should point out, however, that for N104H-GCAP1-stimulated GC1 the absolute levels of cGMP at both high and low [Ca^{2+}] were significantly higher than the corresponding values for the WT (Figure 4A), at odds with the N104K-G105R double mutant, which also induced constitutive activation of GC1, but lower cGMP synthesis at low Ca^{2+} [28]. The cyclase is therefore hyperactivated by N104H-GCAP1 under conditions that mimic both dark- and light-adapted photoreceptors. In this respect, the effects of the N104H-GCAP1 substitution on the photoreceptor physiology could be similar to those observed in other GCAP1 variants, and cell degeneration could be attributed to the dysregulation of the homeostasis of second messengers, which may accumulate in the photoreceptor outer segment due to the constitutive activation of GC [40], thus leading to toxic effects attributed to both Ca^{2+} and cGMP [41,42]. The peculiar ERG response from the patient with the double the N104K-G105R substitution suggests a perturbation of the transmission to downstream neurons and points to a perturbation of the GCAP1-GC1 macromolecular complex at the photoreceptor synaptic terminal [13]. The ERGs observed in this study for N104H-GCAP1 are instead in line with those observed in prior COD patients, and do not suggest significant alterations of the synaptic processes.

In conclusion, we found that point mutations in the same position (Asn104) of the *GUCA1A* gene not only lead to clinically different phenotypes, but also generate distinct molecular phenotypes despite the absence of major structural alterations observed in any case (this study and previous ones [20,28]). Mutation-specific sensitivity toward cations, subtle alterations of protein stability in the presence of Mg^{2+} and Ca^{2+}, specific alteration of protein flexibility in distinct signaling states and the dependence of GCAP1 dimerization on the presence of specific cations [36] all point to a very complex molecular scenario, in which focusing on the effects of mutations on individual proteins might be of little use in advancing the molecular understanding of disease. Instead, unveiling the molecular details of the protein–protein and protein–ion interactions involved in the altered signaling cascade should be the final goal to achieve a molecular-level understanding of the extremely heterogenous retinal dystrophies, including COD, and would constitute a solid basis for designing effective therapeutic interventions.

4. Materials and Methods

4.1. Clinical and Ophthalmological Examinations

Patients were enrolled at the Retinal Dystrophy Unit of ASST Santi Paolo e Carlo Hospital, University of Milan (Italy). They periodically undergo detailed clinical examination, including best-corrected visual acuity (BCVA), slit-lamp examination, spectral-domain optical coherence tomography (SD-OCT), fundus autofluorescence (FAF), and dark- and light-adapted full field electroretinogram (ffERG).

4.2. Genetic Testing

The proband's DNA was extracted from whole blood with a commercial kit (Blood DNA Kit E.Z.N.A.; Omega Bio-Tek Inc., Norcross, GA, USA) and analyzed by targeted Next-Generation Sequencing (NGS) on the Illumina MiSeq instrument, using the PE 2× 150 bp protocol (Illumina, San Diego, CA, USA). Raw sequencing data generated by the NGS platform were analyzed using an in-house pipeline, as described elsewhere [43]. The custom gene-targeted panel comprises of 140 genes associated with non-syndromic retinal dystrophies. The identified variants were subsequently evaluated in compliance with the ACMG standards and guidelines for the interpretation of sequence variants [30], with the help of the human genomic variant search engine VarSome (https://varsome.com, accessed on 18 August 2021) [29]. Genetic testing was performed as part of the diagnostic routine and the proband was invited to sign an informed consent form after pre-test genetic counseling.

4.3. Cloning, Protein Expression and Purification of N104H-GCAP1

The cDNA of wild-type human GCAP1-E6S (Uniprot entry: P43080) was cloned into a pET-11a vector using NdeI and NheI restriction sites (Genscript). The E6S mutation was inserted to obtain the consensus sequence for post-translational N-terminal myristoylation by *S. cerevisiae* N-Myristoyl transferase (yNMT) [44]. Sequence variant c.310A>C p.(Asn104His) was introduced by site-directed mutagenesis using the aforementioned pET-11a-GCAP1-E6S plasmid (Genscript) as template. Heterologous expression of GCAP1 variants was performed in BL21 *E. coli* cells that were previously co-transformed with pBB131-yNMT. The protein was extracted from the inclusion bodies after denaturation in 6M Guanidine-HCl and renatured by dialysis against 20 mM Tris-HCl pH 7.5, 150 mM NaCl, 7.2 mM β-mercaptoethanol buffer. The refolded protein was finally purified after size exclusion chromatography (SEC, HiPrep 26/60 Sephacryl S-200 HR, GE Healthcare), followed by anionic exchange chromatography (AEC, HiPrep Q HP 16/10, GE Healthcare) as previously described [13,44], except for using AEC buffers at pH 8. Protein concentration after purification was assessed by Bradford assay [45] using a GCAP1-specific reference curve based on amino acid hydrolysis assay (Alphalyze). Protein purity was evaluated on a 15% SDS PAGE gel. GCAP1 variants were exchanged against decalcified 50 mM NH_4HCO_3 buffer and lyophilized or against 20 mM Tris-HCl pH 7.5, 150 mM KCl, 1mM DTT buffer with three dialysis cycles (1 L each), and flash-frozen with liquid nitrogen. Samples were stored at −80 °C.

4.4. Guanylate Cyclase Enzymatic Activity Assays

To test whether the N104H substitution in GCAP1 affected the regulation of GC1 activity, specific enzymatic assays were conducted to monitor cGMP synthesis. HEK293 cells were used to stably express human recombinant ROS-GC1 (GC) as previously described [46]. GC assays were performed on isolated membranes obtained after cell lysis (10 mM HEPES pH 7.4, Protease Inhibitor Cocktail 1X, 1 mM DTT), 20 min incubation on ice, 20 min centrifugation at 18,000 × *g*, and resuspension of pelleted membranes in 50 mM HEPES pH 7.4, 50 mM KCl, 20 mM NaCl, 1 mM DTT buffer. Minimal and maximal GC activities were determined by incubating 5 µM of each GCAP1 variant with 2 mM K_2H_2EGTA (GC1-activating buffer) or $K_2CaEGTA$ (GC1-inhibiting buffer), leading, respectively, to <19 nM and ~30 µM free Ca^{2+} conditions. Enzymatic reactions were carried out in 30 mM MOPS/KOH pH 7.2, 60 mM KCl, 4 mM NaCl, 1 mM GTP, 3.5 mM $MgCl_2$,

0.3 mM ATP, 0.16 mM Zaprinast buffer and blocked with the addition of 50 mM EDTA and boiling. Samples were then centrifuged for 20 min at ~18,000× g at 4 °C. The Ca^{2+} concentration at which GC activity is half-maximal (IC_{50}) was determined by incubation of 5 μM of N104H-GCAP1 variant with different free [Ca^{2+}] in the <19 nM–1 mM range. The GCAP1 concentration at which GC activation is half-maximal (EC_{50}) was measured by incubation of increasing concentrations of N104H-GCAP1 (0–10 μM) in the presence of <19 nM free Ca^{2+}. The cGMP synthesized during the enzymatic reactions was quantified by means of HPLC using a C18 reverse phase column (LiChrospher 100 RP-18, Merck). Data are reported as the mean ± standard deviation of at least three data sets. The statistical significance of the differences between the maximal and minimal GC activation by WT- and N104H-GCAP1 was assessed by two-tailed t-test ($p = 0.001$).

4.5. Gel mobility Shift Assay and Limited Proteolysis

SDS-PAGE under denaturing conditions was performed on a 15% acrylamide gel to investigate cation-induced electrophoretic mobility changes of GCAP1 variants. The experiment was carried out diluting proteins to a concentration of 30 μM in 20 mM Tris-HCl pH 7.5, 150 mM KCl, 1 mM DTT and by adding 2 mM EDTA, 1 mM EGTA + 1.1 mM Mg^{2+} or 1 mM Mg^{2+} and 1 mM Ca^{2+}. After a 5-min incubation at 25 °C, samples were boiled and loaded onto the gel. Electrophoresis was run for 50 min at constant voltage (200 V) and protein bands were revealed by Coomassie blue staining. Limited proteolysis was performed on 20 μM WT and N104H-GCAP1 in the same conditions as for the mobility shift assay, with the addition of 0.3 μM trypsin (Sigma-Aldrich, St. Louis, MO, USA) to each reaction mix. To evaluate the optimal incubation time with trypsin (Figure S2), the reaction for WT-GCAP1 was stopped at different time steps, leading to the choice of a 10-min incubation for the comparison of the proteolytic pattern of WT and N104H-GCAP1 shown in Figure 6.

4.6. Ca^{2+}-Binding Assays

The Ca^{2+}-binding ability of N104H-GCAP1 was evaluated by a competition assay with the chromophoric chelator 5,5′Br_2-BAPTA as previously described [21,33,34]. Lyophilized proteins were dissolved in a carefully decalcified buffer (20 mM Tris-HCl pH 7.5, 150 mM KCl, 1 mM Mg^{2+}, 1 mM DTT; residual concentration of Ca^{2+} after decalcification was 0.15–0.7 μM) containing ~25 μM 5,5′Br_2-BAPTA. The absorbance at 263 nm was recorded upon sequential additions of 3 μM Ca^{2+} to the solution at room temperature until a plateau was reached. Data were fitted to a three-sequential binding site model using CaLigator software [31] to estimate the individual macroscopic association constants ($logK_i$) and apparent affinity constants ($K_d^{app} = 10^{-(logK_1 + logK_2 + logK_3)/3}$) reported in Table 1, presented as average ± standard deviation of 5 technical replicates. Data shown in Figure 5 were normalized as follows to account for the total number of Ca^{2+} binding sites:

$$Normalized \left[Ca^{2+}\right] = \frac{\left[Ca^{2+}\right]}{[Q] + 3\,[P]} \quad (1)$$

$$Normalized\ y = \frac{A_{263} - A_{min}}{A_{max} - A_{min}} \quad (2)$$

where [Q] and [P] are the concentrations of 5,5′Br_2-BAPTA and GCAP1 variants, respectively, measured at the end of each repetition by Bradford assay, A_{263} is the absorbance at 263 nm, A_{min} and A_{max} are the minimal and maximal absorbance values registered.

4.7. Circular Dichroism Spectroscopy and Thermal Denaturation Studies

The alterations in thermal stability, secondary and tertiary structure of N104H-GCAP1 upon ion binding were analyzed by means of Circular Dichroism (CD) spectroscopy on a Jasco J-710 spectropolarimeter supplied with a Peltier-type cell holder. Proteins were resuspended in 20 mM Tris-HCl pH 7.5, 150 mM KCl, 1 mM DTT and each recorded spectrum

was the average of 5 accumulations. Far-UV CD spectra and thermal denaturation profiles were recorded in a 0.1-cm quartz cuvette with a protein concentration of 15 μM and 10 μM, respectively, in the presence of 300 μM EGTA, 300 μM EGTA + 1 mM Mg^{2+} or 1 mM Mg^{2+} + 300 μM free Ca^{2+}. Near-UV CD spectra were recorded in a 1 cm quartz cuvette with a protein concentration of ~39 μM after serial additions of 500 μM EGTA, 1 mM Mg^{2+} and 500 μM free Ca^{2+}. Thermal denaturation profiles were recorded by monitoring the ellipticity at 222 nm in a temperature window spanning from 20 °C to 96 °C (scan rate 90 °C/h). Denaturation data were fitted according to the following model, as in [21]:

$$_{222} = \frac{(b_n + k_n T) + (b_u + k_u T)\, exp[-\Delta G_{nu}(T)]}{1 + exp\, exp\left[\frac{-\Delta G_{nu}(T)}{RT}\right]} \quad (3)$$

where n and u are the native and unfolded states, b is the baseline value, T is the temperature, k is the slope of the plateaus and ΔG_{nu} is the Gibbs free energy for folded-to-unfolded transition which can also be expressed in terms of change in enthalpy and heat capacity upon denaturation at constant pressure as follows

$$\Delta G_{nu}(T) = -\left(\Delta H\left(1 - \frac{T}{T_m}\right)\right) + \Delta C_p\left(T - T_m - Tln\frac{T}{T_m}\right) \quad (4)$$

4.8. Analytical Gel Filtration

Analytical gel filtration was employed to analyze the apparent molecular weight and the oligomeric state of GCAP1 variants under Mg^{2+} and Ca^{2+}-saturating conditions. Protein samples (20 μM) were loaded onto a Superose 12 10/300 column (GE Healthcare), previously equilibrated with 20 mM Tris-HCl pH 7.5, 150 mM KCl, 1 mM DTT + 500 μM EGTA and either 1 mM Mg^{2+} or + 1 mM Mg^{2+} and 1 mM Ca^{2+} at room temperature. Elution profiles were collected at 280 nm and the distribution coefficient (D_c) was calculated as follows:

$$D_c = \frac{V_e - V_v}{V_t - V_v} \quad (5)$$

where V_e is the elution volume, V_t represents the total column volume (25 mL) and V_v is the void volume (8 mL). Finally, the molecular weight was estimated from the calibration curve of log (MW) vs. D_c as previously described [47].

4.9. Dynamic Light Scattering Analyses

To investigate the variations in hydrodynamic diameter, oligomeric state, and aggregation propensity of N104H-GCAP1 in different cation-loading states, the samples from aSEC were directly analyzed in a Zetasizer Nano-S (Malvern Instruments, Malvern, UK) at 25 °C using previously established settings [48]. The analysis of the hydrodynamic diameter and of the mean count rate, representing the time evolution of the colloidal properties of the suspension, was carried out for 22 h (~450 measurements, each averaging 13–15 repetitions). The hydrodynamic diameter reported in Table 2 is the mean of the first 30 measurements ± standard error of the mean (s.e.m.).

4.10. Protein Modeling and Molecular Dynamics Simulations

The homology model of Ca^{2+}-loaded myristoylated human GCAP1 (UniProt entry: P43080) was obtained employing the "Advanced Homology Modeling" tool provided by the software Bioluminate (Maestro package v. 12.5.139, Schrödinger), using the Ca^{2+}-loaded myristoylated GCAP1 from *G. Gallus* (PDB entry: 2R2I [49]) as a template. The N104H mutation was performed in silico in the obtained human homology model using the "Mutate Residue" tool by selecting the most probable rotamer. The activating form of human GCAP1 (Mg^{2+}-bound) was obtained by deleting the Ca^{2+} ion bound to EF-4 and substituting the remaining Ca^{2+} ions in EF-2 and EF-3 with Mg^{2+} as performed in earlier work [50]. Molecular Dynamics (MD) simulations were run on the GROMACS 2020.3

package [51] using the all-atom CHARMM36m [52] force field, implemented with the parameters of the N-terminal myristoylated Gly (available upon request). Both Mg^{2+}-bound and Ca^{2+}-loaded GCAP1 variants underwent energy minimization and equilibration procedures as elsewhere described (2 ns in NVT ensemble with and without position restraints) [53] prior to the production phase, which consisted of two independent 1 µs replicas at constant pressure (1 atm) and temperature (310 K) for each state. Protein flexibility was assessed by monitoring the Root-Mean Square Fluctuation of Cα, that is the time-averaged Root-Mean Square Deviation as compared to the average structure of the concatenated 2 µs trajectories, following the analysis of consistency between the replicas [53] based on the root-mean square inner product (RMSIP, Figure S4) of the first 20 principal components (calculated on Cα) representing the largest collective motion of the protein.

Supplementary Materials: The following are available online at https://www.mdpi.com/article/10.3390/ijms221910809/s1.

Author Contributions: Conceptualization, L.C. and D.D.; methodology, A.B., V.M., G.D.C., P.E.M.; software, A.B., V.M.; validation, P.E.M., L.C. and D.D.; formal analysis, A.B. and D.D.; investigation, A.B., V.M., G.D.C., A.M.M., P.E.M.; resources, M.B., and D.D.; writing—original draft preparation, A.B., L.C., D.D.; writing—review and editing, L.C. and D.D.; visualization, A.B., V.M.; supervision, L.C. and D.D.; project administration, M.B. and D.D.; funding acquisition, M.B. and D.D. All authors have read and agreed to the published version of the manuscript.

Funding: This work received financial support from the University of Verona (Joint project 2018, grant no. JPVR184ZZ5 to D.D.) and from CINECA (grant no. HP10C6ZWA1 to V.M.)

Institutional Review Board Statement: The clinical study was conducted according to the guidelines of the Declaration of Helsinki and approved by the Ethics Committee of Azienda Sanitaria dell'Alto Adige, Italy (Approval No. 132-2020).

Informed Consent Statement: Informed consent was obtained from all subjects involved in the study.

Data Availability Statement: The data reported in this work are available upon request from the corresponding authors and are not available to the public because of their size.

Acknowledgments: The Centro Piattaforme Tecnologiche of the University of Verona is acknowledged for providing access to the computational and spectroscopic platforms.

Conflicts of Interest: The authors declare no conflict of interest. The funders had no role in the design of the study; in the collection, analyses, or interpretation of data; in the writing of the manuscript, or in the decision to publish the results.

References

1. Koch, K.-W.; Dell'Orco, D. Protein and signaling networks in vertebrate photoreceptor cells. *Front. Mol. Neurosci.* **2015**, *8*, 67. [CrossRef]
2. Koch, K.-W.; Dell'Orco, D. A calcium-relay mechanism in vertebrate phototransduction. *ACS Chem. Neurosci.* **2013**, *4*, 909–917. [CrossRef]
3. Korenbrot, J.I. Speed, sensitivity, and stability of the light response in rod and cone photoreceptors: Facts and models. *Prog. Retin. Eye Res.* **2012**, *31*, 442–466. [CrossRef]
4. Avesani, A.; Marino, V.; Zanzoni, S.; Koch, K.-W.; Dell'Orco, D. Molecular properties of human guanylate cyclase–activating protein 2 (GCAP2) and its retinal dystrophy–associated variant G157R. *J. Biol. Chem.* **2021**, *296*, 100619. [CrossRef] [PubMed]
5. Dell'Orco, D.; Dal Cortivo, G. Normal GCAPs partly compensate for altered cGMP signaling in retinal dystrophies associated with mutations in GUCA1A. *Sci. Rep.* **2019**, *9*, 20105. [CrossRef]
6. Peshenko, I.V.; Dizhoor, A.M. Guanylyl cyclase-activating proteins (GCAPs) are Ca2+/Mg2+ sensors: Implications for photoreceptor guanylyl cyclase (RetGC) regulation in mammalian photoreceptors. *J. Biol. Chem.* **2004**, *279*, 16903–16906. [CrossRef] [PubMed]
7. Peshenko, I.V.; Dizhoor, A.M. Ca2+ and Mg2+ binding properties of GCAP-Evidence that Mg2+-bound form is the physiological activator of photoreceptor guanylyl cyclase. *J. Biol. Chem.* **2006**, *281*, 23830–23841. [CrossRef]
8. Koch, K.-W.; Duda, T.; Sharma, R.K. Ca2+-modulated vision-linked ROS-GC guanylate cyclase transduction machinery. *Mol. Cell. Biochem.* **2009**, *334*, 105–115. [CrossRef]

9. Dizhoor, A.M.; Olshevskaya, E.V.; Peshenko, I.V. Mg2+/Ca2+ cation binding cycle of guanylyl cyclase activating proteins (GCAPs): Role in regulation of photoreceptor guanylyl cyclase. *Mol. Cell. Biochem.* **2009**, *334*, 117–124. [CrossRef]
10. Peshenko, I.V.; Olshevskaya, E.V.; Savchenko, A.B.; Karan, S.; Palczewski, K.; Baehr, W.; Dizhoor, A.M. Enzymatic properties and regulation of the native isozymes of retinal membrane guanylyl cyclase (RetGC) from mouse photoreceptors. *Biochemistry* **2011**, *50*, 5590–5600. [CrossRef] [PubMed]
11. Manes, G.; Mamouni, S.; Hérald, E.; Richard, A.-C.; Sénéchal, A.; Aouad, K.; Bocquet, B.; Meunier, I.; Hamel, C.P. Cone dystrophy or macular dystrophy associated with novel autosomal dominant GUCA1A mutations. *Mol. Vis.* **2017**, *23*, 198–209. [PubMed]
12. Abbas, S.; Marino, V.; Weisschuh, N.; Kieninger, S.; Solaki, M.; Dell'Orco, D.; Koch, K.-W. The neuronal calcium sensor GCAP1 encoded by GUCA1A exhibits heterogeneous functional properties in two cases of retinitis pigmentosa. *ACS Chem. Neurosci.* **2020**, *11*, 1458–1470. [CrossRef] [PubMed]
13. Marino, V.; Dal Cortivo, G.; Oppici, E.; Maltese, P.E.; D'Esposito, F.; Manara, E.; Ziccardi, L.; Falsini, B.; Magli, A.; Bertelli, M.; et al. A novel p. (Glu111Val) missense mutation in GUCA1A associated with cone-rod dystrophy leads to impaired calcium sensing and perturbed second messenger homeostasis in photoreceptors. *Hum. Mol. Genet.* **2018**, *27*, 4204–4217. [CrossRef]
14. Marino, V.; Scholten, A.; Koch, K.-W.; Dell'Orco, D. Two retinal dystrophy-associated missense mutations inGUCA1Awith distinct molecular properties result in a similar aberrant regulation of the retinal guanylate cyclase. *Hum. Mol. Genet.* **2015**, *24*, 6653–6666. [CrossRef]
15. Dizhoor, A.M.; Boikov, S.G.; Olshevskaya, E.V. Constitutive activation of photoreceptor guanylate cyclase by Y99C mutant of GCAP-1: Possible role in causing human autosomal dominant cone degeneration. *J. Biol. Chem.* **1998**, *273*, 17311–17314. [CrossRef] [PubMed]
16. Sokal, I.; Li, N.; Surgucheva, I.; Warren, M.; Payne, A.; Bhattacharya, S.S.; Baehr, W.; Palczewski, K. GCAP1(Y99C) Mutant is constitutively active in autosomal dominant cone dystrophy. *Mol. Cell* **1998**, *2*, 129–133. [CrossRef]
17. Wilkie, S.E.; Li, Y.; Deery, E.C.; Newbold, R.J.; Garibaldi, D.; Bateman, J.B.; Zhang, H.; Lin, W.; Zack, D.; Bhattacharya, S.S.; et al. Identification and functional consequences of a new mutation (E155G) in the gene for GCAP1 that causes autosomal dominant cone dystrophy. *Am. J. Hum. Genet.* **2001**, *69*, 471–480. [CrossRef]
18. Nishiguchi, K.M.; Sokal, I.; Yang, L.; Roychowdhury, N.; Palczewski, K.; Berson, E.L.; Dryja, T.P.; Baehr, W. A novel mutation (I143NT) in guanylate cyclase-activating protein 1 (GCAP1) associated with autosomal dominant cone degeneration. *Investig. Opthalmol. Vis. Sci.* **2004**, *45*, 3863–3870. [CrossRef]
19. Sokal, I.; Dupps, W.J.; Grassi, M.A.; Brown, J.; Affatigato, L.M.; Roychowdhury, N.; Yang, L.; Filipek, S.; Palczewski, K.; Stone, E.M.; et al. A novel GCAP1 missense mutation (L151F) in a large family with autosomal dominant cone-rod dystrophy (adCORD). *Investig. Opthalmol. Vis. Sci.* **2005**, *46*, 1124–1132. [CrossRef]
20. Jiang, L.; Wheaton, D.; Bereta, G.; Zhang, K.; Palczewski, K.; Birch, D.G.; Baehr, W. A novel GCAP1(N104K) mutation in EF-hand 3 (EF3) linked to autosomal dominant cone dystrophy. *Vis. Res.* **2008**, *48*, 2425–2432. [CrossRef]
21. Dell'Orco, D.; Behnen, P.; Linse, S.; Koch, K.-W. Calcium binding, structural stability and guanylate cyclase activation in GCAP1 variants associated with human cone dystrophy. *Cell. Mol. Life Sci.* **2010**, *67*, 973–984. [CrossRef] [PubMed]
22. Kamenarova, K.; Corton, M.; Garcia-Sandoval, B.; Fernandez-San Jose, P.; Panchev, V.; Avila-Fernandez, A.; Lopez-Molina, M.I.; Chakarova, C.; Ayuso, C.; Bhattacharya, S.S. Novel GUCA1A mutations suggesting possible mechanisms of pathogenesis in cone, cone-rod, and macular dystrophy patients. *Biomed. Res. Int.* **2013**, *2013*, 517570. [CrossRef] [PubMed]
23. Kitiratschky, V.B.; Behnen, P.; Kellner, U.; Heckenlively, J.R.; Zrenner, E.; Jagle, H.; Kohl, S.; Wissinger, B.; Koch, K.W. Mutations in the GUCA1A gene involved in hereditary cone dystrophies impair calcium-mediated regulation of guanylate cyclase. *Hum. Mutat.* **2009**, *30*, E782–E796. [CrossRef]
24. Vocke, F.; Weisschuh, N.; Marino, V.; Malfatti, S.; Jacobson, S.G.; Reiff, C.M.; Dell'Orco, D.; Koch, K.-W. Dysfunction of cGMP signalling in photoreceptors by a macular dystrophy-related mutation in the calcium sensor GCAP1. *Hum. Mol. Genet.* **2016**, *26*, 133–144. [CrossRef] [PubMed]
25. Peshenko, I.V.; Cideciyan, A.V.; Sumaroka, A.; Olshevskaya, E.V.; Scholten, A.; Abbas, S.; Koch, K.-W.; Jacobson, S.G.; Dizhoor, A.M. A G86R mutation in the calcium-sensor protein GCAP1 alters regulation of retinal guanylyl cyclase and causes dominant cone-rod degeneration. *J. Biol. Chem.* **2019**, *294*, 3476–3488. [CrossRef]
26. Gill, J.S.; Georgiou, M.; Kalitzeos, A.; Moore, A.T.; Michaelides, M. Progressive cone and cone-rod dystrophies: Clinical features, molecular genetics and prospects for therapy. *Br. J. Ophthalmol.* **2019**, *103*, 711–720. [CrossRef]
27. Dal Cortivo, G.; Marino, V.; Bonì, F.; Milani, M.; Dell'Orco, D. Missense mutations affecting Ca2+-coordination in GCAP1 lead to cone-rod dystrophies by altering protein structural and functional properties. *Biochim Biophys Acta Mol Cell Res.* **2020**, *1867*, 118794. [CrossRef]
28. Marino, V.; Dal Cortivo, G.; Maltese, P.; Placidi, G.; De Siena, E.; Falsini, B.; Bertelli, M.; Dell'Orco, D. Impaired Ca^{2+} sensitivity of a novel GCAP1 variant causes cone dystrophy and leads to abnormal Synaptic transmission between photoreceptors and bipolar cells. *Int. J. Mol. Sci.* **2021**, *22*, 4030. [CrossRef]
29. Kopanos, C.; Tsiolkas, V.; Kouris, A.; Chapple, C.E.; Aguilera, M.A.; Meyer, R.; Massouras, A. VarSome: The human genomic variant search engine. *Bioinformatics* **2019**, *35*, 1978–1980. [CrossRef]
30. Richards, S.; Aziz, N.; Bale, S.; Bick, D.; Das, S.; Gastier-Foster, J.; Grody, W.W.; Hegde, M.; Lyon, E.; Spector, E.; et al. Standards and guidelines for the interpretation of sequence variants: A joint consensus recommendation of the American College of Medical Genetics and Genomics and the Association for Molecular Pathology. *Genet. Med.* **2015**, *17*, 405–423. [CrossRef]

31. André, I.; Linse, S. Measurement of Ca2+-binding constants of proteins and presentation of the CaLigator software. *Anal. Biochem.* **2002**, *305*, 195–205. [CrossRef] [PubMed]
32. Viviano, J.; Krishnan, A.; Wu, H.; Venkataraman, V. Electrophoretic mobility shift in native gels indicates calcium-dependent structural changes of neuronal calcium sensor proteins. *Anal. Biochem.* **2016**, *494*, 93–100. [CrossRef]
33. Dell'Orco, D.; Sulmann, S.; Linse, S.; Koch, K.-W. Dynamics of conformational Ca2+ -switches in signaling Networks Detected by a Planar Plasmonic Device. *Anal. Chem.* **2012**, *84*, 2982–2989. [CrossRef]
34. Linse, S. Calcium binding to proteins studied via competition with chromophoric chelators. *Methods Mol. Biol.* **2002**, *173*, 15–24. [CrossRef] [PubMed]
35. Lim, S.; Roseman, G.; Peshenko, I.; Manchala, G.; Cudia, D.; Dizhoor, A.; Millhauser, G.; Ames, J.B. Retinal guanylyl cyclase activating protein 1 forms a functional dimer. *PLoS ONE* **2018**, *13*, e0193947. [CrossRef]
36. Bonì, F.; Marino, V.; Bidoia, C.; Mastrangelo, E.; Barbiroli, A.; Dell'Orco, D.; Milani, M. Modulation of guanylate cyclase activating protein 1 (GCAP1) dimeric assembly by Ca^{2+} or Mg^{2+}: Hints to understand protein activity. *Biomolecules* **2020**, *10*, 1408. [CrossRef] [PubMed]
37. Lim, S.; Peshenko, I.V.; Dizhoor, A.; Ames, J.B. Structural insights for activation of retinal guanylate cyclase by GCAP1. *PLoS ONE* **2013**, *8*, e81822. [CrossRef] [PubMed]
38. Peshenko, I.V.; Olshevskaya, E.V.; Lim, S.; Ames, J.B.; Dizhoor, A.M. Identification of target binding site in photoreceptor guanylyl cyclase-activating protein 1 (GCAP1). *J. Biol. Chem.* **2014**, *289*, 10140–10154. [CrossRef] [PubMed]
39. Schrem, A.; Lange, C.; Beyermann, M.; Koch, K.-W. Identification of a domain in guanylyl cyclase-activating protein 1 that interacts with a complex of guanylyl cyclase and tubulin in photoreceptors. *J. Biol. Chem.* **1999**, *274*, 6244–6249. [CrossRef]
40. Behnen, P.; Dell'Orco, D.; Koch, K.-W. Involvement of the calcium sensor GCAP1 in hereditary cone dystrophies. *Biol. Chem.* **2010**, *391*, 631–637. [CrossRef]
41. Das, S.; Chen, Y.; Yan, J.; Christensen, G.; Belhadj, S.; Tolone, A.; Paquet-Durand, F. The role of cGMP-signalling and calcium-signalling in photoreceptor cell death: Perspectives for therapy development. *Pflugers Arch* **2021**, *473*, 1–11. [CrossRef] [PubMed]
42. Power, M.; Das, S.; Schütze, K.; Marigo, V.; Ekström, P.; Paquet-Durand, F. Cellular mechanisms of hereditary photoreceptor degeneration—Focus on cGMP. *Prog. Retin. Eye Res.* **2019**, *74*, 100772. [CrossRef]
43. Marceddu, G.; Dallavilla, T.; Guerri, G.; Manara, E.; Chiurazzi, P.; Bertelli, M. PipeMAGI: An integrated and validated workflow for analysis of NGS data for clinical diagnostics. *Eur Rev. Med. Pharmacol. Sci.* **2019**, *23*, 6753–6765.
44. Hwang, J.-Y.; Koch, K.-W. Calcium- and Myristoyl-Dependent properties of guanylate cyclase-activating protein-1 and protein-2. *Biochemistry* **2002**, *41*, 13021–13028. [CrossRef]
45. Bradford, M.M. A rapid and sensitive method for the quantitation of microgram quantities of protein utilizing the principle of protein-dye binding. *Anal. Biochem.* **1976**, *72*, 248–254. [CrossRef]
46. Zägel, P.; Dell'Orco, D.; Koch, K.-W. The Dimerization domain in outer segment guanylate cyclase is a Ca2+-sensitive control switch module. *Biochemistry* **2013**, *52*, 5065–5074. [CrossRef] [PubMed]
47. Vallone, R.; Dal Cortivo, G.; D'Onofrio, M.; Dell'Orco, D. Preferential Binding of Mg2+ Over Ca2+ to CIB2 triggers an allosteric switch impaired in usher syndrome type 1J. *Front. Mol. Neurosci.* **2018**, *11*, 274. [CrossRef] [PubMed]
48. Marino, V.; Borsatto, A.; Vocke, F.; Koch, K.-W.; Dell'Orco, D. CaF2 nanoparticles as surface carriers of GCAP1, a calcium sensor protein involved in retinal dystrophies. *Nanoscale* **2017**, *9*, 11773–11784. [CrossRef]
49. Stephen, R.; Bereta, G.; Golczak, M.; Palczewski, K.; Sousa, M.C. Stabilizing function for myristoyl group revealed by the crystal structure of a neuronal calcium sensor, guanylate cyclase-activating protein. *Structure* **2007**, *15*, 1392–1402. [CrossRef]
50. Marino, V.; Sulmann, S.; Koch, K.-W.; Dell'Orco, D. Structural effects of Mg2+ on the regulatory states of three neuronal calcium sensors operating in vertebrate phototransduction. *Biochim. Biophys. Acta* **2015**, *1853*, 2055–2065. [CrossRef] [PubMed]
51. Abraham, M.J.; Murtola, T.; Schulz, R.; Páll, S.; Smith, J.C.; Hess, B.; Lindahl, E. GROMACS: High performance molecular simulations through multi-level parallelism from laptops to supercomputers. *SoftwareX* **2015**, *1*, 19–25. [CrossRef]
52. Huang, J.; Rauscher, S.; Nawrocki, G.; Ran, T.; Feig, M.; de Groot, B.L.; Grubmuller, H.; MacKerell, A.D., Jr. CHARMM36m: An improved force field for folded and intrinsically disordered proteins. *Nat. Methods* **2017**, *14*, 71–73. [CrossRef] [PubMed]
53. Marino, V.; Dell'Orco, D. Allosteric communication pathways routed by Ca2+/Mg2+ exchange in GCAP1 selectively switch target regulation modes. *Sci. Rep.* **2016**, *6*, 34277. [CrossRef] [PubMed]

International Journal of
Molecular Sciences

MDPI

Supplementary Materials

A Novel *GUCA1A* Variant Associated with Cone Dystrophy Alters cGMP Signaling in Photoreceptors by Strongly Interacting with and Hyperactivating Retinal Guanylate Cyclase

Amedeo Biasi, Valerio Marino, Giuditta Dal Cortivo, Paolo Enrico Maltese, Antonio Mattia Modarelli, Matteo Bertelli, Leonardo Colombo and Daniele Dell'Orco

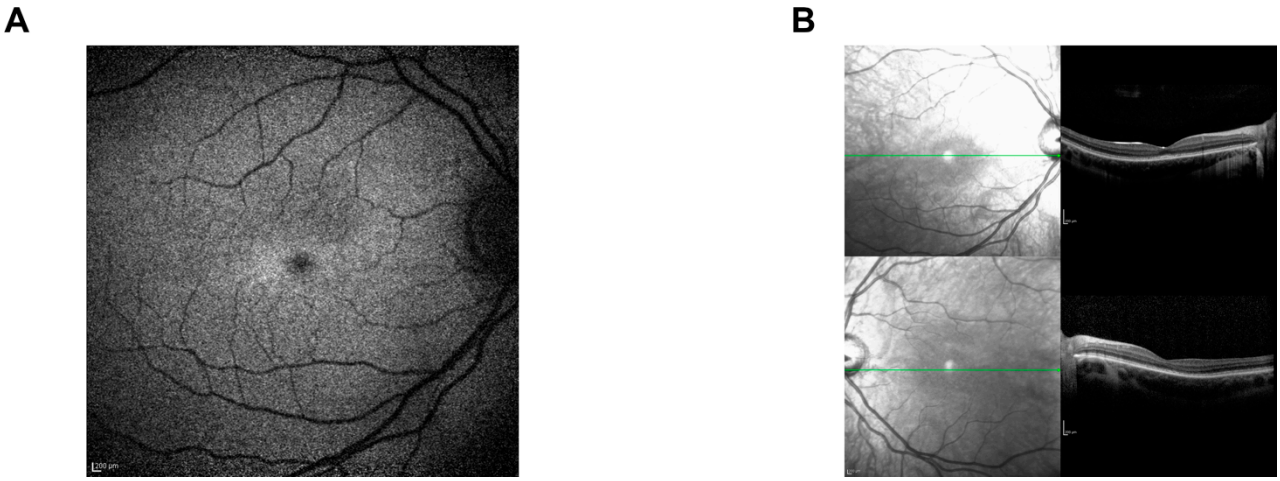

Figure S1. (A) Fundus image of the right eye and (B) SD-OCT scans of right and left eye of patient II:2 at the age of 10. Line corresponding to interdigitation zone is shown in green.

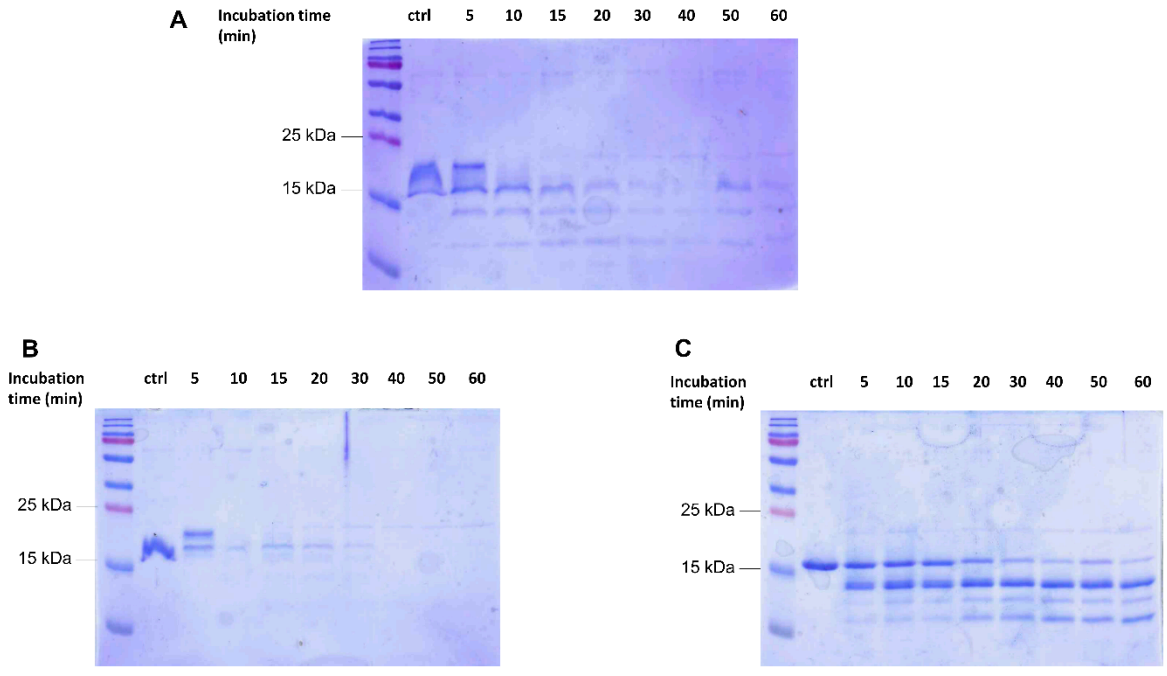

Figure S2. Time-dependent limited proteolysis of 20 μM GCAP1 WT in the presence of (A) 2 mM EDTA (ctrl) or 2 mM EDTA + 0.3 μM trypsin, (B) 1 mM EGTA + 1.1 mM Mg^{2+} (ctrl) or 1 mM EGTA + 1.1 mM Mg^{2+} + 0.3 μM trypsin, (C) 1 mM

Mg^{2+} and 1 mM Ca^{2+} (ctrl) or 1 mM Mg^{2+} and 1 mM Ca^{2+} + 0.3 μM trypsin. Incubation times were (from left to right): 5-10-15-20-30-40 and 60 minutes for each condition.

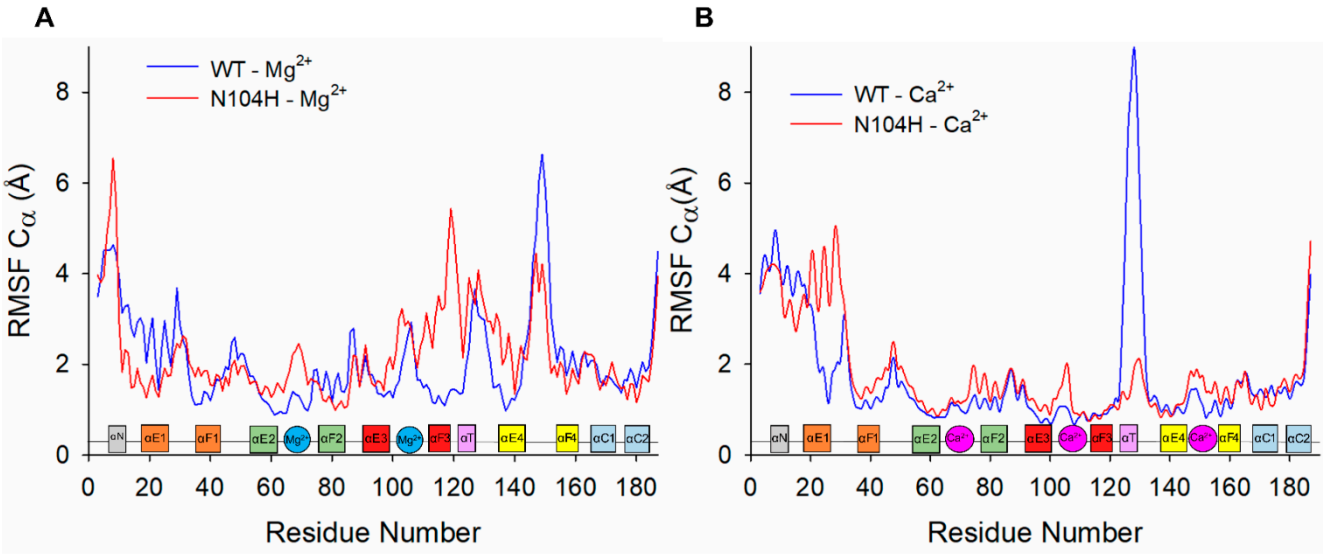

Figure S3. Cα-RMSF profiles (calculated over 2 μs MD simulations) of (A) Mg^{2+}-bound and (B) Ca^{2+}-loaded WT (blue line) and N104H (red line) GCAP1. Insets show secondary structure elements represented with the same coloring scheme as Fig. 5. Ca^{2+} and Mg^{2+} ions are represented respectively as pink and blue circles.

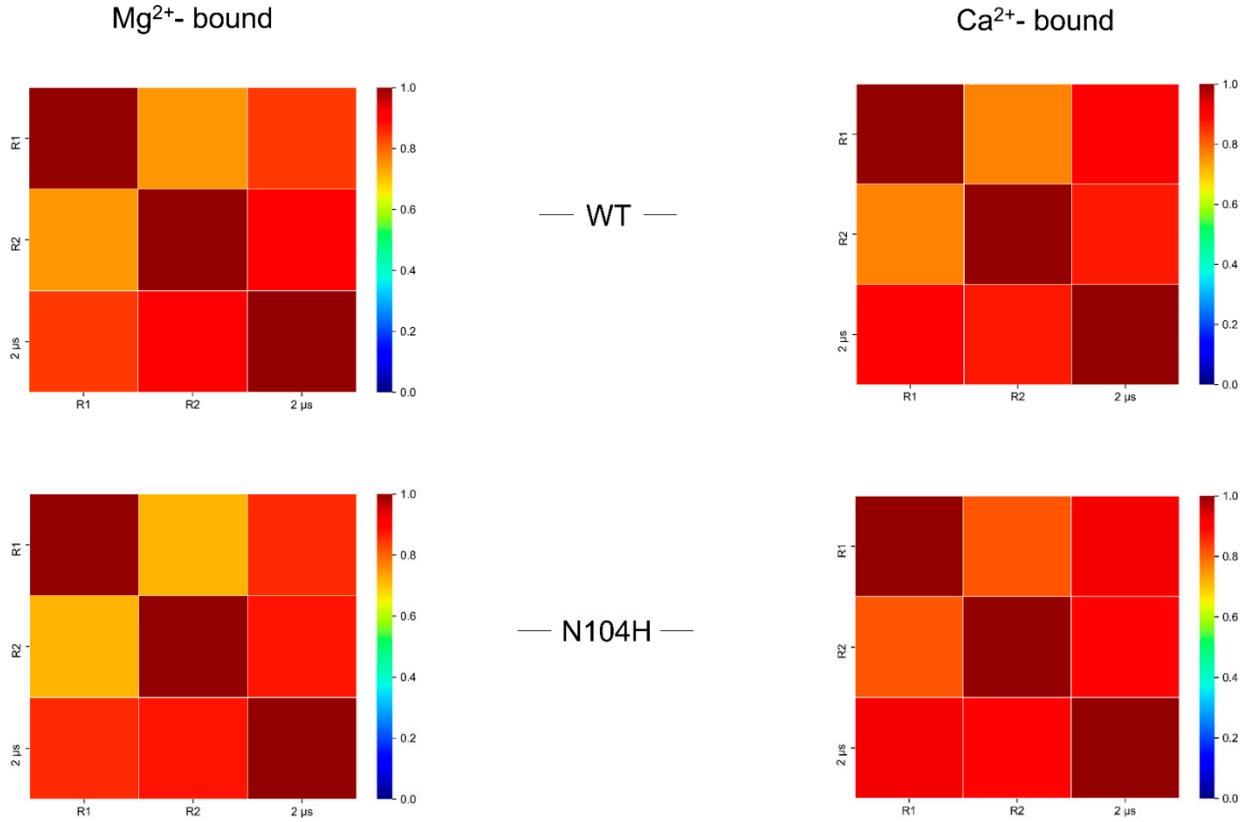

Figure S4. RMSIP of the first 20 principal components of the two 1 μs MD simulation replicas (R1 and R2) and of the concatenated trajectories of WT- and N104H-GCAP1 in their Mg^{2+}-bound and Ca^{2+}-loaded forms.

Supramolecular complexes of GCAP1: implications for inherited retinal dystrophies

Amedeo Biasi[1], Valerio Marino[1], Giuditta Dal Cortivo[1], Daniele Dell'Orco[1]

[1]Department of Neurosciences, Biomedicine and Movement Sciences, Section of Biological Chemistry, University of Verona, 37134 Verona, Italy

Corresponding author:

Daniele Dell'Orco, Department of Neurosciences, Biomedicine and Movement Sciences, Section of Biological Chemistry, University of Verona, Strada Le Grazie 8, 37134 Verona, Italy.

Email: daniele.dellorco@univr.it

Phone: +390458027637

Abstract

Guanylate Cyclase Activating Protein 1 (GCAP1) is a calcium sensor that regulates the enzymatic activity of retinal Guanylate Cyclase 1 (GC1) in photoreceptors in a Ca^{2+}/Mg^{2+} dependent manner. While point mutations in GCAP1 have been associated with inherited retinal dystrophies (IRDs), the protein's ability to form dimers has never been investigated in relation to disease, as has the possible role of its interaction with the potent GC1 inhibitor RD3 (retinal degeneration protein 3). Here, we integrate exhaustive *in silico* investigations with biochemical assays to evaluate the effects of the p.(E111V) substitution, associated with a severe form of IRD, on GCAP1 homo- and hetero-dimerization, and demonstrate that GCAP1 directly interacts with RD3. Although inducing constitutive activation in GC1, the E111V substitution only slightly affects the dimerization of GCAP1. Both wild type and E111V-GCAP1 are predominantly monomeric in the absence of the GC1 target, however E111V-GCAP1 shows a stronger tendency to be monomeric in the Ca^{2+}-bound form, corresponding to GC1 inhibiting state. Reconstitution experiments performed in the co-presence of wild type GCAP1, E111V-GCAP1 and RD3 restored nearly physiological regulation of the GC1 enzymatic activity in terms of cGMP synthesis and Ca^{2+}-sensitivity, suggesting new scenarios for biologics-mediated treatment of GCAP1-associated IRDs.

Keywords: RD3, biologics, guanylate cyclase

1 Introduction

Visual perception is initiated by the phototransduction process in photoreceptors, a complex biochemical cascade which ultimately converts light absorption by visual pigments into cell membrane hyperpolarization, thus triggering the response of downstream neurons [1]. Phototransduction is finely regulated by the interplay between second messengers Ca^{2+} and cyclic guanosine monophosphate (cGMP), whose intracellular concentrations strictly depend on illumination. Indeed, photon detection by the G protein-coupled receptor (rhod)opsin results in the activation of phosphodiesterase 6, which hydrolyzes cGMP, thus causing the closure of cyclic nucleotide-gated (CNG) channels and a subsequent drop of the intracellular Ca^{2+}-concentration from several hundred nM in the dark to less than 150 nM in bright light [2]. Guanylate cyclase-activating proteins (GCAPs) are dimeric neuronal Ca^{2+} sensor (NCS) proteins belonging to the EF-hand super family capable of detecting subtle changes in intracellular Ca^{2+}-concentration, thereby modulating the rate of cGMP synthesis in a Ca^{2+}-dependent fashion by interacting with retinal guanylate cyclases [3-5]. Of the three GCAP isoforms present in human rods and cones, namely GCAP1, GCAP2, and GCAP3, the former emerges as key regulator of GC1, the most relevant isozyme in the phototransduction cascade [6]. In the dark, high Ca^{2+} levels keep GCAP1 in a Ca^{2+}-bound state that inhibits GC1, preventing unnecessary cGMP synthesis; conversely, upon illumination Ca^{2+} levels fall, prompting GCAP1 to exchange Ca^{2+} for Mg^{2+} (**Figure 1A**) and triggering a conformational change that stimulates GC1 activity and rapidly replenishes cGMP, which leads to the opening of CNG channels and, ultimately, the restoration of the Ca^{2+} concentration of the dark state.

Maintaining Ca^{2+} and cGMP homeostasis is imperative for both the viability and the functionality of photoreceptors, as more than twenty mutations in the *GUCA1A* gene (encoding for GCAP1) have been associated with inherited retinal dystrophies (IRDs), such as autosomal dominant cone (COD) and cone-rod (CORD) dystrophies [7-16], due to defective GC1 regulation. These disorders are characterized by progressive central vision loss, color vision impairment, and altered sensitivity to light. The phenotypic heterogeneity observed in such dystrophies can be attributed to the specific amino acid substitutions, each affecting the protein's ability to regulate GC1 differently, thereby disrupting the delicate second messenger equilibrium governing phototransduction. A variant of GCAP1, in which the bidentate coordinator glutamate 111 in the high-affinity Ca^{2+}-binding motif EF3 is replaced by a valine (E111V) leading to constitutive activation of GC1 was recently identified by some of us in a family affected by a severe form of CORD [14]. Constitutive activation of the GC1 target seems to be the common hallmark of all GCAP1-related IRDs [9, 17], which all share autosomal dominant inheritance pattern. This makes the molecular scenario underlying GCAP1-associated IRDs especially intricate, as the protein is known to form dimers in a Mg^{2+}/Ca^{2+} dependent manner [3, 18, 19], which could result in a heterogeneous pool of homo- and heterodimers with unknown effects on GC1 regulation (**Figure 1B**).

Another complication of the molecular scenario involving supramolecular complexes formed by GCAP1 is the yet unknown effect of the interaction between the IRD-associated GCAP1 variants and Retinal degeneration protein 3 (RD3), a 23 kDa alpha-helical protein, recently emerged as a key factor in the preservation and functionality of photoreceptor cells [20, 21]. With its sub-micromolar affinity, RD3 prevents GC1 premature activation within the photoreceptor's inner segment, thus averting potential cellular damage [22, 23]. Indeed, RD3 mutations affecting its binding to GC1 or its inhibitory activity have been associated with Leber congenital amaurosis type 12 (LCA12) and CORD6 [24, 25], while the lack of protein expression is associated with a marked decline of GC1 levels in photoreceptors outer segments and its accumulation in the inner segments, implicating a role for RD3 in the proper trafficking and localization of the cyclase [26-28]. RD3's pivotal inhibitory activity arises from specific surface-exposed residues essential for the interaction with GC1, which are either located in the coiled-coil domain between helices α1 and α2 or in helix α3 (**Figure 1C**) [29].

This study explores the factors affecting the formation of GCAP1 supramolecular complexes both in the absence and in the presence of IRD-associated point mutations, focusing on the E111V variant, that we have previously characterized extensively from a clinical [14] and biomolecular viewpoint [30, 31]. We used an integrated *in silico* and *in vitro* investigation approach to evaluate the functional consequences of the co-presence of a disease-associated point mutation and wild type (WT) GCAP1, as well as RD3 as a full protein or a peptide encompassing the region with stronger inhibitory capacity toward GC1. Besides shedding light on the basic mechanisms underlying GCAP1-mediated protein-protein interactions, our thorough investigation suggests conditions that could be exploited in the context of COD and CORD diseases to facilitate the re-establishment of the physiological homeostasis of cGMP and Ca^{2+}, with interesting applications for biologics-based therapeutics.

2 Materials and Methods

2.1 Protein Expression and Purification

2.1.1 GCAP1 variants

The cDNA of human WT-GCAP1 (Uniprot entry: P43080) was purchased from Genscript and cloned into a pET-11a vector between NdeI and NheI restriction sites, while the E111V variant was introduced in both vectors using QuikChange II Site-Directed Mutagenesis kit (Agilent) as detailed in [14]. All variants were heterologously expressed in *E. coli* BL21(DE3) following co-transformation with pBB131 vector which contains the cDNA of *S. cerevisiae* N-myristoyltransferase (yNMT) necessary to achieve post-translational N-terminal myristoylation [33], and purified using the same

protocol as previously detailed [14]. Briefly, proteins were purified from inclusion bodies after denaturation with 6M guanidine-HCl, then underwent dialysis against 20 mM Tris-HCl pH 7.5, 150 mM NaCl, 7.2 mM β-mercaptoethanol buffer to allow refolding, and two sequential chromatographic steps, namely size exclusion chromatography (SEC, HiPrep 26/60 Sephacryl S-200 HR, GE Healthcare) and anion exchange chromatography (AEC, HiPrep Q HP 16/10, GE Healthcare). Protein concentration was measured by Bradford assay [34] using a GCAP1-specific reference curve based on the amino acid hydrolysis (Alphalyze), and its purity assessed on a 15% SDS-PAGE gel. Finally, GCAP1 variants were exchanged against decalcified 50 mM NH_4HCO_3 buffer, flash-frozen in liquid nitrogen, lyophilized and stored at -80°C until use.

2.1.2 RD3

The pETM-11-RD3 plasmid containing RD3 cDNA was a kind gift of Prof. K.W. Koch (Department of Neuroscience, Carl von Ossietzky Universität Oldenburg). RD3 was expressed in *E. coli* BL21(DE3) and purified by a series of centrifugation steps as previously reported [22]. Briefly, harvested cells were mechanically lysed with 3 sonication cycles on ice (30 s ON, 30 s OFF) and centrifuged at 4 °C at 10000 x g for 10 min, then the insoluble fraction was washed 3 times against 10 mM Tris-HCl pH 7.5, 2 mM EDTA, 14 mM β-mercaptoethanol, 100 µM PMSF and 1X protein inhibitor cocktail (PIC) and centrifuged again at 4 °C at 15000 x g for 15 min. The insoluble fraction was denatured overnight using the same buffer with the addition of 8 M Urea, refolded by dialysis at 4 °C against 2x300 volumes (initial volume: 15 mL) of 10 mM Tris-HCl pH 7.5, 0.1 mM EDTA and 14 mM β-mercaptoethanol and centrifuged at 4 °C at 10000 x g for 10 min. The supernatant containing RD3 was collected to assess protein purity via SDS PAGE and stored at -80°C with 50% v/v glycerol.

2.1.3 RD3 peptide

The RD3 peptide (RD3ppt), essential for the inhibitory activity of the protein [29], encompasses the region K87-E110 of RD3 corresponding to helix α3 (**Figure 1C**), sequence KIHPSYCGPAILRFRQLLAEQEPE) and was purchased by Genscript (purity >95%, checked by HPLC). The lyophilized peptide was resuspended in pure bi-distilled water at a concentration of ~700 µM according to manufacturer instructions and stored at -80°C until use.

2.3 Analytical Size Exclusion Chromatography

The effects of the E111V mutation on GCAP1 dimerization under Ca^{2+} and Mg^{2+} concentrations mimicking the physiological signaling states were evaluated by analytical size exclusion

chromatography (aSEC). Different GCAP1 concentrations (0.8 µM - 80 µM) were injected (200 µL) into a Superose 12 10/300 column (GE Healthcare) previously equilibrated with 20 mM Tris-HCl pH 7.5, 150 mM NaCl, 1 mM DTT, 1 mM Mg^{2+} buffer and either 0.5 mM EGTA or 0.5 mM Ca^{2+}. Elution profiles were collected by monitoring the absorbance at 280 nm, dissociation constants for GCAP1 dimers were obtained by fitting the elution volume (V_e) to the concentration curves using equation 1 as in Ref. [18]:

$$V_e = A \times \log\left(\left(\frac{[P_{TOT}] - \left(\frac{-D_C + \sqrt{{D_C}^2 + 4 \times D_C \times [P_{TOT}]}}{2}\right)}{[P_{TOT}]}\right) \times 22.9 + 22.9\right) + B \quad (1)$$

where V_e represents the elution volume at the peak, A is slope, $[P_{TOT}]$ is the concentration of the protein at the time of injection, B is the y-intercept and 22.9 is the monomer theoretical molecular mass (MM) of hGCAP1 in kDa. The MM of eluted samples was estimated using a calibration curve using cytochrome C (12.4 kDa), carbonic anhydrase (29 kDa), β-amylase (200 kDa) and alcohol dehydrogenase (150 kDa) as standard. Thus, the distribution coefficient D_c was calculated based on the V_e of the samples using equation 2:

$$D_c = \frac{(V_e - V_0)}{(V_i - V_0)} \quad (2)$$

where V_0 represents the void volume of the column (8.26 mL) and V_i is the total volume of the column (~ 24 mL). Ultimately, the MM of the samples was determined by plotting log(MM) vs D_c.

2.4 Guanylate cyclase enzymatic activity assays

The effect of RD3ppt and RD3 on the regulation of GC1 activity by GCAP1 variants was investigated by performing enzymatic assays to monitor cGMP synthesis. Human recombinant GC1 was stably expressed in HEK293 cells after transfection with pcDNA3.1+N-eGFP encoding for a fusion protein constituted by eGFP at the N-terminal and GC1 as previously described [31]. Membranes containing GC1 were isolated after cell lysis and resuspended in 50 mM HEPES pH 7.4, 50 mM KCl, 20 mM NaCl and 1 mM DTT. The inhibitory activity of RD3ppt was evaluated by incubating GC1 with 5 µM WT-GCAP1 and increasin2g concentrations of the peptide (0.05 µM - 15 µM) at low Ca^{2+} (< 73 nM). Minimum and maximum GC1 activities were determined by incubating GC1 with ~200 nM RD3 and WT or E111V-GCAP1 or both to a final concentration of 5 µM, in the presence of high (~30 µM) or low Ca^{2+} (<19 nM). The effects of RD3 on GCAPs Ca^{2+} sensitivity (IC_{50}) were assessed by incubating GC1 with ~200 nM RD3 and either WT or E111V-GCAP1 or their combination at a stoichiometric ratio of 3 WT-GCAP1: 1 E111V-GCAP1 to a final concentration of 5 µM in the presence of increasing

free [Ca^{2+}] ranging from <19 nM to 1 mM. The GCAP1 concentration at which GC1 activation is half-maximal (EC_{50}) was estimated by incubating GC1 in the presence of <19 nM free Ca^{2+} with ~200 nM RD3 and increasing GCAP1 (WT, E111V or both) concentration from 0 to 15 µM. GC1 enzymatic reactions were performed in 30 mM MOPS/KOH pH 7.2, 60 mM KCl, 4 mM NaCl, 1 mM GTP, 3.5 mM MgCl2, 0.3 mM ATP, 0.16 mM Zaprinast buffer and blocked with the addition of 50 mM EDTA and boiling at 95°C. The synthesized cGMP was quantified by means of HPLC using a C18 reverse phase column (LiChrospher 100 RP-18, Merck). Data are reported as the mean ± standard deviation of at least three data sets.

2.5 Circular Dichroism spectroscopy

Circular Dichroism (CD) spectroscopy in the far UV (200-250 nm) was employed to unveil alterations in secondary structure of GCAP1 upon RD3ppt or RD3 binding under different ionic conditions. GCAP1 variants were resuspended in 20 mM Tris-HCl pH 7.5, 150 mM KCl, 1 mM DTT, while RD3 and RD3ppt in 20 mM Tris-HCl pH 7.5, 1 mM DTT. Far-UV CD spectra of 10 µM RD3 or RD3ppt were collected in the presence of 300 µM EGTA; while those of 10 µM GCAP1 were collected in the presence of 300 µM EGTA and after sequential additions of 10 µM RD3 or RD3ppt and 600 µM Ca^{2+}, leading to approximately 300 µM free Ca^{2+}. All CD spectra were recorded on a Jasco J-710 spectropolarimeter equipped with a Peltier-type cell holder in a 0.1-cm pathlength quartz cuvette with the following parameters: 1 nm bandwidth, 1 nm data pitch, 4 s integration time, 50 nm/min scanning speed, 25 °C temperature, 5 accumulations.

2.6 Molecular modelling

The three-dimensional structure of Ca^{2+}-loaded myristoylated human GCAP1 (UniProt entry: P43080), representing the GC1-inhibiting form, was obtained using the "Advanced Homology Modeling" tool provided by Bioluminate (Maestro package v. 12.5.139, Schroedinger) by selecting Ca^{2+}-loaded myristoylated GCAP1 from *G. gallus* (PDB entry: 2R2I [35]) as a template. The E111V substitution was introduced by *in silico* mutagenesis using Bioluminate "Mutate Residue" tool on the human structure by selecting the most likely rotamer for the sidechains. Mg^{2+}-bound GCAP1 variants, representing the GC1-activating form, were obtained by removing the Ca^{2+} ion attached to EF4 and replacing those in EF2 and EF3 with Mg^{2+}, as previously done [36]. Human RD3 structure was obtained by homology modelling using the 10 conformers of human RD3 structure (PDB entry: 6DRF [37]) as templates to revert the mutations introduced for structure resolution, namely A18T, D68R, E154K, E156R, E158R, and S160D. Finally, the structure was truncated at residue T139 to exclude the highly flexible C-terminal from docking simulations to avoid artifacts.

2.7 Molecular Dynamics simulations

Molecular Dynamics (MD) simulations of GCAP1 variants were performed on GROMACS 2020.3 package [38] using CHARMM36m [39] as the all-atom force field previously implemented with the parameters for the N-terminal myristoylated Gly (available on request). Two-step energy minimization and equilibration (2 ns in NVT ensemble with and without position restraints) were carried out as previously described [40]. For each state, namely Ca^{2+}-loaded WT- and E111V-GCAP1 (Ca^{2+}-ions bound to EF2, EF3 and EF4), Ca^{2+}-bound E111V-GCAP1 (Ca^{2+}-ions bound to EF2 and EF4), and Mg^{2+}-bound WT- and E111V-GCAP1 (Mg^{2+}-ions bound to EF2 and EF3) four independent 1 μs trajectories at constant pressure (1 atm) and temperature (310 K) were produced. The exhaustiveness and consistency of the trajectories was assessed by means of Principal Component Analysis of the Cα (representing the largest collective motion of the protein), Linear Discriminant Analysis on the first two principal components and Root-Mean Square Inner Product of the first twenty principal components following a previously detailed pipeline [40]. Once their reproducibility was assessed for each state, the four trajectories were concatenated and the flexibility of the proteins was investigated by means of Root-Mean Square Fluctuation (RMSF) of the Cα, which represents the time-averaged Root-Mean Square Deviation (RMSD) calculated with respect to the average positions along the 4 μs trajectories. Analogously, the RMSF of ions bound to individual EF-hands was calculated to evaluate the mobility of the ions within the loop, indicative of potential alterations of the optimal geometry required for ion coordination.

2.7 Molecular docking simulations

The centroid of the conformations sampled by the 4 μs MD simulations of GCAP1 variants were used as ligand and receptor for protein-protein rigid-body docking simulations of GCAP1 dimers using ZDOCK 3.0.2 [41], which comprised 4 independent docking runs per tested case with a sampling step of 6° (dense sampling) starting from different relative orientations, each resulting in 4000 complexes. Docked poses were categorized into a cohort of structurally analogous conformations, each exhibiting a Cα RMSD < 1 Å relative to the reference complex structure representing the highest-scored dimer described in ref [18], and their average ZDOCK score (ZD-s) was used to estimate the free energy of binding (ΔG^0) based on their correlation with experimental data [42, 43].

3 Results and Discussion

To dissect the formation of the supramolecular complexes involving GCAP1-GC1 and potentially RD3, and to evaluate the putative role of the E111V point mutation, we applied a stepwise procedure, which started from the computational characterization of GCAP1 monomers in the possible signaling states (**Figure 1B**). Exhaustive, 4 microsecond MD simulations formed the basis for studying the stability of the protein and the allosteric mechanisms arising from the specific ligand and/or mutated state; moreover, the output of MD simulations was used to build a reliable structural model of the GCAP1 dimer using protein-protein docking, which permitted direct comparisons with experimental results from analytical size exclusion chromatography. Finally, we tested whether RD3, both in a shorter form via a peptide encompassing helix α3, or in the full-length version, was able to interact with GCAP1 as well as with GC1, and exert a controlled inhibition of the cyclase in the presence of WT- and E111V-GCAP1. The results are summarized in the following paragraphs.

3.1 Conformational properties of WT/E111V-GCAP1 monomers: molecular dynamics simulations suggest increased structural flexibility for E111V-GCAP1

Previous works highlighted that the E111V substitution, in which an acidic glutamate residue involved in the coordination of Ca^{2+} is replaced by the hydrophobic valine, only slightly affects secondary and tertiary structure of GCAP1 [14, 31] while dramatically impairing the affinity for Ca^{2+} and preventing the binding of the cation to EF3. The altered affinity for Ca^{2+} reflects on the dysregulation of GC1 activity and leads to its constitutive activation. In the present study, we investigated at atomistic resolution the molecular determinants underlying ion binding to GCAP1 variants by running 4 μs MD simulations of the protein under GC1-activating (Mg^{2+} bound to EF2 and EF3 in both variants) and GC1-inhibiting conditions (Ca^{2+} bound to EF2, EF3 and EF4 in both variants, and bound only to EF2 and EF4 for the E111V substitution).

In line with previous spectroscopic data [14, 31], exhaustive MD simulations revealed a significant distortion of the EF3 loop of the E111V variant compared to the WT, which significantly destabilized the coordination of Ca^{2+} in EF3 (**Figure 2A**). On the other hand, no significant structural rearrangement was observed throughout the trajectory, although the RMSF profiles highlighted a significantly higher backbone flexibility for E111V-GCAP1 bound to 2 or 3 Ca^{2+} ions compared to the WT, especially in the region corresponding to EF3 (**Figure 2B**); this is not surprising, since the mutated residue is located in that EF-hand motif, thus pointing to a local structural perturbation. Interestingly, this reflected not only in a significantly higher fluctuation of the Ca^{2+}-ion in EF3 (138.2 Å for 3Ca-E111V vs 1.01 for 3Ca-WT-GCAP1, **Supplementary Table ST1**), which spontaneously dissociated in one of the replicas, but also in EF4 (3.22 Å for 3Ca-E111V and 1.63 Å for 2Ca-E111V vs 1.23 Å for 3Ca-WT-GCAP1, **Supplementary Table ST1**) and, to a lesser extent, in EF2 (2.02 Å for 3Ca-E111V and 2.04 Å for 2Ca-E111V vs 1.1 Å for 3Ca-WT-GCAP1, **Supplementary Table**

ST1), suggesting an allosteric effect of the mutation, which was already pointed out in shorter simulations [40]. As to the Mg^{2+}-bound forms, the E111V substitution displayed minor differences with the WT both in terms of backbone flexibility (**Figure 2C**) and in ion coordination, as shown by the comparable RMSF of Mg^{2+}-ions in EF2 (1.30 Å vs 1.23 Å, **Supplementary Table ST1**) and EF3 (2.2 Å vs 1.9 Å, **Supplementary Table ST1**), thus suggesting that the GC1-inhibiting state does not change significantly from the structural viewpoint between IRD-associated and WT condition, at least as far as isolated structures of GCAP1 monomers are concerned. This result is also in line with previous spectroscopic characterizations by us based on near UV CD spectroscopy [14, 31].

3.2 *In silico* dimerization of WT- and E111V-GCAP1 suggests very similar binding modes

The similar structural features of WT- and E111V-GCAP1 monomers suggest that they might dimerize in a comparable manner, although this process was not explicitly investigated yet. The Ca^{2+}- and Mg^{2+}-dependent dimerization of GCAP1 could play a role in the phototransduction cascade, for example affecting the binding to, and therefore the regulation of the GC1 target [3, 44]. The complexity of the molecular scenario is increased in the presence of IRDs, as the autosomal dominant inheritance pattern of mutations associated with COD and CORD suggests that, in the outer segments of photoreceptors under these conditions, a pool of homo- and heterodimers might be present. To test whether and how the presence of the E111V mutation in well-defined signaling states can affect protein dimerization, we used an *in silico* approach based on rigid-body docking, which led to the reconstitution of potential dimeric assemblies of GCAP1 (WT/WT, E111V/E111V, WT/E111V) under the same cation-bound conditions used in MD simulations (see section 3.1). In order to discriminate the poses obtained by docking protein monomers, we considered as “native like” the highest-scored assembly that was previously validated by small-angle X- ray scattering data, characterized by specific hydrophobic contacts at the GCAP1 dimer interface. In particular, dimer formation is driven by the interaction between residues located on αE1 and αF2 from one monomer and amino acids on αE1, αF2 and αE3 from the second monomer [18].

For all tested conditions, docking simulations predicted a comparable number of native-like poses, ranging from 18 to 22 in the case of the E111V and WT homodimer, respectively (**Table 1**), with average RMSD compared to the reference structure spanning between 0.84 ± 0.1 and 0.86 ± 0.1 Å, **Table 1**). Interestingly, the highest-scored pose out of the 16000 complexes outputted by ZDOCK (**Table 1**) was always selected as a native-like pose, thus implying that the assembly of both WT and E111V-GCAP1 is essentially compatible with that previously validated by small-angle X- ray scattering data, and that the binding may indeed occur in an essentially rigid body-like manner. On the same line, the average ZD-s of the native-like solutions in all conditions tested ranged between 54.0 ± 0.8 and 54.9 ± 0.9 in the case of Mg^{2+}-bound WT homodimer and 3 Ca^{2+}-bound E111V, respectively. This average index can be used to empirically derive the free energy of dimerization,

provided that the binding occurs without major conformational changes [42, 43]. The predicted ΔG° values (ranging between -17.22 and -17.55 kcal/mol (**Table 1**) were all very similar to each other, despite the different conditions. Indeed, by inferring state- and variant-specific changes in the free energy of binding (ΔΔG°), docking results highlighted only subtle differences in binding affinities (< -0.2 kcal/mol, **Table 1**), which were more pronounced when residue V111 was involved in ion binding, that is in the case of 3Ca and 2Mg (**Table 1**). Overall, these *in silico* results suggest that the WT and the E111V variants dimerize with very similar quaternary structure and affinity.

3.3 *In vitro* dimerization of GCAP1 variants suggests higher propensity to dimerize in the Mg^{2+}-bound form

Since rigid-body docking simulations predicted neglectable differences in binding affinities upon homo- and heterodimer formation in the presence of either Ca^{2+} or Mg^{2+} ions, the propensity of GCAP1 variants to form dimers under different ion-loading conditions was validated *in vitro* by using analytical SEC with increasing amounts of GCAP1 in the 0.8 μM - 80 μM concentration range. The analysis of elution profiles (**Figure 3**) led to the estimated equilibrium constants for GCAP1 dimerization reported in **Table 1**. An overall agreement with *in silico* docking experiments could be noted in terms of similar binding modes of WT and E111V-GCAP1, regardless of the mutation and the specific signaling state; however, analytical SEC permitted higher precision in determining the binding affinities, which are not affected by the requirement of rigid body-like interaction. Interestingly, a slightly reduced dimer affinity was detected for E111V-GCAP1 in the presence of Ca^{2+} compared to the WT (K_{Dim}^{E111V}= 16.7 ± 3.2 μM vs K_{Dim}^{WT}=12.0 ± 0.8 μM); the slight increase in affinity exhibited by the Mg^{2+}-bound forms compared to the WT (K_{Dim}^{E111V}=4.2 ± 3.4 μM vs K_{Dim}^{WT}=6.1 ± 3.3 μM), was however within the error bars, so not significant. However, when the comparison was done for each variant, looking at the Ca^{2+} vs. Mg^{2+}-bound forms, the increase in the tendency to dimerize in the Mg^{2+}-bound was much higher for the E111V variant (~4-fold) than for the WT (~2-fold). These findings diverge from previously obtained results in which WT-GCAP1 binding affinity decreases switching from a Ca^{2+} (K_{Dim}^{WT}=8.8 ± 0.7 μM) to a Mg^{2+}-bound state (K_{Dim}^{WT}=45 ± 15 μM) [18]. The discrepancies can be attributed to a different ionic strength of the aSEC buffer (100mM vs 150mM NaCl), its pH (8.0 vs 7.5) and a much higher concentration of Mg^{2+}_{free} (~4mM vs ~0.9mM) which altogether determine a less physiological environment if compared to the experimental parameters presented in this work. Overall, these results suggest that the IRD-associated variant has stronger tendency to be monomeric in the Ca^{2+}-bound form, corresponding to GC1 inhibiting state, and to dimerize in the absence of Ca^{2+}, that is in the GC1-activating form. If dimerization of GCAP1 was a requirement for GC1 activation, this result could partly explain the variant's tendency to induce constitutive activation in the target enzyme.

Previous results on the V77E-GCAP1 variant, which was shown to abolish protein dimerization, showed that also the GC1 activation was seriously compromised [45, 46], which would support a mechanism that requires GCAP1 dimerization for the correct activation of GC1. On the other hand, it should be noted that, if the same cellular concentration of GCAP1 measured in bovine rods (3.3 μM [47]) is assumed to be valid for human photoreceptors, our estimated K_{Dim} values would point to the two isolated variants being predominantly monomers under Ca^{2+}-saturating conditions (75.5% and 78.8% for WT- and E111V-GCAP1, respectively) and, to a lesser extent, in the Mg^{2+} -bound form (66.7% and 61.2% for WT- and E111V-GCAP1, respectively). It remains therefore essential to establish whether GCAP1 dimerization is facilitated by the interaction with the GC1 target, and if dimerization is a prerequisite for its activation.

3.4 Using RD3-induced inhibition of GC1 to probe novel therapeutic hypotheses for IRD in the presence of E111V-GCAP1

The modulation of GC1 activity is a fundamental step in phototransduction, to ensure physiological response and photoreceptor viability. We previously demonstrated *in vitro* that WT GCAP1 significantly attenuates the dysregulation of GC1 induced by E111V-GCAP1 [30] and that direct retinal delivery of the mutated protein in a WT mouse induces a disease-phenotype [31]. Although the delivery of extra WT GCAP1 was shown to partly restore the Ca^{2+} sensitivity of GC1, numerical simulations suggest that this amelioration is not enough to fully prevent retinal degeneration as the levels of Ca^{2+} and cGMP would remain higher than normal [30]. These preliminary data nonetheless suggest that the combination of WT GCAP1 and GC1 inhibitors could be a promising avenue for addressing the dysregulated cGMP production implicated in IRDs in the presence of variants such as E111V-GCAP1. In this study we probed whether the potent GC1-inhibitor RD3 could contribute to this effective combination. We therefore tested the effects on GC1 regulation by WT- and E111V-GCAP1 variants of RD3 as a full-length protein as well as a peptide (named RD3ppt) corresponding to the interacting helix α3 (**Figure 1C**), which was described as a fundamental component for achieving high inhibiting capacity of the cyclase [25].

We first checked the GC1 activity at increasing amounts of RD3ppt in the 50 nM - 15 μM range. While RD3ppt was observed to inhibit GC1 activity only partially and at low micromolar concentrations in the presence of either WT- (**Figure 4A**) or E111V-GCAP1 (**Figure S4**), full-length RD3 showed significatively enhanced inhibitory efficacy of the WT-GCAP1-GC1 complex (**Figure 4B**), with an IC_{50} of 68.4 ± 4.9 nM. This high inhibition capability of RD3 is in line with previous observations [25, 28, 48] and could be used as a further element to attenuates the dysregulation of GC1 induced by E111V-GCAP1 [30].

Although it has been established that RD3 interacts with GC1 to promote its correct targeting to the photoreceptor outer segment, the interaction between RD3 and GCAP1 is thought to constitute a functional requirement to properly achieve such targeting; indeed, *in vivo* studies suggested that disrupting the GC1-GCAP1 and RD3 complex in the endoplasmic reticulum is associated with Leber congenital amaurosis 1 [28]. Despite the strong evidence of interaction by *in cyto* and *ex vivo* imaging, the interplay between RD3 and GCAP1 is still poorly understood. We have hence investigated by CD spectroscopy the interaction between GCAP1 variants and RD3 (both RD3ppt and the whole protein), to possibly elucidate the molecular fingerprints defining the RD3-GCAP1 complex.

The far UV CD spectrum of RD3ppt (**Figure 5A**) indicated that the peptide is unfolded in solution, whereas Mg^{2+}-bound WT-GCAP1 exhibited, as expected, the spectrum of a typical all-α helical protein with minima at 208 and 222 nm, similarly to full-length RD3 (**Figure 5B-C**). In addition, both WT- and E111V-GCAP1 variants exhibited a small but significant increase in ellipticity upon switching from the Mg^{2+}-bound form to the Ca^{2+}-bound form (3% and 2.6% for WT- and E111V-GCAP1, respectively, **Figure 5B-C**, **Table 2**), accompanied by a change in spectral shape, which was more evident for WT-GCAP1 ($\theta_{222}/\theta_{208}$ = 0.89 vs 0.92, **Table 2**), compared to E111V ($\theta_{222}/\theta_{208}$ = 0.89 vs 0.90, **Table 2**). Such variations in spectral shape were most probably due to the different content in secondary structure between the Mg^{2+}-bound and the Ca^{2+}-bound forms of GCAP1 variants. Indeed, spectral deconvolution suggested that upon Ca^{2+}-binding WT-GCAP1 displayed a 1% increase in α-helical content and a 1.4% decrease in β-sheet content, at odds with E111V-GCAP1, whose α-helical content decreased from 33.4% to 32.7% while its β-sheet content exhibited a 3% increase (**Table 2**). The interaction between RD3(ppt) and GCAP1 variants was assessed by comparing the spectrum of the putative complex with that of the sum of the isolated proteins; the fact that the spectrum obtained when incubating the protein and the peptide differed from to the sum of those of the individual proteins points to an interaction between the two macromolecules. Interaction was detected for both RD3ppt (**Figure 5D**) and full-length RD3 upon incubation with GCAP1 variants (**Figure 5E-F**), although with some differences. While RD3ppt interaction with Mg^{2+}-bound WT-GCAP1 resulted in a ~10% lower ellipticity with respect to the theoretical sum of the spectra, the full-length RD3-GCAP1 variants complexes showed an almost halved signal compared to the sum, regardless of the variant or the ion-binding state. Ca^{2+}-binding did not significantly change the spectral shape of the complex RD3-WT-GCAP1 ($\theta_{222}/\theta_{208}$ = 0.98 vs 0.99, **Figure 5E**, **Table 2**), at odds with the complex constituted by RD3 and E111V-GCAP1, whose $\theta_{222}/\theta_{208}$ changed from 0.99 to 1.07, suggesting different interaction modes between the two variants.

Once verified the direct interaction between RD3 and GCAP1, the potential of their co-presence with respect to GC1 inhibition was explicitly probed. We thus monitored the effects of RD3 on the Ca^{2+}-dependent regulation of GC1 by both GCAP1 variants starting form the case of high and low Ca^{2+} levels, corresponding to dark-adapted and illuminated cells, respectively (**Figure 6A**). As expected,

the presence of RD3 significantly diminished the rate of cGMP synthesis under both inhibiting and activating conditions, in the presence of each of the two GCAP1 variants, although in the case of the E111V-GCAP1 a persistent activation was observed in the presence of Ca^{2+}, indicative of the strong constitutive activation of GC1 induced by the mutant. Interestingly, the incomplete shut-down of the cyclase activity detected for both variants, observed in this study (**Figure 6A**) and in previous ones [22, 27] might be attributed to the direct interaction of GCAP1 with RD3, an interplay that, as discussed above, is still poorly understood [28].

As mentioned above, the delivery of extra WT-GCAP1 on a background of E111V-GCAP1 was shown to bring the Ca^{2+}-dependent regulation of GC1 closer the physiological Ca^{2+}-range [30]; to test any synergistic effect in the presence of a potent GC1 inhibitor, we monitored the effects of RD3 on GC1 regulation in the presence of GCAP1 variants at a stoichiometric ratio WT:E111V of 3:1. Remarkably, RD3 was found to almost totally revert the molecular phenotype of the GC1-GCAP1 machinery to that of the WT (**Figure 6B**), with an IC_{50} shifting from 8.49 ± 6.05 μM to 0.29 ± 0.05 μM (**Table 3**), thus comparable to that of the WT both in the absence (0.32 ± 21.6 μM) and in the presence of RD3 (0.22 ± 0.01 μM). A similar conclusion could be drawn as to the cooperativity of the GC1's Ca^{2+}-regulation, as displayed by the Hill coefficient switching from 0.68 ± 0.28 in the absence of RD3 to 2.24 ± 0.94 in its presence (**Table 3**), again very close to the values exhibited by the WT under the same conditions (2.14 ± 0.27 and 2.23 ± 0.28, respectively). Remarkably, RD3 substantially moderated the aberrant cGMP synthesis instigated by the E111V-GCAP1 mutation especially when complemented with an excess of the WT form (**Figure 6**, **Table 3**)**.**

Conclusions

The comprehensive analysis presented here provides new insights into the supramolecular complexes formed by GCAP1 under both physiological and pathological conditions. We used the E111V-GCAP1 variant as representative of more than twenty COD/CORD associated mutations and investigated the dimerization process of GCAP1, which probably plays a role in the regulation of GC1 enzymatic activity. We found that the point mutation does not significantly alter the GCAP1 dimerization. However, the slight changes in affinity detected for E111V-GCAP1 homodimers in the presence of Ca^{2+} suggests that even slight perturbations of the GCAP1 monomer/dimer equilibrium may result in severe dysregulation of GC1, although the dimerization process occurs in a similar manner in structural terms. It remains essential, however, to determine the three-dimensional structure of the GC1-GCAP1 complex and to assess the correct stoichiometry of the interaction, since *per se*, GCAP1 could be predominantly monomeric in the absence of the target. We also explored the influence of RD3 in co-presence with WT- and E111VGCAP1 on GC1 activity. Enzymatic assays revealed the ability of RD3to mitigate the aberrant cGMP synthesis caused by

the E111V mutation, especially when combined with an excess of WT GCAP1. This suggests a potential role for RD3 in restoring near-physiological levels of GC1 activity *in vitro*, thus contributing to the restoration of the disrupted Ca^{2+} and cGMP homeostasis in photoreceptor pathophysiology associated with the E111V mutation. This is particularly interesting in light of our recent findings [31] that support a possible role for protein delivery to the retina to modulate the phototrasduction cascade and virtually counterbalance the constitutive activation of IRD-associated GCAP1 variants.

Acknowledgments

The Centro Piattaforme Tecnologiche of the University of Verona is acknowledged for providing access to the computational and spectroscopic platforms. This study was supported by a grant from the Velux Stiftung (Project No. 1410) and by the Next Generation EU/Ministry of University and Research project: “A multiscale integrated approach to the study of the nervous system in health and disease (MNESYS)”, CUP B33C22001060002, PE00000006 missione 4, componente 2, investimento 1.3.

References

[1] K.-W. Koch, D. Dell’Orco, Protein and Signaling Networks in Vertebrate Photoreceptor Cells, Frontiers in Molecular Neuroscience 8 (2015).

[2] J.I. Korenbrot, Speed, sensitivity, and stability of the light response in rod and cone photoreceptors: Facts and models, Progress in Retinal and Eye Research 31(5) (2012) 442-466.

[3] J.B. Ames, Dimerization of Neuronal Calcium Sensor Proteins, Frontiers in Molecular Neuroscience 11 (2018).

[4] A. Dizhoor, The human photoreceptor membrane guanylyl cyclase, RetGC, is present in outer segments and is regulated by calcium and a soluble activator, Neuron 12(6) (1994) 1345-1352.

[5] D.G. Lowe, A.M. Dizhoor, K. Liu, Q. Gu, M. Spencer, R. Laura, L. Lu, J.B. Hurley, Cloning and expression of a second photoreceptor-specific membrane retina guanylyl cyclase (RetGC), RetGC-2, Proceedings of the National Academy of Sciences 92(12) (1995) 5535-5539.

[6] I.V. Peshenko, E.V. Olshevskaya, A.B. Savchenko, S. Karan, K. Palczewski, W. Baehr, A.M. Dizhoor, Enzymatic Properties and Regulation of the Native Isozymes of Retinal Membrane Guanylyl Cyclase (RetGC) from Mouse Photoreceptors, Biochemistry 50(25) (2011) 5590-5600.

[7] A. Biasi, V. Marino, G. Dal Cortivo, P.E. Maltese, A.M. Modarelli, M. Bertelli, L. Colombo, D. Dell'Orco, A Novel GUCA1A Variant Associated with Cone Dystrophy Alters cGMP Signaling in Photoreceptors by Strongly Interacting with and Hyperactivating Retinal Guanylate Cyclase, International Journal of Molecular Sciences 22(19) (2021) 10809.

[8] G. Dal Cortivo, V. Marino, F. Bonì, M. Milani, D. Dell'Orco, Missense mutations affecting Ca2+-coordination in GCAP1 lead to cone-rod dystrophies by altering protein structural and functional properties, Biochimica et Biophysica Acta (BBA) - Molecular Cell Research 1867(10) (2020) 118794.

[9] D. Dell'Orco, P. Behnen, S. Linse, K.-W. Koch, Calcium binding, structural stability and guanylate cyclase activation in GCAP1 variants associated with human cone dystrophy, Cellular and Molecular Life Sciences 67(6) (2010) 973-984.

[10] A.M. Dizhoor, S.G. Boikov, E.V. Olshevskaya, Constitutive Activation of Photoreceptor Guanylate Cyclase by Y99C Mutant of GCAP-1, Journal of Biological Chemistry 273(28) (1998) 17311-17314.

[11] L. Jiang, D. Wheaton, G. Bereta, K. Zhang, K. Palczewski, D.G. Birch, W. Baehr, A novel GCAP1(N104K) mutation in EF-hand 3 (EF3) linked to autosomal dominant cone dystrophy, Vision Research 48(23-24) (2008) 2425-2432.

[12] K. Kamenarova, M. Corton, B. García-Sandoval, P. Fernández-San Jose, V. Panchev, A. Ávila-Fernández, M.I. López-Molina, C. Chakarova, C. Ayuso, S.S. Bhattacharya, NovelGUCA1AMutations Suggesting Possible Mechanisms of Pathogenesis in Cone, Cone-Rod, and Macular Dystrophy Patients, BioMed Research International 2013 (2013) 1-15.

[13] V.B.D. Kitiratschky, P. Behnen, U. Kellner, J.R. Heckenlively, E. Zrenner, H. JÃ¤gle, S. Kohl, B. Wissinger, K.-W. Koch, Mutations in theGUCA1Agene involved in hereditary cone dystrophies impair calcium-mediated regulation of guanylate cyclase, Human Mutation 30(8) (2009) E782-E796.

[14] V. Marino, G. Dal Cortivo, E. Oppici, P.E. Maltese, F. D'Esposito, E. Manara, L. Ziccardi, B. Falsini, A. Magli, M. Bertelli, D. Dell'Orco, A novel p.(Glu111Val) missense mutation in GUCA1A

associated with cone-rod dystrophy leads to impaired calcium sensing and perturbed second messenger homeostasis in photoreceptors, Human Molecular Genetics (2018).

[15] V. Marino, A. Scholten, K.-W. Koch, D. Dell'Orco, Two retinal dystrophy-associated missense mutations inGUCA1Awith distinct molecular properties result in a similar aberrant regulation of the retinal guanylate cyclase, Human Molecular Genetics 24(23) (2015) 6653-6666.

[16] K.M. Nishiguchi, I. Sokal, L. Yang, N. Roychowdhury, K. Palczewski, E.L. Berson, T.P. Dryja, W. Baehr, A Novel Mutation (I143NT) in Guanylate Cyclase-Activating Protein 1 (GCAP1) Associated with Autosomal Dominant Cone Degeneration, Investigative Opthalmology & Visual Science 45(11) (2004) 3863.

[17] P. Behnen, D. Dell'Orco, K.-W. Koch, Involvement of the calcium sensor GCAP1 in hereditary cone dystrophies, Biological Chemistry 391(6) (2010).

[18] F. Bonì, V. Marino, C. Bidoia, E. Mastrangelo, A. Barbiroli, D. Dell'Orco, M. Milani, Modulation of Guanylate Cyclase Activating Protein 1 (GCAP1) Dimeric Assembly by Ca2+ or Mg2+: Hints to Understand Protein Activity, Biomolecules 10(10) (2020) 1408.

[19] E.A. Permyakov, S. Lim, G. Roseman, I. Peshenko, G. Manchala, D. Cudia, A.M. Dizhoor, G. Millhauser, J.B. Ames, Retinal guanylyl cyclase activating protein 1 forms a functional dimer, Plos One 13(3) (2018) e0193947.

[20] L.L. Molday, H. Djajadi, P. Yan, L. Szczygiel, S.L. Boye, V.A. Chiodo, K. Gregory-Evans, M.V. Sarunic, W.W. Hauswirth, R.S. Molday, RD3 gene delivery restores guanylate cyclase localization and rescues photoreceptors in the Rd3 mouse model of Leber congenital amaurosis 12, Human Molecular Genetics 22(19) (2013) 3894-3905.

[21] I.V. Peshenko, E.V. Olshevskaya, A.M. Dizhoor, Functional Study and Mapping Sites for Interaction with the Target Enzyme in Retinal Degeneration 3 (RD3) Protein, Journal of Biological Chemistry 291(37) (2016) 19713-19723.

[22] I.V. Peshenko, E.V. Olshevskaya, S. Azadi, L.L. Molday, R.S. Molday, A.M. Dizhoor, Retinal Degeneration 3 (RD3) Protein Inhibits Catalytic Activity of Retinal Membrane Guanylyl Cyclase (RetGC) and Its Stimulation by Activating Proteins, Biochemistry 50(44) (2011) 9511-9519.

[23] A.M. Dizhoor, I.V. Peshenko, Regulation of retinal membrane guanylyl cyclase (RetGC) by negative calcium feedback and RD3 protein, Pflügers Archiv - European Journal of Physiology 473(9) (2021) 1393-1410.

[24] J.S. Friedman, B. Chang, C. Kannabiran, C. Chakarova, H.P. Singh, S. Jalali, N.L. Hawes, K. Branham, M. Othman, E. Filippova, D.A. Thompson, A.R. Webster, S. Andréasson, S.G. Jacobson, S.S. Bhattacharya, J.R. Heckenlively, A. Swaroop, Premature Truncation of a Novel Protein, RD3, Exhibiting Subnuclear Localization Is Associated with Retinal Degeneration, The American Journal of Human Genetics 79(6) (2006) 1059-1070.

[25] A.M. Dizhoor, E.V. Olshevskaya, I.V. Peshenko, Retinal degeneration-3 protein promotes photoreceptor survival by suppressing activation of guanylyl cyclase rather than accelerating GMP recycling, Journal of Biological Chemistry 296 (2021) 100362.

[26] S. Azadi, L.L. Molday, R.S. Molday, RD3, the protein associated with Leber congenital amaurosis type 12, is required for guanylate cyclase trafficking in photoreceptor cells, Proceedings of the National Academy of Sciences 107(49) (2010) 21158-21163.

[27] H. Wimberg, U. Janssen-Bienhold, K.-W. Koch, Control of the Nucleotide Cycle in Photoreceptor Cell Extracts by Retinal Degeneration Protein 3, Frontiers in Molecular Neuroscience 11 (2018).

[28] R. Zulliger, M.I. Naash, R.V.S. Rajala, R.S. Molday, S. Azadi, Impaired Association of Retinal Degeneration-3 with Guanylate Cyclase-1 and Guanylate Cyclase-activating Protein-1 Leads to Leber Congenital Amaurosis-1, Journal of Biological Chemistry 290(6) (2015) 3488-3499.

[29] I.V. Peshenko, A.M. Dizhoor, Two clusters of surface-exposed amino acid residues enable high-affinity binding of retinal degeneration-3 (RD3) protein to retinal guanylyl cyclase, Journal of Biological Chemistry 295(31) (2020) 10781-10793.

[30] D. Dell'Orco, G. Dal Cortivo, Normal GCAPs partly compensate for altered cGMP signaling in retinal dystrophies associated with mutations in GUCA1A, Scientific Reports 9(1) (2019).

[31] S. Asteriti, V. Marino, A. Avesani, A. Biasi, G. Dal Cortivo, L. Cangiano, D. Dell'Orco, Recombinant protein delivery enables modulation of the phototransduction cascade in mouse retina, Cellular and Molecular Life Sciences 80(12) (2023).

[32] I.V. Peshenko, E.V. Olshevskaya, A.M. Dizhoor, Retinal degeneration-3 protein attenuates photoreceptor degeneration in transgenic mice expressing dominant mutation of human retinal guanylyl cyclase, Journal of Biological Chemistry 297(4) (2021) 101201.

[33] J.-Y. Hwang, K.-W. Koch, Calcium- and Myristoyl-Dependent Properties of Guanylate Cyclase-Activating Protein-1 and Protein-2, Biochemistry 41(43) (2002) 13021-13028.

[34] M. Bradford, A Rapid and Sensitive Method for the Quantitation of Microgram Quantities of Protein Utilizing the Principle of Protein-Dye Binding, Analytical Biochemistry 72(1-2) (1976) 248-254.

[35] R. Stephen, G. Bereta, M. Golczak, K. Palczewski, M.C. Sousa, Stabilizing Function for Myristoyl Group Revealed by the Crystal Structure of a Neuronal Calcium Sensor, Guanylate Cyclase-Activating Protein 1, Structure 15(11) (2007) 1392-1402.

[36] V. Marino, S. Sulmann, K.-W. Koch, D. Dell'Orco, Structural effects of Mg2+ on the regulatory states of three neuronal calcium sensors operating in vertebrate phototransduction, Biochimica et Biophysica Acta (BBA) - Molecular Cell Research 1853(9) (2015) 2055-2065.

[37] I.V. Peshenko, Q. Yu, S. Lim, D. Cudia, A.M. Dizhoor, J.B. Ames, Retinal degeneration 3 (RD3) protein, a retinal guanylyl cyclase regulator, forms a monomeric and elongated four-helix bundle, Journal of Biological Chemistry 294(7) (2019) 2318-2328.

[38] M.J. Abraham, T. Murtola, R. Schulz, S. Páll, J.C. Smith, B. Hess, E. Lindahl, GROMACS: High performance molecular simulations through multi-level parallelism from laptops to supercomputers, SoftwareX 1-2 (2015) 19-25.

[39] J. Huang, S. Rauscher, G. Nawrocki, T. Ran, M. Feig, B.L. de Groot, H. Grubmüller, A.D. MacKerell, CHARMM36m: an improved force field for folded and intrinsically disordered proteins, Nature Methods 14(1) (2016) 71-73.

[40] V. Marino, D. Dell'Orco, Allosteric communication pathways routed by Ca2+/Mg2+ exchange in GCAP1 selectively switch target regulation modes, Scientific Reports 6(1) (2016).

[41] O. Keskin, B.G. Pierce, Y. Hourai, Z. Weng, Accelerating Protein Docking in ZDOCK Using an Advanced 3D Convolution Library, PLoS ONE 6(9) (2011) e24657.

[42] D. Dell'Orco, P.G. De Benedetti, F. Fanelli, In silico screening of mutational effects on enzyme-proteic inhibitor affinity: a docking-based approach, BMC Structural Biology 7(1) (2007).

[43] D. Dell'Orco, Fast predictions of thermodynamics and kinetics of protein–protein recognition from structures: from molecular design to systems biology, Molecular BioSystems 5(4) (2009) 323.

[44] J.B. Ames, Structural basis of retinal membrane guanylate cyclase regulation by GCAP1 and RD3, Frontiers in Molecular Neuroscience 15 (2022).

[45] S. Lim, I.V. Peshenko, E.V. Olshevskaya, A.M. Dizhoor, J.B. Ames, Structure of Guanylyl Cyclase Activator Protein 1 (GCAP1) Mutant V77E in a Ca2+-free/Mg2+-bound Activator State, J Biol Chem 291(9) (2016) 4429-41.

[46] S. Lim, G. Roseman, I. Peshenko, G. Manchala, D. Cudia, A.M. Dizhoor, G. Millhauser, J.B. Ames, Retinal guanylyl cyclase activating protein 1 forms a functional dimer, PLoS One 13(3) (2018) e0193947.

[47] J.Y. Hwang, C. Lange, A. Helten, D. Höppner-Heitmann, T. Duda, R.K. Sharma, K.W. Koch, Regulatory modes of rod outer segment membrane guanylate cyclase differ in catalytic efficiency and Ca2+-sensitivity, European Journal of Biochemistry 270(18) (2003) 3814-3821.

[48] Y. Chen, A.U. Bräuer, K.-W. Koch, Retinal degeneration protein 3 controls membrane guanylate cyclase activities in brain tissue, Frontiers in Molecular Neuroscience 15 (2022).

[49] A. Micsonai, É. Moussong, F. Wien, E. Boros, H. Vadászi, N. Murvai, Y.-H. Lee, T. Molnár, M. Réfrégiers, Y. Goto, Á. Tantos, J. Kardos, BeStSel: webserver for secondary structure and fold prediction for protein CD spectroscopy, Nucleic Acids Research 50(W1) (2022) W90-W98.

Table 1. Results from Rigid-Body Docking simulations of GCAP1 dimers and from analytical SEC experiments. [a] Number of docked complexes with Cα-RMSD < 1 Å with respect to the experimentally validated dimeric model [18]; [b] Average RMSD of the native-like poses; [c] Average ZDOCK score (ZD-s) of native-like poses; [d] Rank of the best native-like pose out of the total 16000 proposed; [e] Gibbs free energy of binding; [f] Difference in Gibbs free energy of binding calculated with respect to WT dimers; [g] Dimerization constant obtained by analytical SEC.

Assembly	Ions	Native-like poses[a]	RMSD[b] (Å)	ZD-s[c]	Best ranked[d]	ΔG^0 [e] (kcal/mol)	$\Delta\Delta G^0$ [f] (kcal/mol)	K_{Dim}[g] (μM)
WT-WT	3Ca	22	0.85 ± 0.1	54.4 ± 0.8	1	-17.36	-	12.0 ± 0.8
	2Mg	22	0.84 ± 0.1	54.0 ± 0.8	1	-17.20	-	6.1 ± 3.3
WT-E111V	2Ca	21	0.86 ± 0.1	54.6 ± 0.8	1	-17.41	-0.06	-
	3Ca	21	0.86 ± 0.1	54.8 ± 0.8	1	-17.50	-0.14	
	2Mg	21	0.85 ± 0.1	54.3 ± 0.8	1	-17.32	-0.12	
E111V-E111V	2Ca	18	0.84 ± 0.1	54.5 ± 0.9	1	-17.39	-0.04	16.7 ± 3.2
	3Ca	18	0.84 ± 0.1	54.9 ± 0.9	1	-17.55	-0.20	
	2Mg	18	0.84 ± 0.1	54.4 ± 0.9	1	-17.36	-0.16	4.2 ± 3.4

Table 2. Results from CD spectroscopy. Secondary structure content estimated from CD spectra by deconvolution with BeStSel software [49]; [a] calculated as $(\theta_{222}^{ion}–\theta_{222}^{EGTA})/\theta_{222}^{EGTA}$.

Variant	Δθ/θ (%)[a]	$\theta_{222}/\theta_{208}$	α-helix (%)	β-sheet (%)	Other (%)
RD3	-	-	27.7	12.7	59.6
Mg^{2+}-bound					
WT-GCAP1	-	0.89	28.3	16.6	55.1
E111V-GCAP1	-	0.89	33.4	9.6	57
RD3 + WT-GCAP1	-	0.98	12.4	29	58.6
RD3 + E111V-GCAP1	-	0.99	13.5	29.4	57.1
Ca^{2+}-bound					
WT-GCAP1	3.02	0.92	29.3	15.2	55.5
E111V-GCAP1	2.60	0.90	32.7	12.6	54.6
RD3 + WT-GCAP1	1.23	0.99	12.4	30.8	56.8
RD3 + E111V-GCAP1	3.44	1.07	12.9	29.4	57.7

Table 3. Results from enzymatic assays. [a] Human GC1 activity as a function of free [Ca^{2+}] in the presence of 5 μM GCAP1 variants and 200 nM RD3; [b] Hill coefficient; [c] GCAP1 concentration at which GC1 activity is half-maximal; [d] fold change in cGMP production calculated as (GC_{max} - GC_{min})/GC_{min}; [e] Data from [31]. Data are reported as mean ± standard deviation of three technical replicates.

	Variant	IC_{50}[a] (μM)	h[b]	EC_{50}[c] (μM)	X-fold[d]
- RD3	**WT** [e]	0.32 ± 21.6	2.14 ± 0.27	1.88 ± 0.22	26
	E111V[e]	20.2 ± 20.53	0.60 ± 0.38	1.55 ± 0.21	1.1
	3xWT/E111V	8.49 ± 6.05	0.68 ± 0.28	-	3.3
+ RD3	**WT**	0.22 ± 0.01	2.23 ± 0.28	6.36 ± 1.17	14.4
	E111V	118 ± 44.8	0.67 ± 0.95	5.62 ± 1.61	0.76
	3xWT/E111V	0.29 ± 0.05	2.24 ± 0.94	-	4.6

Illustrations

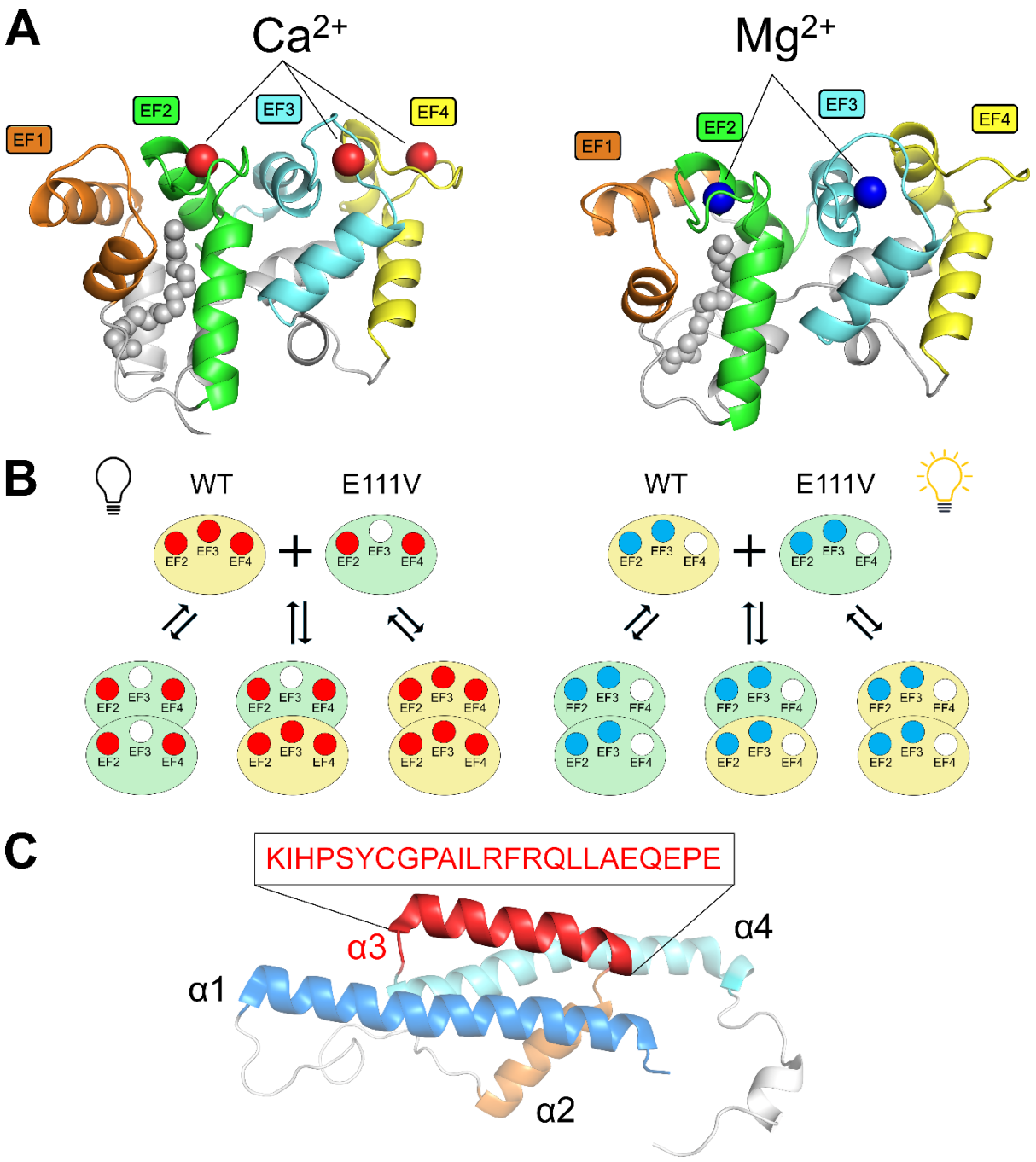

Figure 1. (A) Cartoon representation of the three-dimensional homology model of monomeric Ca^{2+}-loaded (left) and Mg^{2+}-bound (right) human WT-GCAP1; EF1 is colored in orange, EF2 in green, EF3 in cyan and EF4 in yellow. N- and C-terminal are represented in light grey; Ca^{2+} and Mg^{2+} ions are shown as red and blue spheres, respectively, and the myristoyl as grey spheres. (B) Schematic representation of the dimerization of WT- (yellow) and E111V-GCAP1 (green) in their GC1-inhibiting (left) and activating states (right), Ca^{2+} and Mg^{2+} ions are shown as red and blue circles, respectively, empty EF hands are shown as white circles. Equilibria leading to possible homo- and hetero-dimers are represented. (C) Cartoon representation of the three-dimensional structure of RD3 (PDB entry 6DRF); helix α1 is colored in blue, helix α2 in orange, helix α3 in red and helix α4 in cyan. The sequence of helix α3 representing the RD3 peptide (RD3ppt) is reported.

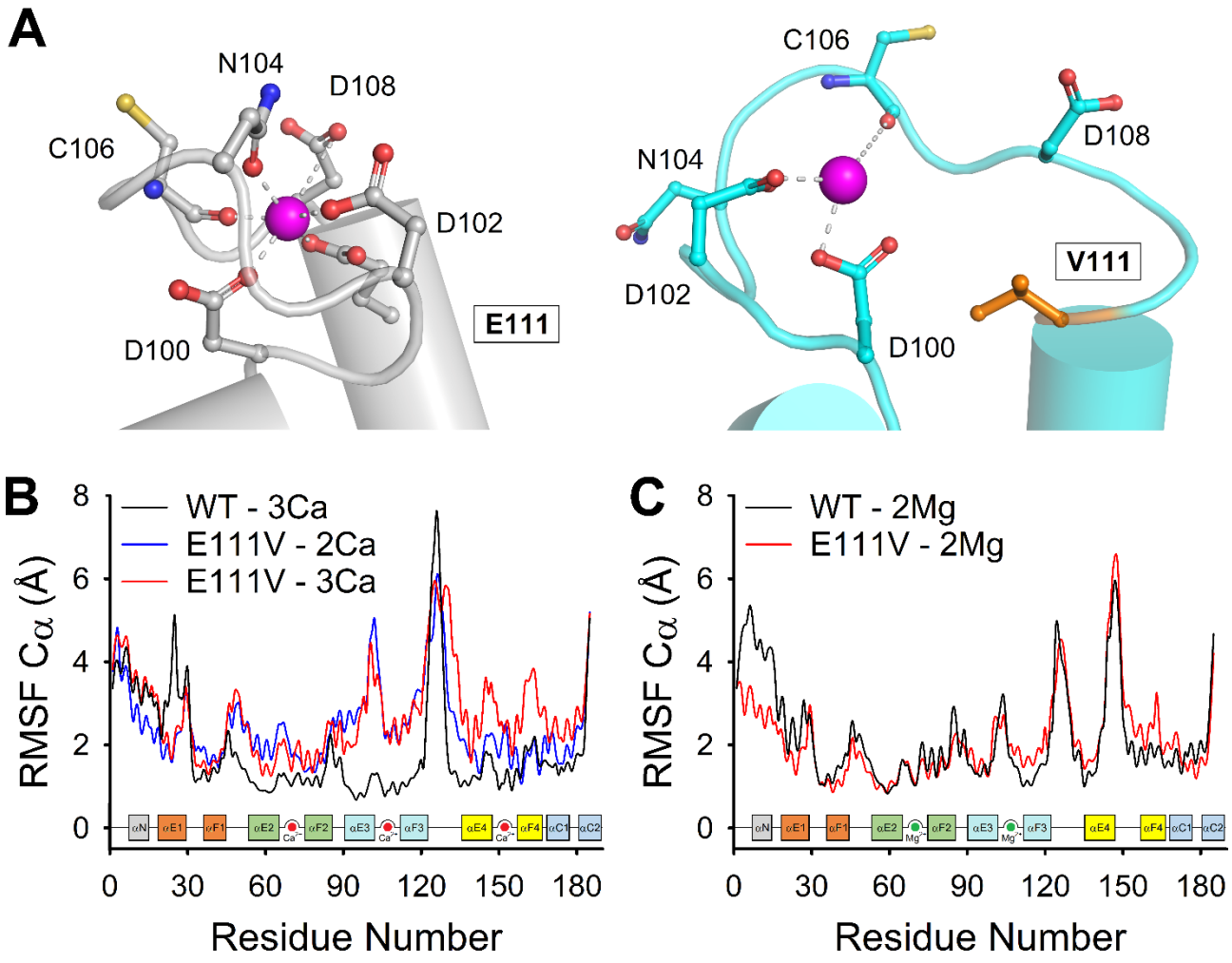

Figure 2. Results from exhaustive 4 μs MD simulations. (A) Representative Ca^{2+}-coordination in EF3 of WT-GCAP1 (left) and E111V-GCAP1 (right) after 1 μs MD simulations. WT-GCAP1 and E111V-GCAP1 structures are shown as grey and cyan cartoon, respectively; Ca^{2+}-coordinating residues are labelled and represented as sticks with C atoms in the same color as the structure, O atoms in red, N atoms in blue and S atoms in yellow; Ca^{2+} ions are shown as purple spheres; CORD-associated V111 is shown as orange sticks. (B) Cα-RMSF of WT-GCAP1 bound to 3 Ca^{2+} ions (black), E111V-GCAP1 with ions bound in EF2 and EF4 (blue), and E111V-GCAP1 bound to Ca^{2+} ions (red). (C) Cα-RMSF of WT-GCAP1 (black) and E111V-GCAP1 (red) with Mg^{2+} ions bound to EF2 and EF3. Insets show the secondary structure elements colored according to Figure 1A and the position of ion-binding loops.

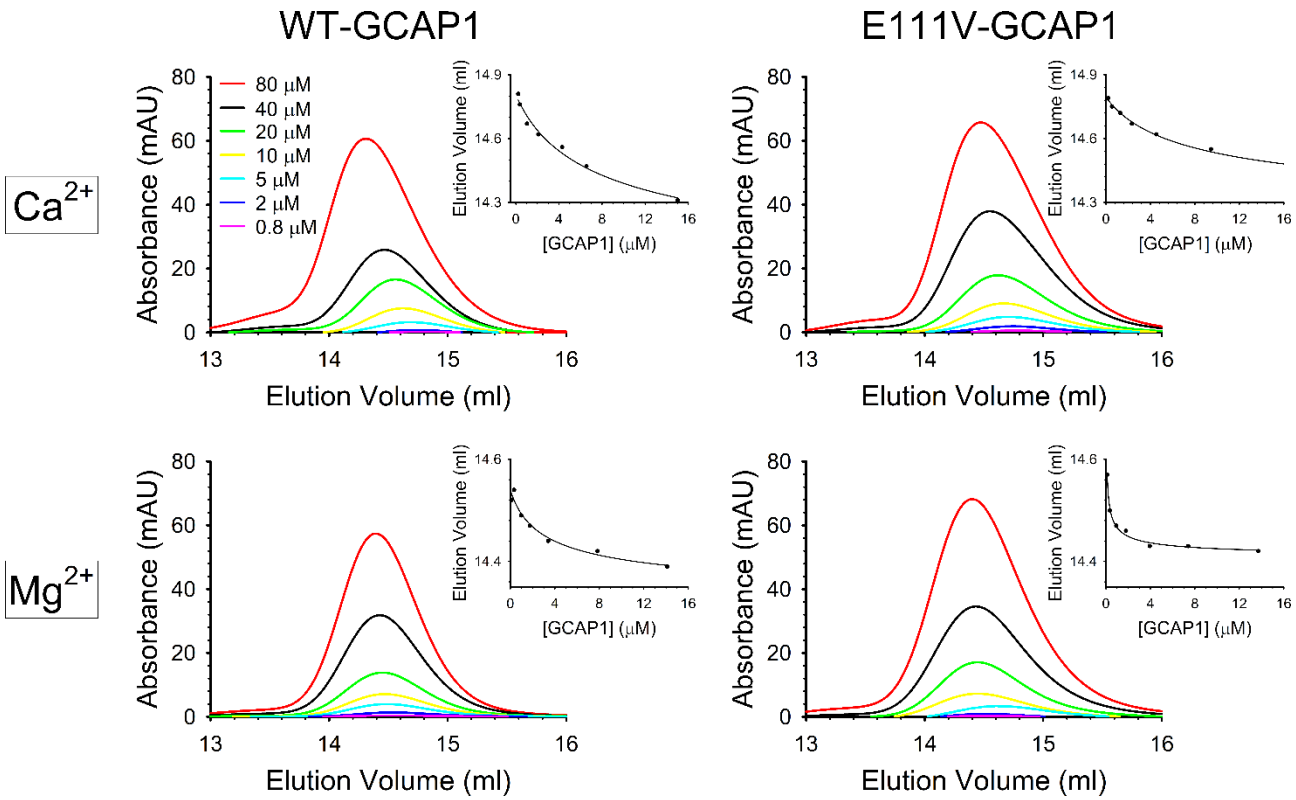

Figure 3. Representative analytical SEC chromatograms of 80 µM (red), 40 µM (black), 20 µM (green), 10 µM (yellow), 5 µM (cyan), 2 µM (blue), and 0.8 µM WT-GCAP1 (left panels) or E111V-GCAP1 (right panels) in the presence of 1 mM Mg^{2+} and 0.5 mM Ca^{2+} (upper panels) or 0.5 mM EGTA and 1 mM Mg^{2+} (lower panels). Insets show the elution volume as a function of the protein concentration estimated from the absorbance at the chromatographic peak together with the theoretical fitting curve (Equation 1) detailed in section 2.3. Three theoretical replicates were performed for each condition and independently fitted to Equation 1, the estimated equilibrium constants for the dimerization process are reported in **Table 1** as mean ± standard deviation.

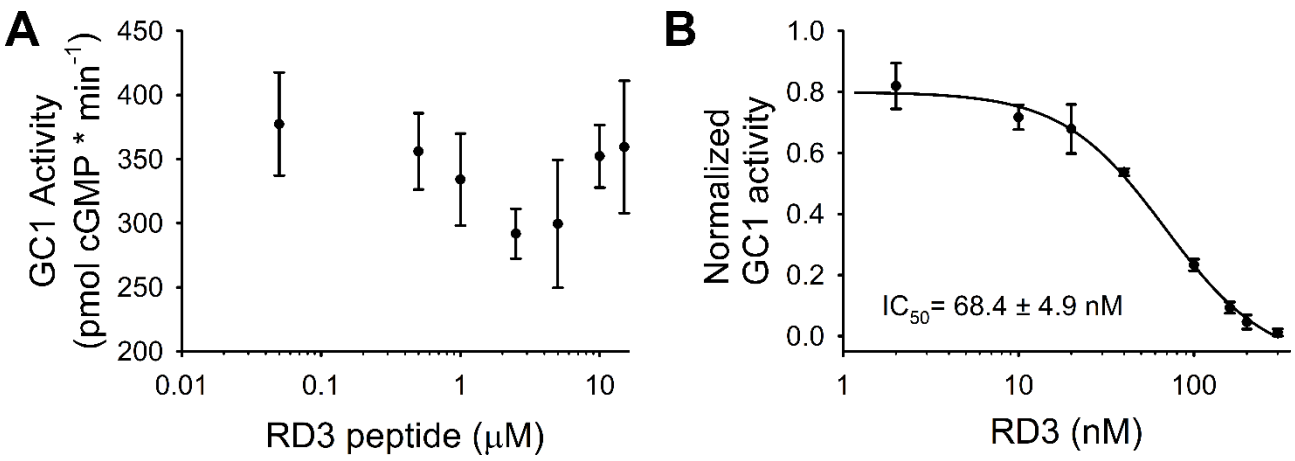

Figure 4. GC1 regulation by RD3 peptide and full-length RD3. (A) GC1 activity was measured in the presence of 5 μM WT-GCAP1 and increasing concentrations (0 - 15 μM) of RD3 peptide. (B) GC1 activity was measured in the presence of 5 μM WT-GCAP1, < 20 nM free Ca^{2+} and increasing concentrations (0-300 nM) of RD3. Data are reported as average ± standard deviation of three technical replicates. When possible, data were fitted to a 4-parameter Hill equation.

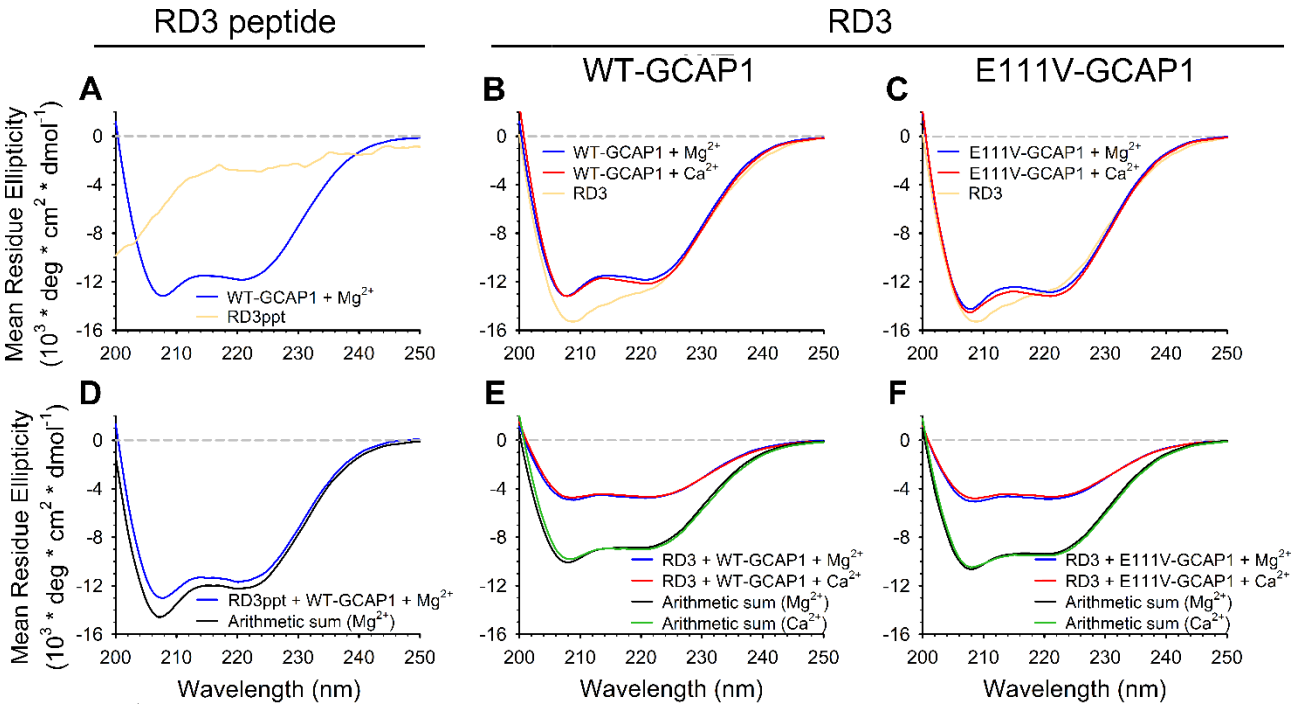

Figure 5. Effects of RD3 (peptide (RD3ppt) or full-length) interaction and ion binding on the secondary structure of GCAP1 variants. Far UV CD spectra of: (A) 10 μM WT-GCAP1 (blue) or RD3ppt (yellow) in the presence of 300 μM EGTA; (B) 10 μM RD3 (yellow) in the presence 300 μM EGTA, 10 μM WT-GCAP1 in the presence 300 μM EGTA (blue) and upon addition of 600 μM Ca^{2+} (300 μM free Ca^{2+}, red); (C) 10 μM RD3 (yellow) in the presence 300 μM EGTA, 10 μM E111V-GCAP1 in the presence 300 μM EGTA (blue) and upon addition of 600 μM Ca^{2+} (300 μM free Ca^{2+}, red); (D) 10 μM WT-GCAP1 and 10 μM RD3ppt in the presence 300 μM EGTA (blue), arithmetic sum of the spectra of the isolated molecules in the presence 300 μM EGTA (black); (E) 10 μM RD3 and 10 μM WT-GCAP1 in the presence 300 μM EGTA (blue) and upon addition of 600 μM Ca^{2+} (300 μM free Ca^{2+}, red), arithmetic sum of the spectra of the isolated molecules in the presence 300 μM EGTA (black) or 300 μM free Ca^{2+} (green); (F) 10 μM RD3 and 10 μM E111V-GCAP1 in the presence 300 μM EGTA (blue) and upon addition of 600 μM Ca^{2+} (300 μM free Ca^{2+}, red), arithmetic sum of the spectra of the isolated molecules in the presence 300 μM EGTA (black) or 300 μM free Ca^{2+} (green).

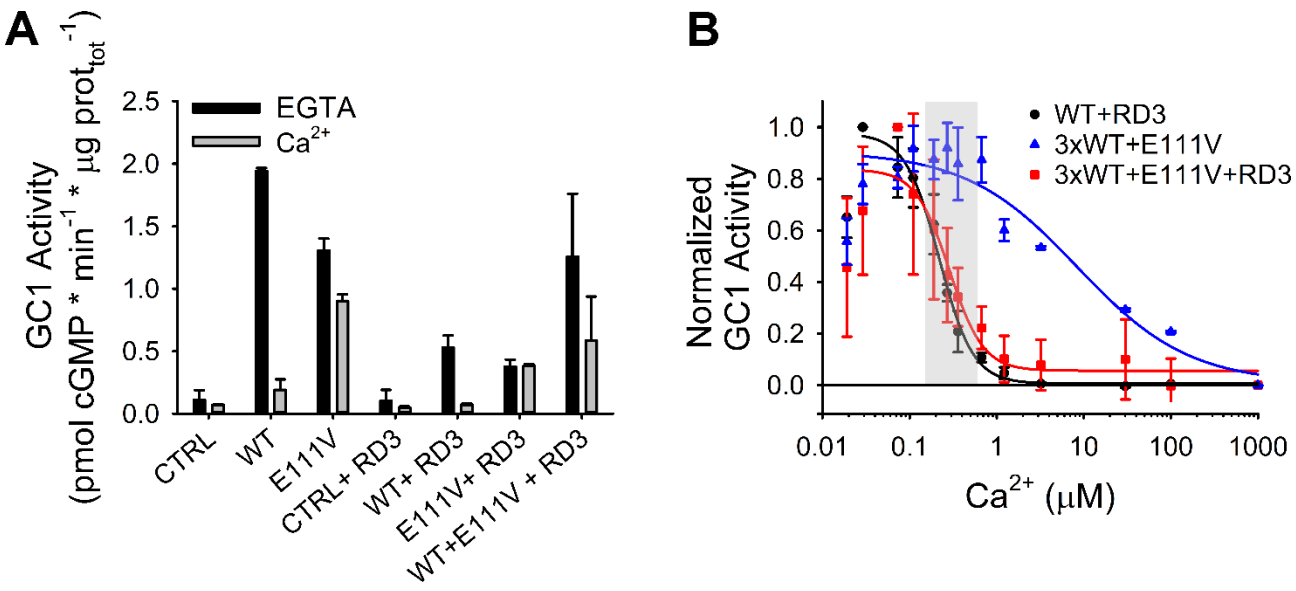

Figure 6. GC1 regulation by GCAP1 variants in the absence and in the presence of 200 nM RD3. (A) GC1 activity was measured in the presence of 5 µM WT-GCAP1 or E111V-GCAP1 or their combination at a stoichiometric ratio of 3 WT-GCAP1: 1 E111V-GCAP1 and <19 nM Ca^{2+} (black) or ~30 µM free Ca^{2+} (grey); membranes with no GCAP1 were used as control. (B) GC1 activity as a function of [Ca^{2+}] was measured in the presence of 5 µM WT-GCAP1 + 200 nM RD3 (black circles), 3.75 µM WT-GCAP1 + 1.25 µM E111V-GCAP1 (blue triangles), and 3.75 µM WT-GCAP1 + 1.25 µM E111V-GCAP1 + 200 nM RD3 (red squares). Normalized GC1 activity was fitted to a 4-parameter Hill sigmoid, the grey box indicates the physiological Ca^{2+} range in photoreceptors (150 - 600 nM). Data are presented as average ± standard deviation of three technical replicates.

Cellular and Molecular Life Sciences (2023) 80:371
https://doi.org/10.1007/s00018-023-05022-0

ORIGINAL ARTICLE

Recombinant protein delivery enables modulation of the phototransduction cascade in mouse retina

Sabrina Asteriti[1,2] · Valerio Marino[1] · Anna Avesani[1] · Amedeo Biasi[1] · Giuditta Dal Cortivo[1] · Lorenzo Cangiano[2] · Daniele Dell'Orco[1]

Received: 24 July 2023 / Revised: 10 October 2023 / Accepted: 27 October 2023 / Published online: 25 November 2023

Abstract

Inherited retinal dystrophies are often associated with mutations in the genes involved in the phototransduction cascade in photoreceptors, a paradigmatic signaling pathway mediated by G protein-coupled receptors. Photoreceptor viability is strictly dependent on the levels of the second messengers cGMP and Ca^{2+}. Here we explored the possibility of modulating the phototransduction cascade in mouse rods using direct or liposome-mediated administration of a recombinant protein crucial for regulating the interplay of the second messengers in photoreceptor outer segments. The effects of administration of the free and liposome-encapsulated human guanylate cyclase-activating protein 1 (GCAP1) were compared in biological systems of increasing complexity (in cyto, ex vivo, and in vivo). The analysis of protein biodistribution and the direct measurement of functional alteration in rod photoresponses show that the exogenous GCAP1 protein is fully incorporated into the mouse retina and photoreceptor outer segments. Furthermore, only in the presence of a point mutation associated with cone-rod dystrophy in humans p.(E111V), protein delivery induces a disease-like electrophysiological phenotype, consistent with constitutive activation of the retinal guanylate cyclase. Our study demonstrates that both direct and liposome-mediated protein delivery are powerful complementary tools for targeting signaling cascades in neuronal cells, which could be particularly important for the treatment of autosomal dominant genetic diseases.

Keywords Protein therapy · Protein delivery · Inherited retinal dystrophy · Liposome · Cone dystrophy · Cone-rod dystrophy

Introduction

The molecular processes underlying vision are triggered by the absorption of photons by opsins in retinal photoreceptors. Located in specific membranous compartments in the outer segments of rods and cones, opsins are G protein-coupled receptors (GPCRs) that activate the signaling cascade known as phototransduction. For many years, phototransduction has been considered paradigmatic for the largest class of GPCR-mediated signaling pathways (rhodopsin-like or class-A GPCRs), and the accumulated knowledge about the structural, biochemical, and physiological details of this cascade has enabled significant advances in

Sabrina Asteriti and Valerio Marino have contributed equally to this work.

✉ Lorenzo Cangiano
lorenzo.cangiano@unipi.it

✉ Daniele Dell'Orco
daniele.dellorco@univr.it

Sabrina Asteriti
sabrina.asteriti@univr.it

Valerio Marino
valerio.marino@univr.it

Anna Avesani
anna.avesani@univr.it

Amedeo Biasi
amedeo.biasi@univr.it

Giuditta Dal Cortivo
giuditta.dalcortivo@univr.it

[1] Department of Neurosciences, Biomedicine and Movement Sciences, Section of Biological Chemistry, University of Verona, 37134 Verona, Italy

[2] Department of Translational Research, University of Pisa, 56123 Pisa, Italy

drug design and pharmacological approaches for many other signaling pathways [1, 2].

The phototransduction cascade converts the light signal detected by the opsins into a chemical signal, culminating in the transient fall of vesicular glutamate release from the photoreceptor synaptic terminal, which is sensed by downstream neurons [3]. Rods and cones adapt to dramatic changes in ambient light by modifying the kinetics of phototransduction, a finely regulated process orchestrated by the second messengers Ca^{2+} and cyclic guanosine monophosphate (cGMP). Absorption of light by rhodopsin (or cone opsins) triggers the hydrolysis of cGMP by activating the phosphodiesterase 6, thereby causing the dissociation of cGMP from cyclic nucleotide-gated channels (CNG) and their closure. The ensuing decrease in the inflow of Na^+ and Ca^{2+} hyperpolarizes the cell which, in turn, causes a reduction in neurotransmitter release. In parallel to these events, the light-independent extrusion of Ca^{2+} from the Na^+/Ca^{2+}, K^+-exchanger leads to a drop of Ca^{2+} concentration in the outer segments (from ~ 600 nM in the dark to below 100 nM in bright light [4]).

These light-evoked alterations of second messenger levels in the photoreceptor outer segment trigger feedback mechanisms necessary for the timely shutoff of the cascade, as well as for the adaptation to specific light or dark conditions [3, 5]. Subtle changes in Ca^{2+} concentration are promptly detected by guanylate cyclase-activating proteins (GCAPs), members of the neuronal calcium sensors family [6]. Two isoforms (GCAP1 and GCAP2) are expressed in rods and cones, but in human only GCAP1 seems to be actively involved in the phototransduction cascade as a modulator of retinal guanylate cyclase (GC) activity, with the most prominent contribution arising from the GC1 isozyme [7]. In human photoreceptors GCAP2 is probably involved in biochemical processes other than phototransduction [8], although its role in mouse phototransduction has been demonstrated [9].

GCAP1, the main regulator of GC1, is a 23 kDa protein belonging to the EF-hand superfamily [10] that ensures rapid detection of Ca^{2+} oscillations in the submicromolar range with a nanomolar affinity for Ca^{2+} [11]. When Ca^{2+} concentration drops because of phototransduction activation, Ca^{2+} is replaced by Mg^{2+}, which can bind in the same metal binding loops of motifs EF2, EF3 and EF4 (Fig. 1a) [12–14]. This mechanism allows GCAP1 to switch between different signaling states, namely Ca^{2+}-bound (GC1-inhibitor) and Mg^{2+}-bound (GC1-activator), regulated by specific allosteric mechanisms involving the protein, the metal cations and the myristoyl group bound at its N-terminal [13, 15]. The conformation adopted by Mg^{2+}-GCAP1 stimulates the synthesis of cGMP by GC1, thus permitting rapid restoration of dark-adapted cell conditions by reopening of the CNG channels [12, 16]. The Ca^{2+}–Mg^{2+} exchange results in relatively minor conformational changes for GCAP1 [13, 15] (Fig. 1a), which are nevertheless sufficient to trigger the GC1 inhibitor-to-activator transition over the narrow physiological range of Ca^{2+} variation in the photoreceptor outer segment.

GCAP1 has been associated with autosomal dominant cone (COD) or cone-rod dystrophies (CORD) [17–31], a class of severe inherited retinal dystrophies (IRD) characterized by central vision loss, impaired color vision, and photophobia, due to photoreceptor degeneration [32]. Indeed, more than twenty point-mutations in the gene encoding for GCAP1 (*GUCA1A*) have been found to be linked to COD or CORD. Recently, some of us identified a missense mutation in *GUCA1A* responsible for a particularly severe form of CORD. At the protein level, the mutation substitutes a glutamate residue in position 111 with a valine [24]. E111 is the twelfth residue of the Ca^{2+}-binding loop of the EF3 motif and it is directly responsible for Ca^{2+}-coordination by providing two negatively charged oxygen atoms from the carboxyl group (Fig. 1b); this bidentate ligation is fundamental to ensure the correct pentagonal bipyramidal geometry required for coordination of Ca^{2+}-ions by seven oxygen atoms. The hydrophobic sidechain of V111, on the other hand, leads to a structural distortion of the EF3 loop, which becomes unable to coordinate Ca^{2+}-ions (Fig. 1b), thus resulting in an 80-fold lower apparent affinity for Ca^{2+} [24].

COD and CORD remain incurable diseases, and the nature of their transmission — often dominant — makes gene therapy-based approaches particularly challenging. Alternative approaches, for example based on protein delivery, are therefore needed to mitigate the effects of the mutations and re-establish the physiological functionality of the signaling cascade. In this work, we explored the possibility of using direct or liposome-mediated administration of recombinant human GCAP1 to modulate the phototransduction cascade in mouse rods. Our rationale in comparing these two approaches was that free protein could offer high intraocular mobility and acute action, while liposomes delayed but prolonged release. We initially used a model eukaryotic cell culture for protein delivery experiments, and then increased the complexity with in vivo and ex vivo experiments aimed at assessing the biodistribution of proteins in mouse retinas. Imaging experiments were complemented by functional ones, in which acute changes in flash responses were monitored while incubating the retinas ex vivo. The administration of the free and liposome-encapsulated protein was compared in each case. Our findings reveal that direct and liposome-mediated protein delivery are powerful complementary tools for targeting signaling cascades in retinal neurons and could be particularly important for the treatment of autosomal dominant genetic diseases.

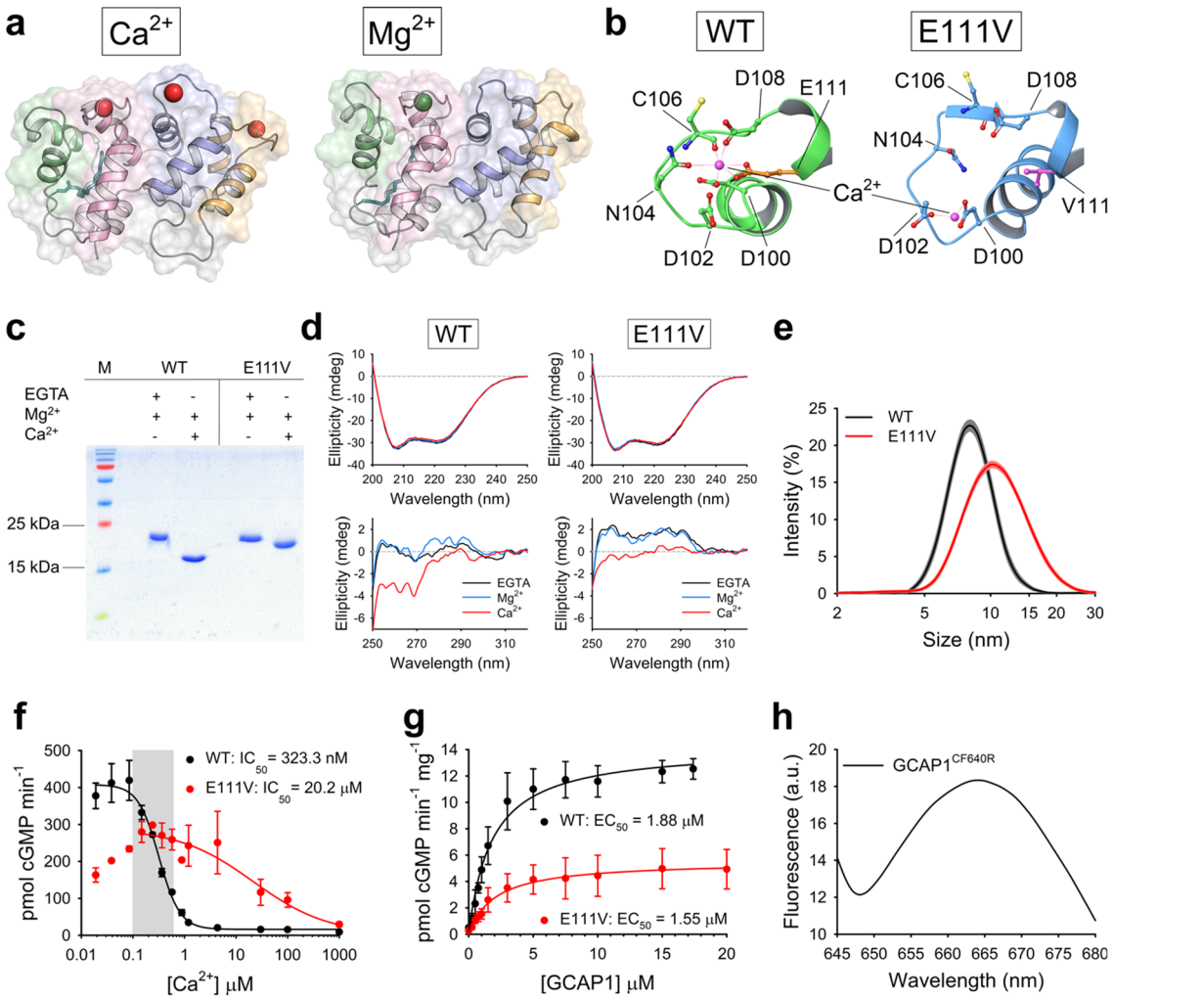

Fig. 1 Biochemical and biophysical characterization of GCAP1 variants. **a** Three-dimensional structure of E111V-GCAP1 in its Ca^{2+}-loaded (left) and Mg^{2+}-bound (right) state after 200 ns Molecular Dynamics (MD) simulations (trajectories are from Ref [24]). Protein structure is represented as cartoons with EF1, EF2, EF3 and EF4 colored in green, pink, blue and orange, respectively; the myristoyl moiety is shown as teal sticks, Ca^{2+} and Mg^{2+} ions are depicted as red and green spheres, respectively. **b** Detail of the Ca^{2+}-binding loop of EF3 in WT-GCAP1 (left) and E111V-GCAP1 (right) after 200 ns MD simulations. Protein structure is shown as cartoons colored in green for WT-GCAP1 and blue for E111V-GCAP1; the sidechains of Ca^{2+}-coordinating residues are labelled and are represented as sticks with O atoms in red, N atoms in blue, S atoms in yellow and C atoms in the same color as cartoons; the C atoms of E111 and V111 residues are colored in orange and magenta, respectively. Ca^{2+}-ions are represented as pink spheres and labelled, zero-order bonds with Ca^{2+}-coordinating residues are shown as dashed red lines; the seventh O atom required for Ca^{2+}-coordination is provided by a water molecule (not shown). **c** 15% SDS-PAGE of ~ 30 µM WT-GCAP1 and E111V-GCAP1 in the presence of 1 mM EGTA + 1.1 mM Mg^{2+} and 1 mM Mg^{2+} + 1 mM Ca^{2+}. **d** Representative far UV (upper panels) and near UV (lower panels) CD spectra of WT-GCAP1 (left panels) and E111V-GCAP1 (right panels) recorded at 25 °C in PBS pH 7.4. Protein concentration for far and near UV was 10 and 33 µM, respectively. Far UV CD spectra were registered in the presence of 300 µM EGTA (black) and after serial additions of 1 mM Mg^{2+} (blue) and 600 µM Ca^{2+} (red), thus resulting in 300 µM free Ca^{2+}. Near UV CD spectra were registered in the presence of 500 µM EGTA and after serial additions of 1 mM Mg^{2+} and 1 mM Ca^{2+} (500 µM free). **e** Hydrodynamic diameter estimation by Dynamic Light Scattering of ~ 40 µM WT-GCAP1 (black) and E111V-GCAP1 (red) at 25 °C in the presence of 1 mM Ca^{2+}; standard errors are shown in grey and orange, respectively. **f** GC1 enzymatic activity as a function of Ca^{2+} concentration (< 19 nM to 1 mM) upon regulation by 5 µM WT-GCAP1 (black) or E111V-GCAP1 (red); cGMP synthesis was half maximal (IC_{50}) at (323.3 ± 15.1) nM and (20.2 ± 7.6) µM with Hill coefficients of 2.16 and 0.99, respectively. The Ca^{2+}-concentration range in photoreceptor cells is represented by the grey box. Data are presented as average ± standard deviation of 3 technical replicates. **g** GC1 activity as a function of WT-GCAP1 (black) and E111V-GCAP1 (red) concentration (0–20 µM range); cGMP synthesis was half maximal (EC_{50}) at (1.88 ± 0.15) µM and (1.55 ± 0.24) µM, respectively. Data are presented as average ± standard deviation of 3 technical replicates after normalization on the amount of GC1 present in cell pellets. **h** Fluorescence emission spectrum of 5 µM $GCAP1^{CF640R}$ upon excitation at 639 nm

Results

Perturbed Ca^{2+}-sensing properties of E111V-GCAP1 lead to constitutive activation of GC1

The purity and functionality of recombinantly expressed GCAP1 variants were verified by a combination of biophysical and biochemical techniques, to exclude potential effects of protein delivery treatments due to impurities or structural/functional defects. Ca^{2+}-sensor proteins, including GCAP1, are known to modify their electrophoretic mobility in SDS-PAGE experiments under denaturing conditions [11], depending on their Ca^{2+}-loading state. Indeed, Ca^{2+}-free proteins appear as single bands at their theoretical molecular weight, whereas their Ca^{2+}-bound forms exhibit an electrophoretic shift to smaller apparent molecular weight proportional to their apparent Ca^{2+}-affinity. Such peculiar behavior exhibited by many other Ca^{2+}-sensor proteins can be attributed to the fact that Ca^{2+}-ions significantly stabilize the structure of the protein and are retained even under denaturing conditions, resulting in a protein that is not fully unfolded, even in the presence of sodium dodecyl sulfate. This makes electrophoretic migration dependent on factors other than just the mass of the protein in the Ca^{2+}-bound form, such as Ca^{2+}-affinity, because the higher the affinity, the greater the probability of partial structure retention. We exploited this peculiar feature to assess both the purity of protein samples and the capability of wild type (WT)-GCAP1 and E111V-GCAP1 to function as Ca^{2+}-sensors (Fig. 1c). In the absence of Ca^{2+}, both purified GCAP1 variants showed a single band around their theoretical molecular weight (23 kDa), which shifted to ~ 17 kDa in the case of WT-GCAP1 and to ~ 20 kDa in the case of E111V-GCAP1 upon Ca^{2+}-binding, thus implying a substantial reduction in Ca^{2+}-affinity for the pathological variant, confirming previous results from some of us [24].

The structural response of GCAP1 variants to ion binding was monitored by circular dichroism (CD) spectroscopy, which allows monitoring changes in protein secondary and tertiary structure in solution at protein concentrations (~ 10 to 40 μM) that mimic physiological ones (~ 3 to 4 μM, Fig. 1d). Both variants exhibited a far ultraviolet (UV) (200–250 nm) CD spectrum compatible with an all α-helix protein, with minima at 208 and 222 nm (Fig. 1d, top panels) and negligible variations in shape and intensity upon ion binding. This behavior was partly in contrast to that previously shown [24], most likely attributable to the different buffer and temperature (PBS pH 7.4 and 25 °C vs 20 mM Tris, 150 KCl, 1 mM DTT, pH 7.5 and 37 °C). Concerning the tertiary structure (near UV CD spectrum, 250–320 nm), both variants displayed a significant rearrangement of aromatic residues upon Ca^{2+}-binding in PBS pH 7.4 at 25 °C (Fig. 1d, bottom panels), indicative of a change in protein tertiary structure. Mg^{2+}-binding instead resulted in a minor conformational change, which was more pronounced in the case of WT-GCAP1. These results were substantially in line with the spectra recorded by some of us at 37 °C, with minor differences attributable to the different buffer and temperature [24], which was found to affect also the hydrodynamic diameter of GCAP1 variants (Fig. 1e). As assessed by dynamic light scattering (DLS), both WT-GCAP1 and E111V-GCAP1 in PBS, pH 7.4 displayed a significantly larger hydrodynamic diameter ((8.68 ± 1.07) nm and (11.08 ± 0.07) nm, respectively), compared to their counterparts in 20 mM Tris, 150 mM KCl, 1 mM DTT, pH 7.5 buffer ((6.47 ± 0.03) nm and (6.08 ± 0.04) nm, respectively) [24], a difference ascribable to the absence of the reducing agent and of a centrifugation step in this study, which nevertheless did not trigger any aggregation process (results not shown). The slightly different experimental conditions of the present and the previous study [24] lead to the same conclusions that the E111V substitution significantly impairs the Ca^{2+}-sensitivity of GCAP1 with minor structural repercussions.

The enzymatic activity of the GCAP1-GC1 complex and its Ca^{2+}-dependence creates a tight interconnection between Ca^{2+} and cGMP levels, which is crucial for both light adaptation and photoreceptor viability. Regulation of the GC1 enzymatic activity by GCAP1 variants was assessed both in terms of Ca^{2+} sensitivity and dependence on the level of protein regulator by measuring, respectively, the Ca^{2+} concentration at which GC1 activation is half-maximal (IC_{50}) and the concentration of GCAP1 at which the synthesis of cGMP is half-maximal (EC_{50}). The activation profile of GC1 by WT-GCAP1 exhibited an IC_{50} of (323.3 ± 15.1) nM (Fig. 1f), thus falling in the physiological intracellular Ca^{2+}-range (< 100 to 600 nM) [5]. On the other hand, the pathological variant E111V significantly dysregulated the activity of GC1, with an IC_{50} value ((20.2 ± 7.6) μM, p-value < 0.05) ~ 63-fold higher than that of the WT, indicative of constitutive cGMP synthesis under physiological Ca^{2+} levels. Nevertheless, both variants displayed comparable EC_{50} values ((1.88 ± 0.14) μM for WT-GCAP1 and (1.55 ± 0.23) μM for E111V-GCAP1 (p-value > 0.1), Fig. 1g), suggesting a similar affinity for the target enzyme, in line with previous results from some of us [24].

Liposome-mediated GCAP1 delivery to HEK293 cells

To assess the potential of liposome (LP)-mediated delivery of GCAP1 in biological systems of increasing complexity (in cyto, ex vivo, and in vivo) and investigate its biodistribution by minimizing the contribution of tissue auto-fluorescence

(see Methods), the far-red fluorescent dye CF640R was conjugated to the primary amines of solvent-exposed Lys residues of GCAP1 (namely, either of K8, K23, K24, K46, K87, K97, K142 or K162, Movie S1) to obtain the GCAP1^{CF640R} complex. SDS-PAGE confirmed the purity of protein samples and the success of the conjugation reaction (Fig. S1a). The effective removal of the unconjugated dye (Fig. S1b) and the number of CF640R molecules bound to each GCAP1 protein were then assessed by absorption spectroscopy (degree of labelling = 1.96, see Methods). Finally, the emission fluorescence spectrum of GCAP1^{CF640R} (Fig. 1h) upon excitation at 639 nm was recorded before imaging experiments to verify the compatibility of the conjugated dye with our optical setups. The unconjugated dye (CF640R), GCAP1^{CF640R}, WT-GCAP1 and E111V-GCAP1 were then encapsulated in LPs with a lipid composition corresponding to that of rod outer segment membranes (see Methods for details).

The suitability of LP as carriers of small molecules and proteins was assessed by evaluating the size and monodispersion of the liposome suspensions loaded with different molecules. Regardless of the type of encapsulated molecule, nanoparticle tracking analysis (NTA) measured a LP diameter between (149.1 ± 3.0) nm and (168.7 ± 0.7) nm (Fig. S2a–c, Table S1), with minor differences in both size and concentration (Table S1) up to 180 days (Fig. S2d–f), suggesting that the LP suspension is stable over time. Finally, effective encapsulation of fluorescent molecules was also visually confirmed by the display of point-like fluorescence emission when LPs were filled with unconjugated CF640R and immobilized in agarose gel (Fig. S2g).

The capability of LPs to deliver recombinant GCAP1^{CF640R} was assessed on two different HEK293 stable cell lines. The first was transfected with pIRES plasmid encoding for eGFP and GC1 under the same promoter, characterized by a cytosolic green fluorescence (from now on cGFP); the second was transfected with pcDNA3.1 encoding for the eGFP-GC1 fusion protein, thus showing membrane green fluorescence (mGFP).

To address the potential direct membrane uptake of free-CF640R due to its small size (~832 Da) we monitored the cGFP cell line for 6 h (Movie S2) and visualized the mGFP cell line for 6 h and 24 h after incubation with free-CF640R (Fig. 2a). The absence of intracellular red fluorescence in both cell lines after 6 h and 24 h suggested that free-CF640R is per se unable to penetrate cell membranes.

Indeed, a diffused red fluorescence signal was observed only in the extracellular milieu, in the same time frames (Fig. 2a). This signal is likely attributable to the presence

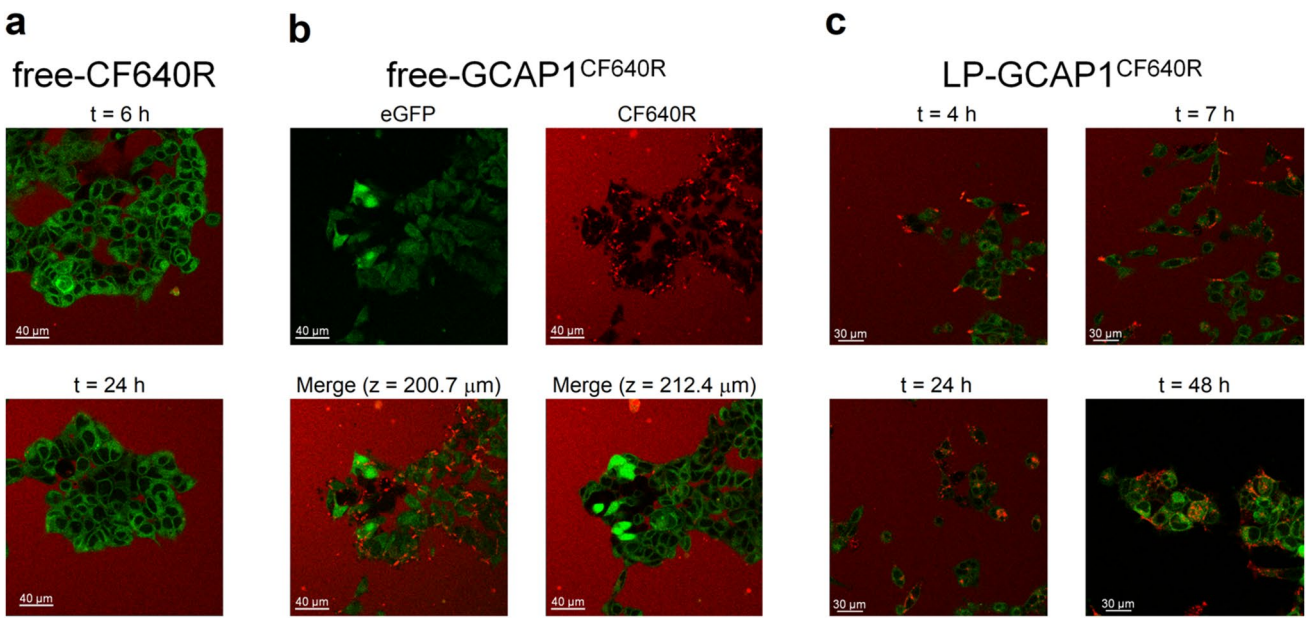

Fig. 2 Live imaging of HEK293 cells incubated with free-CF640R, free-GCAP1^{CF640R} and GCAP1-encapsulating liposomes. **a** representative images at a fixed z-plane of the mGFP cell line incubated with 100 µl of 140 µM free-CF640R after 6 h (top) and 24 h (bottom); **b** representative images of the mGFP cell line after 24 h incubation with 100 µl of 104 µM free-GCAP1^{CF640R}, top panels show eGFP (left) and CF640R (right) fluorescence, bottom panels show the merged fluorescence at z = 200.7 µm (left) and z = 212.4 µm (right). **c** Live-cell imaging at the same z-plane of the mGFP cell line after 4 h, 7 h, 24 h, and 48 h incubation with 100 µl of 4.3 nM LP-GCAP-1^{CF640R} (containing the same number of GCAP1^{CF640R} molecules in the aqueous core as compared to the free protein solution case). After 24 h the cell medium was replaced with FluoroBrite DMEM to avoid interference from phenol red, which gave rise to the red background fluorescence present in all but bottom right panel

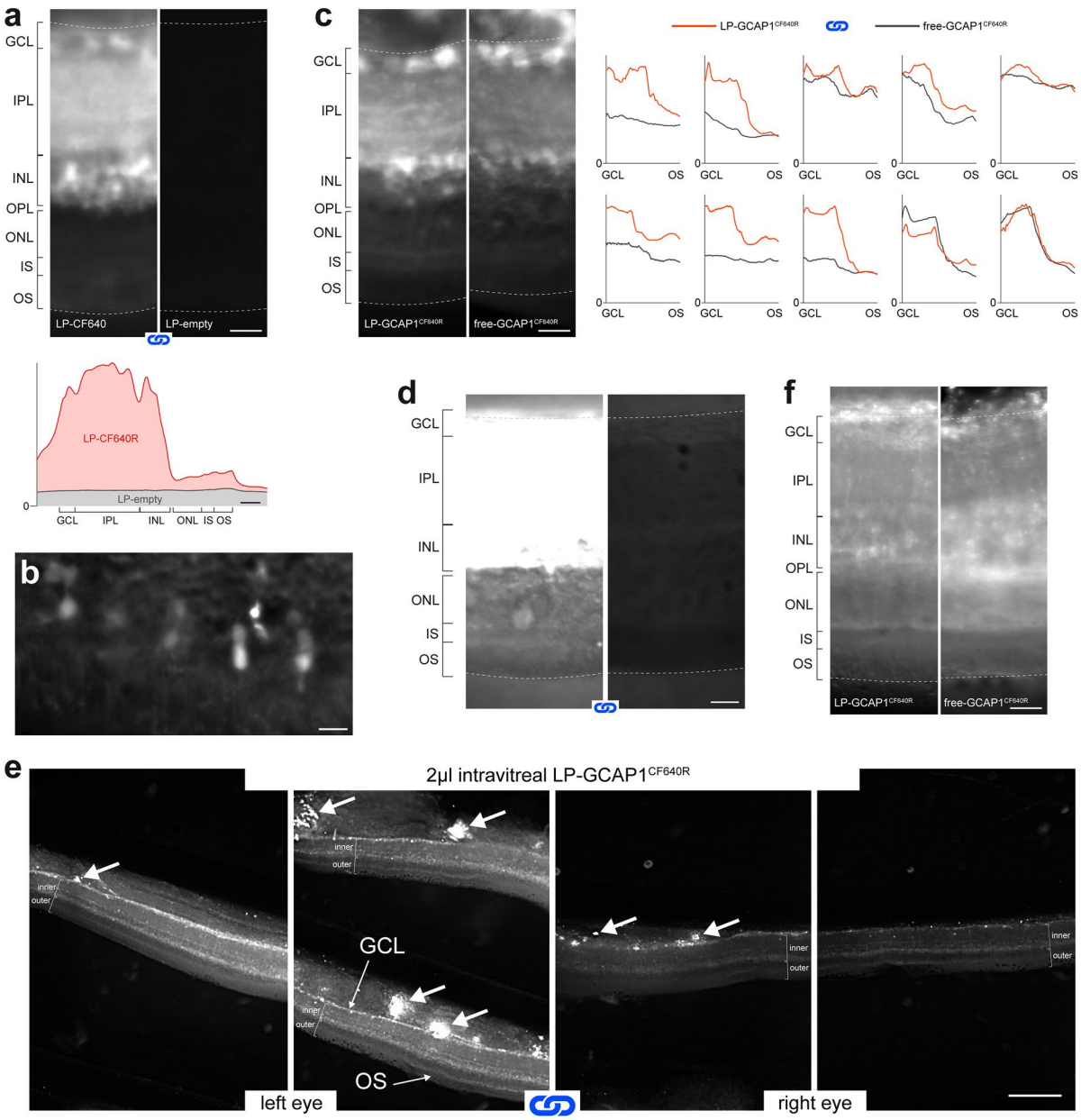

Fig. 3 Biodistribution of free GCAP1 and liposome-encapsulated GCAP1 in living mouse retinas following ex vivo incubation and in vivo intravitreal injections. **a** Distribution of fluorescence in 250 µm thick live slices obtained from a pair of retinas incubated ex vivo with 20 µl of 3.9 nM LP-CF640R and 5.1 nM LP-empty, respectively: the same image acquisition and display parameters were used (blue chain links symbol). Plot shows the average fluorescence along the vertical axis of the same images. Scale bars 25 µm. **b** Fluorescent cones in a slice from a retina incubated with 20 µl of 3.9 nM LP-CF640R. Scale bar 10 µm. **c** Distribution of fluorescence after ex vivo incubation with 20 µl of 88.4 µM free-GCAP-1^{CF640R} and 4.3 nM LP-GCAP1^{CF640R} (containing the same number of GCAP1^{CF640R} molecules in the aqueous core as compared to the free protein solution case). In the example images the focal plane was intentionally set to display zones rich with stained neuronal somata. Scale bar 25 µm. Plots show radial fluorescence profiles across retina pairs in each experiment; blue chain links: the same acquisition parameters were used in each retina pair. **d** Distribution of fluorescence after ex vivo incubation with 88.4 µM free-GCAP1^{CF640R} and PBS. The white point of the images was adjusted to enhance the outer retina: same acquisition and display parameters. **e** Low magnification examples of retinal slices from the eyes of a mouse, both intravitreally injected with identical aliquots of 4.3 nM LP-GCAP-1^{CF640R}: the same acquisition and display parameters were used (blue chain links). Thick white arrows: zones of accumulation of fluorescence in the vitreous humor near the inner limiting membrane. Inner: GCL + IPL + INL; outer: ONL + IS + OS. Scale bar 250 µm. **f** Examples of the distribution of fluorescence in retina slices after intravitreal injection with 2 µl of 88.4 µM free-GCAP1^{CF640R} and 4.3 nM LP-GCAP1^{CF640R} (containing the same number of GCAP1^{CF640R} molecules in the aqueous core as compared to the free protein solution case). Scale bar 25 µm. In all images of this figure the focal plane lies deep in the slice. In all experiments retinal layer boundaries were identified as shown in Fig. S9

of phenol red in the medium, as in real time imaging no medium replacement was performed.

Similar experiments performed with fluorescently labelled GCAP1 (GCAP1^{CF640R}), showed punctuated fluorescence spots which tended to accumulate on the surface of mGFP cells after 6 h (Movie S3; punctuated red fluorescence is attributable to the interaction of GCAP1^{CF640R} with other molecules in the cell medium or with cell membrane, at odds with the diffused phenol red fluorescence). The intracellular space was not reached by the labelled protein even after 24 h (Fig. 2b, top panels). Further analysis at specific z-plane values (bottom panels in Fig. 2b) clearly confirmed that the accumulation of fluorescence attributed to GCAP1^{CF640R} is limited to the cell membrane, as no signal was detected at the intracellular space. To confirm this finding, we repeated the same experiment with cGFP cells, which would allow the detection of overlapped green and red fluorescence signals in case of GCAP1^{CF640R} entering the intracellular milieu. Indeed, this was not observed in 6 h (Movie S4). To dampen the contribution of diffused red fluorescence from the extracellular milieu, we replaced the cell medium with FluoroBrite DMEM, which does not contain phenol. The same results were confirmed (Fig. S3), indicating that GCAP1^{CF640R} did not enter HEK293 cells in the observed timeframe.

As both cGFP and mGFP cell lines exhibited the same impermeability to free-CF640R and free-GCAP1^{CF640R}, the capability of liposomes to deliver GCAP1^{CF640R} was tested only on the mGFP cell line. Live-cell imaging showed that 4 h after incubation (Fig. 2c, Movie S5), a punctuated red fluorescence, compatible with that emitted by LP-GCAP-1^{CF640R}, was accumulating on the cell surface. At t = 7 h, the same punctuated red fluorescence was distinctly detected in the cytosol, suggesting whole liposome internalization by the cells. Only after 24 h the fluorescence pattern started to change. A more diffused red signal initially appeared at around 24 h, indicative of the release of GCAP1^{CF640R} from LPs. The observation of red and green colocalized fluorescence was more apparent at t = 48 h, indicative of a more unhindered diffusion of GCAP1^{CF640R} in the cytosol (Fig. 2c and Fig. S4), although the persistence of the punctuated pattern suggests the residual presence of internalized liposomes. Finally, 48 h after incubation with LP-GCAP1^{CF640R} the cell medium was replaced with FluoroBrite DMEM to improve the signal-to-noise ratio; while a more diffused colocalization of red and green fluorescence attributed to the intracellular release of GCAP1^{CF640R} was more clearly observed (Fig. S4d), residual quantal fluorescence was present.

Retinal distribution in live tissue of GCAP1^{CF640R} and LP-GCAP1^{CF640R} following ex vivo incubation and intravitreal injection

Ex vivo incubations

To move to a higher level of biological complexity, we first assessed LP-mediated delivery of molecules by ex vivo incubation of isolated retinas. The rationale here was to eliminate variability related to in vivo transport across tissues, focusing solely on intraretinal mechanisms. Far red fluorescence was chosen because in preliminary tests we found that the extremely low tissue autofluorescence in this band greatly improved signal-to-noise ratio. Retina pairs (n = 3) were incubated in parallel with LP-CF640R and LP-empty suspensions for 2 h at 37 °C. After incubation, these live retinas were rinsed with fresh medium and immediately viewed with a widefield fluorescent microscope either as wholemounts or 250 µm thick slices, with the two treatment partners placed adjacent in the dish. In all cases the LP-CF640R-treated retina showed fluorescence much above the control one. Unexpectedly, fluorescence was unevenly distributed across the thickness of the retina, being much stronger in the inner layers (Fig. 3a). Nonetheless, even the outer retina showed a significant signal. Control slices had a flat autofluorescence profile, at the level of the chamber background. Interestingly, in the LP-CF640R-treated retinas sparse cell bodies in the ganglion cell (GCL) and inner nuclear layer (INL) could be clearly distinguished. In the outer retina cones were also occasionally stained (Fig. 3b), albeit much more rarely than the aforementioned neurons. These data suggest enrichment of LPs in the inner retina, although it remained unclear whether they were internalized as intact nanovesicles or their fluorescent cargo released in the cell.

To determine whether LP encapsulation affects the tissue access of large molecules, we incubated retina pairs (n = 10) with free-GCAP1^{CF640R} protein solution or LP-GCAP1^{CF640R} suspension for 3.5 h at 37 °C, followed by slicing and imaging with identical parameters. The average fluorescence of the inner retina (GCL + IPL + INL) and photoreceptors (ONL + IS + OS) was measured to quantitatively assess tissue distribution. As we had observed qualitatively for LP-CF640R, fluorescence in the inner retina was 168% (SD 50%) of that in photoreceptors following incubation with LP-GCAP1^{CF640R} ($p < 0.01$, n = 10; paired Wilcoxon test) and 160% (SD 55%) of photoreceptors with free-GCAP1^{CF640R} ($p < 0.001$, n = 12) (Fig. 3c). Furthermore, treatment with LP-encapsulated protein led to significantly higher fluorescence compared to free protein in both the inner retina (150% of free protein, SD 52%; p-value < 0.05, n = 10) and photoreceptors (127% of free protein, SD 21%; p-value < 0.01, n = 10) (Fig. 3c). In

the GCL and INL distinctly stained neuronal somata were observed after both types of incubations (Fig. 3c, images). It must be noted that, even in the photoreceptor layer, signal from retinas incubated with the free protein was well above the level of tissue autofluorescence. This was confirmed by comparing incubation with free protein and PBS for 3.5 h at 37 °C (n = 2; 152% and 162%) (Fig. 3d). Interestingly, the peculiar distribution of both free and LP-encapsulated GCAP1^{CF640R} was also observed in retinas incubated with free CF640R fluorophore (Fig. S5a). We ruled out a significant contribution of the unbound fluorophore to the distribution observed with free-GCAP1^{CF640R}, as its concentration in our samples was estimated to be < 1% of the labelled protein (see Methods). Furthermore, during the preparation of LP-GCAP1^{CF640R} (encapsulation and subsequent washing) any residual unbound fluorophore would have fallen to even lower levels. Thus, had such traces of unconjugated fluorophore played a significant role in our experiments, we would have obtained results opposite to those shown in Fig. 3c (i.e. a higher signal in free-GCAP1^{CF640R}-incubated retinas).

Intravitreal injections

We went on to examine retinal delivery in vivo by injecting intravitreally free-GCAP1^{CF640R} solution and LP-GCAP-1^{CF640R} suspension in the two eyes. After 20–24 h in darkness the animals were sacrificed, their retinas isolated, sliced 250 µm thick and viewed as live tissue with a widefield fluorescence microscope. Both retinas were imaged in the same session using identical acquisition parameters. We found that most injections led to some degree of retinal fluorescence (LP-GCAP1^{CF640R}: n = 9 out of 12; free-GCAP1^{CF640R}: n = 6 out of 11). Notably, while fluorescence was similar in different slices from the same retina, it varied greatly from eye to eye despite our utmost care in performing reproducible injections. This intrinsic variability was confirmed in a subset of animals in which both eyes were injected with identical solutions (n = 3 pairs; Fig. 3e). Importantly, it hindered our ability to detect any significant differences in the delivery of LP-GCAP1^{CF640R} and free-GCAP1^{CF640R} to the retina (n = 9 pairs). It is worth noting that residues of vitreous humor still adhering to the inner limiting membrane were often strongly fluorescent (Fig. 3e thick white arrows). Similarly to ex vivo incubated retinas, average fluorescence was quantified in the inner retina and photoreceptors. In those retinas displaying fluorescence after intravitreal injection, the inner layers were significantly brighter than the photoreceptors, both in the case of LP-GCAP1^{CF640R} (120% of photoreceptors, SD 22%; p-value < 0.05, n = 8) and free-GCAP1^{CF640R} (121% of photoreceptors, SD 19%; p-value < 0.05, n = 6) (Fig. 3f). This mimicked what was observed in ex vivo incubations. However, following intravitreal injections individual cell bodies did not stand out (Fig. 3f): perhaps in these experiments there was sufficient time for uniform uptake by all neurons. Diffuse retinal fluorescence could be similarly observed after intravitreal injection of free CF640R fluorophore (Fig. S5b). In summary, we found that intravitreal injections are a viable, albeit rather inconsistent, means of delivery of free or encapsulated proteins to the retina.

Immunofluorescence reveals different timing for free and LP-encapsulated GCAP1 internalization

Despite some discrepancies in the observed biodistribution, partly due to its inherent variability, the ex vivo incubation and intravitreal injection experiments suggested that fluorescently labeled GCAP1 can be internalized by all retinal layers. To study biodistribution by a complementary methodology, we repeated the ex vivo incubation experiments using a variant of GCAP1 with a His-tag at the C-terminus (GCAP1^{His}), which allowed direct detection by immunofluorescence. Incubation was performed for both free GCAP1^{His} and LP-GCAP1^{His} using the same protocol used for CF640R-conjugated counterparts, at three different time intervals, namely, (i) 30 min; (ii) 4 h and 30 min; and (iii) 24 h (Fig. 4).

Incubation of the untreated tissue with a primary antibody against the His-tag resulted in an almost nonexistent background signal (Fig. 4a), which allowed high-resolution detection of the internalized GCAP1^{His} protein by immunofluorescence.

A substantially different time-course of protein internalization was observed when comparing the free and LP-encapsulated protein. Delivered free-GCAP1^{His} (Fig. 4b) was observed in both inner and outer retina even after 30 min, with a detectable signal at the photoreceptor layer (yellow arrow). Fluorescence increased with incubation time, resulting in a clear accumulation of protein in the photoreceptor layer, with specific signals both in the IS and OS layers. Interestingly, 24 h after incubation the delivered protein was clearly visible in the somata of several ganglion cells (yellow arrow in Fig. 4b, right panel), but a much stronger signal was present in the photoreceptor layer even within individual cones (Fig. 5a, yellow arrows and insets). In the case of LP-GCAP1^{His}, the intra-retinal signal became detectable only after a few hours, and at t = 4 h 30 min a speckled signal was observed at the level of the OPL (yellow arrow in Fig. 4c), suggesting that LPs were only partially internalized and did not release their content. However, at t = 24 h, a strong signal was observed in both inner and outer retina and individual ganglion cell somata became visible, along with the photoreceptor layer region. At this time, an overlap of the signal with that of the individual cones was observed (Fig. 5b and inset), indicating that the liposomes released their contents within the individual photoreceptors.

In summary, our comparative experiments show a substantially different timing of retinal internalization for free

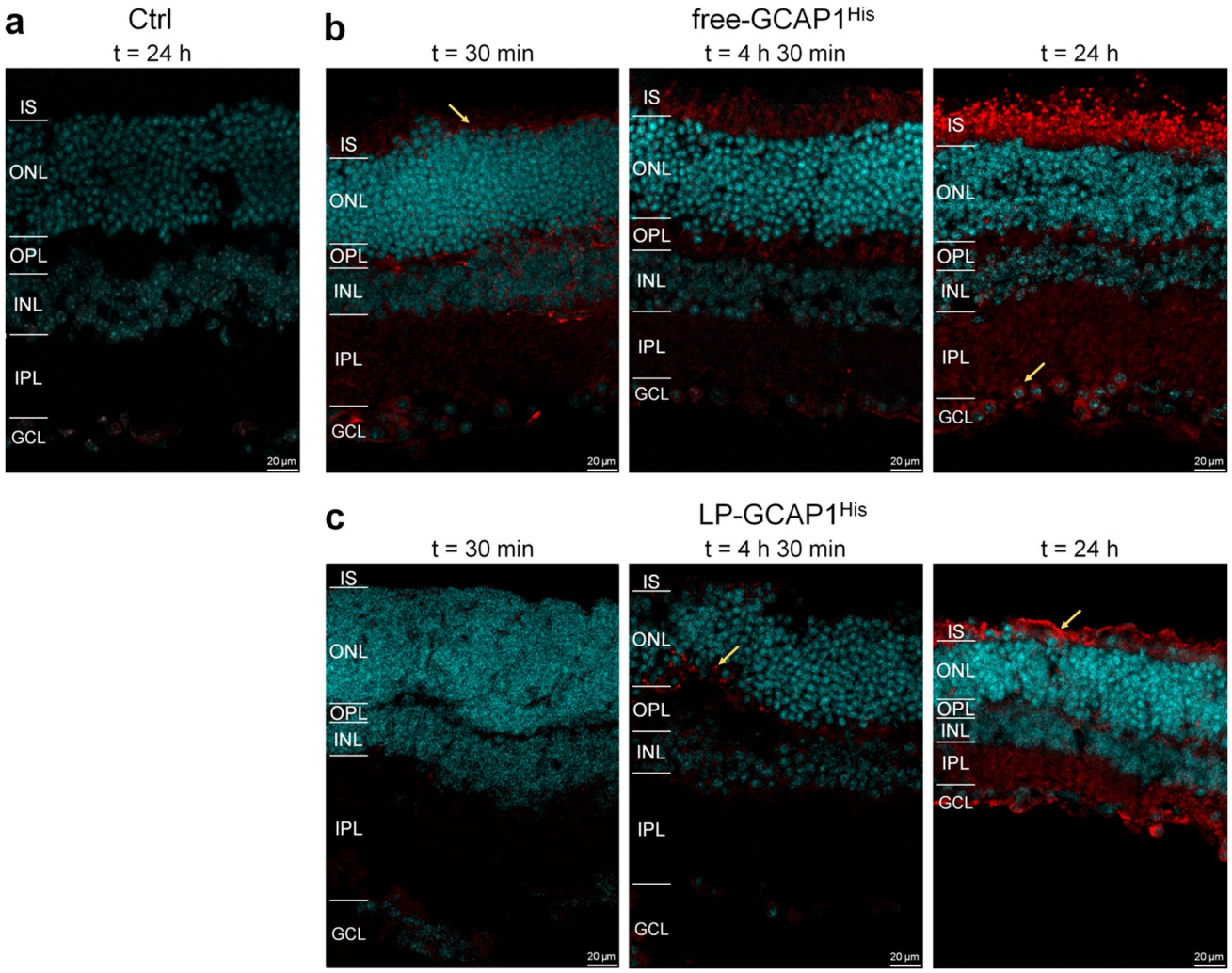

Fig. 4 Distribution of delivered recombinant GCAP1^{His} in mouse retinas following ex vivo incubation as detected by immunofluorescence. Representative central plane of Z-stack of retinal cryosections after **a** 24 h of incubation with 180 µl PBS; **b** 30 min, 4 h 30 min and 24 h incubation with 180 µl of 99.6 µM free-GCAP1^{His}. **c** 30 min, 4 h 30 min and 24 h incubation with 180 µl of 4.5 nM LP-GCAP1^{His} (containing the same number of GCAP1^{His} molecules in the aqueous core as compared to the free protein solution case). Sections were stained with an anti-His antibody (red) and DAPI (light blue). The same image acquisition and display parameters were used in all samples

and LP-encapsulated GCAP1, which reflects in a slightly different biodistribution of exogenous protein across the retinal layers, as shown by the alternative presence of more diffused and speckled signals (Fig. S6).

Delivery of E111V-GCAP1 induces a CORD-like phenotype in WT mouse retinas

If a protein such as GCAP1 was able to gain access to retinal neurons in sufficient concentration, it could potentially be used to modulate biochemical processes [33]. As a proof of concept, we tested the functional effects on photoreceptors of E111V-GCAP1, known to be associated with CORD [24]. Ex vivo ERG recordings were made in a novel purpose-built chamber (see Methods), which enabled prolonged incubation of retinas with relatively high concentrations of expensive test substances (i.e., using tiny overall amounts). ERG recordings were made at 35 °C (except when stated otherwise) under pharmacological blockade of synaptic transmission to ON-bipolars (40 µM AP4) [34]. Except in one case, we did not remove the slow glial component with $BaCl_2$ in order to avoid any direct or secondary effects on photoreceptor physiology, which could affect unpredictably liposome and/or protein uptake [35]. The above conditions were associated to stable recordings of scotopic flash responses for over 4 h. Two parameters were extracted: (*i*) light sensitivity measured by the flash intensity required to obtain a 50% response (i_{50}); (*ii*) time to peak of the 50% response (TTP@

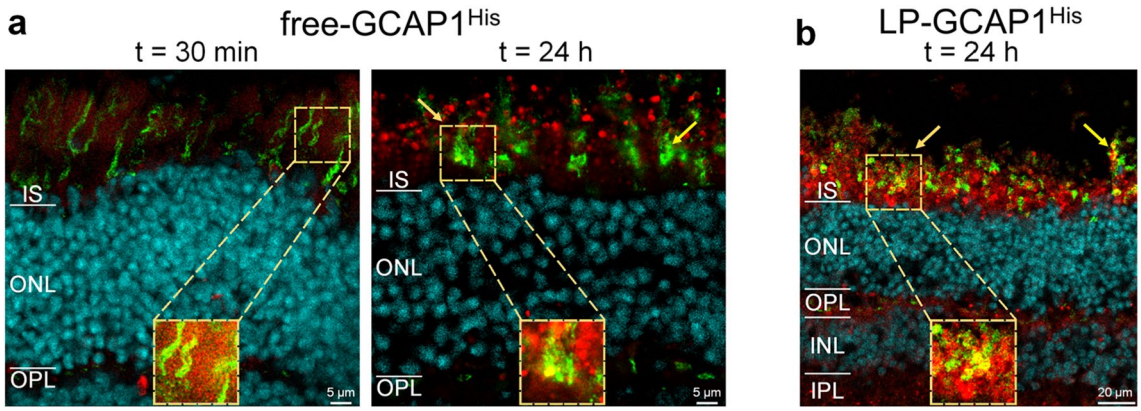

Fig. 5 Cellular distribution of delivered recombinant GCAP1^{His} in mouse retinas following ex vivo incubation as detected by immunofluorescence. Representative central plane of Z-stack of cryosections of retinas after **a** 30 min and 24 h incubation with 180 µl of 99.6 µM free-GCAP1^{His}; or **b** 24 h incubation with 180 µl of 4.5 nM LP-GCAP1^{His} (containing the same number of GCAP1^{His} molecules in the aqueous core as compared to the free protein solution case). Sections stained with an anti-His antibody (red), DAPI (light blue) and Peanut Agglutinin (PNA, green). The same image acquisition and display parameters were used in all samples. Insets show individual cones with the red point of the images adjusted to enhance the signal for GCAP1^{His}. Note the signal overlap from the two channels, resulting in yellow pixels, indicating intracellular location.

i_{50}) (Fig. S7). These were normalized to their pre-treatment levels and processed to remove any trends also present in the control retina, leaving us with (ideally) the net effect of treatment (see Methods).

We first compared the incubation with WT-GCAP1 to PBS (n = 14 animals; Fig. 6a). Over three hours of incubation no significant and systematic effects were detected either on sensitivity or kinetics (Fig. 6a). However, the incubation with free-E111V-GCAP1 slowed response kinetics when compared to PBS (n = 14; Fig. 6b), an effect highly significant already from the first minutes after delivery through the entire three hours of incubation ($p < 0.01$). We confirmed this surprising result by comparing the same concentration of free-E111V-GCAP1 and free-WT-GCAP1, again observing a highly significant slowing of kinetics at most time points (n = 8; Fig. 6c), which indicated that the effect is attributable solely to the E111V point mutation. It should be noted that, even 30 min after incubation, the exogenous protein was observed to be internalized by the retina and was detected in the photoreceptor layer (Fig. 4b). The phenotypic effect was therefore induced very rapidly.

We then went on to examine the effect of LP encapsulation. According to immunofluorescence data (Fig. 4c), LPs were observed after 4 h 30 min incubation in the OPL and, to a lesser extent also in the photoreceptor layer, although the fluorescence pattern suggested that their cargo may not have been released during this time. When LPs-empty were compared to PBS no significant effects were detected (n = 13; Fig. 6d), suggesting that LPs by themselves do not perturb phototransduction. Interestingly, LP-E111V-GCAP1 compared to PBS did not replicate the effects seen with the free mutant protein (n = 9; Fig. 6e). Based on our experience with LPs holding fluorescent molecules we hypothesized that LPs might be scavenged by the filter paper supporting the retina in the chamber. To exclude this possibility, we modified our approach to hold the retinas in place during the recordings thereby dispensing with the filter paper. Furthermore, to promote LP fusion/internalization in cells we raised the incubation temperature to 37°C. Despite these efforts no significant effects were detected over the course of 3 h (n = 21; Fig. 6f). We also compared the incubation of free-E111V-GCAP1 with LP-E111V-GCAP1 (n = 7) and, given previous results, we were not surprised to find a significant slowing of kinetics throughout incubation (Fig. 6g). A weakly significant increase in light sensitivity, not seen in previous comparisons was observed. Furthermore, we confirmed that free-E111V-GCAP1 slow response kinetics also when 50 µM $BaCl_2$ is present in the bath solution (n = 5; Fig. 6h; Fig. S8), although these incubations were terminated after about 1 h. Taking into account the results from immunofluorescence, we reasoned that while LPs might be rapidly internalized, their contents could be released over much longer time scales, also in line with previous findings [36, 37]. To begin examining this hypothesis we exploited recent advances by some of us in long duration ex vivo ERG [38] and succeeded to prolong incubations of LP-encapsulated protein to 18 h. When comparing LP-E111V-GCAP1 to PBS, we detected a significant slowing of the response kinetics only in the final few time bins (n = 18; Fig. 6i), thus approaching 24 h after incubation. This result is fully in line with immunofluorescence experiments, which clearly show that efficient release of the protein following LP encapsulation takes longer than delivery of the free protein, particularly to reach adequate levels in the photoreceptor layer and

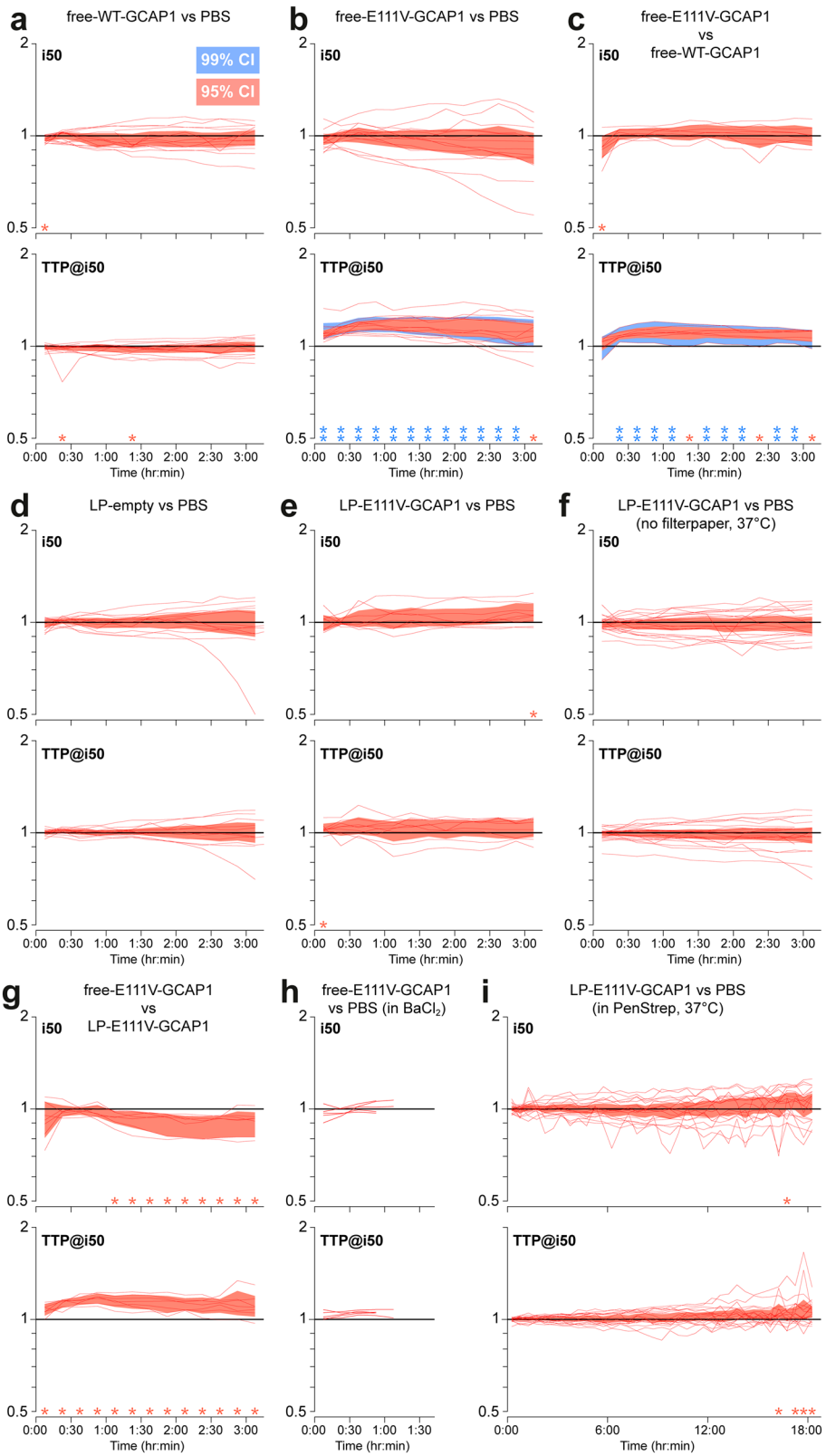

Fig. 6 Functional effects on isolated retinas of incubation with free or LP-encapsulated recombinant GCAP1. The ex vivo ERGs of retina pairs were obtained in control conditions (Time < 0) and during parallel incubation with test and reference solutions for up to 3 h or 18 h. Changes in light sensitivity (i_{50}) and response kinetics (TTP@i_{50}) were monitored by normalizing for pre-treatment control and reference solution. **a**–**i** Red lines represent individual experiments, each involving both retinas from an animal. Red (blue) shaded areas cover the 95% (99%) confidence interval. Loci above unity indicate a decrease in sensitivity or a slowing in kinetics. Red stars: p-value < 0.05; double blue stars: p-value < 0.01

specifically in the outer segment. While our recordings are the state of the art in terms of duration, only future technical developments will allow to monitor the effects of slow drug release by liposomes over several days.

Discussion

In recent years, delivery of proteins and peptides to the eye have emerged as promising avenues for the treatment of a variety of ocular diseases [39], although significant physiological and anatomical challenges remain [40], especially when the goal is to modify biochemical processes occurring in the outer retina. In particular, to assist the development of effective therapies, basic knowledge is needed on whether and how different proteins/peptides move across the ocular compartments [41]. Our investigation represents a proof of concept that protein delivery to the retina may indeed be an effective strategy to modify the phototransduction cascade, which could be relevant to the treatment of IRDs.

Our experiments were based on the delivery of recombinant GCAP1 variants, whose in vitro characterization showed that the CORD-associated E111V-GCAP1 mutant constitutively activates GC1 as a consequence of its impaired Ca^{2+} sensing, although without altering its affinity (EC_{50}) for the target. Furthermore, the Ca^{2+} sensitivity of the GC1-GCAP1 system reconstituted in vitro was perfectly in line with the intracellular Ca^{2+} changes that occur in photoreceptors during phototransduction activation, thus demonstrating the functionality of recombinant proteins.

The simplest system used in this work for testing the potential of protein delivery was eukaryotic cell lines. Experiments with two different lines of HEK293 cells expressing GC1 clearly showed that fluorescently labelled GCAP1 ($GCAP1^{CF640R}$) tended to accumulate near the membrane but did not cross it. In contrast, 4 h after incubation, the same LP-encapsulated protein (LP-$GCAP1^{CF640R}$) started to enter the cell and was clearly observed in the cytoplasm 24 and even 48 h later. Considering that HEK293 cells were impermeable to the unconjugated dye and that $GCAP1^{CF640R}$ failed to cross cell membrane in a 24 h timeframe, this suggests that liposomes are indeed required to transport GCAP1 inside these cells.

Experiments performed with mouse retinas unveiled a completely different scenario. Both free and LP-encapsulated $GCAP1^{CF640R}$ were found to enter retinal neurons in the short time span of our ex vivo incubations (4.5 h), although with different timing and efficacy, as highlighted by immunofluorescence experiments. This also occurred 20–24 h after intravitreal injection, although in this case the fluorescence was locally uniform in the tissue. This could be due to the relatively short time following injection and lower effective protein concentration in intravitreal injections, as immunofluorescence suggests that only prolonged incubation results in cell-specific distribution. The mechanisms underlying retinal biodistribution of endogenous proteins deserves dedicated attention in future studies, using ad hoc model systems, such as organotypic retina cultures that permit high-resolution monitoring of the biodistribution of delivered protein. Besides the efficient delivery to the outer retina, in both ex vivo incubation and intravitreal experiments we detected particularly efficient delivery to the inner retina, suggesting that ocular diseases affecting retinal ganglion cells may be particularly well suited to protein therapy approaches relying on the delivery of recombinant proteins, either with or without the use of LPs as vectors. On the other hand, our functional studies demonstrate that the extent of delivery of exogenous GCAP1 into the photoreceptor outer segments is sufficient to modify the phototransduction cascade.

Taken together, the contrasting data obtained when comparing cell cultures and mouse retinas suggest that cell membrane composition plays an important role in determining the fate of free extracellular GCAP1. The lipid composition of HEK293 membranes [42] significantly differs from that of photoreceptors, which is known to change during retinal development [43] as well as between cone- or rod-dominant retinas [44], and in pathological conditions [43, 45]. Moreover, photoreceptors possess a host of complex and only partially understood molecular mechanisms of communication with the extracellular environment, including a high rate of synaptic membrane turnover due to synaptic vesicles exo/endocytosis [46] or disk membrane and nutrient recycling [47]. Thus, the complexity of retinal lipid composition and metabolism could partly explain the differences observed in the two cell types. Indeed, liposomes with a lipid composition that mimics the photoreceptor membrane are apparently able to enter both HEK293 and retinal neurons, although the process takes at least 24 h in the former, while being significantly faster in the latter. Our results indicate that exogenous GCAP1 can, in the absence of lipid carrier, cross retinal cell membranes and quickly achieve a detectable concentration in both the inner and outer layers, at odds with HEK293 cells, where no protein internalization was observed even after 24 h. While we did not anticipate such behavior, comparably challenging feats by exogenously applied proteins are not unprecedented. Indeed, even without clarifying the inherent mechanisms, several studies performed both in murine and human systems have previously shown that nerve growth factors can potentially cross several barriers in the visual system upon topical (eyedrops) [48] or intravitreal administration [49], leading to tangible clinical outcomes. Nevertheless, the mechanism by which intracellular distribution of exogenous GCAP1 can be observed across different neuronal layers remains currently unknown. Perhaps the protein distribution among photoreceptors is somehow related to the recently discovered nanotube-like connections [50, 51] that allow the exchange of intracellular material [52] including whole proteins. As for the inner-to-outer retina protein exchange, it could be mediated by glial transcytosis operated by Müller cells [53]. These cells generate the

inner limiting membrane between the vitreous humor and the retina and span the whole retina longitudinally. Uptake of proteins and liposomes by Müller cells following intravitreal injections could therefore explain the broad retina biodistribution observed in our in vivo experiments. These hypotheses, which have tremendous implications for protein targeted therapy of retinal diseases, need further investigation.

In a comprehensive set of electrophysiological experiments, we found that free human E111V-GCAP1 rapidly induces a significant slowing of the photoresponse. Crucially, the WT protein did not evoke this effect, thereby pointing to a key role of the E111V point mutation. On the broader level this finding provides strong independent confirmation that free GCAP1 is taken up by retinal neurons and reaches the OS, where the phototransduction machinery is located. On the specific level of phototransduction it is striking, considering the compensating effect played by GCAP2 in murine photoreceptors [9, 33, 54]. In stark contrast, when the mutant protein was delivered encapsulated in LPs no such effects on kinetics were observed in 3 h long incubations and recordings. However, electrophysiological recordings performed over a longer time scale of up to 18 h, suggest that liposomes could be initially internalized intact, while only over longer times scales release their cargo, in line with immunofluorescence in this study and previous results [36, 37]. In fact, the latter property can be considered a major benefit in terms of sustained release and drug pharmacokinetics, be it the case of encapsulated small molecules [55] or, as shown by our study, recombinant proteins.

In a previous study we incubated mouse retinas for 2 h at 37 °C with LPs containing either the protein recoverin (homologous to GCAP1) or an antibody against the same protein [56]. In that case, we observed a significant difference in saturating response kinetics between the two treatments. The lipid composition of those liposomes was somewhat different (phosphatidylcholine/cholesterol at various molar ratios) than that used in the present work. Also different was the electrophysiological recording technique (loose seal patch clamp from single rods), which did not require a pharmacological blockade of synaptic transmission nor involve the presence of a slow glial ERG response component. Aside from these relatively minor differences, a key factor could be the relative ability of the different proteins to perturb phototransduction. If, as postulated above, liposomes slowly release their cargo once inside the photoreceptors, a functional effect after 2–3 h may only be detectable when delivering a strongly impacting protein. Recoverin antibody could, in principle, possess such an effect, considering the crucial role of the recoverin-mediated Ca^{2+}-feedback on rhodopsin kinase in accelerating the shutoff [57]. In contrast, in the present study the recombinant GCAP1 mutant had to outcompete the endogenous WT protein and the compensating effect of GCAP2, which would overall occur when a sufficiently high amount of exogenous GCAP1 has reached the photoreceptor outer segment.

An unexpected finding of this study is that intravitreal injections in mice show extreme trial-to-trial variability in the translocation of delivered molecules to the retina. It must be noted that while mouse eyeballs are approximately tenfold smaller than human eyeballs (3 mm vs 24 mm diameter), their respective vitreous chambers exhibit a 1000-fold difference in volume (4.4 µl vs 4.3 ml [58]). This, together with the high intraocular pressure after injection, renders the entire procedure much more difficult to reproduce in mice than in human, for which several approved eye therapies are administered via intravitreal injections, and could result in lower effective concentration of delivered protein. We intentionally injected an excess volume of 2 µl to ensure that, despite some inevitable backward reflux through the injection hole, a significant amount of test solution always remained in the eye (utmost care was taken in this respect). We would thus tend to attribute a significant part of the variability observed to complex flow dynamics or inhomogeneities in the vitreous. Whatever the mechanism, studies employing intravitreal injections in mice should carefully consider whether variability in their observed therapeutic effects may have the same origin. Clearly, demonstrating significant effects of a drug candidate (or conversely excluding any medically relevant effects) may require a high number of test subjects.

Our study shows that direct and liposome-mediated protein delivery, while acting over different time scales, are powerful complementary tools for targeting signaling cascades in neuronal cells and could be particularly important for the treatment of retinal diseases. While genome editing represents the most promising therapeutic approach for the treatment of IRDs [59], a number of issues remain to be addressed, such as the risk of integrating viral DNA into the host genome increasing the likelihood of oncogenesis in the case of widely used viral vectors. Moreover, persistent expression of the editing machinery could give rise to antiviral immune responses in the long term; finally, the viral vectors currently in use pose severe limitations for the delivery of large genes needed for most gene therapies [60]. On the one hand, our study shows that LPs may represent ideal nonviral vectors for even large gene delivery, or they could be used to deliver ribonucleoproteins by eliciting a low immunogenic response, thus representing a promising strategy for genome editing in the eye. On the other hand, we have clearly shown that administration of recombinant proteins that mimic endogenous ones can induce a specific phenotype in retinal neurons, and this could have therapeutic relevance, especially in cases of autosomal dominant transmission, where a pool of mutated protein is responsible for the disease-phenotype. In the specific case of COD-CORD associated with missense mutations in GCAP1, a possible

mutation-independent approach to therapy could be the delivery of WT-GCAP1 to overcome the effect of the mutant protein. In the case of the E111V variant, this strategy relies on two robust findings. First, WT- and E111V-GCAP1 show very similar apparent affinity for GC1 (EC_{50}), therefore could stoichiometrically compete for the same GC1 target. Second, our previous findings [33] demonstrated in vitro that the prolonged administration of exogenous GCAP1 could attenuate the pathological phenotype by: (i) shifting the IC_{50} towards physiological values, with an increase in cooperativity of cGMP synthesis; (ii) reshaping the photoresponses towards a wild-type like kinetics; (iii) re-establish a wild-type-like homeostasis of second messengers (Ca^{2+} and cGMP) in dark-adapted cells. The proof-of-concept study presented here has therefore high therapeutic potential.

The implications of our findings could extend to a broader scale. Indeed, the GPCR-mediated molecular machinery building up the phototransduction cascade is shared by other signal transduction processes, including chemotaxis, neurotransmission, cell communication, activation of olfaction and taste, and many others [61]. Understanding the mechanisms that influence this signaling cascade and achieving its controlled modulation is critical for drug discovery, since about one-third of all drugs on the market target members of class A GPCRs [2]. More specifically, considering that GCAP1 is the major regulator of GC1 in human photoreceptors and that an increasing number of point mutations in its gene are associated with autosomal dominant COD or CORD, the development of novel biological therapies targeting this protein may help to restore the dysregulation of second messenger homeostasis in IRDs, ultimately slowing or blocking cell death.

Materials and methods

Materials

Tris(hydroxymethyl)aminomethane (Tris), Guanidine-HCl, NaCl, KCl, $CaCl_2$, $MgCl_2$, DTT, EGTA, β-mercaptoethanol, NH_4HCO_3, 4-(2-hydroxyethyl)-1-piperazineethanesulfonic acid) (HEPES), Ames' medium, ethanolamine, phosphatidylethanolamine, phosphatidylcholine, phosphatidylserine, cholesterol, acrylamide, Coomassie blue, cGMP, polyethyleneimine, sucrose, OCT, NH_4Cl, citric acid, Triton X-100, Tween 20, Bovine Serum Albumin, chloramphenicol, cOmplete EDTA-free Protease Inhibitor Cocktail, paraformaldehyde, ketamine, xylazine, atropine, hydrocortisone and $BaCl_2$ were purchased from Merck (Darmstadt, Germany).

DMEM, OptiMEM, penicillin, streptomycin, 2-(4-amidinophenyl)-1H-indole-6-carboxamidine (DAPI), Phosphate Saline Buffer (PBS), Fetal Bovine Serum (FBS), HBSS, glutamine, Normal Goat Serum, Normal Donkey Serum were purchased from ThermoFisher Scientific (Waltham, MA, USA).

Cloning, expression, and purification of GCAP1 variants

Human myristoylated WT-GCAP1 was expressed in *E. coli* BL21 (DE3) after co-transformation with pBB131 containing the cDNA of *S. cerevisiae* N-myristoyl transferase (yNMT) [62]. The cDNA for E111V variant was obtained by PCR using QuikChange II Site-Directed Mutagenesis kit (Agilent, Milan, Italy) as described in Ref [24], while the cDNA for His-tagged WT-GCAP1 ($GCAP1^{His}$) was purchased from Genscript. Both variants were expressed and purified following the same protocol as for the WT [33], briefly consisting of: (*i*) denaturation of inclusion bodies with 6 M Guanidine-HCl; (*ii*) refolding by dialysis against 20 mM Tris–HCl pH 7.5, 150 mM NaCl, 7.2 mM β-mercaptoethanol, and a combination of (*iii*) Size Exclusion Chromatography (SEC, HiPrep 26/60 Sephacryl S-200 HR, GE Healthcare, Chicago, IL, USA) and (*iv*) Anionic Exchange Chromatography (AEC, HiPrep Q HP 16/10, GE Healthcare, Chicago, IL, USA). The purity of GCAP1 variants was assessed by 15% acrylamide SDS-PAGE, samples were either exchanged against PBS, aliquoted and frozen with liquid nitrogen, or exchanged against NH_4HCO_3, aliquoted and lyophilized. Protein samples were finally stored at -80 °C.

The three-dimensional structure of human GCAP1 was obtained by homology modeling using the structure of Ca^{2+}-loaded chicken GCAP1 [63] following the procedure illustrated in Ref [18]. In silico mutagenesis of E111V variant was obtained according to the protocol detailed in Ref [24]. The structures presented in Fig. 1a and b were extracted from the last frame of 200 ns Molecular Dynamics simulations from Ref [24], whose settings and protocols for energy minimization, equilibration and production phases were elucidated in Refs [13, 15].

Electrophoretic mobility shift assay

WT-GCAP1 and E111V-GCAP1 were dissolved in 20 mM Tris–HCl pH 7.5, 150 mM KCl, 1 mM DTT at a concentration of 30 µM, incubated for 5 min at 25 °C with either 1 mM EGTA + 1.1 mM Mg^{2+} or 1 mM Mg^{2+} + 1 mM Ca^{2+}, boiled, and run for 50 min at 200 V on a 15% acrylamide gel under denaturing conditions. Finally, protein bands were visualized by Coomassie blue staining.

Circular dichroism (CD) spectroscopy

The effects of ion binding and of the E111V substitution on the secondary and tertiary structure of GCAP1 were

evaluated by CD spectroscopy using a J-710 spectropolarimeter (Jasco, Cremella, Italy) thermostated by a Peltier-type cell holder. Lyophilized proteins were dissolved in PBS pH 7.4 buffer at a concentration of 35 and 10 µM for near UV and far UV spectra, respectively. Five accumulations of each spectrum were recorded at 25 °C in the absence of ions (500 µM EGTA for near UV, 300 µM for far UV) and after serial additions of 1 mM Mg^{2+} and Ca^{2+} (1 mM for near UV, 600 µM for far UV, leading to a free Ca^{2+} concentration of 500 and 300 µM, respectively). All spectra were subtracted with that of the buffer, near UV spectra were also zeroed by subtracting the average ellipticity between 310 and 320 nm, where no signal was expected.

Dynamic light scattering (DLS)

The hydrodynamic diameter of Ca^{2+}-loaded WT-GCAP1 and E111V-GCAP1 was estimated by DLS using a Zetasizer Nano-S (Malvern Instruments, Malvern, UK). Proteins were dissolved in PBS pH 7.4 at 42 µM concentration and filtered with a Whatman Anotop 10 filter (20 nm cutoff, GE Healthcare, Chicago, IL, USA) before starting the measurements. Samples were equilibrated for 2 min at 25 °C and for each variant at least 100 measurements were collected, each consisting of 13 runs.

Guanylate cyclase activity assay

GC1 enzymatic activity as a function of Ca^{2+} and GCAP1 concentration was measured after reconstituting WT-GCAP1 and E111V-GCAP1 with cell membranes of mGFP-GC1 cells (see below) previously extracted by lysis (10 mM HEPES pH 7.4, Protease Inhibitor Cocktail 1×, 1 mM DTT buffer) and 20 min centrifugation at 18,000×g, as previously described [30, 64, 65]. Cell membranes were resuspended in 50 mM HEPES pH 7.4, 50 mM KCl, 20 mM NaCl, 1 mM DTT and incubated with 5 µM GCAP1 variants at increasing [Ca^{2+}] (< 19 nM to 1 mM, controlled by Ca^{2+}-EGTA buffer solutions [66]) to estimate the Ca^{2+} concentration at which cGMP synthesis by GC1 was half-maximal (IC_{50}). To estimate the GCAP1 concentration at which GC1 activation was half-maximal (EC_{50}), cell membranes were reconstituted with increasing amounts of each GCAP1 variant (0–20 µM) at low Ca^{2+} (< 19 nM). Reported IC_{50} and EC_{50} values are represented as average ± standard deviation of 3 technical replicates. The statistical significance of the differences in IC_{50} and EC_{50} between WT-GCAP1 and E111V-GCAP1 was evaluated by means of two-tailed t tests (p value = 0.05).

Conjugation of CF640R-N-hydroxysuccinimide (NHS) ester with WT-GCAP1

Far-red fluorescent dye CF640R (Biotium, Fremont, CA, USA) was conjugated via NHS to WT-GCAP1 primary amines (Lys residues, Movie S1) according to the manufacturer protocol. Briefly, GCAP1 was diluted in PBS pH 7.4 and 1 mM DTT to a final concentration of 76 µM in a final volume of 900 µl; then the solution was added with 100 µl sodium bicarbonate 1 M pH 8.3 and 2 CF640R-NHS aliquots previously resuspended in 50 µl total DMSO. The mixture was then wrapped in aluminum and incubated in rotation at RT for 1 h. Unconjugated dye was removed by washing 4 times the protein solution (see Fig. S1b for representative spectra of the 4 flowthrough) with PBS pH 7.4 for 10 min at 4400 × g and 4 °C using an Amicon Ultra-4 concentrator with 3 kDa cutoff (Merck Millipore, Burlington, MA, USA). The degree of labelling (DOL = 1.96) was calculated as the ratio between the concentration of dye in the protein solution measured based on the absorbance at 642 nm ($\varepsilon = 105.000\ cm^{-1}\ M^{-1}$), and the concentration of protein calculated by considering the dilution factor and the retention of Amicon concentrators (95%, according to manufacturer instructions). The concentration of free-CF640R in the protein solution was calculated by measuring the absorbance at 642 nm of wash 4, which was < 1% with respect to protein concentration in all conjugation experiments. Unconjugated dye was blocked with 50 µl ethanolamine 1 M.

Fluorescence spectroscopy

The emission fluorescence spectrum of 2 µM $GCAP1^{CF640R}$ (645–680 nm) dissolved in PBS pH 7.4 was collected at 25 °C on a FP-750 spectrofluorometer (Jasco, Cremella, Italy) after excitation at 639 nm; the spectrum reported in Fig. 1h is an average of 3 accumulations after subtraction of the emission spectrum of the buffer in the same range.

Liposome preparation

LPs were prepared by hydrating a thin lipid film of the same composition as photoreceptors rod outer segment membranes [67] (phosphatidylethanolamine, phosphatidylcholine, phosphatidylserine, and cholesterol at a molar ratio of 40:40:15:5) previously mixed in chloroform and dried in a speed-vac concentrator. Four mg of lipid film were hydrated with 1 ml PBS pH 7.4, vortexed for 30 min at room temperature, sonicated for 15 min in a water bath on ice and extruded 20 times through a 200 nm polycarbonate filter (Whatman, Maidstone, UK). The encapsulation of CF640R, WT-GCAP1, E111V-GCAP1, $GCAP1^{His}$, or $GCAP1^{CF640R}$ in LPs was achieved by dissolving the molecule to be loaded in PBS before lipid film hydration. Unencapsulated

molecules were removed by washing at least 4 times the LPs suspensions with PBS pH 7.4 for 20 min at 4 °C and 5000×g using an Amicon Ultra-4 concentrator with 100 kDa cutoff (Merck Millipore, Burlington, MA, USA). The degree of encapsulation was calculated by subtracting from the total mass of the molecule to be encapsulated that present in the flow-through and was found to be higher than 75% in all LP preparations. The efficient separation of non-encapsulated proteins was assessed by measuring protein concentration of the flowthrough of the 4 washing steps, similarly to what was done for CF640R. The concentration of non-encapsulated protein in LP suspensions was estimated from the concentration of protein in the last washing step and was found to be < 7% of the encapsulated protein.

Nanoparticle tracking analysis (NTA)

The concentration and size of LP suspensions were measured at 25 °C by means of NTA on a NanoSight (Malvern Instruments, Malvern, UK) by recording 3 videos of 1 min each at 25 fps by setting 20 µl/min flow rate; camera level and detection threshold were automatically optimized for each measurement to maximize the signal-to-noise ratio. LP size reported in Fig. S2 and LP concentration reported in Table S1 represent the average ± standard error of 3 technical replicates.

Fluorescence imaging of gel-immobilized liposomes

Stock suspensions of LPs, either filled with free-CF640R or empty, were diluted 1:400 v/v in 0.5% low gelling temperature agarose in Ames' medium at 37 °C. A thin film was polymerized over a pure agarose meniscus in a Petri dish and covered with Ames' medium. 3D image stacks were acquired with a 63x/0.9NA water immersion objective and a CCD camera (DFC350 FX, Leica Microsystems, Milan, Italy) in an upright widefield fluorescence microscope (DM LFSA, Leica Microsystems, Milan, Italy) using a Cy5 filterset (49,006; Chroma, Olching, Germany). Stacks were deconvolved and max projected along the z-axis using Fiji/ImageJ as detailed in Ref [68].

Generation of cGFP-GC1 and mGFP-GC1 stable HEK293 cell lines

HEK293 cells were cultured in DMEM medium supplemented with fetal bovine serum (10%, v/v), penicillin (100 units/ml) and streptomycin (100 µg/ml) at 37 °C in humidified atmosphere with 5% CO_2. Cells (6.25×10^5) were seeded in 6-well plates in DMEM medium and grown overnight; the next day cell medium was replaced with OptiMEM reduced serum medium and cells were transfected using polyethyleneimine (PEI) as transfection reagent and 2 different vectors to obtain eGFP-expressing stable cell lines: (*i*) pIRES encoding for eGFP and human GC1 under the same promoter, thus resulting in a cytosolic fluorescence (cGFP), and (*ii*) pcDNA3.1 + N-eGFP encoding for GC1-eGFP fusion protein for localizing fluorescence on the membrane (mGFP). DNA (2.5 µg) was mixed dropwise to 10 µl PEI solution at a concentration of 1 µg/µl (DNA:PEI ratio of 1:5 w/w), added dropwise to 500 µl of pre-warmed OptiMEM, mixed and incubated 30 min at room temperature to allow DNA-PEI polyplex formation. Polyplexes were finally added dropwise to each well and the plate was incubated overnight at 37 °C and 5% CO_2. The next day, OptiMEM medium was replaced with DMEM and 48 h after transfection eGFP positive cells were selected using geneticin (500 µg/ml).

Live-cell imaging

Cells (8×10^4) were seeded in 4-well chambers (Ibidi, Graefelfing, Germany) in DMEM medium; two days later the medium was replaced with OptiMEM reduced serum medium, then cells were incubated with 100 µl LP suspension per well (containing each ~ 0.4 mg lipid) and monitored in live-cell imaging. Experiments with fluorescently labelled $GCAP1^{CF640R}$ were performed taking care of incubating the cells with the same nominal concentration of protein encapsulated in the LP aqueous core.

Live-cell imaging was performed using TCS-SP5 Inverted Confocal Microscope (Leica Microsystems, Milan, Italy) equipped with temperature and CO_2 controller and motorized stage that provides precise and automated acquisition of multiple fields of view. Images were collected simultaneously on different points of the sample immediately after cell-LP incubation and at 30 min interval for 24 h or 48 h total acquisition time. Images were captured after 488 nm and 633 nm laser excitation with a 40× objective (1.2 NA oil immersion) and further analyzed by Imaris 9.8 software (Oxford Instruments, Abingdon-on-Thames, UK). The fluorescence intensity profiles of mGFP and LP-$GCAP1^{CF640R}$ reported in Fig. S4 were collected along the line across the cell shown in the insets using ImageJ.

Fluorescence microscopy of mouse retinas following ex vivo incubation

All animal experiments made use of adult C57Bl/6 J mice of both sexes. These were reared at around 22 °C in small groups with the addition of environmental enrichment items, a 12 h day/12 h night cycle, ad libitum food and water. As in previous studies by our group, and in accordance with authorized protocols, dark adapted mice were deeply anesthetized with ketamine (80 mg/kg) + xylazine (5 mg/kg) and their retinas extracted through a corneal incision in room temperature Ames' medium under dim red light. This

approach avoided even brief exposure of the tissue to anoxic conditions, which could affect protein and/or liposome uptake. Animals were then immediately sacrificed with an overdose of anesthetic. After removing the vitreous each retina was placed, freely floating, in a plastic well containing incubation solution (1–2 ml depending on the experiment), and the wells inserted in an airtight box with a water layer at the bottom and a 95%O_2/5%CO_2 atmosphere. Incubation solutions consisted in the test suspension/solution diluted in Ames' medium, taking care of reaching virtually the same final concentration for each suspension. The box was left floating in a water bath at 37 °C. After the prescribed time the retinas were returned to room temperature Ames' medium, made to adhere to black filter paper (AABP02500; Merck, Burlington, MA, USA) with gentle suction and, optionally, sliced at 250 µm thickness with a manual tissue chopper. Image stacks were acquired as described for the imaging of gel-immobilized LPs, with 4x/0.1NA air, 20x/0.5NA and 40x/0.8NA water immersion objectives. Excitation was provided by an Hg lamp preheated to achieve stable output. Stacks were lightly deconvolved (Richardson-Lucy algorithm, 10 iterations) and a single image obtained by averaging along the z-axis a few adjacent slices of the stack, in all cases chosen well below the cut surface. The borders of retinal layers were identified by imaging the same tissue volume in the near IR (Fig. S9). Cones were identified based on their characteristic location and morphology, leveraging our experience with their intracellular staining. Identical acquisition parameters were used when comparing retinas treated with different incubation solutions.

Immunofluorescence experiments with mouse retinas following ex vivo incubation

Mice were anesthetized with isoflurane, euthanized via cervical dislocation and their retinas extracted through a corneal incision in room temperature DMEM medium supplemented with FBS (25%, v/v), HBSS (25% v/v), glutamine (1% v/v), penicillin (100 units/ml) and streptomycin (100 µg/ml). After 30 min incubation at 37 °C and 5% CO_2, tissues were incubated with 180 µl PBS, 180 µl of 100 µM free-GCAP1^{His} or 180 µl of 4.5 nM LP-GCAP1^{His} (containing the same number of GCAP1^{His} molecules in the aqueous core as compared to the free protein solution case) for 30 min, 4 h 30 min, and 24 h, and finally washed 3 times with PBS.

Retina sections were then fixed for 40 min in 10% formalin in PBS buffer, washed 3 times with PBS, incubated with 10%, 20% and 30% sucrose for 1 h each at RT, and kept overnight at 4 °C. The next day samples were incubated at RT for 1 h with OCT compound: 30% sucrose at a 1:1 ratio and processed for cryo-sectioning at – 14 °C.

Sections (14 µm thickness) were fixed for 5 min with paraformaldehyde, washed 3 times with PBS, incubated with 0.1% Triton X-100 in PBS for 1 h at RT, washed 3 times with PBS, incubated with ammonium chloride for 20 min, and washed 5 times with PBS.

Sections were incubated overnight at RT with mouse anti-His primary antibody (1:1000 dilution, SouthernBiotech, Birmingham, AL, USA) and PNA (1:250 dilution, Molecular Probes, Eugene, OR, USA) in blocking solution (5% Normal Goat Serum, 1% Bovine Serum Albumin, 0.3% Triton X-100 in PBS). The following day samples were washed 3 times with PBS and incubated with an Alexa Fluor 647-conjugated goat anti-mouse secondary antibody (1:1000 dilution, Invitrogen, Waltham, MA, USA). Cell nuclei were stained with a 1:1000 DAPI dilution in PBS; slides were coverslipped with Dako fluorescence mounting medium (Agilent, Milan, Italy). Sections were visualized using TCS-SP5 Inverted Confocal Microscope (Leica Microsystems, Milan, Italy), images were captured after 405 nm and 633 nm laser excitation with a 63× objective (1.2 NA oil immersion) and further analyzed by Imaris 9.8 software (Oxford Instruments, Abingdon-on-Thames, UK).

Intravitreal injections

Mice were first anesthetized with ketamine (80 mg/kg) + xylazine (5 mg/kg), followed by application of eyedrops containing atropine and chloramphenicol (1%) + hydrocortisone (0.5%). Intravitreal injections were made under a stereomicroscope and dim blue light as follows: (*i*) a hole was made in the cornea near the *ora serrata* with the tip of a 31G insulin needle; (*ii*) glass micropipettes with a broken tip, connected to a 25 µl syringe (Hamilton, Reno, NV, USA) via PE tubing filled with mineral oil (330,779; Merck, Burlington, MA, USA), were front loaded with 2 µl of solution; (*iii*) the micropipette was inserted in the hole and the entire volume slowly injected in the vitreous. Mice were returned to their cages and allowed to recover in a paper blanket. After 20–24 h we performed retinal dissection, slicing and imaging as described for ex vivo incubations.

Long duration ex vivo ERG recordings

ERG experiments were made in a custom designed incubation and recording chamber [38]. Retina pairs were isolated as described for ex vivo incubations, made to adhere to white filter paper (SMWP02500; Merck, Burlington, MA, USA) and placed at the bottom of two adjacent plastic wells, containing 2 ml/retina of 40 µM AP4 (0101; Tocris, Milan, Italy) in Ames' medium. Retinas were centered on a hole leading to the anode, while the cathode was in the chamber itself. In some experiments we dispensed with

the filter paper and used instead small transparent cups to immobilize the retinas (Fig. 1b in Ref [38]). Both electrodes were silver chloride wires inserted in an agar bridge. The well assembly was placed on an aluminum platform covered with a layer of water, inside a sealed incubation chamber purged with 95% O_2/5% CO_2. The temperature of the platform was actively controlled with a custom apparatus [69]. Small diameter PTFE tubing, leading from inside the wells to syringes residing outside the chamber, allowed injection and mixing of test solutions (100 µl/retina) into the wells during the recordings with minimal perturbation. Immediately above the wells, attached to the lid of the chamber, a LED (505 nm; ND filters) delivered the same flash sequence every 15 or 30 min: (ph/µm^2|no. of flash repetitions) 3.98|12, 8.27|10, 18.9|8, 50.5|6, 151|6, 510|4, 1660|3. Transretinal potentials were amplified by 5000, filtered in the band DC-100 Hz, digitized at 5 kHz and acquired with pClamp 9 (Molecular Devices, San Jose, CA, USA). Electrophysiological records were analyzed in Axograph X with automated custom scripts. i_{50} was determined by fitting a Hill function to a plot of response amplitudes measured 90–130 ms after the flash (Fig. S7). This range minimized the contribution of the very slow glial response and gave parameter values close to those in $BaCl_2$ [38]. TTP@i_{50} was estimated as the weighted average of the TTPs of the two flash responses straddling i_{50} (10 Hz Gaussian filtered records). Two rounds of normalization were applied to these raw data, as follows. We assumed that the two retinas, being from the same animal, behaved identically except for (*i*) an initial stabilization phase due to slight variations in their isolation and manipulation, and (*ii*) a scaling factor in their steady state light sensitivity due to small differences in their orientation in the recording chamber. We first normalized the two sets of raw values over their respective pre-treatment levels. We then removed any trends common to both retinas by dividing the normalized values of the treated retina by those of the control. We were thus left with a single time series that shows the net effect of the tested drug (Fig. 6, red lines). Treated and control retina positions in the wells were alternated from animal to animal to cancel out any environmental biases. In a limited number of tests (Fig. 6h) $BaCl_2$ was injected in the wells using the syringe system after an initial stabilization period and stirred to obtain a final concentration of 50 µM. In a subset of the experiments, we included HyClone PenStrep (SV30010; Cytiva, Breisgau, Germany) in the incubation medium at 1% vol/vol, which enabled us to prolong our recordings up to 18 h.

Statistics

Statistical analyses were performed with the open-source software JASP 0.16 (jasp-stats.org; RRID:SCR_015823), Kaleidagraph 5 and Excel (Microsoft, Redmond, WA, USA). For ERG recordings visual representation of the population effect of a tested drug (Fig. 6) were given by the confidence interval of the Hodges-Lehmann estimator [38]. Statistical significance was estimated by the following parametric and non-parametric tests as mentioned in the text: two tailed t-test, paired Wilcoxon signed-rank, one sample Wilcoxon signed-rank.

Supplementary Information The online version contains supplementary material available at https://doi.org/10.1007/s00018-023-05022-0.

Acknowledgements The Centro Piattaforme Tecnologiche of the University of Verona is acknowledged for providing access to spectroscopic and imaging platforms. We thank Carmen Longo for helpful discussions.

Author contributions SA and LC performed the ex vivo and in vivo experiments. VM, AB and GDC performed in vitro experiments. AA performed in cyto and live imaging experiments. DD and LC conceived and designed the study and supervised the project. All authors analyzed the data and contributed to design and write the manuscript with the supervision of LC and DD. All authors have read and approved the manuscript.

Funding Open access funding provided by Università degli Studi di Verona within the CRUI-CARE Agreement. This study was supported by a grant from the Velux Stiftung (Project No. 1410), by the following Next Generation EU/Ministry of University and Research projects: *(i) "Tuscany Health Ecosystem (THE)", CUP I53C22000780001, milestones 4.3.2 (spoke 4) and 8.9.1 (spoke 8); (ii) "A multiscale integrated approach to the study of the nervous system in health and disease (MNESYS)", CUP B33C22001060002, PE00000006 missione 4, componente 2, investimento 1.3. The kind support of Retina Italia OdV is gratefully acknowledged.*

Availability of data and materials The datasets generated during and/or analyzed during the current study are available from the corresponding authors on reasonable request. Source data are provided with this paper.

Declarations

Conflict of interest The authors have no relevant financial or non-financial interests to disclose.

Ethics approval and consent to participate This study was performed in line with the principles of the Declaration of Helsinki. Approval for all the animal procedures employed was granted by the Ethics Committee of Universities of Verona and Pisa, and the Italian Ministry of Health (authorization n. 937/2021-PR referred to prot. n. 56DC9.74), in accordance with the Italian (D.lgs.vo 116/92 and D.lgs 26/2014) and EU regulations (Council Directive 86/609/EEC).

Consent for publication Not applicable.

References

1. Deupi X (2014) Relevance of rhodopsin studies for GPCR activation. Biochim Biophys Acta 1837:674–682. https://doi.org/10.1016/j.bbabio.2013.09.002
2. Zhou Q et al (2019) Common activation mechanism of class A GPCRs. Elife. https://doi.org/10.7554/eLife.50279
3. Koch KW, Dell'Orco D (2015) Protein and signaling networks in vertebrate photoreceptor cells. Front Mol Neurosci 8:67. https://doi.org/10.3389/fnmol.2015.00067
4. Korenbrot JI (2012) Speed, sensitivity, and stability of the light response in rod and cone photoreceptors: facts and models. Prog Retin Eye Res 31:442–466. https://doi.org/10.1016/j.preteyeres.2012.05.002
5. Koch KW, Dell'orco D (2013) A calcium-relay mechanism in vertebrate phototransduction. ACS Chem Neurosci 4:909–917. https://doi.org/10.1021/cn400027z
6. Dell'Orco D, Koch KW, Kreutz MR, Naranjo JR, Schwaller B (2019) Editorial: neuronal calcium sensors in health and disease. Front Mol Neurosci 12:278. https://doi.org/10.3389/fnmol.2019.00278
7. Peshenko IV et al (2011) Enzymatic properties and regulation of the native isozymes of retinal membrane guanylyl cyclase (RetGC) from mouse photoreceptors. Biochemistry 50:5590–5600. https://doi.org/10.1021/bi200491b
8. Avesani A, Marino V, Zanzoni S, Koch KW, Dell'Orco D (2021) Molecular properties of human guanylate cyclase-activating protein 2 (GCAP2) and its retinal dystrophy-associated variant G157R. J Biol Chem 296:100619. https://doi.org/10.1016/j.jbc.2021.100619
9. Vinberg F, Peshenko IV, Chen J, Dizhoor AM, Kefalov VJ (2018) Guanylate cyclase-activating protein 2 contributes to phototransduction and light adaptation in mouse cone photoreceptors. J Biol Chem 293:7457–7465. https://doi.org/10.1074/jbc.RA117.001574
10. Heizmann CW (2019) Ca(2+)-binding proteins of the EF-hand superfamily: diagnostic and prognostic biomarkers and novel therapeutic targets. Methods Mol Biol 1929:157–186. https://doi.org/10.1007/978-1-4939-9030-6_11
11. Dell'Orco D, Sulmann S, Linse S, Koch KW (2012) Dynamics of conformational Ca2+-switches in signaling networks detected by a planar plasmonic device. Anal Chem 84:2982–2989. https://doi.org/10.1021/ac300213j
12. Dizhoor AM, Olshevskaya EV, Peshenko IV (2010) Mg2+/Ca2+ cation binding cycle of guanylyl cyclase activating proteins (GCAPs): role in regulation of photoreceptor guanylyl cyclase. Mol Cell Biochem 334:117–124. https://doi.org/10.1007/s11010-009-0328-6
13. Marino V, Sulmann S, Koch KW, Dell'Orco D (1853) Structural effects of Mg(2)(+) on the regulatory states of three neuronal calcium sensors operating in vertebrate phototransduction. Biochim Biophys Acta 2055–2065:2015. https://doi.org/10.1016/j.bbamcr.2014.10.026
14. Peshenko IV, Dizhoor AM (2004) Guanylyl cyclase-activating proteins (GCAPs) are Ca2+/Mg2+ sensors: implications for photoreceptor guanylyl cyclase (RetGC) regulation in mammalian photoreceptors. J Biol Chem 279:16903–16906. https://doi.org/10.1074/jbc.C400065200
15. Marino V, Dell'Orco D (2016) Allosteric communication pathways routed by Ca(2+)/Mg(2+) exchange in GCAP1 selectively switch target regulation modes. Sci Rep 6:34277. https://doi.org/10.1038/srep34277
16. Koch KW, Duda T, Sharma RK (2010) Ca(2+)-modulated vision-linked ROS-GC guanylate cyclase transduction machinery. Mol Cell Biochem 334:105–115. https://doi.org/10.1007/s11010-009-0330-z
17. Biasi A et al (2021) A novel GUCA1A variant associated with cone dystrophy alters cGMP signaling in photoreceptors by strongly interacting with and hyperactivating retinal guanylate cyclase. Int J Mol Sci. https://doi.org/10.3390/ijms221910809
18. Dell'Orco D, Behnen P, Linse S, Koch KW (2010) Calcium binding, structural stability and guanylate cyclase activation in GCAP1 variants associated with human cone dystrophy. Cell Mol Life Sci 67:973–984. https://doi.org/10.1007/s00018-009-0243-8
19. Dizhoor AM, Boikov SG, Olshevskaya EV (1998) Constitutive activation of photoreceptor guanylate cyclase by Y99C mutant of GCAP-1. Possible role in causing human autosomal dominant cone degeneration. J Biol Chem 273:17311–17314. https://doi.org/10.1074/jbc.273.28.17311
20. Jiang L et al (2008) A novel GCAP1(N104K) mutation in EF-hand 3 (EF3) linked to autosomal dominant cone dystrophy. Vis Res 48:2425–2432. https://doi.org/10.1016/j.visres.2008.07.016
21. Kamenarova K et al (2013) Novel GUCA1A mutations suggesting possible mechanisms of pathogenesis in cone, cone-rod, and macular dystrophy patients. Biomed Res Int 2013:517570. https://doi.org/10.1155/2013/517570
22. Kitiratschky VB et al (2009) Mutations in the GUCA1A gene involved in hereditary cone dystrophies impair calcium-mediated regulation of guanylate cyclase. Hum Mutat 30:E782-796. https://doi.org/10.1002/humu.21055
23. Manes G et al (2017) Cone dystrophy or macular dystrophy associated with novel autosomal dominant GUCA1A mutations. Mol Vis 23:198–209
24. Marino V et al (2018) A novel p.(Glu111Val) missense mutation in GUCA1A associated with cone-rod dystrophy leads to impaired calcium sensing and perturbed second messenger homeostasis in photoreceptors. Hum Mol Genet 27:4204–4217. https://doi.org/10.1093/hmg/ddy311
25. Marino V, Scholten A, Koch KW, Dell'Orco D (2015) Two retinal dystrophy-associated missense mutations in GUCA1A with distinct molecular properties result in a similar aberrant regulation of the retinal guanylate cyclase. Hum Mol Genet 24:6653–6666. https://doi.org/10.1093/hmg/ddv370
26. Nishiguchi KM et al (2004) A novel mutation (I143NT) in guanylate cyclase-activating protein 1 (GCAP1) associated with autosomal dominant cone degeneration. Invest Ophthalmol Vis Sci 45:3863–3870. https://doi.org/10.1167/iovs.04-0590
27. Peshenko IV et al (2019) A G86R mutation in the calcium-sensor protein GCAP1 alters regulation of retinal guanylyl cyclase and causes dominant cone-rod degeneration. J Biol Chem 294:3476–3488. https://doi.org/10.1074/jbc.RA118.006180
28. Sokal I et al (2005) A novel GCAP1 missense mutation (L151F) in a large family with autosomal dominant cone-rod dystrophy (adCORD). Invest Ophthalmol Vis Sci 46:1124–1132. https://doi.org/10.1167/iovs.04-1431
29. Sokal I et al (1998) GCAP1 (Y99C) mutant is constitutively active in autosomal dominant cone dystrophy. Mol Cell 2:129–133. https://doi.org/10.1016/s1097-2765(00)80121-5
30. Vocke F et al (2017) Dysfunction of cGMP signalling in photoreceptors by a macular dystrophy-related mutation in the calcium sensor GCAP1. Hum Mol Genet 26:133–144. https://doi.org/10.1093/hmg/ddw374
31. Wilkie SE et al (2001) Identification and functional consequences of a new mutation (E155G) in the gene for GCAP1 that causes autosomal dominant cone dystrophy. Am J Hum Genet 69:471–480. https://doi.org/10.1086/323265

32. Gill JS, Georgiou M, Kalitzeos A, Moore AT, Michaelides M (2019) Progressive cone and cone-rod dystrophies: clinical features, molecular genetics and prospects for therapy. Br J Ophthalmol. https://doi.org/10.1136/bjophthalmol-2018-313278
33. Dell'Orco D, Dal Cortivo G (2019) Normal GCAPs partly compensate for altered cGMP signaling in retinal dystrophies associated with mutations in GUCA1A. Sci Rep 9:20105. https://doi.org/10.1038/s41598-019-56606-5
34. Vinberg F, Kefalov V (2015) Simultaneous ex vivo functional testing of two retinas by in vivo electroretinogram system. J Vis Exp. https://doi.org/10.3791/52855
35. Vinberg F, Koskelainen A (2010) Calcium sets the physiological value of the dominant time constant of saturated mouse rod photoresponse recovery. PLoS ONE 5:e13025. https://doi.org/10.1371/journal.pone.0013025
36. Liu P, Chen G, Zhang J (2022) A review of liposomes as a drug delivery system: current status of approved products, regulatory environments, and future perspectives. Molecules. https://doi.org/10.3390/molecules27041372
37. Wang N, Wang T, Li T, Deng Y (2009) Modulation of the physicochemical state of interior agents to prepare controlled release liposomes. Colloids Surf B Biointerfaces 69:232–238. https://doi.org/10.1016/j.colsurfb.2008.11.033
38. Cangiano L, Asteriti S (2023) An ex vivo electroretinographic apparatus for the ml-scale testing of drugs to one day and beyond. Int J Mol Sci. https://doi.org/10.3390/ijms241411346
39. Mandal A et al (2018) Ocular delivery of proteins and peptides: challenges and novel formulation approaches. Adv Drug Deliv Rev 126:67–95. https://doi.org/10.1016/j.addr.2018.01.008
40. Attia SA, MacKay JA (2022) Protein and polypeptide mediated delivery to the eye. Adv Drug Deliv Rev 188:114441. https://doi.org/10.1016/j.addr.2022.114441
41. El Sanharawi M et al (2010) Protein delivery for retinal diseases: from basic considerations to clinical applications. Prog Retin Eye Res 29:443–465. https://doi.org/10.1016/j.preteyeres.2010.04.001
42. Dawaliby R et al (2016) Phosphatidylethanolamine is a key regulator of membrane fluidity in eukaryotic cells. J Biol Chem 291:3658–3667. https://doi.org/10.1074/jbc.M115.706523
43. Hamano F et al (2021) Mapping membrane lipids in the developing and adult mouse retina under physiological and pathological conditions using mass spectrometry. J Biol Chem 296:100303. https://doi.org/10.1016/j.jbc.2021.100303
44. Agbaga MP et al (2018) Differential composition of DHA and very-long-chain PUFAs in rod and cone photoreceptors. J Lipid Res 59:1586–1596. https://doi.org/10.1194/jlr.M082495
45. Verra DM et al (2022) Intrinsic differences in rod and cone membrane composition: implications for cone degeneration. Graefes Arch Clin Exp Ophthalmol 260:3131–3148. https://doi.org/10.1007/s00417-022-05684-9
46. Moser T, Grabner CP, Schmitz F (2020) Sensory processing at ribbon synapses in the retina and the cochlea. Physiol Rev 100:103–144. https://doi.org/10.1152/physrev.00026.2018
47. Lewandowski D et al (2022) Dynamic lipid turnover in photoreceptors and retinal pigment epithelium throughout life. Prog Retin Eye Res 89:101037. https://doi.org/10.1016/j.preteyeres.2021.101037
48. Falsini B et al (2016) Nerve growth factor improves visual loss in childhood optic gliomas: a randomized, double-blind, phase II clinical trial. Brain 139:404–414. https://doi.org/10.1093/brain/awv366
49. Domenici L et al (2014) Rescue of retinal function by BDNF in a mouse model of glaucoma. PLoS ONE 9:e115579. https://doi.org/10.1371/journal.pone.0115579
50. Henderson JM, Zurzolo C (2021) Seeing eye to eye: photoreceptors employ nanotube-like connections for material transfer. EMBO J 40:e109727. https://doi.org/10.15252/embj.2021109727
51. Kalargyrou AA et al (2021) Nanotube-like processes facilitate material transfer between photoreceptors. EMBO Rep 22:e53732. https://doi.org/10.15252/embr.202153732
52. Heisterkamp P et al (2022) Evidence for endogenous exchange of cytoplasmic material between a subset of cone and rod photoreceptors within the adult mammalian retina via direct cell-cell connections. Exp Eye Res 219:109033. https://doi.org/10.1016/j.exer.2022.109033
53. Reid SN, Farber DB (2005) Glial transcytosis of a photoreceptor-secreted signaling protein, retinoschisin. Glia 49:397–406. https://doi.org/10.1002/glia.20131
54. Dell'Orco D, Sulmann S, Zagel P, Marino V, Koch KW (2014) Impact of cone dystrophy-related mutations in GCAP1 on a kinetic model of phototransduction. Cell Mol Life Sci 71:3829–3840. https://doi.org/10.1007/s00018-014-1593-4
55. Vighi E et al (2018) Combination of cGMP analogue and drug delivery system provides functional protection in hereditary retinal degeneration. Proc Natl Acad Sci U S A 115:E2997–E3006. https://doi.org/10.1073/pnas.1718792115
56. Asteriti S et al (2015) Effective delivery of recombinant proteins to rod photoreceptors via lipid nanovesicles. Biochem Biophys Res Commun 461:665–670. https://doi.org/10.1016/j.bbrc.2015.04.088
57. Beelen CJ, Asteriti S, Cangiano L, Koch KW, Dell'Orco D (2021) A hybrid stochastic/deterministic model of single photon response and light adaptation in mouse rods. Comput Struct Biotechnol J 19:3720–3734. https://doi.org/10.1016/j.csbj.2021.06.033
58. Sun YJ et al (2021) An intravitreal implant injection method for sustained drug delivery into mouse eyes. Cell Rep Methods. https://doi.org/10.1016/j.crmeth.2021.100125
59. Suh S, Choi EH, Raguram A, Liu DR, Palczewski K (2022) Precision genome editing in the eye. Proc Natl Acad Sci U S A 119:e2210104119. https://doi.org/10.1073/pnas.2210104119
60. Yan AL, Du SW, Palczewski K (2023) Genome editing, a superior therapy for inherited retinal diseases. Vision Res 206:108192. https://doi.org/10.1016/j.visres.2023.108192
61. Tuteja N (2009) Signaling through G protein coupled receptors. Plant Signal Behav 4:942–947. https://doi.org/10.4161/psb.4.10.9530
62. Hwang JY, Koch KW (2002) Calcium- and myristoyl-dependent properties of guanylate cyclase-activating protein-1 and protein-2. Biochemistry 41:13021–13028. https://doi.org/10.1021/bi026618y
63. Stephen R, Bereta G, Golczak M, Palczewski K, Sousa MC (2007) Stabilizing function for myristoyl group revealed by the crystal structure of a neuronal calcium sensor, guanylate cyclase-activating protein 1. Structure 15:1392–1402. https://doi.org/10.1016/j.str.2007.09.013
64. Hwang JY et al (2003) Regulatory modes of rod outer segment membrane guanylate cyclase differ in catalytic efficiency and Ca(2+)-sensitivity. Eur J Biochem 270:3814–3821. https://doi.org/10.1046/j.1432-1033.2003.03770.x
65. Zagel P, Dell'Orco D, Koch KW (2013) The dimerization domain in outer segment guanylate cyclase is a Ca(2)(+)-sensitive control switch module. Biochemistry 52:5065–5074. https://doi.org/10.1021/bi400288p
66. Tsien R, Pozzan T (1989) Measurement of cytosolic free Ca2+ with quin2. Methods Enzymol 172:230–262. https://doi.org/10.1016/s0076-6879(89)72017-6
67. Lange C, Koch KW (1997) Calcium-dependent binding of recoverin to membranes monitored by surface plasmon resonance spectroscopy in real time. Biochemistry 36:12019–12026. https://doi.org/10.1021/bi970938d
68. Asteriti S, Ricci V, Cangiano L (2020) Two simple criteria to estimate an objective's performance when imaging

in non design tissue clearing solutions. J Neurosci Methods 332:108564. https://doi.org/10.1016/j.jneumeth.2019.108564
69. Asteriti S, Cangiano L (2020) Versatile bipolar temperature controller for custom in vitro applications. HardwareX 8:e00155. https://doi.org/10.1016/j.ohx.2020.e00155

Supplementary Information

Recombinant protein delivery enables modulation of the phototransduction cascade in mouse retina

Sabrina Asteriti, Valerio Marino, Anna Avesani, Amedeo Biasi, Giuditta Dal Cortivo, Lorenzo Cangiano and Daniele Dell'Orco

This PDF file includes:

Figures S1 to S9
Table S1
Captions for Movies S1 to S5

Other Supplementary Materials for this manuscript include the following:

Movies S1 to S5

Figure S1

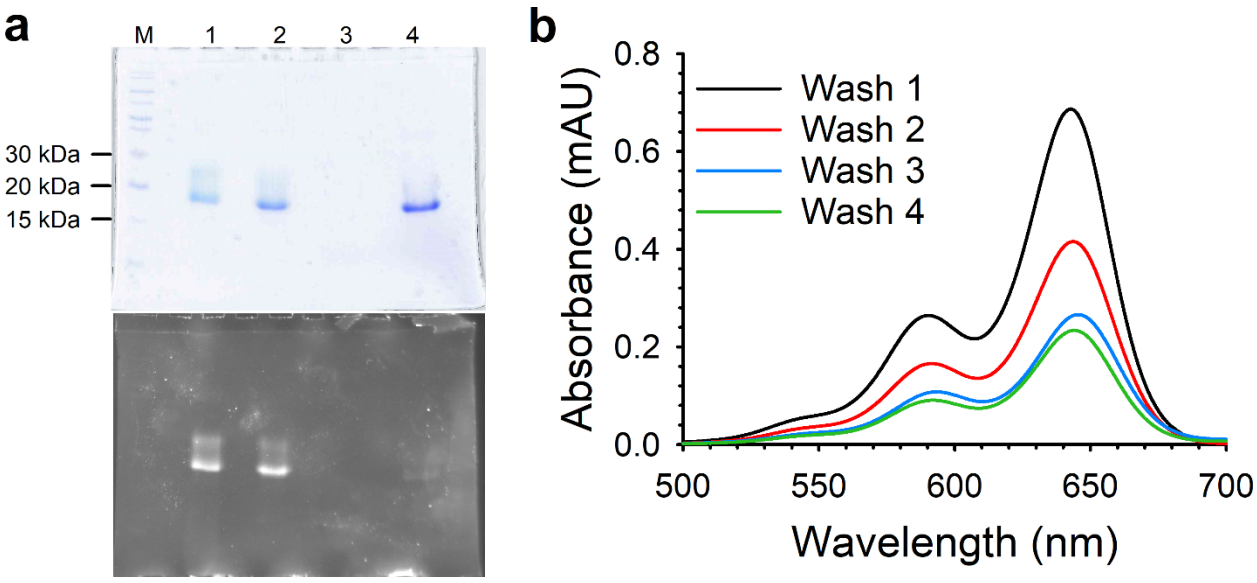

Assessment of the conjugation of GCAP1 with CF640R and removal of free dye. **a)** 15% SDS-PAGE of GCAP1 before and after conjugation with CF640R and after encapsulation in LPs. Lanes: M) marker, 1) LP-GCAP1^{CF640R}, 2) free-GCAP1^{CF640R}, 3) free-CF640R, 4) WT-GCAP1, stained with Coomassie blue (top panel) and upon excitation at 580 nm (bottom panel). **b)** Representative absorption spectra of the flowthrough of the 4 sequential washing steps to remove unconjugated dye.

Figure S2

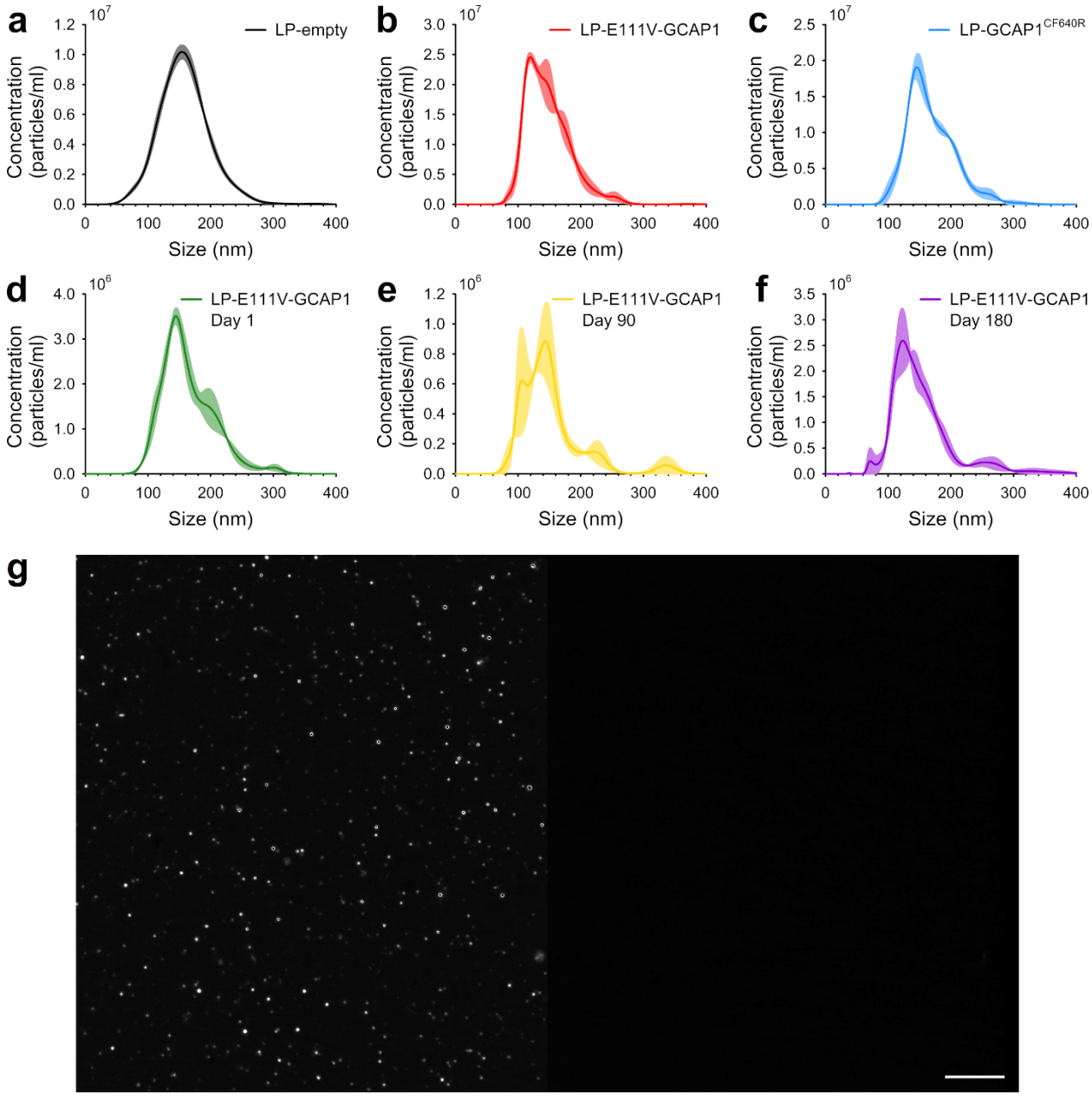

Representative profiles of the size of **a)** 5.1 nM LP-empty (black), **b)** 4.3 nM LP-E111V-GCAP1 (red), **c)** 4.6 nM LP-GCAP1^{CF640R} (blue) estimated by NTA. Monitoring of the size of ~2.9 nM (**Table S1**) LP-E111V-GCAP1 after **d)** 1 (green), **e)** 90 (yellow) and **f)** 180 days (violet). Each plot represents the average of 3 independent measurements, standard errors are displayed as a

lighter shade of the color of each trace. Concentrations refer to the stock solutions, before dilutions required for NTA analysis. **g**) LP-CF640R appear as point-like (diffraction limited) fluorescence when suspended in agarose gel (left field) while empty LPs do not (right field). The two fields were acquired, processed, and displayed with identical parameters. Scale bar 10 μm.

Figure S3

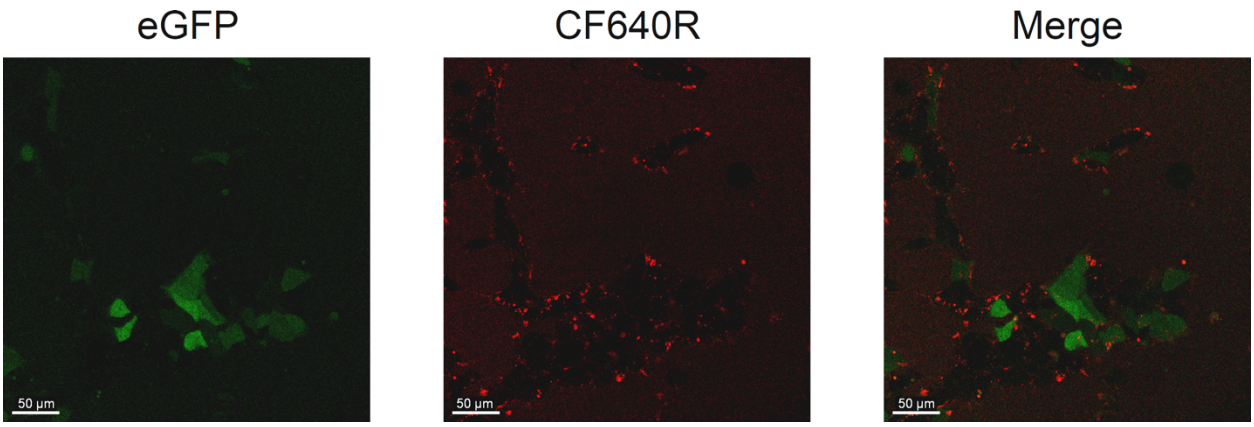

Representative images of cGFP cell line after 24 h incubation with 100 µl of 104 µM free-GCAP1^{CF640R} after replacing cell medium with FluoroBrite DMEM. Left panel shows eGFP fluorescence, center panel shows CF640R fluorescence, left panel shows merged fluorescence.

Figure S4

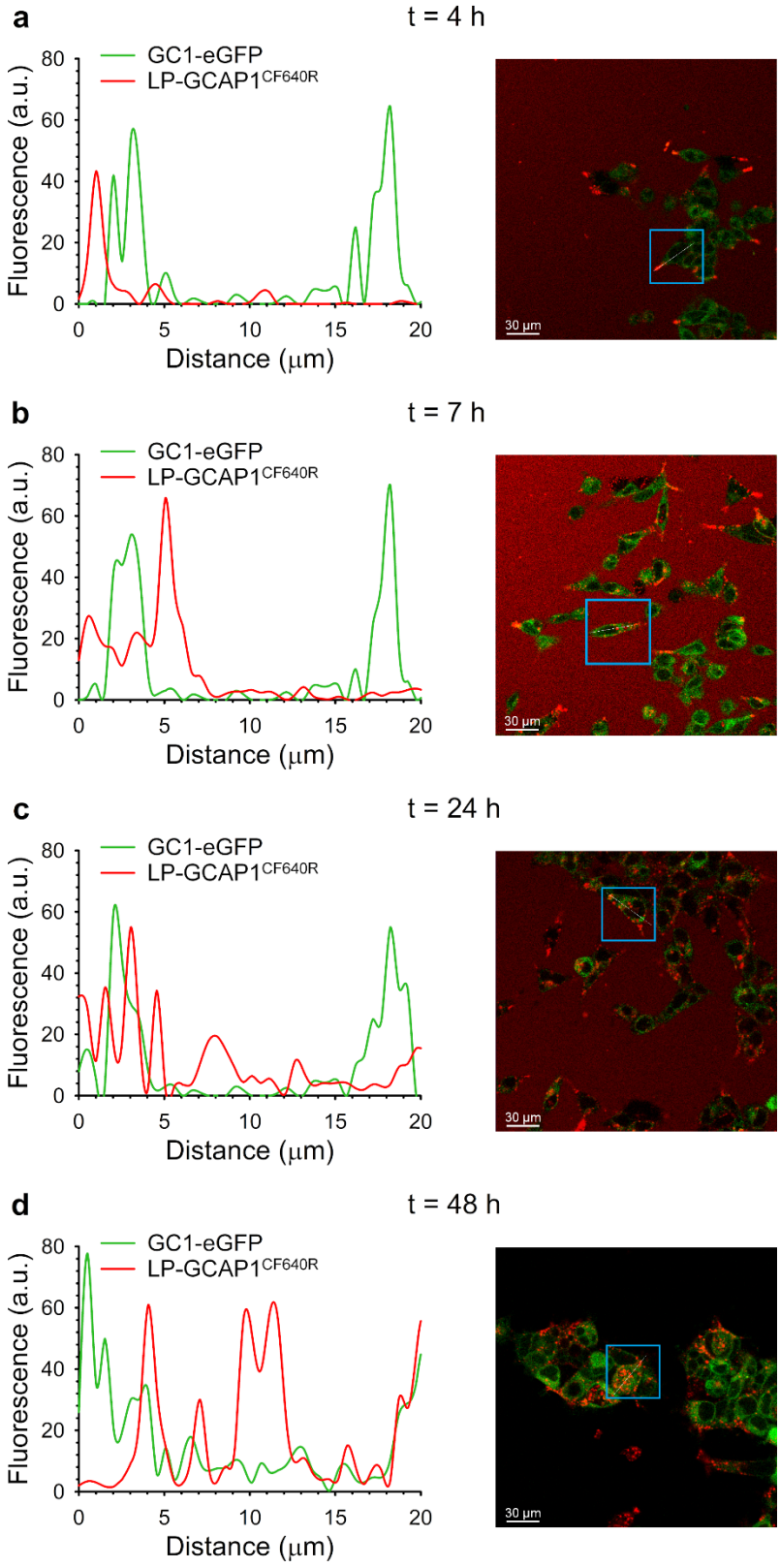
a
t = 4 h
GC1-eGFP
LP-GCAP1CF640R
Fluorescence (a.u.)
Distance (μm)
30 μm
b
t = 7 h
GC1-eGFP
LP-GCAP1CF640R
Fluorescence (a.u.)
Distance (μm)
30 μm
c
t = 24 h
GC1-eGFP
LP-GCAP1CF640R
Fluorescence (a.u.)
Distance (μm)
30 μm
d
t = 48 h
GC1-eGFP
LP-GCAP1CF640R
Fluorescence (a.u.)
Distance (μm)
30 μm

Representative (n= 6) fluorescence intensity profiles (left column) of live cell imaging (right column) of mGFP cell line (green) after **a)** 4 h, **b)** 7 h, **c)** 24 h and **d)** 48 h incubation with 100 µl of 4.6 nM LP-GCAP1^{CF640R} (containing 27.4 µM GCAP1^{CF640R} in the aqueous core, red). Fluorescence profiles were collected on the same z- plane as in **Fig. 3c**. Representative profiles refer to the cell framed in blue along the white line.

Figure S5

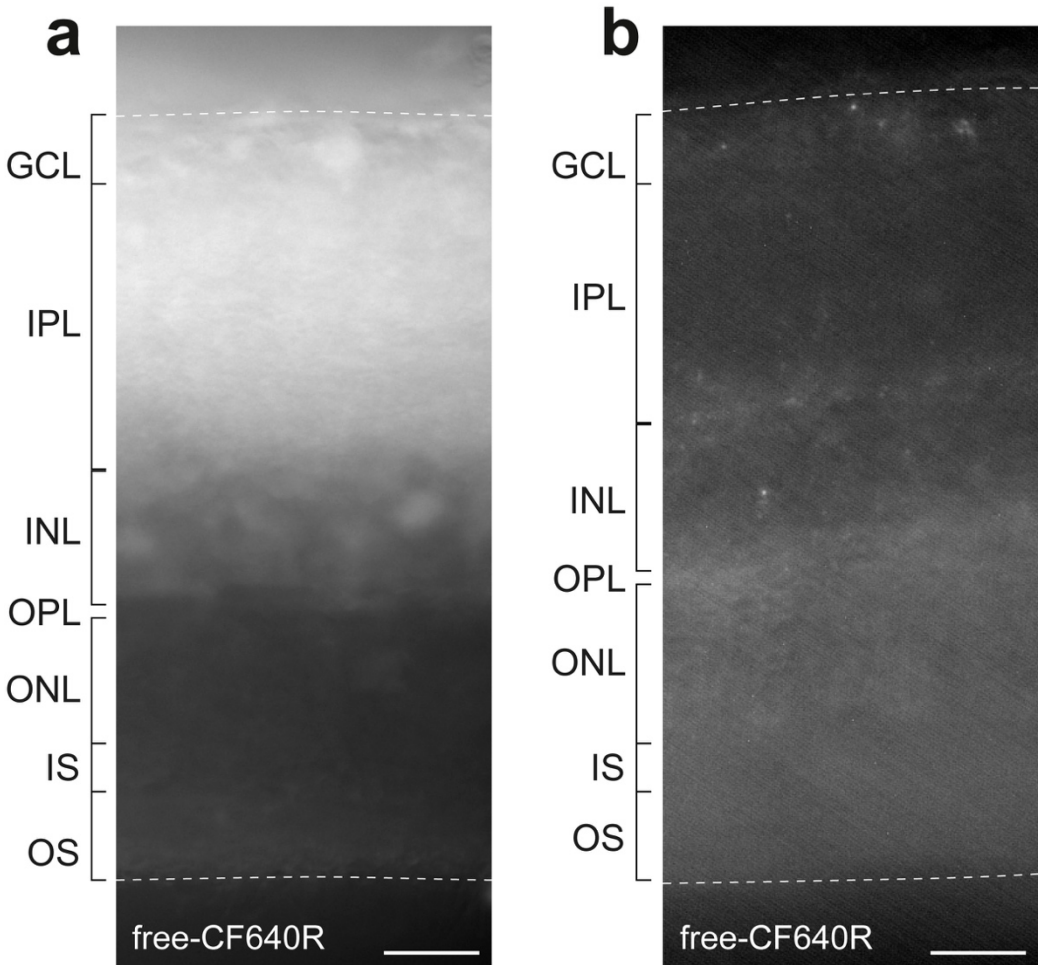

Biodistribution of free CF640R in mouse retinal slices following either **a)** *ex vivo* incubation with 20 µl of 140 µM CF640R in 2 ml Ames' medium (3.5 h at 37°C), or **b)** intravitreal injection of 2 µl of the same stock solution (24 h). Scale bars 25 µm.

Figure S6

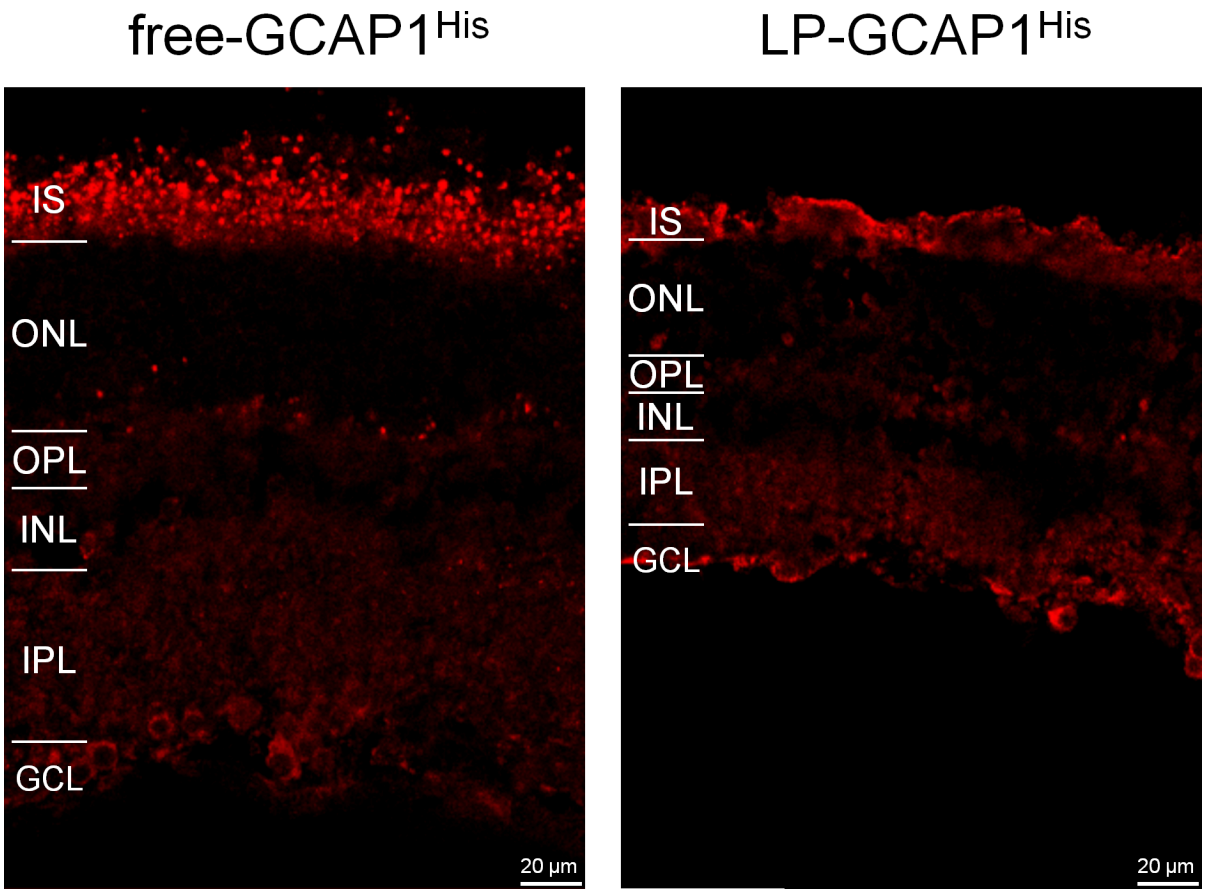

Representative central plane of Z-stack of retinal cryosections after 24 h incubation with 180 µl of 99.6 µM free-GCAP1^{His} (left panel) and 4.5 nM LP-GCAP1^{His} (right panel). Sections were stained with an anti-His antibody (red) using the same image acquisition and display parameters (compare with Fig. 4 in the main text, where nuclei have been stained). Note the presence of more diffused and speckled signals in the case of delivered free-protein, and the prevalence of diffused signal in the case of LP-encapsulated protein at this time frame.

Figure S7

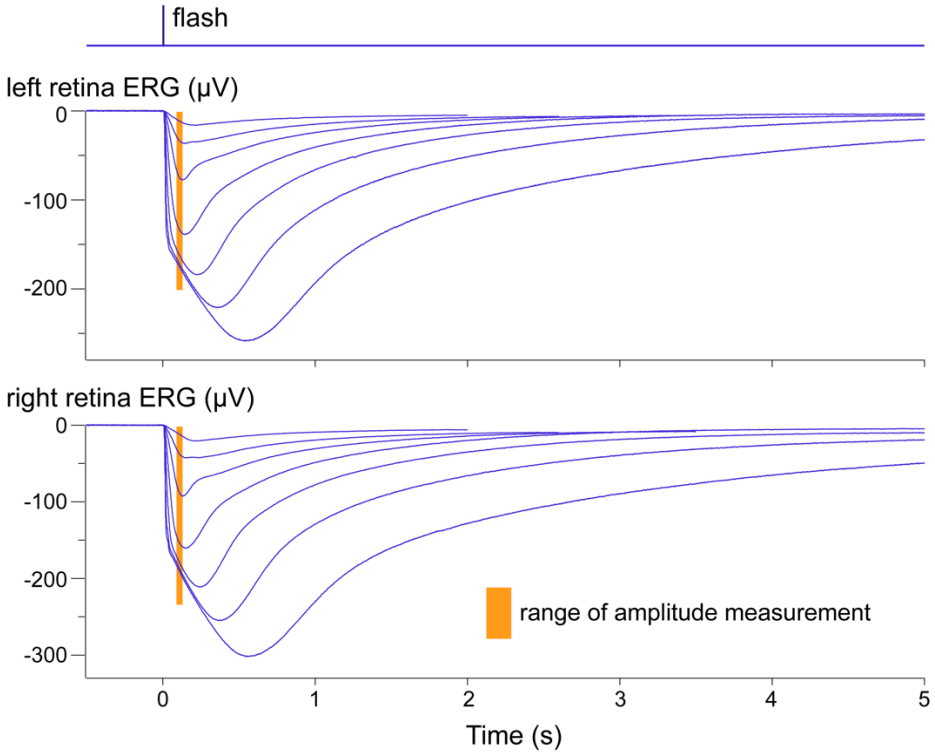

Examples of concurrently recorded *ex vivo* ERG from the two retinas of a mouse. Each trace is the average of several flash responses, with an entire flash family being delivered every 15 min. Flash strengths (ph/µm^2)|no. of repetitions: 3.98|12, 8.27|10, 18.9|8, 50.5|6, 151|6, 510|4, 1660|3. Light sensitivity (i_{50}) was estimated by fitting a Hill function to the response amplitudes measured in the range 90–130 ms after the flash (orange areas). Kinetics (TTP@i_{50}) was estimated as the time to peak of the hypothetical response at i_{50}. Left retina: i_{50} = 23.2 ph/µm^2; TTP@i_{50} = 136 ms. Right retina: i_{50} = 20.7 ph/µm^2; TTP@i_{50} = 136 ms.

Figure S8

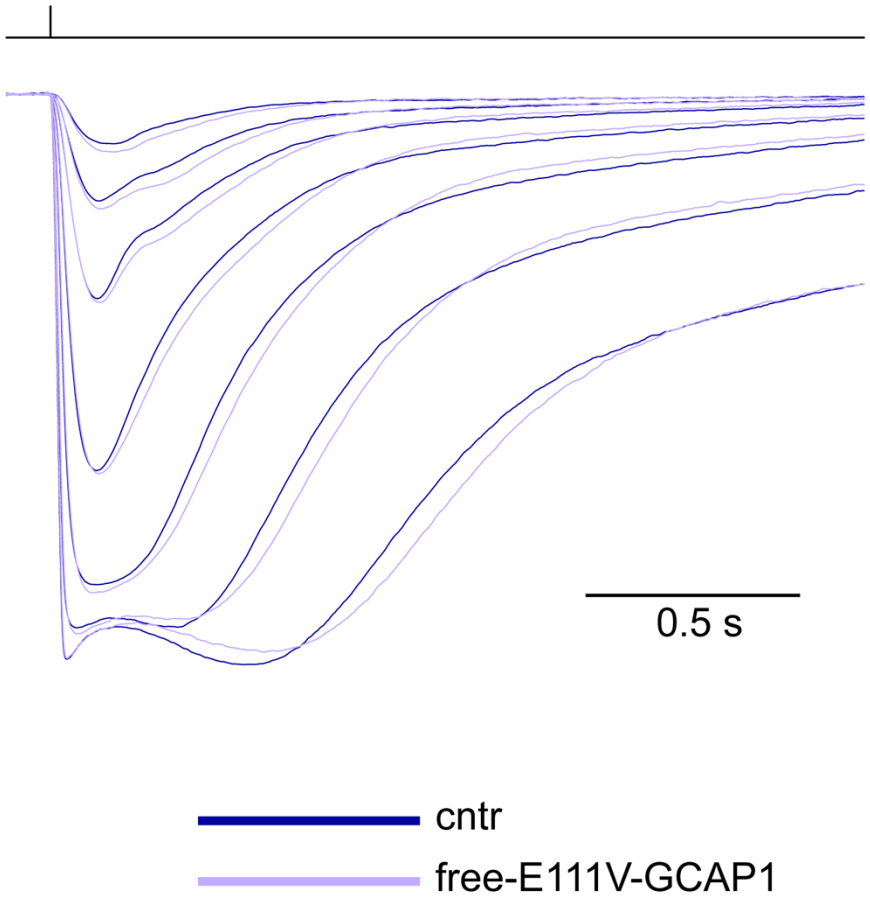

Example of the effect of free-E111V-GCAP1 in slowing scotopic flash response kinetics. $BaCl_2$ (50 µM) was first injected in the 2 ml well followed, after 45 min, by injection of 100 µl free-E111V-GCAP1. The control flash family (blue traces) was recorded just before protein injection, while the treated one (purple traces) after 37 min. Each trace is the average of several responses and the data shown here is from one of the experiments that also contributed to fig. 6h. Note that the effect of the free protein on response kinetics is underestimated in this figure, since the untreated retina in this pair showed a slight acceleration of kinetics over the same period. This highlights the importance of analyzing the effect of the injected formulations by normalizing 'treated' over 'control' retinas, as done in Fig. 6 (see also the Methods section).

Figure S9

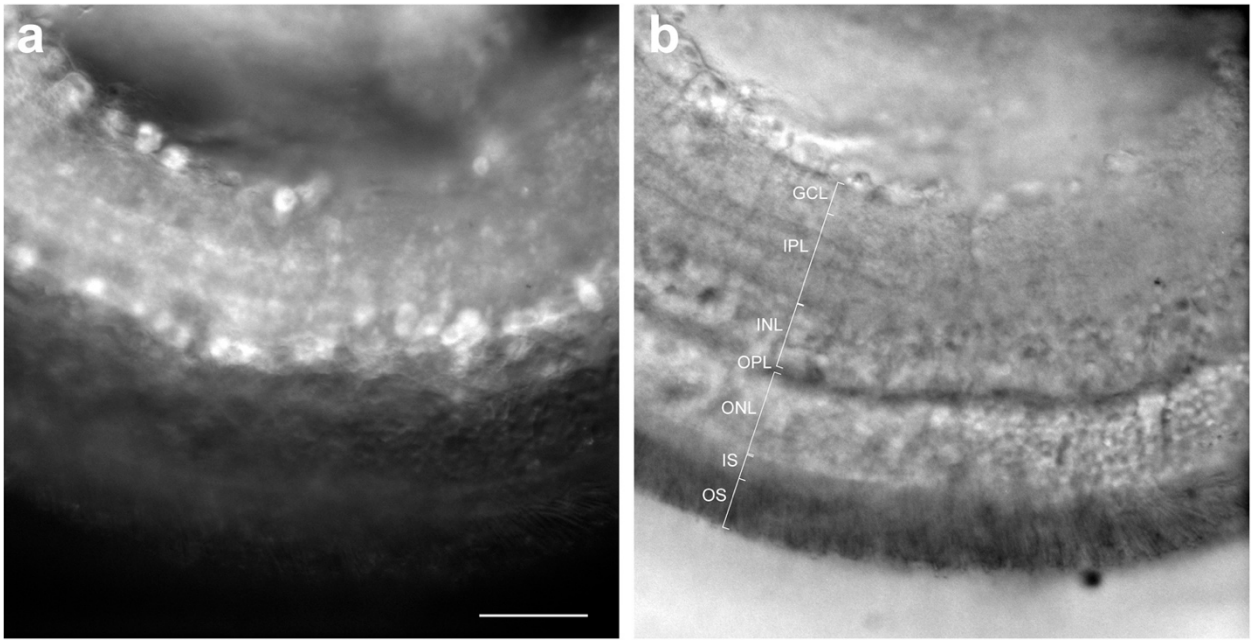

Method of identification of layer boundaries in live slices from *ex vivo* incubated and intravitreally injected retinas. This example shows a slice from a retina incubated *ex vivo* with LP-GCAP1^{CF640R}. **a)** Fluorescence image obtained with the widefield microscope (CY5 filterset, epi-illumination). **b)** The same field and focal plane illuminated and imaged in the near infrared (750 nm LED source, trans-illumination): the various retinal layers were readily distinguishable. All slices used in the analyses of **Fig. 3** were similarly imaged both in fluorescence and in the IR to facilitate layer recognition. Scale bar 50 µm.

Table S1

Liposomes	Size (nm)	Concentration (nM)
LP-empty	158.6 ± 1.1	5.1 nM
LP-E111V-GCAP1	153.3 ± 2.9	4.3 nM
LP-GCAP1^{CF640R}	168.7 ± 0.7	4.6 nM
LP-empty (day 1)	149.1 ± 3.0	4.6 nM
LP-empty (day 90)	151.0 ± 5.4	3.2 nM
LP-empty (day 180)	157.4 ± 2.0	4.0 nM
LP-E111V-GCAP1 (day 1)	164.3 ± 0.4	2.9 nM
LP-E111V-GCAP1 (day 90)	152.1 ± 3.4	2.6 nM
LP-E111V-GCAP1 (day 180)	153.7 ± 1.8	3.0 nM
LP-CF640R	160.5 ± 1.2	3.9 nM
LP-GCAP1^{His}	171.3 ± 4.8	4.5 nM

Size, concentration, and stability over 180 days of LPs loaded with different molecules (dissolved in PBS) monitored by NTA. Data refer to the mean ± standard error of 3 technical replicates.

Movie S1

The three-dimensional structure of GCAP1 is shown as light-grey cartoon with the molecular surface in transparency, Ca^{2+}-ions are displayed as green spheres, the sidechains of Lys residues are labelled represented as red sticks with N atoms in blue. The molecular surface of the primary amines belonging to Lys sidechains is shown in blue in transparency.

Movie S2

Live-cell imaging at 6 h of cGFP cell line incubated with 100 µl of 140 µM free-CF640R, snapshots were acquired at a 30 min interval, green fluorescence refers to eGFP, red fluorescence refers to free-CF640R molecules.

Movie S3

Live-cell imaging at 6 h of mGFP cell line incubated with 100 µl of 104 µM free-GCAP1^{CF640R}, snapshots were acquired at a 30 min interval, green fluorescence refers to eGFP, red fluorescence refers to free-GCAP1^{CF640R} molecules.

Movie S4

Live-cell imaging at 6 h of cGFP cell line incubated with 100 µl of 104 µM free-GCAP1^{CF640R}, snapshots were acquired at a 30 min interval, green fluorescence refers to eGFP, red fluorescence refers to free-GCAP1^{CF640R} molecules.

Movie S5

Live-cell imaging at 24 h of mGFP cell line incubated with 100 µl of 4.3 nM LP-GCAP1^{CF640R} (containing in the aqueous core the equivalent number of GCAP1^{CF640R} molecules present in a 104 µM solution) snapshots were acquired at a 30 min interval, green fluorescence refers to eGFP, red fluorescence refers to LP-GCAP1^{CF640R}.